EXPERIMENTAL VERIFICATION OF NUMERICAL MODELS OF GRANULAR FLOW THROUGH WIRE MESH SCREENS

A Dissertation
Presented to
The Academic Faculty

By

Matthew Sandlin

In Partial Fulfillment
of the Requirements for the Degree
Doctor of Philosophy in the
School of Mechanical Engineering

Georgia Institute of Technology

December 2017

EXPERIMENTAL VERIFICATION OF NUMERICAL MODELS OF GRANULAR FLOW THROUGH WIRE MESH SCREENS

Approved by:

Dr. Said Abdel-Khalik, Advisor
School of Mechanical Engineering
Georgia Institute of Technology

Dr. Sheldon Jeter
School of Mechanical Engineering
Georgia Institute of Technology

Dr. Peter Loutzenhiser
School of Mechanical Engineering
Georgia Institute of Technology

Dr. Michael Schatz
School of Physics
Georgia Institute of Technology

Dr. Seungwon Shin
School of Mechanical and System Design Engineering
Hongik University

Date Approved: November 7, 2017

For Mom, Dad, and Annie.

ACKNOWLEDGEMENTS

I have several people I would like to acknowledge that made this study possible.

First, Dr. Rick Couvillon and Dr. James Davis, of the School of Mechanical Engineering at The University of Arkansas, and Mr. Mark Rouk of Public Service Company of Oklahoma. Without your belief in me, this research never would have gotten off the ground.

Second, Mr. Dennis Sadowski, Mr. Matt Golob, and Mr. Clayton Nguyen, former and current research engineers at Georgia Tech. Their assistance in building the physical experiments was of enormous help.

Third, Dr. Danial Goldman, of the School of Physics at the Georgia Institute of Technology, and his students working in the CRAB Lab. His generous loan of high speed video equipment and training made one third of this research possible.

Fourth, Dr. J. David Frost and Alejandro Martinez of the School of Civil and Environmental Engineering at the Georgia Institute of Technology. Their loan of the Jenike shear cell provided a very important tool used in this research.

Fifth, the members of my reading committee. A comment here, a question there: every one of our interactions provided me with something useful. You not only helped me write a better dissertation, you helped me become a better researcher.

And Finally, my advisor, Dr. Said Abdel-Khalik. Simply put, your guidance helped this dream come true. You have my life-long thanks.

TABLE OF CONTENTS

LIST OF TABLES

LIST OF FIGURES

SUMMARY

A proposed design for concentrating solar power receiver uses a granular material - such as sand, which is inert, inexpensive, and able to operate at relatively high temperatures, thereby increasing thermodynamic efficiency - as the heat transfer and energy storage medium. An early design of particle heating receivers (PHR) utilizes a falling curtain of particles which directly absorbs the concentrated solar radiation. However, falling curtain receivers have several disadvantages including significant heat and particle losses and short residence time within the irradiation zone. One design proposal which overcomes these challenges is the so called impeded flow PHR design, in which the particles flow over, around, or through a series of obstacles in the flow path. This reduces the average velocity of the particles, thereby increasing residence time in the irradiation zone of the receiver. It also reduces heat and particle losses from the receiver. However, the hydrodynamics of complex granular flows are not well understood, rendering a priori design of impeded flow PHR geometries difficult. This investigation had two main goals. First, a series of representative impeded flow PHR geometries were constructed, instrumented and tested, allowing detailed quantitative measurement of such parameters such as mass flux and particle velocity distribution within the receiver geometry. This allowed the development of performance envelopes for the various receiver geometries, which may be useful for future receiver designers. Second, numerical models of the receiver designs were developed using two different approaches - the discrete element method (DEM), which tracks individual particles and models particle collisions as small overlaps, and a two-fluid finite volume method (FVM), in which a granular flow is modeled using typical computational fluid dynamics methods. Predictions of both models were compared against experimental data. It was found that the DEM models generally described the granular flow characteristics better than the FVM models, and were generally able to run faster on parallel computing resources. However, inclusion of heat transfer may be more easily accomplished in future

FVM models.

CHAPTER 1
INTRODUCTION AND MOTIVATION

The use of concentrated solar power (CSP) for electricity production has received increasing amounts of research and public interest in recent years [1]. The renewable nature of the energy source and the lack of pollution during operations are the two chief advantages of CSP.

CSP takes on several forms, including parabolic trough designs, Fresnel lens reflectors, and solar power towers [2], which is the design of interest in this study. All CSP technologies operate using the same principles. A series of mirrors reflects sunlight onto a heat absorbing material, such as water, pressurized air, or a liquid salt solution. This medium can then be used to generate electricity using a typical power cycle, or can store that heat to enable power generation during the night. Figure 1.1 shows a schematic of some currently available CSP technologies [2].

A CSP power tower design consists of a large field of flat or concave mirros called heliostats. These mirrors track the sun throughout the day, reflecting the incident sunlight on a receiver target located on top of a fixed tower. A heat transfer fluid flows through the target, absorbing radiation and increasing temperature. This fluid is then either used to transfer heat to the working fluid of a power cycle, or store the thermal energy for later use. Figure 1.2 shows an image of the Gemasolar power plant in Spain. Claimed as the first commercial scale central heating receiver in the world, it can generate up to 19.9 MW_e and has the capacity for 15 hours of power generation without any solar input [3].

Most current power tower designs use molten salt - a 60/40 % by weight mixture of sodium nitrate and potassium nitrate[4]. However, it must be maintained above a certain temperature, otherwise it would recrystallize and solidify, and the salts themselves are relatively expensive [2]. Another potential drawback is that molten salt has an upper temper-

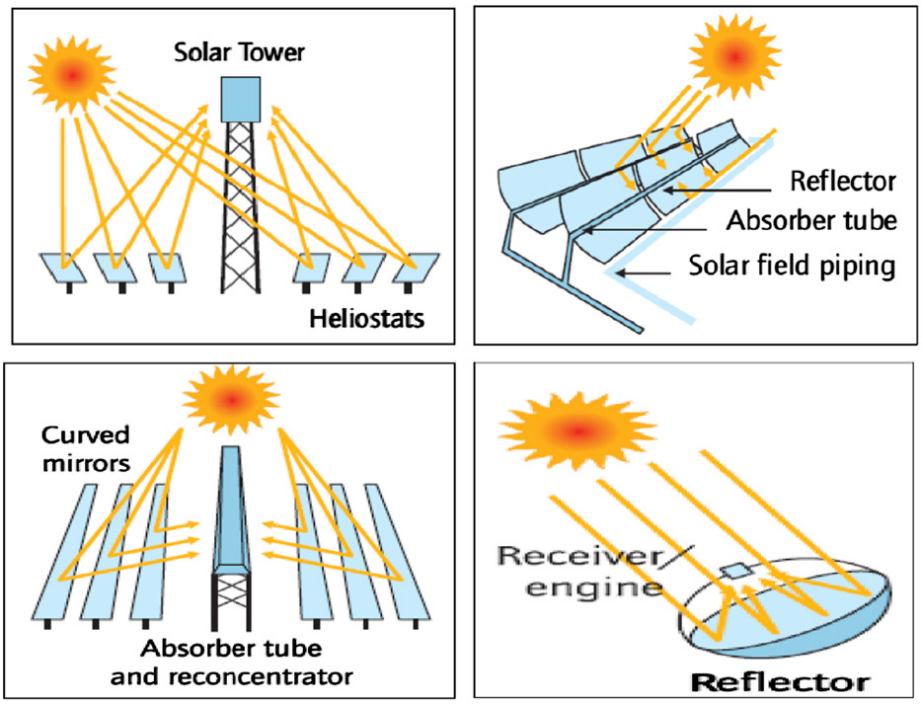

Figure 1.1: Currently available concentrated solar power technologies [2].

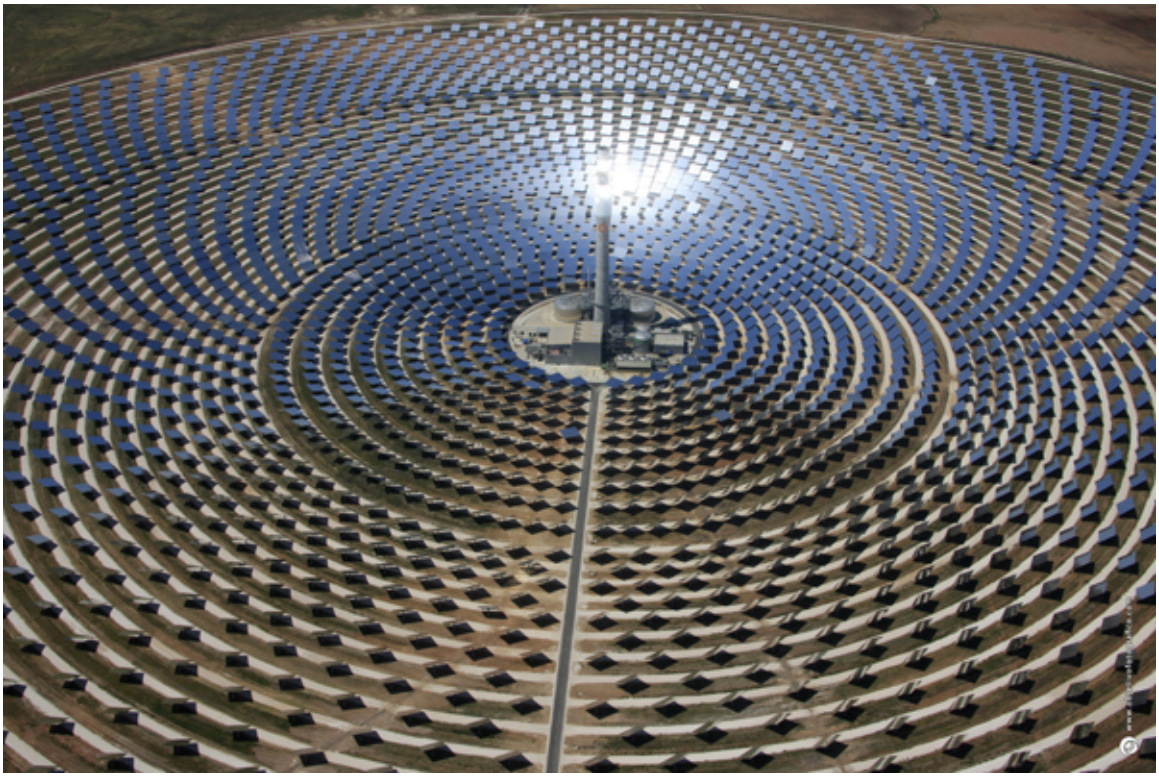

Figure 1.2: The Gemasolar power plant in Seville, Spain [3].

ature limit of only 600 °C due to the limits of both the boiling point of the salt solution and the limitations of the associated piping network with such a high temperature and corrosive environment [4].

A proposed central power tower design attempts to overcome these issues by using a natural or man made granular material (such as sand) as the heat transfer and storage medium. The granular material can be operated at much higher temperatures - potentially 1000 °C - without degradation. It can also be used to heat the working fluid in a power cycle (such as air for a gas turbine) or it can be directly stored for later use.

The use of solid particles for a heat transfer and storage medium has been under investigation since the early 1980's [5]. Extensive research in the area of falling curtain solid particle receivers [6–14], as the design is relatively simple, yet allows for direct heating of the particles by concentrated solar irradiation. However, falling particle curtain designs share a common disadvantage: particle hydrodynamics play a large role in receiver design and particle selection, not only from increased convective heat losses from the particle curtain, but from particle loss from the receiver as well. In fact, particle aerodynamics and heat transfer performance may be at odds, as smaller particles absorb heat faster via irradiation, but lose heat faster due to convective losses, and are more easily blown around by air currents in the receiver. Larger particles can be used to offset some of the particle loss issues, but their higher terminal velocity means that residence time in the receiver is shorter, leading to lower heat absorption (i.e. a lower temperature rise across the receiver). Some of the proposed falling particle designs use particle recirculation systems to overcome this issue, but that adds mechanical complexity and parasitic load. The recirculation system also needs to be carefully controlled to ensure high efficiency.

One proposed receiver design to overcome these issues is a so called impeded flow particle heating receiver. In this receiver design, particles flow over a series of obstacles in the flow path. This design should greatly reduce the issues related to particle loss and convective loss by controlling maximum particle velocities and an overall reduction in air velocity

within the particle flow zone in the receiver cavity. The reduction in maximum particle velocity also increases the residence time of particles in the irradiated zone, allowing high particle temperatures to be achieved without complicated particle recirculation systems.

However, testing of various impeded flow designs has only begun fairly recently. One design variant uses a porous foam structure through which the particles flow [15]. By flowing through a porous foam structure, the average particle velocity is greatly reduced, thus increasing particle residence time in the receiver and increasing heat absorption. Heat transfer may also be enhanced by conduction from the foam structure itself. King Saud Univeristy in Riyadh, Saudi Arabia, has constructed a 300 kW_{th} concentrated solar power plant demonstration facitily for the design and development of a solar heat supply system, with the eventual goal of building a larger combined heat and power CSP plant [16]. This test facility will enable the design and optimization of several sub-systems of a central solar power plant, including the particle heating receiver. Experimental and numerical investigations of granular flow through a high temperature ceramic foam were recently conducted [17].

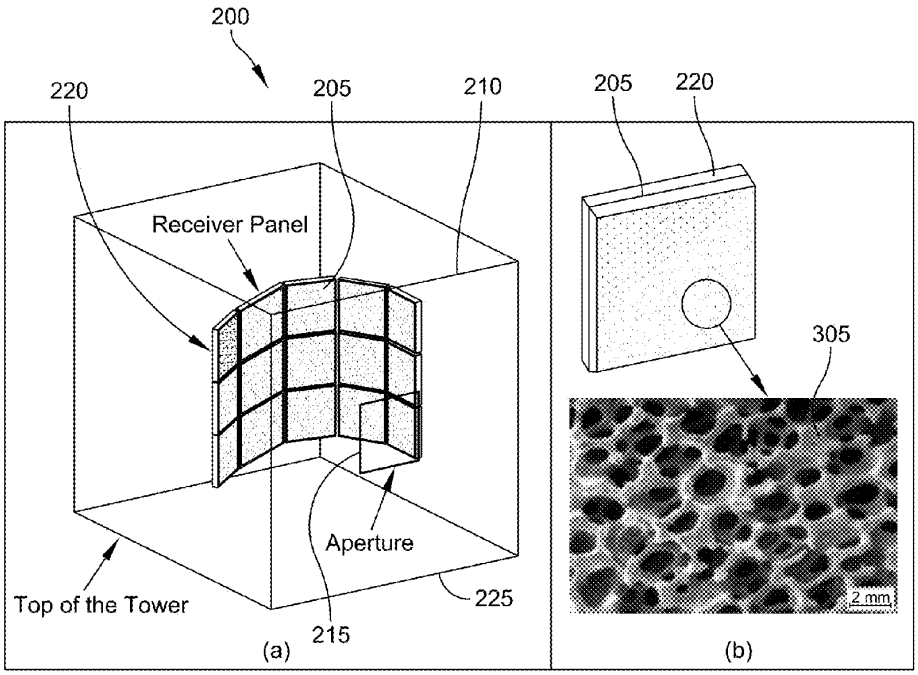

Figure 1.3: General receiver layout of the Al-Ansary patent [15].

Another design variation of the impeded flow particle heating receiver uses wire mesh screens bent into a concave down chevron shape, allowing the particles to flow through the holes in the mesh without significant accumulation on any one screen [18]. Figure 1.4 shows a front view of a test mock up of the inverted chevron configuration.

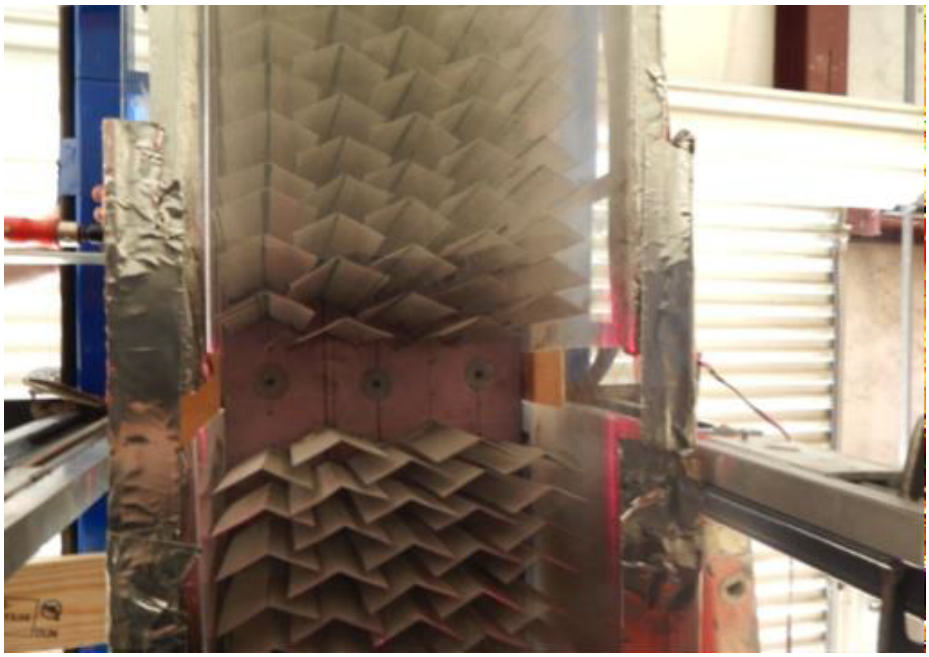

Figure 1.4: Front view of the inverted chevron receiver design [18].

On sun testing of this receiver design at Sandia National Laboratories has shown that high temperatures (>700 °C) and efficiency (>80%) can be obtained [19, 20]. However, during one round of on sun testing, thermal expansion caused the slot that fed particles into the receiver to shrink, thus restricting flow. The loss of flow, and hence cooling, led to failure of the wire mesh structures. In some cases, particles were sintered onto the wire mesh itself, which had severely oxidized and become brittle (the wires were stainless steel). In other cases, the wires had completely vanished, either due to breakage or from completely melting away due to the high power input [20]. Figure 1.5 shows views of the damaged wire mesh receiver.

While this highlights the remaining challenges related to materials selection for this receiver design, it also shows the unfamiliarity with the basic flow phenomena that occur

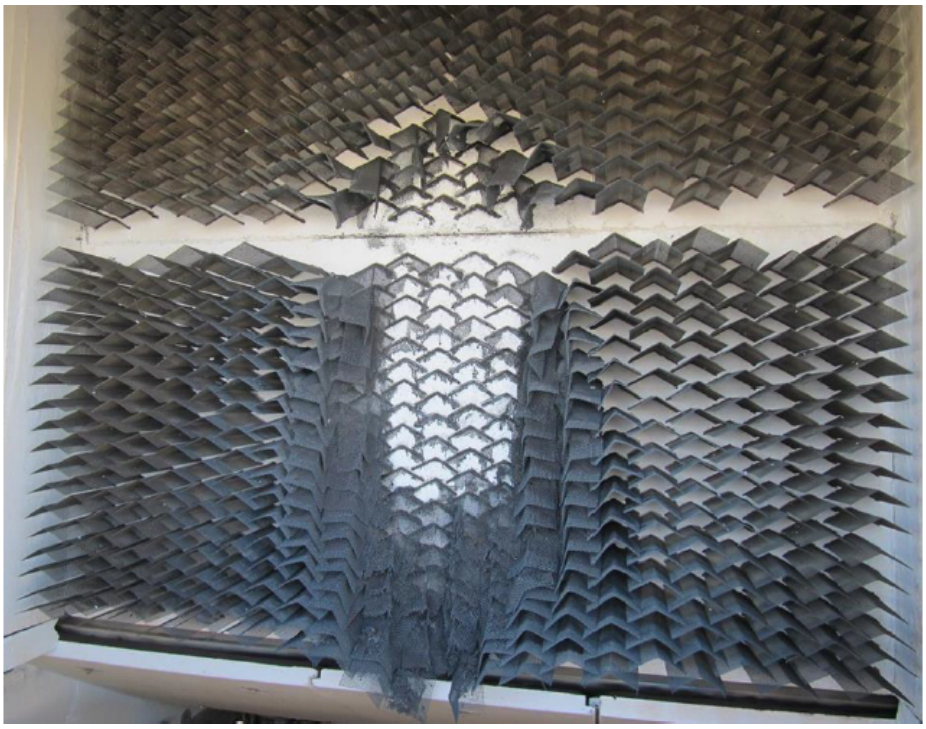

(a) Front view of damaged receiver

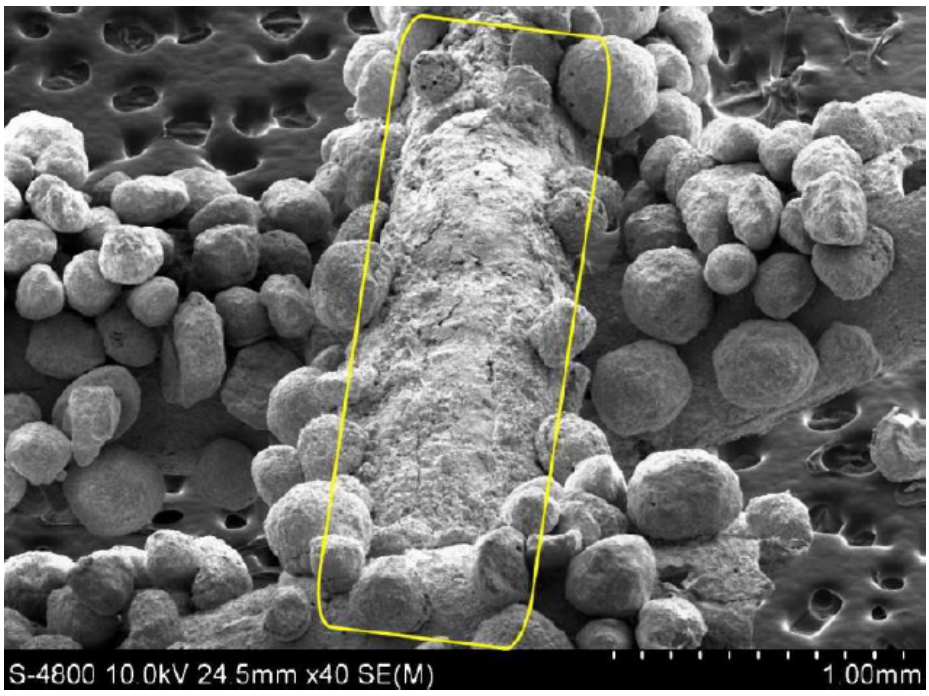

(b) SEM of oxidized wires with sintered particles

Figure 1.5: Views of the damaged wire mesh receiver [20].

through these complex structures. Thus, it was decided to recreate this and other potential impeded flow receiver designs at lab scale. Due to the nature of granular flows, there is always some data that are either very hard or impossible to collect. Also, running flow tests at full scale is time consuming and costly (even without the damage seen in figure 1.5). Therefore, using the lab scale flows as validation, numerical models of the granular flow tests were developed using two different methods: the discrete element method, and the finite volume method. Parametric studies were also performed, showing the relative effect that different model parameters have on the outcome of a simulation. Going forward, these numerical models could assist designers of impeded flow particle heating receivers in evaluating the flow performance of a selected design. The addition of heat transfer modes would enable a more complete simulation of these complex flow systems.

The objectives of this investigation were two fold. First, small representative geometries of proposed impeded flow particle heating receiver designs were constructed to enable study of the steady state mass flow, volume fraction, and velocity distributions of particles within the proposed geometry. Then, the representative geometries were simulated using two different numerical methods. These simulations were compared not only to the experimental results, but to each other, to determine the suitability of each method for simulating granular flows through relatively complex geometries. The results of this investigation will not only enable performance envelopes to be developed for the proposed receiver geometries, but will enable future research to identify and apply the best numerical method for a given set of simulation parameters.

This dissertation is divided into five main parts. First, a brief literature review is conducted of experimental and numerical flow studies, especially those that pertain to concentrated solar thermal power receiver designs. Then, a description of the experimental apparatus and procedure is presented, including information of particle characterization and the use of particle image velocimetry to quantify the velocity of particles through the experiment. Then, a review of both numerical methods and their specific implementation

for this study is laid out. The experimental and numerical results are then presented and compared, along with some parametric studies for one particular geometry. Finally, conclusions are drawn and opportunities for future study are discussed.

CHAPTER 2
LITERATURE REVIEW

2.1 Experimental and Analytic Work

Understanding granular flow has long important in such areas as agriculture and mining. One of the most important aspects of granular flow, at least from an industrial stand point, is being able to predict the mass flow rate of a given material from a hopper or chute. Most early work on granular flows focused on flow through orifices and from hoppers. One of the earliest attempts to find a relationship between material properties, hopper outlet geometry, and mass flow rate was done by Hagen in 1852 [21]. He was the first to postulate a so called "5/2" law relating granular mass flow rate to both the outlet diameter and the particle diameter. He also mentions an outfall arch forming above the outlet taking the shape of a parabola, which would become an item of continuous study.

Beverloo et al. [22] were one of the first to combine a dimensional analysis of the granular flow from an outlet with flow data for several different particles, deriving what is now known as the Beverloo equation. The dimensional analysis is as follows. The rate of flow of any material through an opening $\dot{m}$ is proportional to the density of the material ρ, the area of the opening A, and the average velocity through the opening V

$$\dot{m} \propto \rho A V. \tag{2.1}$$

For a granular material, the bulk density ρ_B is used in place of the actual density of the material, since there will always be a non-zero void fraction in the area of the opening. Thus, equation 2.1 becomes

$$\dot{m} \propto \rho_B A V. \tag{2.2}$$

For simplicity, assume the outlet is circular. Then, the area of the outlet is proportional to its diameter D squared. Thus, equation 2.2 becomes

$$\dot{m} \propto \rho_B D^2 V. \tag{2.3}$$

Finally, the velocity must be computed. It is usually assumed that particles passing through a hopper outlet are in free fall as if released from rest from a surface. This velocity can be easily found via conservation of energy as

$$V \propto \sqrt{gh}. \tag{2.4}$$

While the shape of this surface is still under some debate - whether a paraboloid [21, 23], a spherical section [24], or a full hemisphere [25] - it is assumed that the height that a particle is released from this "free fall arch" is proportional to the diameter of the orifice. Thus, the final form of equation 2.1 becomes

$$\dot{m} \propto \rho_B \sqrt{g} D^{5/2}. \tag{2.5}$$

After plotting their data, Beverloo et al. noticed that the exponent in equation 2.1 tended to be larger than the 2.5 suggested by dimensional analysis. They reasoned that there was an area near the edge of the orifice where flow was still obstructed that was proportional to the diameter of the particle d. They required an additional empirical constant to turn the proportionality into an equality. The final form of the Beverloo equation is then given by

$$\dot{m} = C \rho_B \sqrt{g} (D - kd)^{5/2} \tag{2.6}$$

or, if using a non-circular orifice,

$$\dot{m} = C' \rho_B A' \sqrt{g D'} \tag{2.7}$$

where the effective hydraulic diameter $D' = D - kd$ is used and A' is the area calculated from D'.

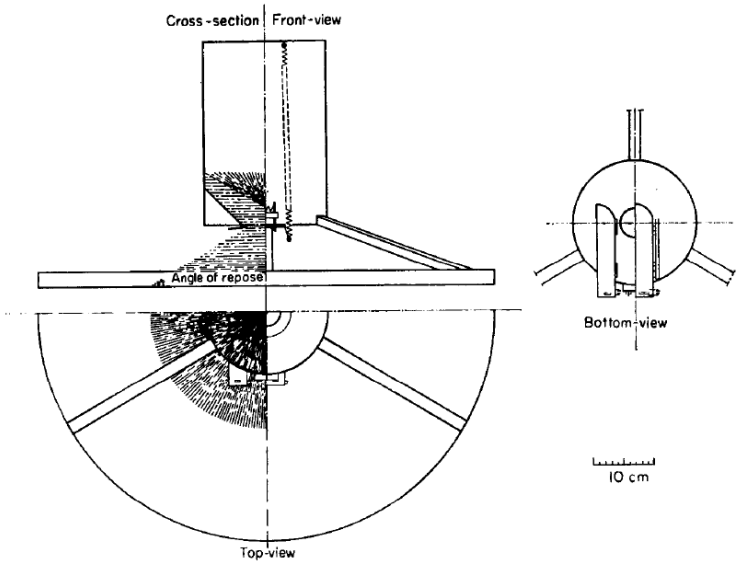

Figure 2.1: Sketch of apparatus used in Beverloo experiment [22]

The Beverloo study used a variety of seeds and a material called "sand." A particle size distribution of the sand is not given, but it is likely that the various seeds used, while far from being circular, were likely very similar in size [26]. Thus, the Beverloo equation is frequently cited for mono-dispersed particles. It should also be noted that the Beverloo study found that the constants C and k didn't vary significantly between the different seeds (the value of k for the sand was twice the value found for the seeds, but they admit that they couldn't measure this quantity with much accuracy). Thus, it appears that the values for C and k are only weakly related to the different material properties.

Other restrictions have been found that place limits on the applicability of this equation. The Beverloo equation has been widely used to predict the flow rate of granular flow from orifices provided that D is roughly six times larger than d to prevent clogging and intermittent flow [26].

Another restriction of the Beverloo equation is on the size of the particles themselves. As the particles shrink, pressure gradients and relative velocities due to entrapped gas start

to impact measured mass flow rates. Generally, the cutoff for a "small" particle is $500\,\mu\mathrm{m}$ [27].

There are a few corrections to the Beverloo equation for small particles. Crewdson et al. [27] reasoned that the pressure gradient acted as a body force in addition to the $\rho_B g$ term in equation 2.6, so the new equation has the form

$$\dot{m} = C\rho_B(g + \frac{1}{\rho_B}\frac{dp}{dz})^{1/2}(D - kd)^{5/2} \tag{2.8}$$

where p is the pressure and z is the axial coordinate. At low Reynolds numbers (< 10), the pressure gradient can represented by the Carman-Kozeny equation

$$-\frac{dp}{dz} = \frac{K_s\mu(1-\epsilon)^2 V_s}{d^2\epsilon^2} \tag{2.9}$$

where V_s is the slip velocity, μ is the viscosity of the surrounding fluid (typically air), ϵ is the void fraction, and K_s is a constant with a value of 180 for spheres. At higher Reynolds numbers, the Ergun correlation should be used [28], given by

$$\frac{dp}{dz} = \left(\frac{150}{\frac{\rho_g V_{mf} d}{(1-\epsilon)\mu_g}} + 1.75\right)\frac{\rho_g V_{mf}^2}{d}\frac{1-\epsilon}{\epsilon^2} + \rho_g g \tag{2.10}$$

where V_{mf}^2 is the minimum fluidization velocity. By making appropriate assumptions about velocities and voidage fractions, equation 2.8 can be used to better estimate the flow rate of small particles from orifices.

There are other general correlations found for predicting flow rates from orifices in the literature. Many of them, such as those found in [26] and [29], follow the simple form of a general power law equation, such as

$$\dot{m} = A\rho D^b \tag{2.11}$$

where D is the outlet diameter and A can be one or several constants. While these

equations can sometimes offer good accuracy, they are not as general as equation 2.6. The theoretical basis behind many of them is not as satisfying as used in the derivation as equation 2.6 [26].

Typically, real world bulk solids are not made of identically sized particles. While particles such as seeds may only show minor variations in particle size, materials such as sand can often have size distributions that can show particles sizes being orders of magnitude in difference. Two possible models for particle size distribution are given by the Rosin-Rammler distribution (also known as the Weibull distribution) and the log-normal distribution [30]. The Rosin-Rammler distribution is given by

$$\begin{aligned} P(z) &= 1 - exp(-z^k) \\ z &= \frac{D}{D_R} \end{aligned} \tag{2.12}$$

where k and D_R are chosen to best fit the experimentally acquired data.

The log-normal distribution is given by

$$P(x) = \frac{1}{2}\left[1 + erf\left(\frac{x}{\sqrt{2}\sigma}\right)\right] \tag{2.13}$$

where erf is the error function and σ is the standard deviation. It can be shown that if particles follow a log-normal in number, they also follow the same distribution with mass, making for simpler analysis.

There has been considerable discussion about the exact nature of the granular flow pattern near an outlet, also known as the "free fall arch." Hagen assumed that it took the shape of a paraboloid [21], while Brown and Richards [24] showed experimentally that this could take the shape of a circular arch (which was also implied in the derivation of equation 2.6).

Hilton and Cleary [25] began their analysis by assuming the shape of the free fall arch was a hemisphere, and then integrated the velocities of individual particles from this sur-

face. When the effects of gas drag were ignored, they were able to recover equation 2.6. When the effects of drag are considered, however, the equation turns into

$$Q = \pi \rho_b R_B^2 \tau_\eta g \left[1 + \frac{1}{k^2} \left(\frac{5}{6} + \frac{w_k^2}{6}(2w_k + 3) + w_k(w_k + 2)(k + 1) \right) \right], \tag{2.14}$$

where

$$\tau_n = \left(1 - \alpha \frac{1 - \epsilon_b}{\epsilon_b} \right)^{-1} \frac{\rho_p d^2}{18\eta} \tag{2.15}$$

is the viscous time scale, and

$$\tau_i = \sqrt{\frac{R_B}{g}} \tag{2.16}$$

is the inertial time scale,

$$k = (\tau_i / \tau_n)^2 \tag{2.17}$$

and

$$w_k = W(-e^{-k-1}), \tag{2.18}$$

where η is the gas viscosity, ϵ_b is the bulk voidage fraction, R_B is the radius of the outlet, and W is the Lambert-W function.

Janda et al. [23] based their analysis on particle velocities and volume fraction at the orifice. By plotting profiles of these variables for different orifice sizes, they found that these profiles took the form of a parabola. They also stressed the similarity of profiles between small orifices, where flow may be intermittent, and large orifices, where flow is essentially constant, showing the generality of their analysis. They derived an expression

for the mass flow rate from an orifice given by

$$\dot{m} = C''\sqrt{g}\phi_\infty[1 - \alpha_1 e^{-R/\alpha_2}]R^{3/2}, \tag{2.19}$$

where the constant C'' depends on the particle diameter d, and is given by

$$C'' = 4\beta\left(\frac{\nu+2}{2\nu}, \frac{1}{2}\right)/\pi d^2 \tag{2.20}$$

where ϕ_∞ is the asymptotic volume fraction for a large orifice, and ν, α_1, and α_2 are fitting parameters. While this analysis was carried out in two dimensions, they note that they three dimensional analysis recovers the familiar $R^{5/2}$ factor of previous equations. Figure 2.2 shows the region where the velocity and volume fraction profiles where determined.

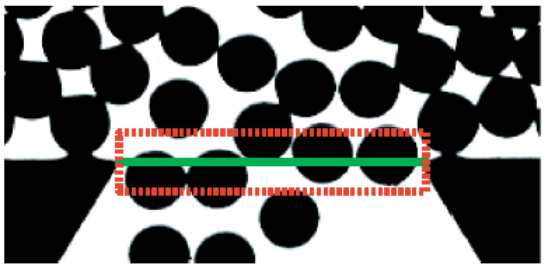

Figure 2.2: Region near orifice used for plotting velocity and volume fraction profiles. The dotted line is where the velocities are determined, while the box shows where the volume fraction was determined [23].

One of the important considerations implied by the previous analyses is the type of flow being described. All of the preceding relations were developed for flat bottomed hoppers, or at least hoppers with a very shallow bottom angle. In this so called "funnel flow" or "plug flow," the material forms a flowing cone above the orifice, eventually growing in size until it reaches the hopper walls, leaving small areas of stagnant material in the bottom corners of the hopper.

Another flow mode is when all of the material in a hopper is in motion. So called "mass flow" occurs in hoppers with sufficiently steep, smooth walls [31]. While mass flow

hoppers have a smaller volume for a given height of material, they are very useful when the material being stored has a finite life or experiences segregation during flow. This type of flow ensures that there are no regions of immobile material. However, this type of flow also means that there is no arching around the orifice, and thus the free fall arch theory does not apply [32]. This means that none of the previous correlations work for predicting the rate of flow through an orifice in the mass flow regime.

Predicting the flow from steep walled hoppers usually involves solving for the stress and velocity fields. Typically, the analysis involves solving for conical hoppers as that geometry simplifies the mathematics somewhat, and because that geometry is commonly used for mass flow hoppers (although solutions exists for wedge shaped hoppers [33]). In a simplified analysis, when the hopper walls are taken as frictionless, the dimensionless mass flow rate can be given as

$$\frac{\dot{m}}{\frac{1}{4}\pi D^{5/2}\sqrt{g}} \simeq \left[\frac{1+k}{2(2k-3)\sin\theta_w}\right]^{1/2} \tag{2.21}$$

where k is given by

$$k = \frac{1+\sin\delta}{1-\sin\delta} \tag{2.22}$$

where δ is the internal angle of friction of the material and θ_w is the angle of the hopper wall as seen in figure 2.3. Notice that equation 2.21 still contains a $D^{5/2}$ term. As might be expected from a simplified analysis (especially one which ignores the effect of wall friction), this relation over-estimates flow rates [34].

Accounting for wall friction adds some complexity to the analysis. Owing to the difficulty in obtaining analytical solutions for the conservation equations in a general sense, one approach provides solutions down the centerline of a hopper and along the wall of a hopper, thus giving upper and lower bounds on the flow rate [35]. The upper limit on discharge rate

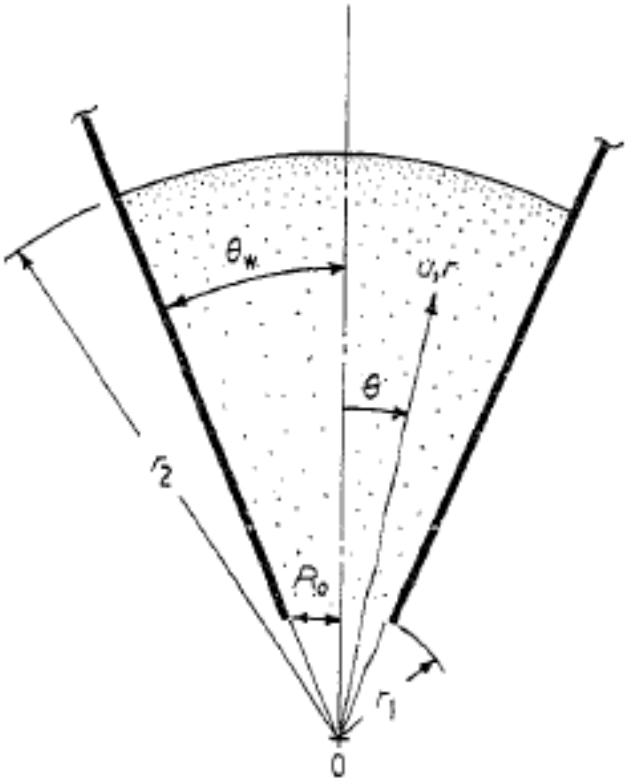

Figure 2.3: Gravity flow through a converging channel [34].

is nearly identical to the form given in equation 2.21

$$\frac{\dot{m}}{\frac{1}{3}\pi D^{5/2}\sqrt{g}} = \left[\left(\frac{1+k}{2(2k-3)}\right)\left(\frac{1-\cos^{3/2}\theta_w}{\sin^{5/2}\theta_w}\right)\right]^{1/2}. \tag{2.23}$$

The lower limit on discharge rate given by

$$\frac{\dot{m}}{\rho} = \frac{4\pi(1-\cos^{3/2}\theta_w)}{3\cos^{1/2}\theta_w}V_w \tag{2.24}$$

where the solution to V_w is given in [35]. As these limits differ by only about 20%, the mean of those two equations can be used for engineering design purposes. However, as this analysis neglects air pressure gradients, it begins over-predicting the mass flow rates for particles smaller than about 500 μm.

Accounting for pressure gradients leads to a rather complex analysis. One proposed solution casts the flow rate Q as a quadratic equation

$$aQ^2 + bQ - c = 0 \tag{2.25}$$

where a, b, and c are constants that depend on the specific model being used [36, 37].

While there have been experimental studies of granular flows through screens (for example [38, 39]), those studies were typically done to study how particle size, bed height, screen size, etc., effected the performance of a screen to classify a material based on size. Therefore, estimations for total mass flux were not derived.

In summary, there are several relations that predict the granular mass flow rate through orifices which range from semi-empirical to analytical. However, most of those are only valid under certain conditions or for rather simple geometries. No general continuum analysis of granular flows appears to exist at present [40].

2.2 Numerical Studies

Numerical studies of granular flows can generally be placed in two broad categories: discrete methods (sometimes called Langrangian methods), and continuum methods (sometimes called Eulerian methods). While each method has its own set of advantages and disadvantages, the use of each method is expected to increase as computational power increases.

Discrete methods typically involve tracking individual particles. The discrete element method (DEM) solves Newton's laws of motion for individual particles and models particle collision as a small overlap [41]. Due to computational limitations, early simulations were implemented on two dimensional disks. However, continuous improvement in computing power has led to the increasing adoption of DEM models for simulating a wide variety of granular phenomena [42].

One of the keys to a successful DEM simulation is choosing appropriate materials properties (such as density, Young's modulus, friction coefficient, etc.) for the study of interest. There are two general approaches to this [43]. The most direct method is the actual measurement of the necessary material properties. While this is generally a simple matter for many intensive properties (and has already been done for many different materials), it is not always feasible to do so (for example, the rolling resistance of the particles that make up a very fine powder). The other method is a so called calibration approach. In this method, a DEM simulation is set up to duplicate an granular flow experiment, such as a shear test or hopper flow. Through successive simulated runs, various input parameters are altered until the experimental behavior is replicated to the desired accuracy. While this method can help narrow down a reasonable range for properties that aren't easily measured, this approach has two main drawbacks. First, it can be time consuming to run multiple simulations should the study call for it. Second, the influence of material properties on bulk behavior are often not independent of each other. Thus, there does not exist a unique set of material properties

that will give the desired behavior.

Yan et al. [44] performed a three level statistical analysis of input parameters for DEM simulations to understand their impact on the model outcome. By altering the Young's modulus, coefficient of restitution, and the coefficients of normal and rolling friction, they determined the relative impact of those inputs on the flow rate, particle velocity, and angle of repose for a small hopper draining onto a flat plate. While they concede that their results may be system dependent, they show that the coefficients of normal and rolling friction have a large impact on both the flow rates and the angles of repose of the system, while the coefficient of restitution and the Young's modulus has a very small effect on the outcome. Particle velocities remained relatively stable for each parametric simulation.

There have been a few DEM simulations of particles flowing through a wire mesh screen. Among other things, Cleary and Sawley [45] simulated a vibrating screen to study the ability of DEM to model a geometrically complex, yet industrially important, industrial process. While mostly qualitative in nature, they demonstrated that DEM was capable of simulating real world processes, and could contribute to engineering design.

Recently, more quantitative analysis has been done on the screening process. Delaney et al. compared DEM results of a horizontal vibrating classifying screen to experimental results using quarry rock. While reasonable agreement was found at very low feed rates, higher feed rates induced errors that were determined to be the result of using spherical particles in the DEM model as substitutes for the highly irregular pieces of rock [39]. Figure 2.4 shows a comparison of the experimental and numerical geometry used in [39]. The very bottom image shows the domain without the sidewalls, allowing for a visualization of the particle feed.

Another vibrating screen study was performed by Dong et al. [46] using an angled vibrating screen. They were able to obtain reasonable results compared to previous experiments [38], and were able to produce simple relations of screening performance based particle and screen geometry to be estimated. Figure 2.5 shows a view of the screen geom-

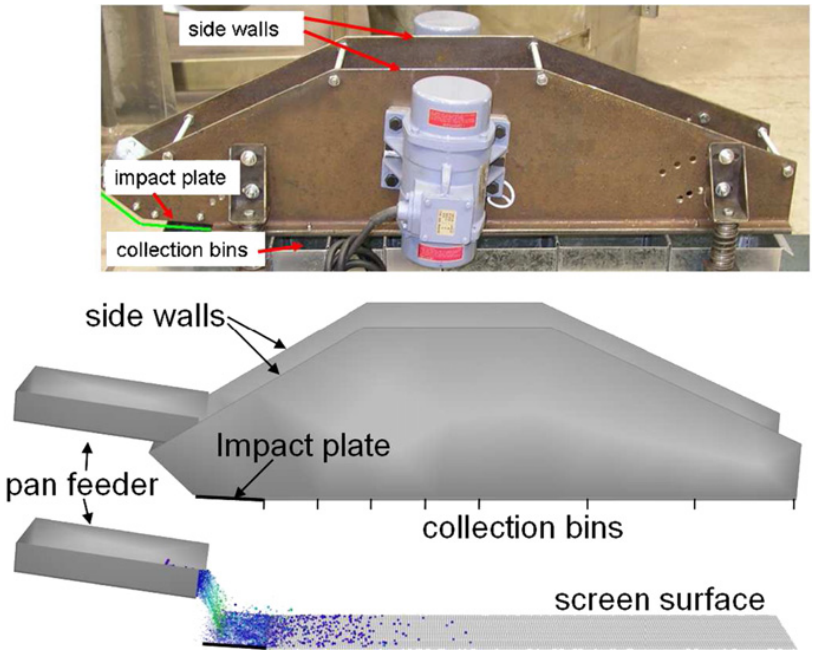

Figure 2.4: Comparison of experimental and numerical set up from Delaney et al. [39].

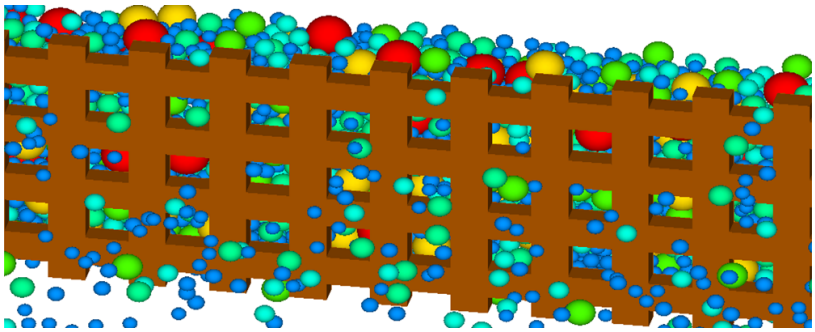

Figure 2.5: View of the screening process from Dong et al. [46].

etry and different particle sizes used in [46].

Due to the large number of particles present in particle heating receivers (as with many industrial applications), the adoption of the DEM model for simulation such processes has been somewhat slow. Zanino et al. performed a preliminary investigation of a falling particle curtain using effective particle sizes that were many times the volume of the actual particles under investigation [14]. However, the model was able to reproduce the qualitative and quantitative behavior of falling particle curtains.

In contrast, continuum methods attempt to describe granular behavior by modeling a

granular flow as a fluid and using methods from statistical mechanics. Modeling a granular "fluid" as it interacts with a separate gas or liquid continuum is known as an Euler-Euler model, or twin fluid model (TFM).

One of the advantages of a TFM over a DEM model is that particle loading has no effect on computational performance, as only the local volume fraction of the granular phase is tracked. However, the selection of closure models for granular momentum exchange, granular viscosity, and granular pressure, as well as appropriate granular boundary conditions, are very important to a successful TFM simulation.

Several studies have been performed to asses the importance of various model parameters on a TFM simulation of fluidized beds and risers. While the specific details differ somewhat, the consensus appears to be that the choice of granular viscosity model and the treatment of particle-wall boundaries are critically important. The effects of solids pressure, drag models, and particle-particle interactions have a much smaller impact on the final results [47–49].

Darelius et al. conducted a TFM simulation of a high shear mixing process, including mesh elements to model the impeller. Their results also found that particle-wall boundary conditions were key to describing material bed height and velocity magnitudes near the wall. However, velocity directions were poorly predicted, highlighting the need for better partial slip boundary conditions in areas of sustained wall contact where the particle-wall coefficient of restitution is not a critical parameter [50]. Figure 2.6 shows the velocity vectors on a vertical plane through the center of the high shear mixer. The large velocity vectors near the blade on the right and the larger scale swirling flows can be seen.

Wardjiman et al. conducted experimental and numerical TFM studies of falling particle curtains in a horizontally flowing gas stream and in stagnant air. Both numerical studies showed good agreement with the experimental results, particularly when compared to a very simple single particle model. This is likely due to the full curtain model being able to capture entrained gas flow within the curtain that the single particle model could not.

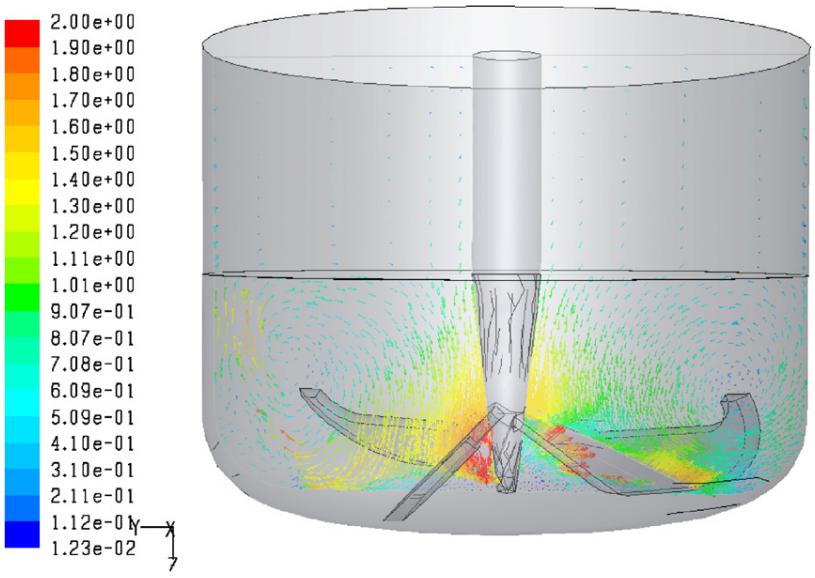

Figure 2.6: Velocity vectors on a vertical plane in a high shear mixer, from Darelius et al. [50].

They also were able to reproduce the behavior of a the particle stream near the outlet of a variable width slot. For narrow slots, the particle curtain initially diverged, while for wide slots the particle curtain began converging (much like a typical fluid flow) [51, 52].

Lee et al. [17] performed two fluid CFD modeling of granular material flowing through a complex porous structure (after the work of [15]) by simulating the structure with a packing of spheres in three dimensions, or an array of infinite cylinders in two dimensions (essentially turning the porous structure into a packed bed). The results show not only good qualitative and quantitative agreement between the simulations and experiments, but also highlight the ability to render a very complex geometry as a much simpler approximation. However, selecting appropriate sizes and distributions of the spheres/cylinders a priori continues to be a challenge. Therefore, this study may be most useful in conducting parametric studies of how the properties of the porous structure effect the flow. Figure 2.7 shows a photograph of the porous foam block structure that was modeling as a pseudo packed bed. Despite their findings, there does not appear to be much literature available on granular flows through particle scale geometries using TFM simulations.

Finally, investigations are increasingly using combinations of discrete and continuum

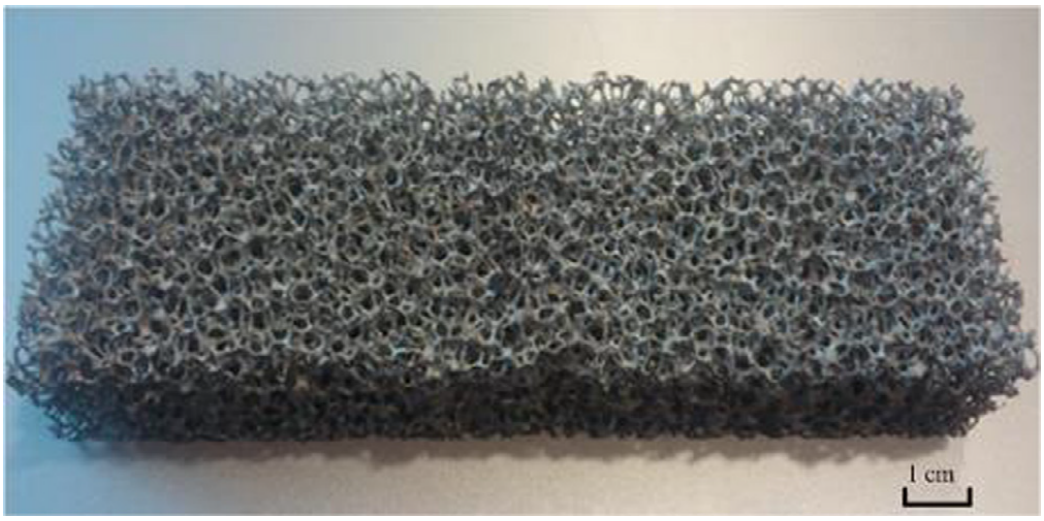

Figure 2.7: Photo of the foam block that was modeled using spheres and cylinders [17].

methods to model the hydrodynamic performance of granular flows. In this method, individual particles and particle-particle interactions are tracked in a Langrangian frame, while particle-fluid interactions are accounted for in an Eularian frame. This allows models to fully resolve both particle scale behavior and particle-fluid interactions, at greater computational cost.

While several investigations using a combined Langranian-Eulerian framework have been undertaken pertaining to particle heating receivers (specifially falling particle curtains, as in [7, 10, 12, 13]), these studies have several key differences that make their application for this particular study questionable. First, they usually assume a very low solids volume fraction everywhere in the domain. Second, particle-particle interactions and particle to fluid momentum transfer are often neglected.

In summary, both discrete and continuous computational models have been widely used to study granular flows, and critical model parameters have been identified for both methods. However, their adoption to flows through complex geometries has been somewhat limited.

2.3 Receiver Designs

Particle heating receivers generally come in five variations, each with their own strengths and weaknesses, summarized in table 2.1 [53].

Table 2.1: Summary of particle heating receiver designs [53].

Design	Advantages	Disadvantages
Free-Falling direct absorption	Direct heating; scalable to large capacities	Increased convective losses; particle loss through open aperture
Impeded flow direct absorption	Increased heating from increased residence time; reduced convective and particle loss	Overheating of obstruction materials; added cost and complexity
Centrifugal direct absorption	Controllable particle residence time	Large rotating receiver; scalable design
Enclosed indirect absorption receiver	No particle loss and reduced convective loss	Large heat transfer resistance between walls and particles; potential for hot spots and limitations on solar flux
Enclosed fluidized particle receiver	Increased particle heat transfer; no particle loss	Increased complexity; heat loss from fluidized gas; scalability

While simple falling particle curtain receivers are the simplest design and have the potential for large heat transfer due to direct irradiation of the particles, the aerodynamics can limit particle size [6] and lead to particle loss [9].

Kim et al. [8] conducted an experimental and numerical study of a falling particle curtain at various flow rates (controlled by a variable thickness slot) and particle sizes. They determined that the particles reached terminal velocity after falling about 3 meters, and that the curtain opacity approached steady state at this point. The overall solids fraction in the curtain was determined to be less than 3 percent, indicating that intra-particle interactions were negligible. Their numerical model agreed quite well for the particle velocity and solids fraction, but the curtain thickness diverged considerably from the experimental results. The curtain thickness appeared to be mostly influenced by the thickness of the

slot from which the particles were dropped, with wide slots producing an initially converging curtain (much like a fluid flow), but narrow slots producing an initially diverging curtain. This likely indicates the dependence of flow structures on intra-particle interactions in highly packed areas (i.e. near the hopper outlet). They also noted a strong relationship between particle size and curtain opacity, but note that smaller particles are much less aerodynamically stable in an open receiver, especially under windy conditions. A later study by Kim et al. [9] showed the effect that wind had on particle loss through an open receiver on a falling particle curtain. This study indicated that a relatively deep cavity with the particle curtain close to the back wall can be made somewhat resistant the effects of particle loss from windy conditions. However, this study was done on a cold receiver, neglecting the effects of convection currents from warm particles. This study indicates a strength of a particle receiver with some sort of structure in the flow path, as wind is likely to be less of a factor, thus allowing for a wider selection of potential particles.

Several subsequent studies on falling particle curtains which include heat transfer models have been performed [7, 10, 12]. Convective losses are cited as a primary area for design improvements in all studies. Methods to control convective losses include different receiver cavity designs, the placement of the particle curtain in the receiver, and air curtains at the receiver opening.

Another attempt to combat particle and heat loss is to use a face down receiver with particle recirculation. Röger et al. [11] performed an energy balance of a face down receiver using correlations for parameters such as particle curtain absorption and air entrainment (i.e. not a full CFD/DEM analysis). They found that the face down design mitigated some of the particle and heat loss found in a typical particle curtain, but required a larger heliostat field and a taller tower. Particle recirculation was also found to greatly increase part load efficiency, at the cost of increases parasitic load. Figure 2.8 shows a drawing of the face down receiver concept, and the large surrounding heliostat field, used in the Röger et al. study. A more recent study of a similar face down geometry with recirculation has

been done by Gobereit et al. [13], including a combined Lagrangian-Eularian model for the falling particles. This study shows the same general results as the Rögers et al. study, but the addition of CFD modeling showed that side winds increase convective heat loss due to vortex formation inside the receiver.

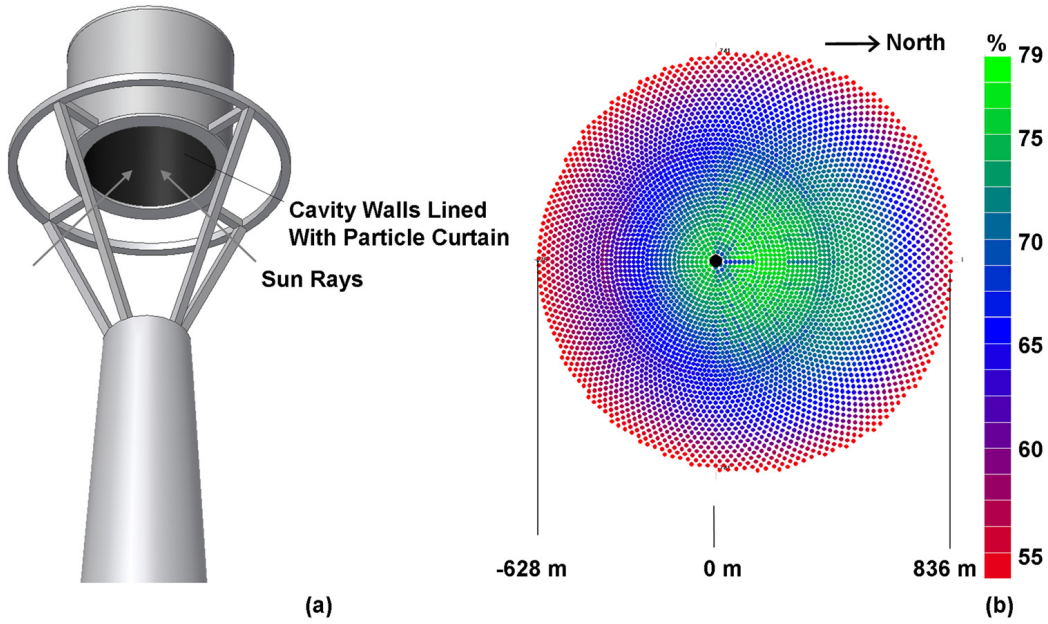

Figure 2.8: Face down heating particle reciever and surrounding heliostat field from the Röger et al. study [11].

Impeded flow receivers are the focus of the current study. Several on sun tests have been performed of a proposed design using an array of wire mesh screens in the flow path. The screens increase the residence time of particles in the receiver while ensuring uniform particle flow. Studies by Ho et al. [19, 20] have shown that the proposed design is able to achieve particle temperature rises in the range of 25-100 °C, receiver efficiencies greater than 80 %, and better control of particle loss and convective heat loss. However, near the end of one of the on sun tests, a decrease of particle flow in the receiver caused the wire meshes to overheat and fail. This highlights the need for careful material choices in such a receiver design (the wire meshes were stainless steel), and a better understanding of the hydro- and thermodynamic performance of future receiver designs of this type.

Another design to control particle and heat loss and increase particle residence time

is with the use of a rotating receiver. Wu et al. [54] performed numerical modeling of a rotating receiver design. Particles are fed onto the inner surface of a rotating drum, which forces the particles into a small layer on the inner surface of the rotating drum. Their model showed good agreement with experimental data with regards to particle outlet temperature, but show large deviations for wall temperatures inside the cavity, likely due to the uncertainties present in the incoming radiation flux model. Their model predicts particle temperatures in excess of 900 °C and efficiencies greater than 85% for a 1 MW_{th} receiver design. However, the rotating drum adds additional mechanical complexity and parasitic loss, and there are questions about scaling the design up to larger capacities. Figure 2.9 shows a schematic of the rotating receiver design proposed by Wu et al.

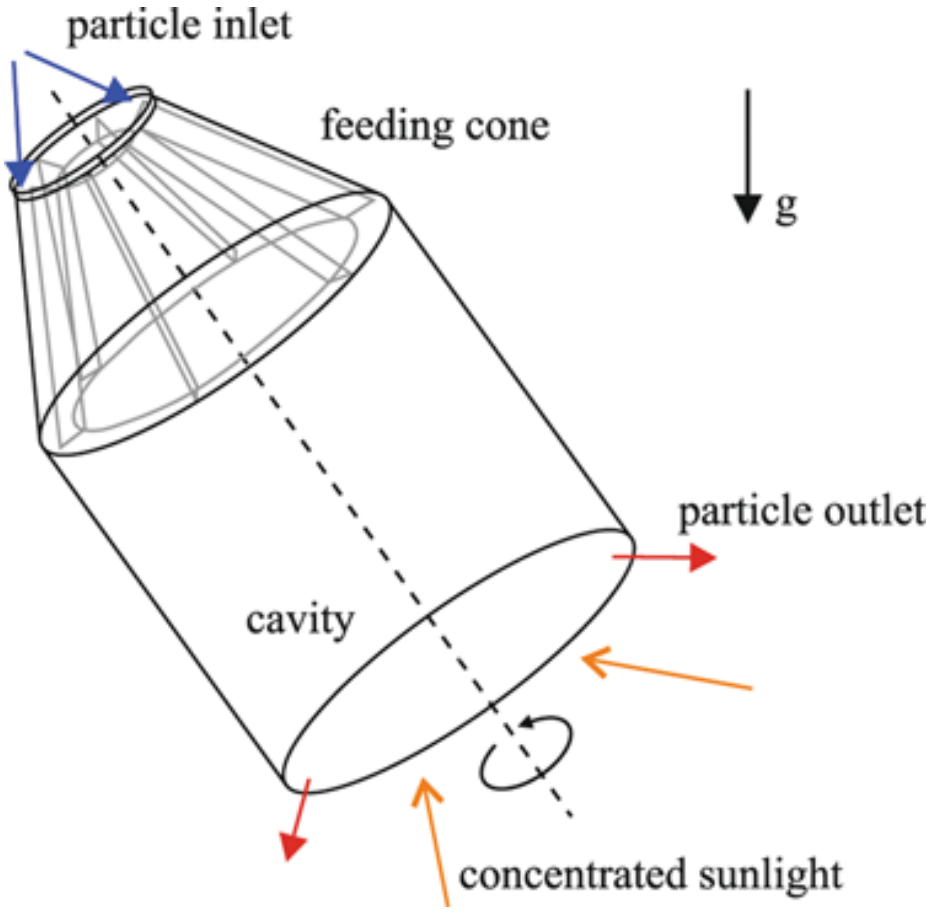

Figure 2.9: Schematic of a rotating particle receiver used in the Wu et al. study [54].

One particle receiver design features similar hydrodynamics to an impoeded flow de-

sign, in which particles flow through an array of heated tubes. However, the main mode of heat transfer to the particles is from the tube surface; it is the tubes themselves which abosrb the bulk of the solar radiation. Martinek and Ma [55] performed a two fluid CFD simulation of a solid particle receiver that consists of granular material flowing through an array of absorber tubes. Initially, the model was provided with uniform inlet conditions to give a desired solids flow rate. After achieving steady state, the spatial inlet profiles were used as the initial conditions of another simulation. These simulations were also used to study heat transfer between the granular flow and the absorber tube walls. It was found that the CFD models were not able to calculate random flow fluctuations that were found in the experimental studies of the same geometries. These random oscillations in the experimental receiver were shown to greatly enhance the particle-wall heat transfer, but the CFD model consistently under-predicted the global heat transfer coefficient. The discrepancy increased at higher solids flow rates. They determined that the likely causes of this discrepancy were the simplified boundary conditions of inlet flow (noting that completely uniform and symmetric flow are not achievable in practice, and due to the enhancement of wall heat transfer, perhaps undesirable), and the failure of the fundamental physics modeling available in the two fluid model to provide adequate closure for the particle interaction equations. They suggested that enhanced closure models could be developed from experimental calibration and DEM modeling, but note that the computational requirements of a DEM model makes it difficult to apply to anything but a very small simulation. Figure 2.10 shows an example of the CFD model of the flow around the hexagonal tubes, while figure 2.11 shows snapshots of the experimental flow. The small instabilities are clearly visible in the experimental flow.

Building on the work of [55], Morris et al. [56] performed parametric DEM studies of the same hexagonal absorber tube array while varying parameters such as tube spacing, hexagon geometry, and particle size. It was found that the particle size had the strongest effect on heat transfer, but also had the strongest effect on computation time. The results

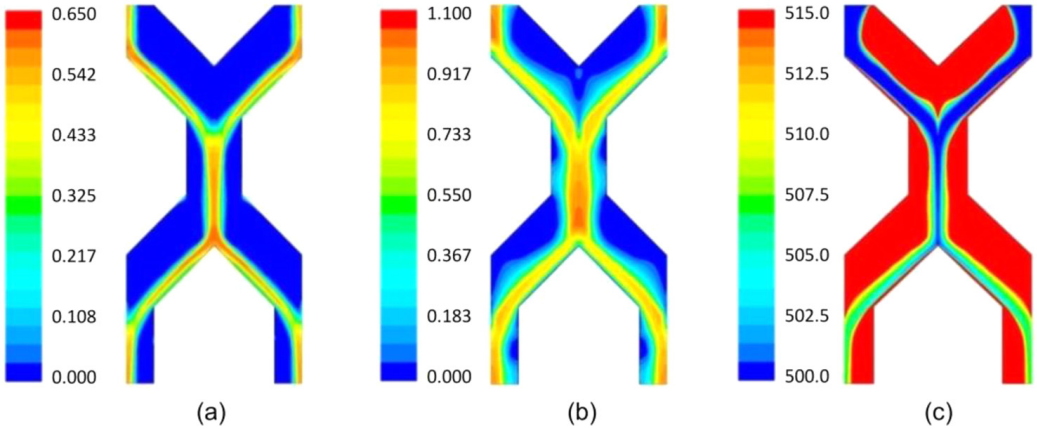

Figure 2.10: Contours of (a) solids volume fraction, (b) solids velocity (m/s), and (c) temperature (K) for the baseline dimensions and solids flow rate from the Martinek and Ma study [55].

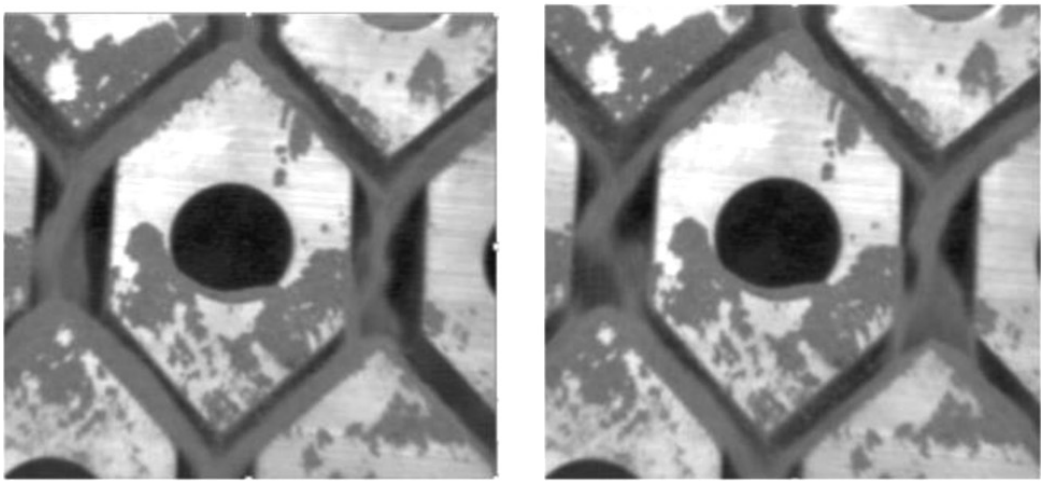

Figure 2.11: Snapshots of granular flow around hexagonal abosrber tubes from the Martinek and Ma study. The CFD model was not able to capture the random flow instabilities present in the experimental flow [55].

of the DEM model were used to validate a continuum model of surface to granular heat transfer [57]. The continuum model was able to agree with the DEM heat transfer data to within about 5 percent. This study only validated the heat transfer performance of the continuum model; more work is needed to validate the overall hydrodynamics of the system, as [55] showed that near wall particle volume fraction contributes significantly to overall heat transfer. Furthermore, the continuum model was shown to be sensitive to the coefficient of restitution (with poorer performance as lower values), and very sensitive to the solids concentration [57]. This study neglected any radiation heat transfer effects, which could be significant at higher temperatures. Figure 2.12 shows a snapshot of the DEM study for the granular flow over the hexagonal absorber tubes in the Morris et al. study.

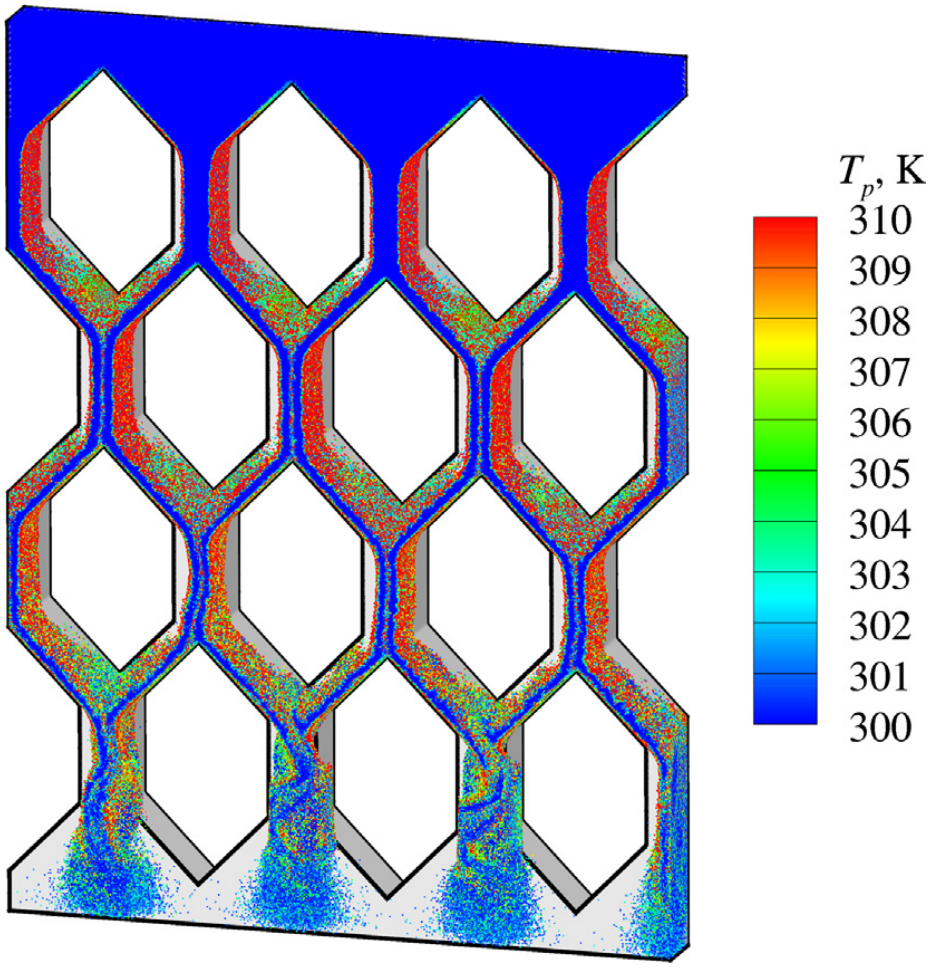

Figure 2.12: DEM model of granular flow over hexagonal absorber tubes from the Morris et al. study [56].

Owing to its large scale adoption by other industries and its potential for high particle heat transfer, receiver designs based on particle fluidization are also under study. Flamant et al. [58] and Benoit et al. [59] have conducted on sun testing of a receiver based on a dense suspension of particles. Typical fluidization processes are characterized by a high fluid velocity and low solids fraction. However, this leads to high parasitic load, accelerated particle and component wear, and low wall to particle to wall heat transfer. The dense suspension concept uses much lower fluid velocities and higher solids fractions to negate these issues. In their design, aerated particles flow through a section of tube that is directly heated with solar flux, and particles absorb heat from the tube walls. Heat transfer to the particles is enhanced by counter-current flow within the tube, which also acts to pre-heat the particles before entering the irradiated zone of the tube (figure 2.13 shows a schematic view of the recirculating flow patterns). While high wall to particle heat transfer coefficients have been achieved (up to 1100 $W/m^2 - K$), the design has so far only been tested for a single tube. More testing is needed to determine the scalability of the design.

Finally, one design proposal to reduce particle and heat loss involves enclosing the particle heating cavity with a transparent window. Del Campo et al. [60] and Mecit et al. [61] have performed modeling of overall receiver cavity performance and the thermodynamic study of the window itself. Their results indicate that convective losses are reduced as expected. However, window design is critical: not only does the window need to be transparent to the spectrum of incoming solar radiation (important due to the magnified flux levels), but ideally should be transparent to the longer wavelength radiation re-emitted by the particles and the cavity itself. Otherwise, performance is degraded and window damage can result (it should be noted that the proposed receiver design in [60] and [61] differs from the other particle heating receiver designs summarized here in that their design is based on heating up very small carbon particles entrained in an air stream, which in turn heat up the surrounding air. However, the benefits and drawbacks of the window concept should be generally applicable to a "typical" particle heating receiver).

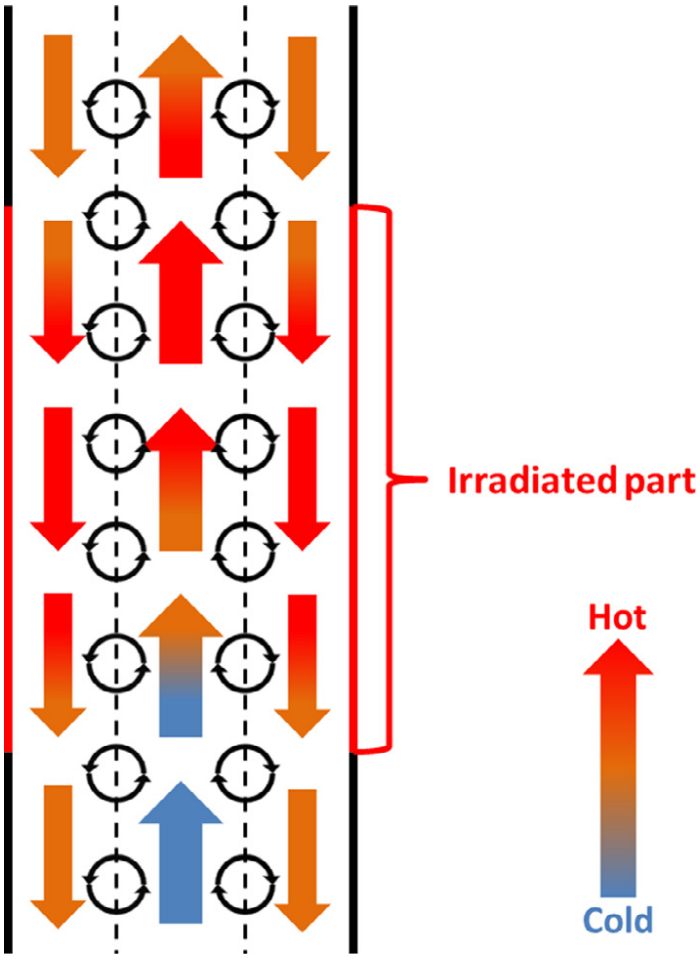

Figure 2.13: Schematic view of particle recirculation in the heat flux tube from the Benoit et al. study [59].

In summary, there are several potential designs under development for a particle heating receiver for use in solar thermal power applications, each with its own set of advantages and drawbacks. The proposed development of an impoeded flow particle receiver seeks to minimize convective heat loss and particle loss and increase heat transfer without the need for additional parasitic load loss due to particle recirculation. However, understanding the hydrodynamics of particle flow through the receiver is a critical area of study.

CHAPTER 3
EXPERIMENTAL WORK

This section will provide details about the experimental work performed for this study, including characterization of the granular material, details of the experimental apparatus, steps performed during testing, and a brief overview of particle interpolated velocimetry analysis.

3.1 Tested Granular Materials

Two different granular materials were used in this study, which were chosen because of their different mechanical and geometric properties. One material could be thought of as a "natural" material, while the other could be thought of as an "engineered" material. Both materials (or similar substitutions) are readily available from industrial suppliers.

The "natural" material is a product called Carboaccucast ID50-K, made by Carbo Ceramics Inc. It is a ceramic composite material used in metal casting applications. It has a well known composition and particle size distribution as seen in tables 3.1 and 3.2. In addition, it has good thermal and optical properties that make it a good candidate for solar thermal power applications [62–64].

Table 3.1: Chemical composition of ID50-K [65]

Al_2O_3	SiO_2	TiO_2	Fe_2O_3	LOI (%)	Moisture (%)	pH
70.00	17.00	4.00	7.00	0.20	0.02	7.00

The "engineered" material is a product called ballotini mil 8 ("mil" not referring to a unit of measurement, but rather to the specification MIL-PRF-9954D [66]), made by Potters Industries LLC. As the name implies, they are small glass beads used in sand blasting and

Table 3.2: Published particle size distribution of ID50-K [65]

Sieve No.	40	50	70	100	140
% weight	0.1	37.4	44.6	16.4	1.5

peening applications. The glass beads are much more uniform in size and shape than the ceramic material, as seen in table 3.3. This material was chosen to attempt to use a material with different flow properties and a different size distribution than the ID50-K material.

Table 3.3: Typical Potters Beads ballotini sizes per MIL-PRF-9954 [67].

Designation	US sieve	In. max	In. min	μm max	μm min	Min % round
6	50-70	0.0117	0.0083	300	212	80
8	70-100	0.0083	0.0059	212	150	80

As particle size is an important parameter for determining the mass flow rate of a given material through an aperture, attempts were made to verify the size distribution of both materials. Sieve tests using ASTM E11 sieves were performed for both materials at various points during testing to see if the material being used was the same size distribution as the published specifications called for, and to see if the size distribution was changing over time (for example, losing or creating very fine particles).

The ceramic material was sieved several times during the course of flow testing. The results obtained from sieving the ceramic material seemed to indicate that the material being tested had a larger average diameter than published, with nearly all of the material being screened out before the # 70 mesh, as seen in figure 3.1. The lack of fines was especially noticeable.

None of the material tested was from a sealed container straight from the manufacturer, and different batches of material were used at various times in the testing apparatus. There are two likely explanations for the lack of fines as seen in the sieving results. The first is the sampling procedure. There is no single “best” way to prepare a sample of granular material

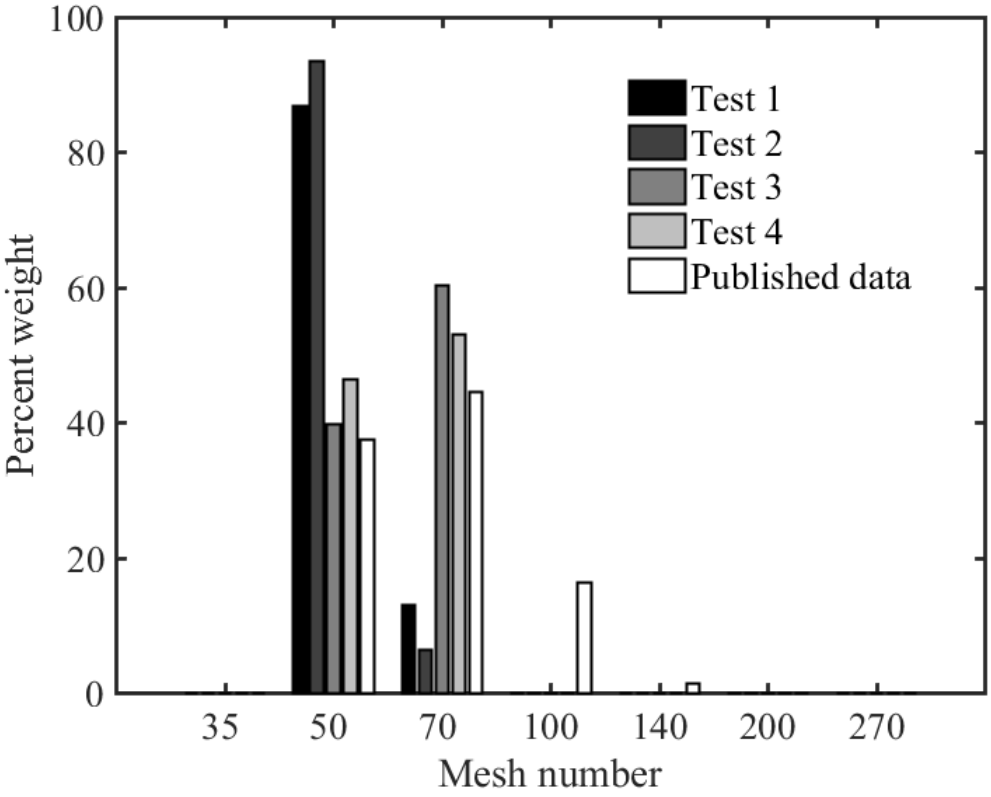

Figure 3.1: Comparison of sieve analysis of ID50-K material against published size data. The material used for these sieve tests had been used previously for flow testing.

for sieve testing, as both the material itself and its matter of handling and transport will effect the sample (i.e. coal being carried in rail cars, sand being moved by conveyor belt, fine powder using pneumatic transport, etc.) [68]. Several methods and devices have been proposed to ensure that the sample obtained for testing is a good representation of the rest of the material [68]. For these tests, a collection pan was held under the test section while in operation for a few seconds until several hundred grams were collected. It was felt that this would be the quickest way to obtain a thoroughly randomized sample.

Another possible explanation could simply be a major loss of fines during testing. As previously mentioned, none of the ceramic material put through a sieve test was from a sealed container; it had all gone through some amount of flow testing. As the flow tester wasn't a sealed experiment, there was always a chance for material to be lost, either due to occasional spillage, or during testing itself. It was often observed during flow testing that the ceramic material was able to build up a substantial static electrical charge while flowing through the test section, and some of the very fine particles were likely thrown clear of the collection bucket during testing. While it is likely impossible to estimate the impact this effect on the recorded mass flow data or to the overall particle size distribution, the effect was evident.

The results obtained from sieving the glass ballotini deviated even further from the published specifications, with the size distribution appearing to consist of the size 6 material, rather than the size 8 material. While there were bags of the size 6 material on hand in the lab, it is unlikely that cross contamination was a factor in the errant sieve tests. Rather, an effect called blinding is the likely culprit. Blinding occurs when very spherical particles which are the exact diameter of the sieve opening become lodged in the mesh, thereby blocking flow, as seen in figure 3.2. It was observed after each sieving test of the ballotini material that the # 70 sieve was almost totally blocked. Figure 3.3 shows the results of a sieve test of the ballotini 8 mil material against published size data.

To attempt to verify the size of the materials being used (especially the ballotini mate-

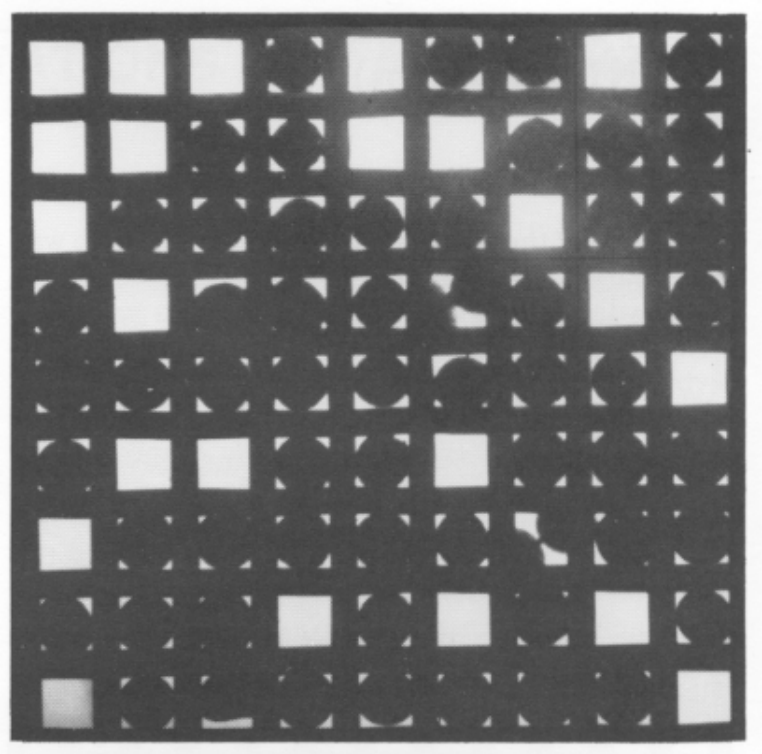

Figure 3.2: Example of blinded sieve [69]

rial), photomicrographs of both materials were taken, along with some photos of the size 6 ballotini, using a USB webcam and a standard desktop compound microscope. All pictures were taken with a 2 power objective lens. The images were processed with ImageJ [70], an open source image processing software developed by the National Institute of Mental Health. Since the detection field of a microscope is much smaller than that of a sieve, it was assumed that obtaining truly representative samples of the ballotini would be extremely difficult. Therefore, samples of the ballotini from an unopened bag labeled size 6 and the material being tested - assumed to be size 8 - were both photographed. If the manufacturing tolerances were as good as what was advertised in [67], then it was believed that detecting a size difference would be fairly easy. Samples of the ceramic material were also photographed for comparison purposes.

The ImageJ software is able to provide several measurement points for granular samples. First, a calibration image is needed to give a length per pixel correction, which was

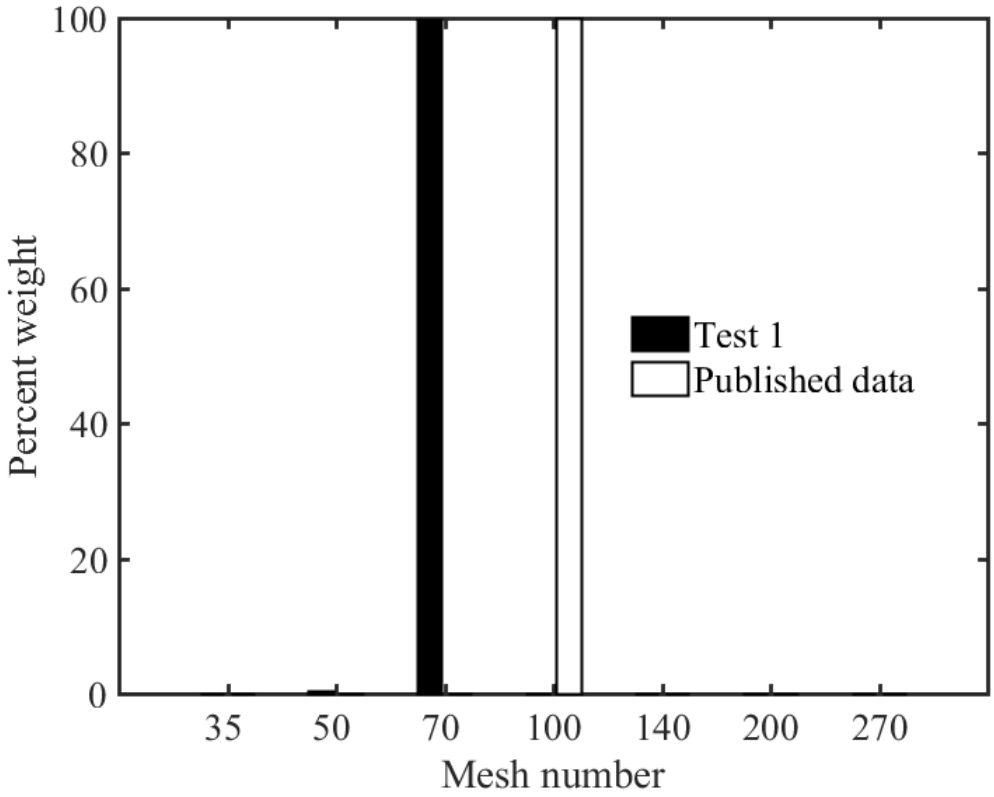

Figure 3.3: Comparison of sieve analysis of ballotini 8 mil material against published size data.

provided by photographing a ruled microscope slide. Then, small samples of a material were set on a clear slide and focused manually for the best possible image. The ImageJ software was able to turn each photograph into a binary image, consisting of particles and the background. ImageJ would then detect and measure each particle in the field and calculate various data about them. Figure 3.4 shows examples of how ImageJ can analyze particles, including different limits on particle size, roundness, particles on the image boundary, and including "holes" in the particles. Boundaries had to be set up for ImageJ to perform the calculations, which took the form of size and roundness limits. ImageJ calculates the roundness of a particle by

$$circularity = 4\pi \frac{area}{perimeter^2} \tag{3.1}$$

where the area and perimeter are measured by counting pixels. A particle that is perfectly circular will have a roundness of 1. While the limits were fairly generous to make sure no actual particles were excluded from the calculations, it was desirable to screen out artifacts such as lighting flares (in the case of the ballotini) and 2 particles in contact (often the case with the ceramic material), thus creating a much larger "particle".

Figure 3.5 shows the results of the optical analysis of the ceramic material and two different sized glass bead materials using ImageJ software. While ImageJ provides a measurement of the maximum Feret's diameter (also known as the caliper diameter) of a particle, an equivalent diameter was calculated by assuming the equivalent particle was perfectly circular. The equivalent diameter D_{eq} is given by

$$D_{eq} = \frac{1}{\pi}\sqrt{4\pi \frac{area}{circularity}}. \tag{3.2}$$

Thus, the equivalent particle diameter increases as the original shape becomes less circular. Equation 3.2 may be thought of as a two dimensional analog of the Sauter mean diameter, which is a ratio of particle volume to surface area [71]. The data presented in

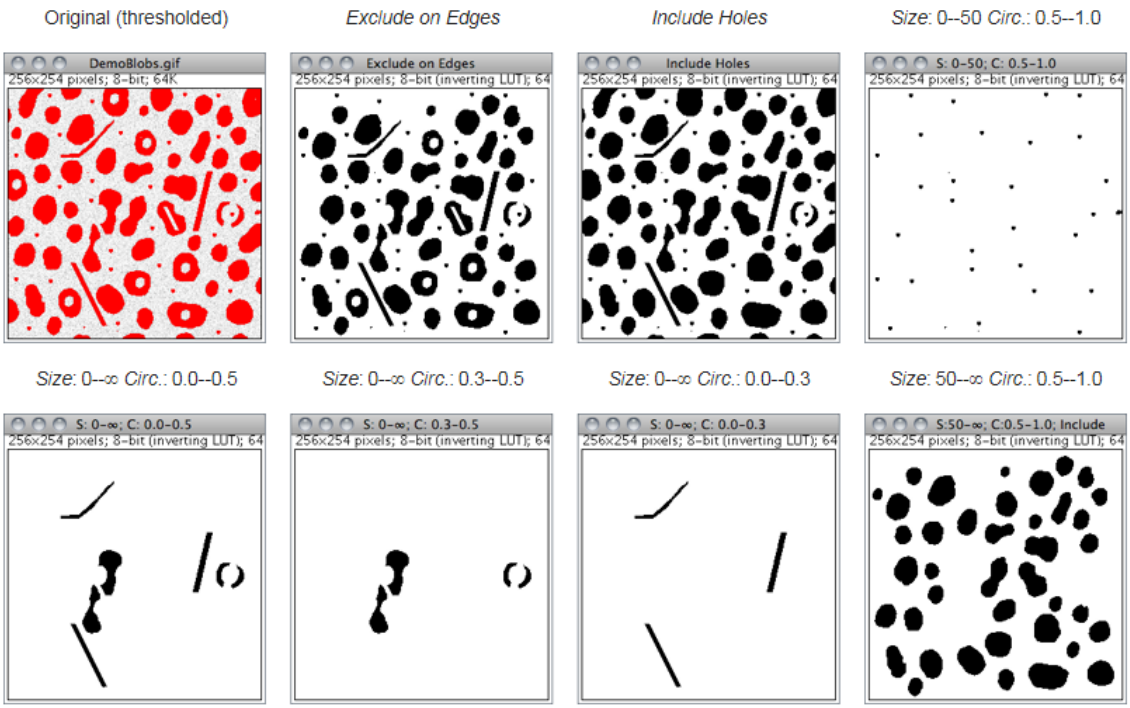

Figure 3.4: Examples of how ImageJ software analyzes particles.

figure 3.5 are for the equivalent particle diameter, not the maximum Feret's diameter (also known as the maximum caliper diameter, or the maximum distance between two points in a straight line anywhere on the particle outline). Through optical analysis, it was determined that the ballotini material being flow tested was much closer in size to the published value for the size 8 ballotini. Most of the discrepancies in the particle size distribution seen in figure 3.5 are likely related to image artifacts that could not be eliminated, but there is a clear difference in peaks between the size 8 and size 6 material.

Figures 3.6-3.8 show examples photomicrographs of the 6-mil and 8-mil ballotini and the ceramic ID50-K set to the same scale. Clearly, both ballotini materials are much more circular and uniform than the ceramic material, although they are not perfectly monosized or spherical. Both images of ballotini have an example of a non-spherical particle. The 6 mil material appears to have an irregularly shaped piece of glass in the image, while the 8 mil material appears to have a piece of the ceramic material mixed in. The photo of the ID50-K material shows the relatively wider particle size distribution, non-spherical

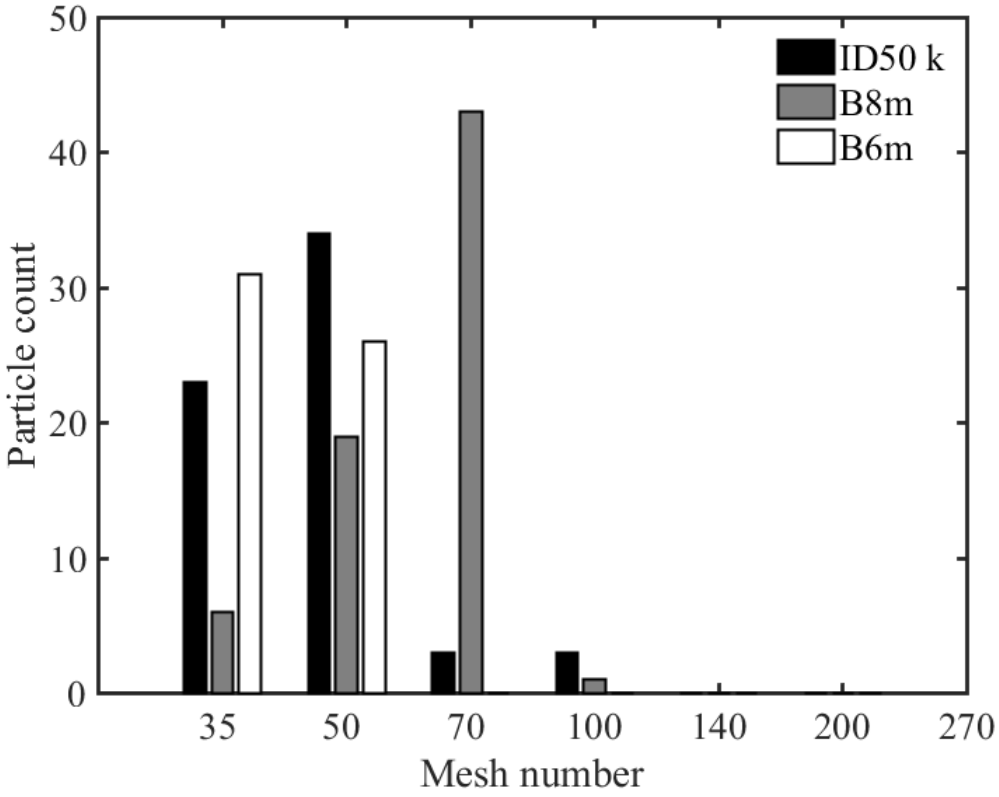

Figure 3.5: Results from the optical analysis of three different materials. Mesh sizes have been matched to what was used in the sieve testing.

particles, and the irregular surface profiles of the individual grains.

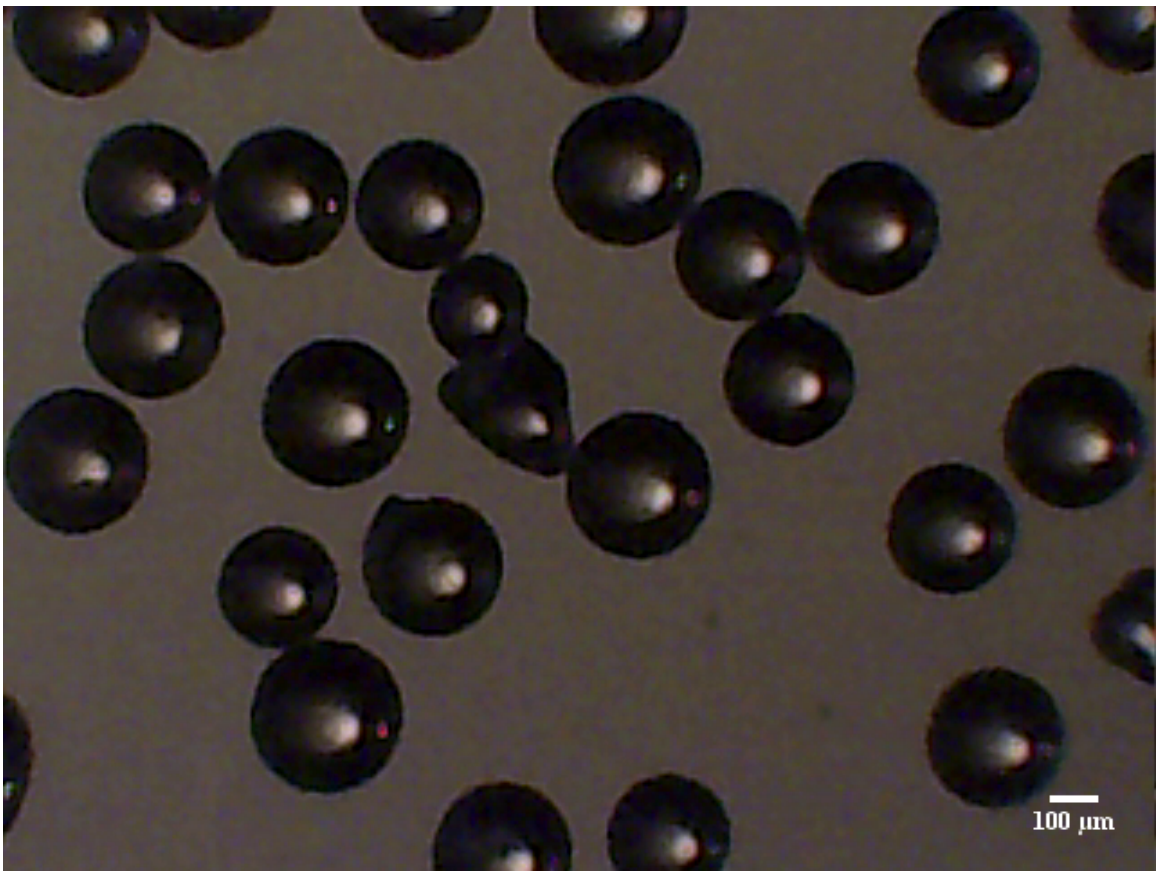

Figure 3.6: Photomicrograph of Ballotini 6-mil

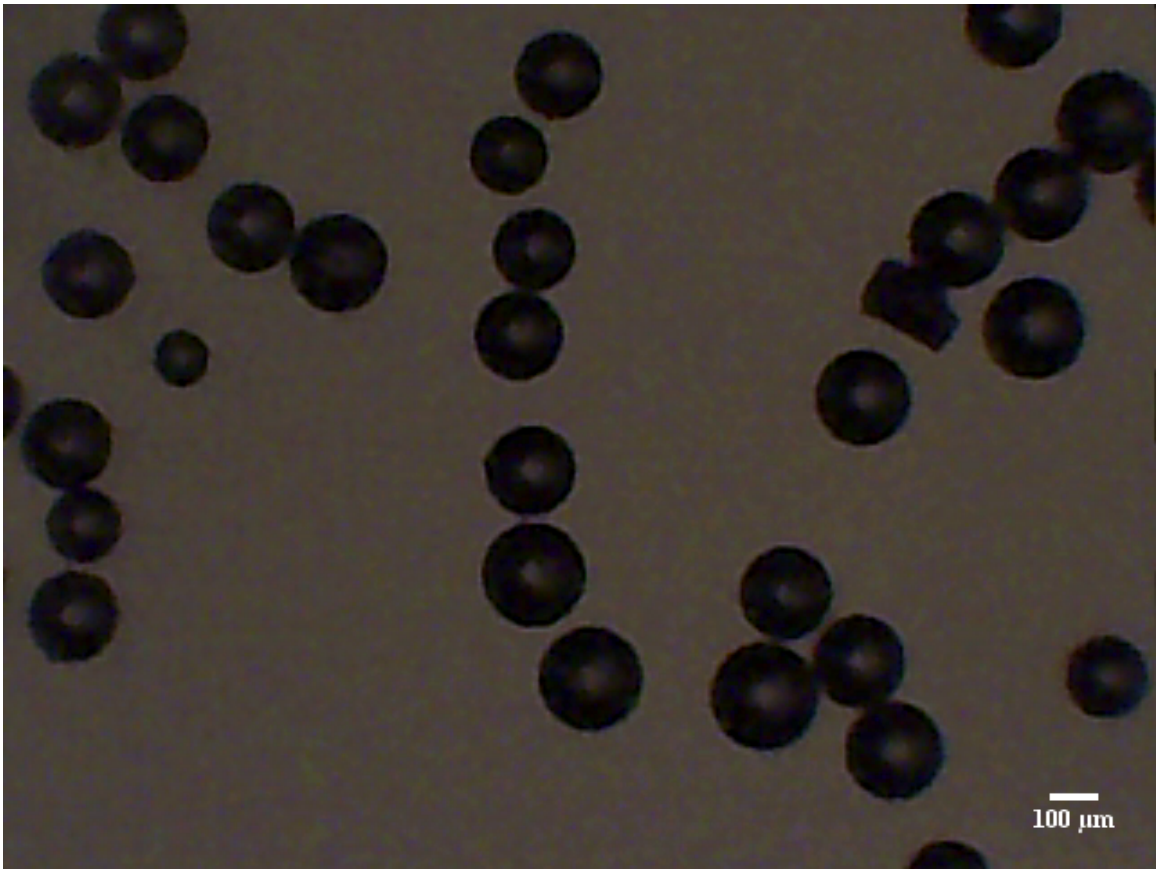

Figure 3.7: Photomicrograph of Ballotini 8-mil

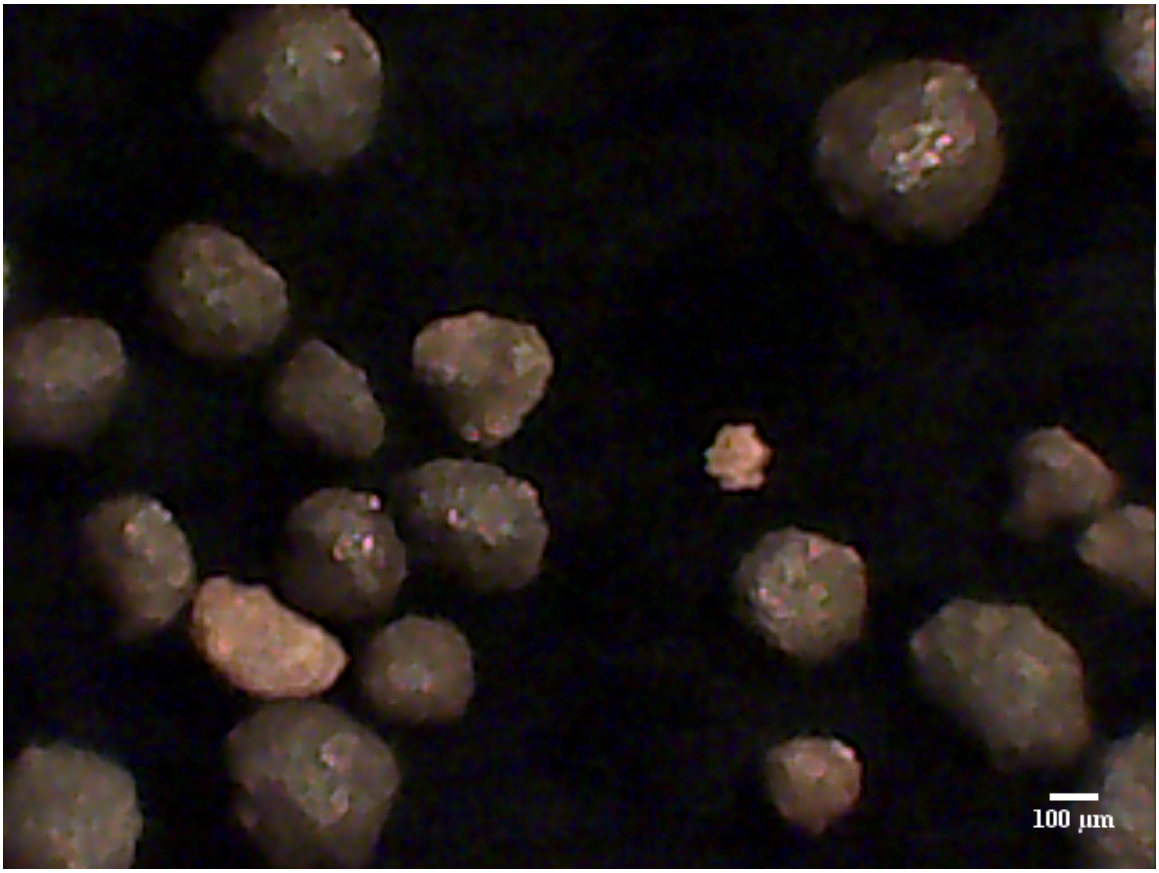

Figure 3.8: Photomicrograph of ID50-K

Another material property that was tested was the internal angle of friction. The internal angle of friction of a material is a macroscopic property. An example of a microscopic property would be the innate coefficient of friction of the granular material itself. However, the resistance to shear of a granular material is often influenced by many factors, such as size and shape of the grains, whether any cohesive forces are present (such as moisture), or even the amount of time a material has been under stress [30]. There are several methods to determine the angle of internal friction of a material [72]. The type used in this study was a Jenike shear cell. The Jenike shear cell consists of a cylindrical container cut in half along the radial direction, a lid, and the associated actuators and strain gauges (see figure 3.9). A sample of material is loaded into the cylinders, which are free to slide across each other. Then, the lid is set upon the material and compressed with a known force. A shearing force is then applied to the upper cylinder, and the shearing force and height of the lid are recorded. The material fails when the two cylinders start to slide relative to each other. By doing this at different applied normal forces, the relationship between normal and shear forces can be plotted. The internal angle of friction is then directly calculated from the inverse tangent of the slope of the resulting plot.

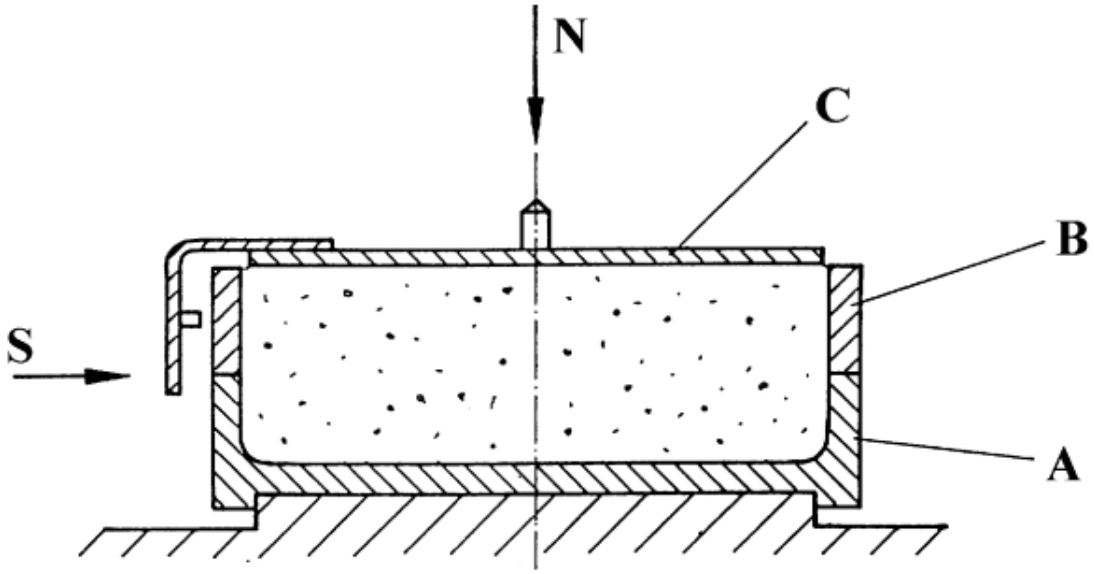

Figure 3.9: Schamntic of a Jenike shear cell [72]

Figure 3.10 shows the results of the shear test performed on the ID50-K material and the ballotini material. While more testing would be needed to increase the accuracy of the results for both materials, the angle of friction of the ID50-K material is in the range of many types of sand and other "natural" materials [73, 74], while the result for the the ballotini is generally in line with other results for small glass beads [74, 75].

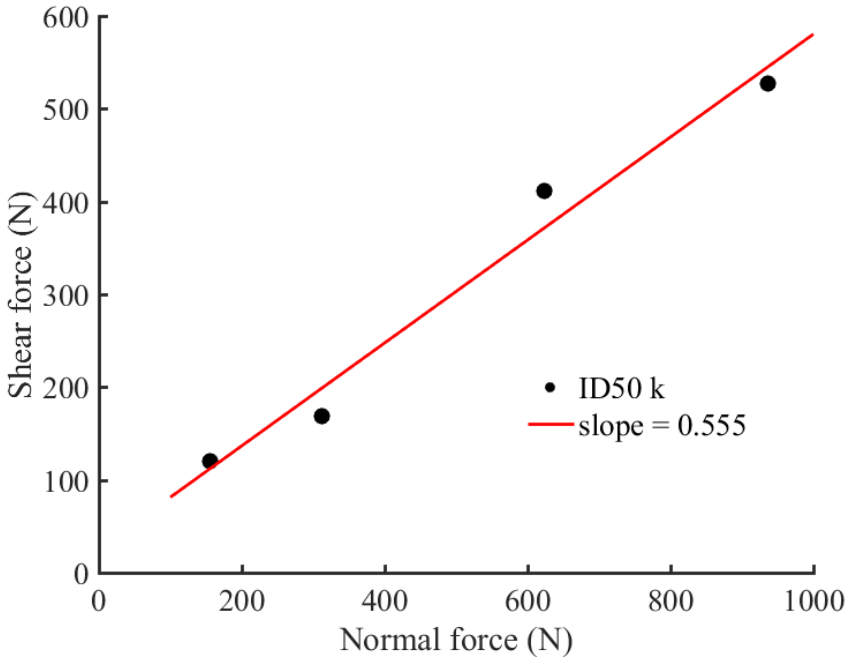

(a) ID50-K material

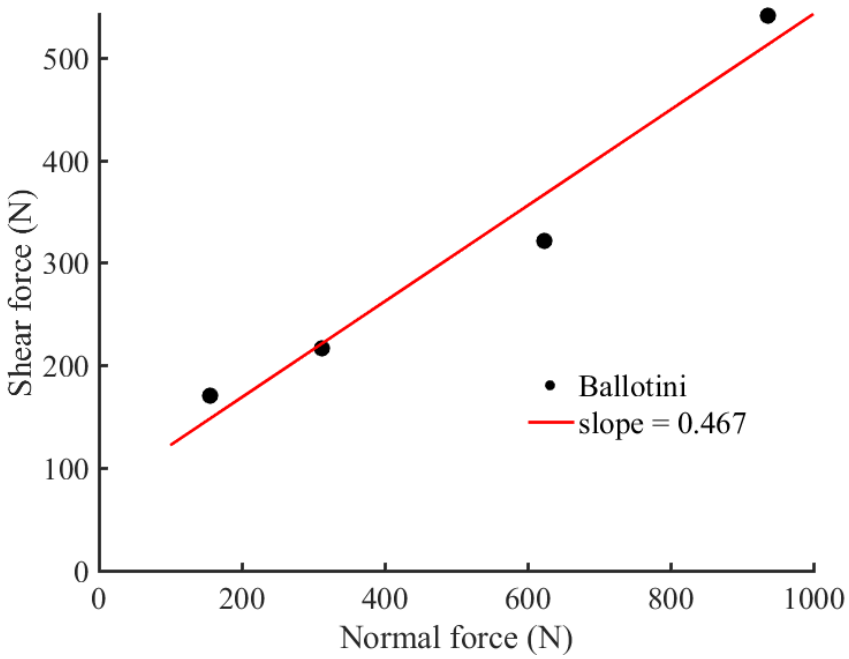

(b) Ballotini material

Figure 3.10: Shear test results for the two tested materials.

3.2 Experimental Apparatus

This section will describe the experimental apparatus used to gather the physical data used for the verification of the numerical models. The goal of the apparatus was to gather as many data points as possible that could be generated by numerical simulation, and to be readily modifiable to accept different granular materials and flow obstruction configurations.

The granular flow studies were conducted for two general wire mesh arrangements: horizontal screens, and inverted chevron shaped screens (referred to as angled screens in this study). In addition, flow studies were conducted for a series of aluminum square tube sections, a series of perforated plate strips bent into squares, and a series of squares cut out of a silicon carbide ceramic foam block. The wire mesh screens, aluminum tube, and perforated plate were purchases from McMaster-Carr, an industrial supply distributor. The silicon carbide foam squares were cut from larger block from the Selee Corporation, a maker of products for industrial foundries. The foam blocks were designed as slag filters for molten metal, but have found potential use in solar particle receivers [15, 17]. Despite different combinations of granular materials and flow obstruction configurations, the overall apparatus maintained identical instrumentation across all experiments, so it will only be described once. Further details will be given about the different test section geometries themselves.

The experimental apparatus contains several main features: The upper hopper, a short "upper section," the "test section" itself, 3 flow control valves, and the instrumentation which consisted of a piezoelectric load cell and a high speed CCD camera. A separate lab scale was used for static measurements. Figure 3.11 shows the entire testing apparatus set up for conducting flow tests with the horizontal mesh test section in place.

The hopper was secured to a Unistrut frame, and used to anchor the rest of the experimental framework. It was large enough to hold enough material for several minutes

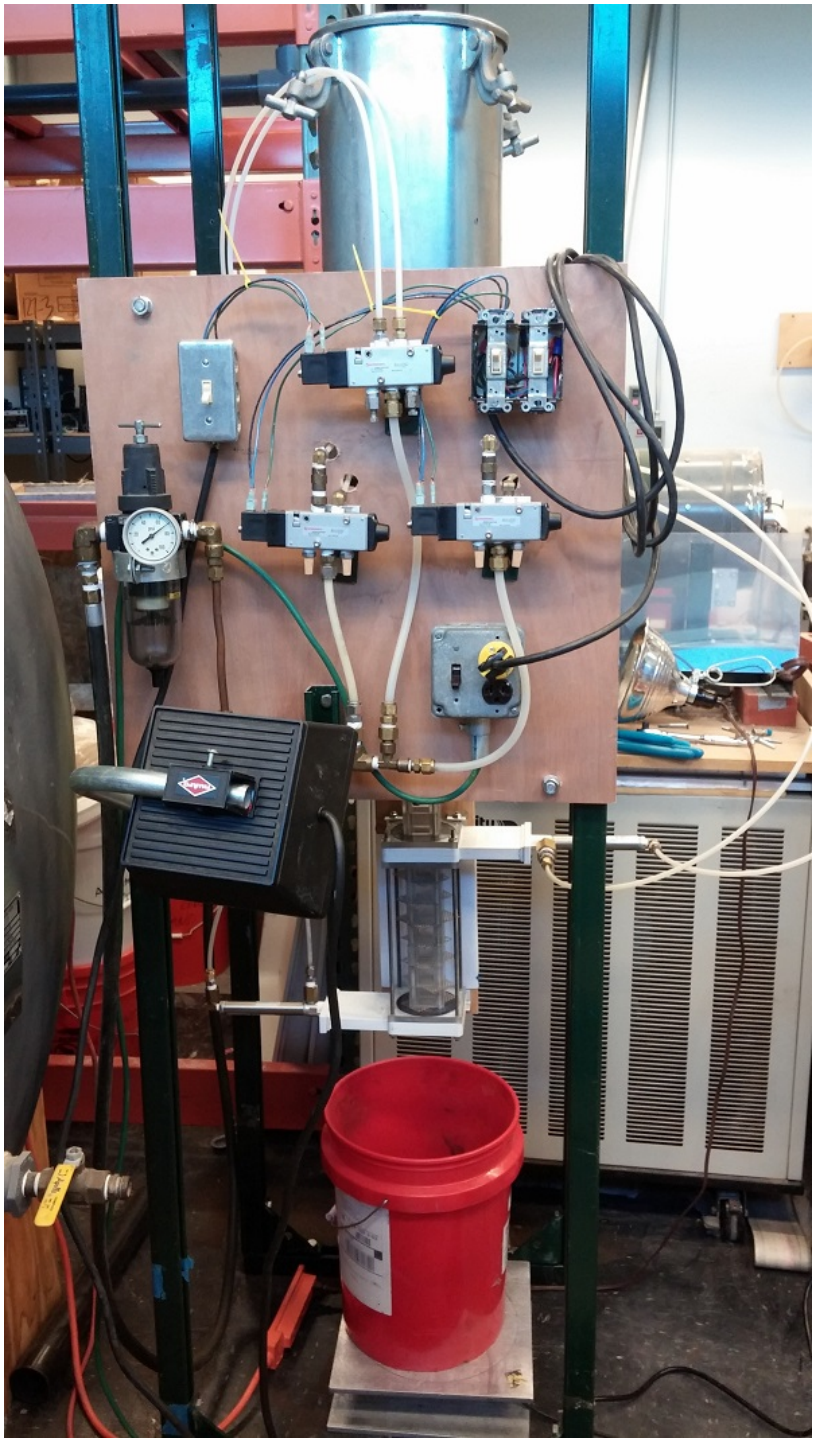

Figure 3.11: Experimental apparatus, showing (from the top): upper hopper, control valves, test section, and the collection bucket sitting on the load cell. The high speed camera is not shown.

of uninterrupted flow, although a typical test lasted between 30 and 60 seconds. Directly below the hopper was a pneumatically actuated 5 cm ball valve. This valve was strictly for on/off control; no flow regulation was intended nor desired. After a short down pipe and some appropriate adapters, a small upper section was attached below the ball valve. The upper section was a shorter version of the main test section, and was designed to try to eliminate any entrance region effects in the main test section; thus, it shared the same mesh configuration as the main test section. Below the upper section was the main test section, bounded by two 7.5 cm pneumatically actuated slide gate valves. All three valves were controlled by separate Norgren 5/2 air solenoid valves. The ball valve had its own switch and power/air supply, while the two slide valves were wired to two parallel switches that were in series with another switch. This enabled the two slide valves to be operated separately from each other, or simultaneously. The upper and main test sections were constructed from sheets of polycarbonate, which allowed both easy manufacturing of parts, and a relatively clear view into the flow. Below the bottom slide gate valve, a collection bucket sat on a small platform containing a Keli DEFY 100/250 load cell (the 100 rated load cell had to be replaced early in testing due to being shorted out by excessive static electricity in the test section and frame. New calibration curves were built for the 250 rated load cell, so all data are corrected). The load cell was connected to an Agilent 34901 multiplexer inserted into an Agilent 34970 data scanner, which was hooked to computer running Agilent BenchLink data logger software. Outside the test section a high speed camera was placed to enable video of the flow for use in PIV analysis. Static mass measurements were made on an O'haus GT8000 balance.

Horizontal mesh screens The horizontal mesh test section was made from a series of square "unit cell" blocks with an internal flow channel of 2.54 cm x 2.54 cm. The blocks were 3.175 cm tall; this was chosen for the initial mesh spacing. This spacing was chosen to closely match the spacing used in previous flow testing of the angled mesh configuration

(details in the next section) [18]. The blocks were attached to each other via holes in their corners into which spring pins were inserted. This enabled consistent location of each unit cell, but made dis-assembly and re-assembly possible. Figure 3.12 shows the test section set up for testing using screens in a double spaced configuration. The unit cells are clearly visible. For single spaced testing, screens would be inserted into the free gaps between cells. Table 3.4 shows the nominal dimensions of the purchased wire mesh screens. The mesh size indicates how many holes (or wires) there are per inch. Thus, the 10 x 10 mesh has 10 wires in both the x and y direction. Since the numbers are the same, the holes are square (a 10 x 6 mesh would have rectangular holes).

Table 3.4: Wire mesh dimensions.

Mesh size	Wire dia.	Hole size	Open area
8 x 8	0.025 in. (0.635 mm)	0.1 in. (2.54 mm)	64%
10 x 10	0.025 in. (0.635 mm)	0.075 in. (1.905 mm)	56%
12 x 12	0.023 in. (0.584 mm)	0.06 in. (1.524 mm)	52%
14 x 14	0.02 in. (0.508 mm)	0.051 in. (1.295 mm)	51%

Originally, testing was conducted with the individual wires of the screens oriented perpendicularly to the unit cells. However, this tended to produce accumulation in various corners, sometimes filling up entire cells in the middle of the test section. This is likely because the wire screens were not oriented perfectly with the inner walls of the test section. This could lead to rows of openings in the screens that were too small for particles to pass through, leading to accumulation in certain sides or corners of unit cells. It was found by orienting the screens at 45 degree angles to the unit cells, this accumulation was eliminated in lower cells, thus giving a better estimate of the steady state mass inventory, and more uniform and accurate PIV data. Figure 3.13 shows a closeup of this 45 degree orientation.

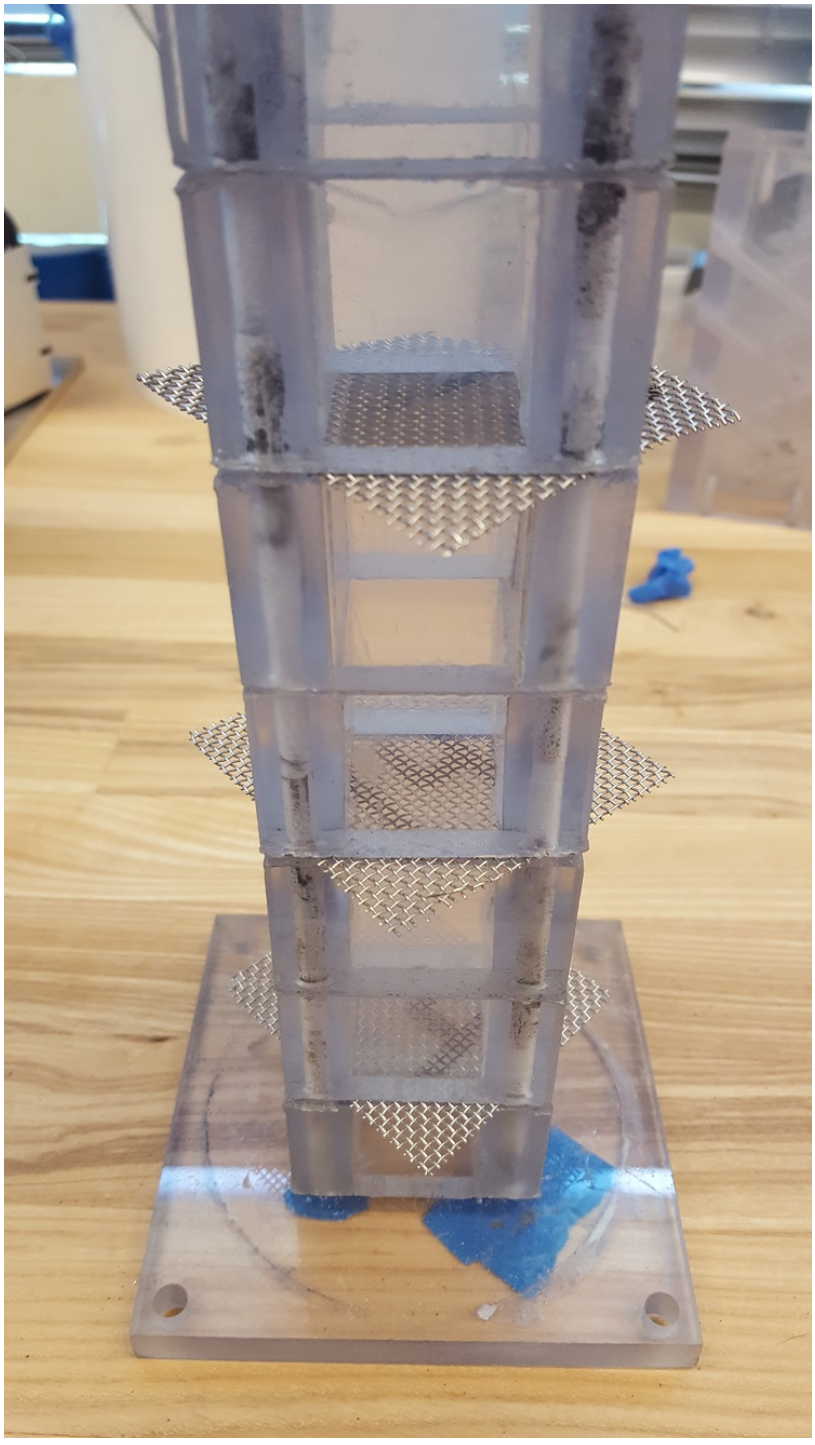

Figure 3.12: Detail of test section set up for double spaced horizontal screens. Note the 45 degree orientation of the screens.

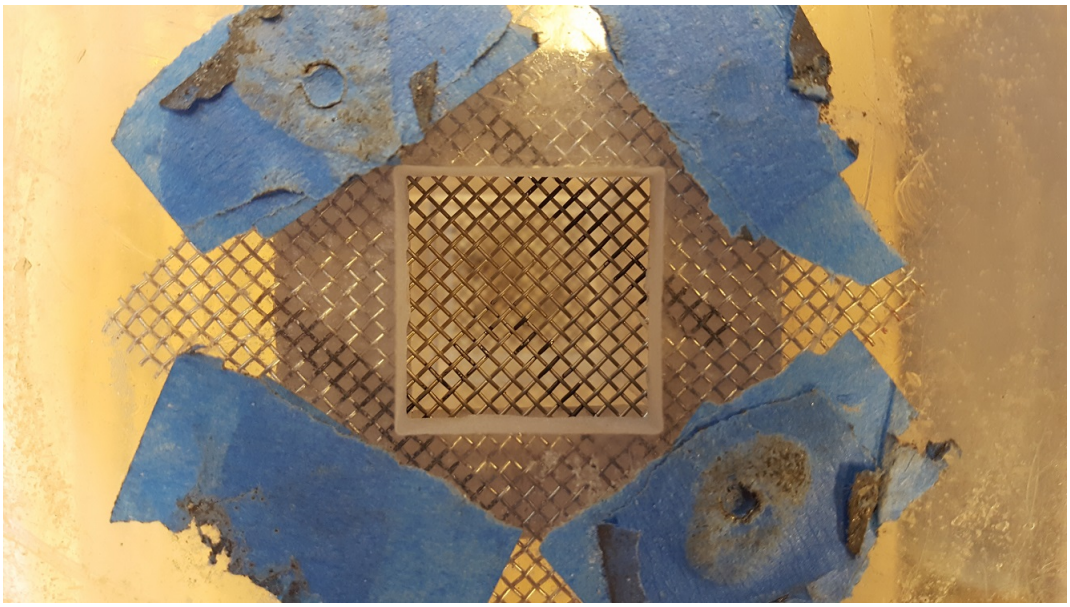

Figure 3.13: Detail of horizontal wire meshes showing 45 degree orientation.

Angled mesh screens The angled mesh test section was a larger, single unit (as opposed to unit cell construction) with an internal flow channel of 2.54 cm x 5.08 cm. The front and rear faces had slots cut into them that were staggered left and right on 3 cm vertical spacing, angled at 30 degrees down from horizontal. This spacing was done to conform to previous experiments [18]. Figure 3.15 shows a detail of the test section set up to test the double spaced angled mesh configuration. To prevent excess leakage, small pieces of felt were inserted in the slots in the rear face of the test section if there wasn't a screen in place.

Square tubes The square aluminum tube had a 5.08 cm by 5.08 cm nominal outside dimension (5.10 cm by 5.10 cm measured) and a wall thickness of 4.76 mm. The tube was cut into 3.18 cm sections. Each face of the tube had six identical holes drilled in a rectangular pattern that was centered around a spot 1.27 cm from the "front" face, with 2.54 cm spacing between each hole. Initially, two different sized holes were employed: a 6.35 mm diameter hole, and a 4.85 mm (a standard number 11 size drill bit) diameter hole. The test section was arranged so that a complete square ran down the middle of the flow path, while the side walls were occupied by tubes that were cut in half along the diagonal

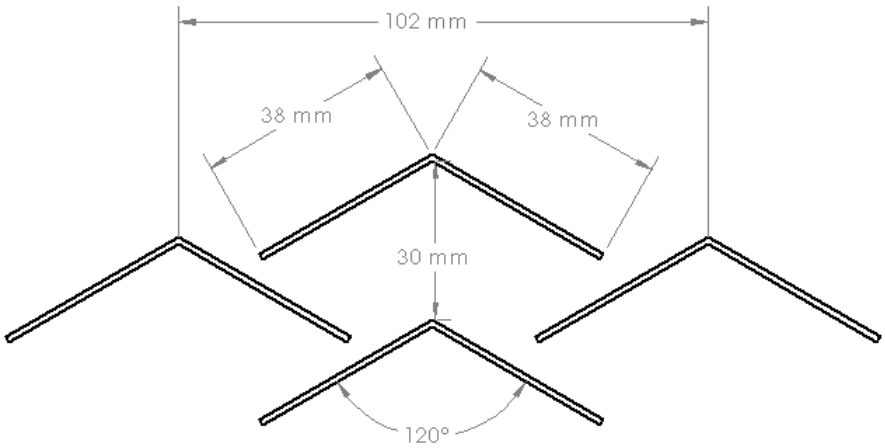

Figure 3.14: Base geometry of angled mesh test section [18]

of the face. To study the effect of different spacing between the tubes, a series of spacers were constructed from 6.35 mm thick plastic sheet. The spacers had 5.10 cm square cutouts surrounded by webbing that was spaced at 1.588 mm, 3.175 mm, 4.76 mm, and 6.35 mm. In contrast to the wire mesh test sections, where the overall flow channel geometry was fixed, the side panels for the square tube test sections were allowed to float. Thus, the overall flow channel dimensions could change, depending on the inter-square spacing. Smaller square cutouts were also inserted into the square tubes, thereby maintaining the overall depth of the test section at 2.54 cm. Each square was oriented so that the flat faces were 45 degrees away from a horizontal or vertical orientation. In an attempt to discourage material accumulation inside the individual square tube sections, slots 6.35 mm were cut out of the bottom corner of each square. The same test section and spacers were used for this slotted square configuration. Aluminum was chosen for this study because it is easily machinable. For on sun testing, a particle heating receiver would likely use a high temperature ceramic material (such as silicon carbide) to manufacture square flow obstructions.

Figure 3.16 shows a detail of the short square tube test section, with the front and one side wall removed for easier viewing. In this figure, the squares are spaced 6.35 mm apart and have had a slot cut into the bottom of them. In the figure, the bottom square insert was bolted to the back wall of the test section to index the rest of the squares. This short

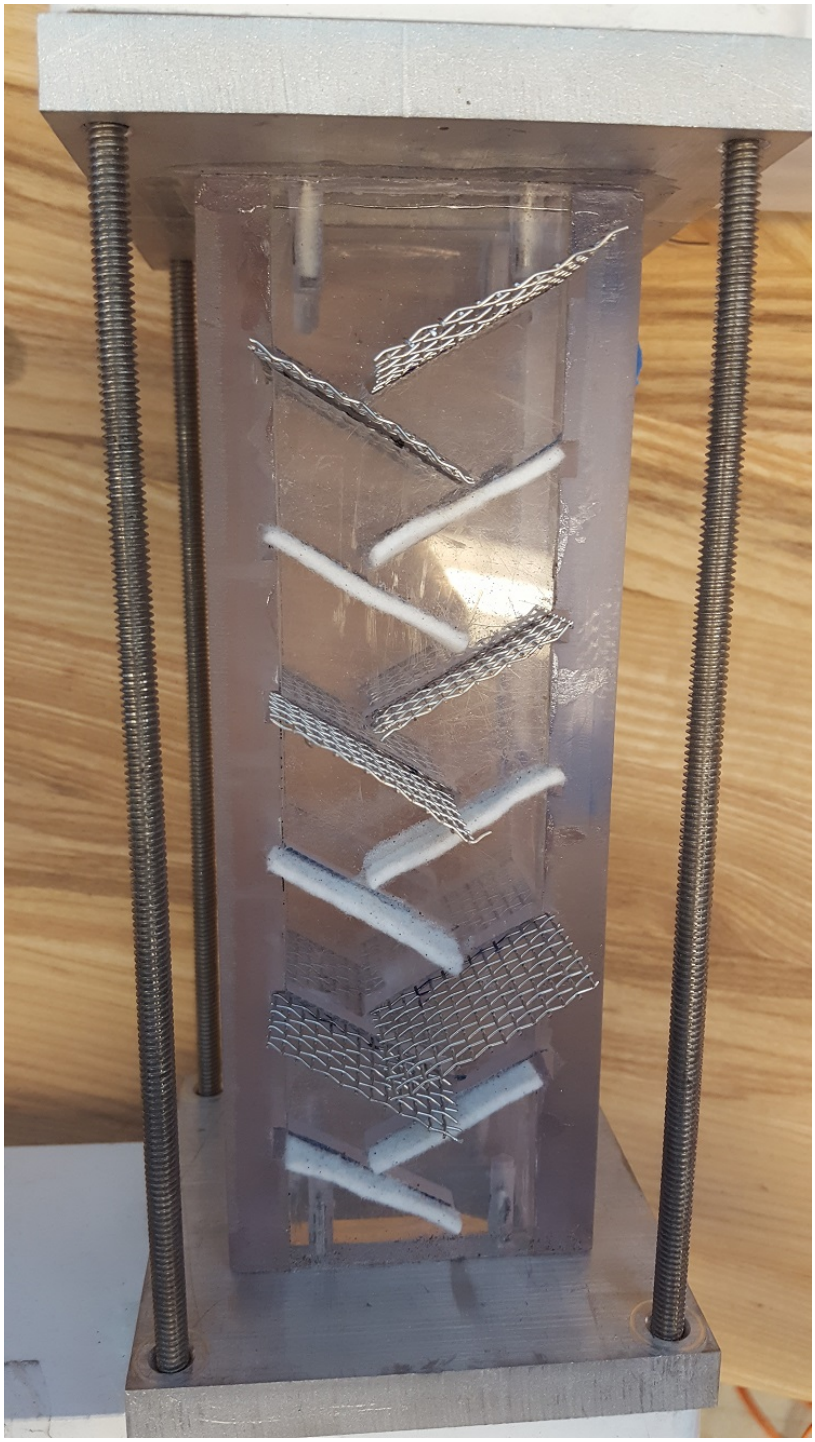

Figure 3.15: Detail of angled mesh test section set up for double spaced meshes. Small pieces of felt are inserted into the empty slots to eliminate leakage.

test section was originally paired with a two square tall upper section above the upper slide gate valve. However, it was felt that the main test section needed to be longer to enable more space for stable flow patterns to develop away from entrance or exit regions of the test section. Thus, a longer test section consisting of six squares down the middle was constructed. This longer test section was mounted without an upper section in place due to height constraints.

Perforated plate tubes The perforated plate experiments were performed in a similar manner to the square tubes. Table 3.5 shows the nominal dimensions of the perforated plate material, along with some small CAD images on the same scale to show the relative size differences. A typical naming convention for circular perforated plate is to size it as "hole diameter x hole-to-hole spacing," and adding the staggered qualifier if needed. Thus, in standard units, the first plate in table 3.5 would be called 3/16 in. x 1/4 in. staggered perforated plate (decimals are used in the table as that is how they are ordered from McMaster-Carr). All perforated plates were steel and had a staggered hole arrangement. The perforated plate material was cut into strips 3.18 cm wide and slightly over 20.3 cm long. They were then manually bent into squares as close to 5.08 cm by 5.08 cm as was practical, in order to achieve the same perimeter diameter dimensions as the aluminum tube sections. However, as the perforated plate was made from 20 gauge steel (0.912 mm thick), it did not have the same inner dimensions as the square tubes. Therefore, the square inserts were not used. The perforated plate squares were held in place with the pressure between the front and back walls of the test section. Figure 3.17 shows a detail of the test section set up for the perforated plate squares using a 6.35 mm spacing and a "slotted" bottom. The small black dots on the side squares are small pieces of rubber glued to the bottom edge of the side squares. Without the square inserts used in the square tube test section, the side squares needed to be propped away from the side walls and therefore closing the gap. The "whole" perforated plate squares didn't use these rubber spacers. Figure 3.18 shows a

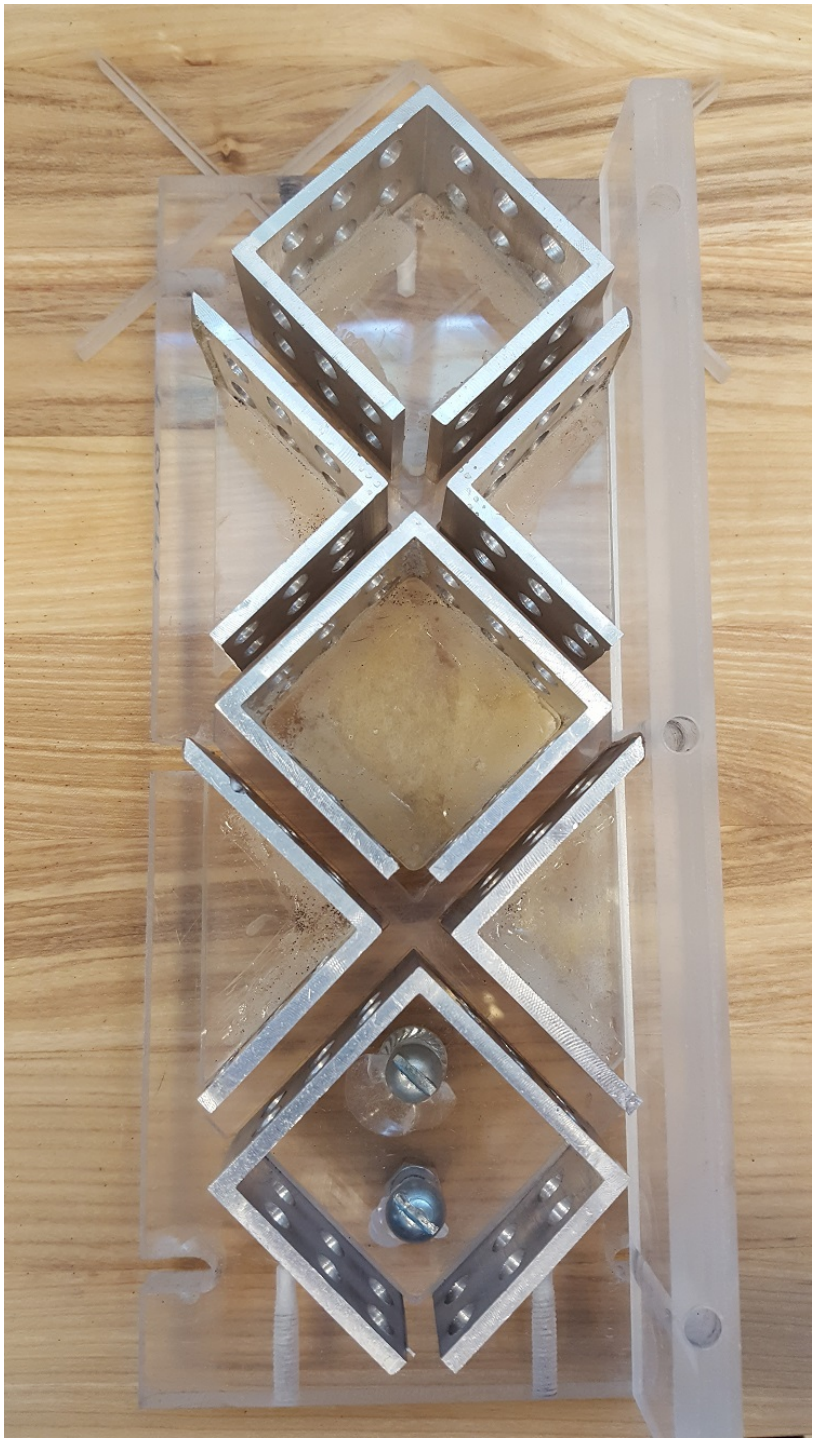

Figure 3.16: Detail of short square tube test section set up with 6.35 mm spacing and slotted bottoms. The bottom square is bolted to the back wall, allowing it to index the rest of the squares.

comparison of the whole and slotted squares. The goal of the slotted squares was to have the total gap be 6.35 mm wide, but this varied slightly between each square due to being hand cut. Figure 3.19 shows a comparison of the three different sized perforated plate materials used in this study. Again, plain steel was used for the perforated plate material due to machinability and cost issues. For on sun testing, a high temperature alloy or possibly also a ceramic material would be used to manufacture perforated square flow obstructions.

Table 3.5: Perforated plate dimensions.

Hole dia.	Center-to-center spacing	Open area	
0.1875 in. (4.76 mm)	0.25 in. (6.35 mm)	51%	
0.1563 in. (3.97 mm)	0.1875 in. (4.76 mm)	63%	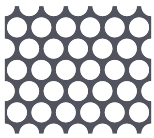
0.25 in. (6.35 mm)	0.313 in. (7.94 mm)	58%	

Silicon carbide foam squares The silicon carbide foam square section was essentially identical to the short aluminum square tube and perforated plate test section. However, the nature of the square pieces necessitated a few key changes. One difference was, due to the total amount of SiC foam on hand being somewhat limited, the main test section only used three squares instead of six, and there was no upper section. The other main differences were due to the fragile nature of the SiC foam squares. The squares were cut out of larger blocks of SiC foam using a CNC water jet cutter, while half squares were cut out of full square sections by hand with a Dremel tool fitted with a diamond cutting wheel. It was found that the minimum square thickness that could reliably be extracted from the larger block was roughly 4.76 mm thick (referring to the thickness of the square walls. The

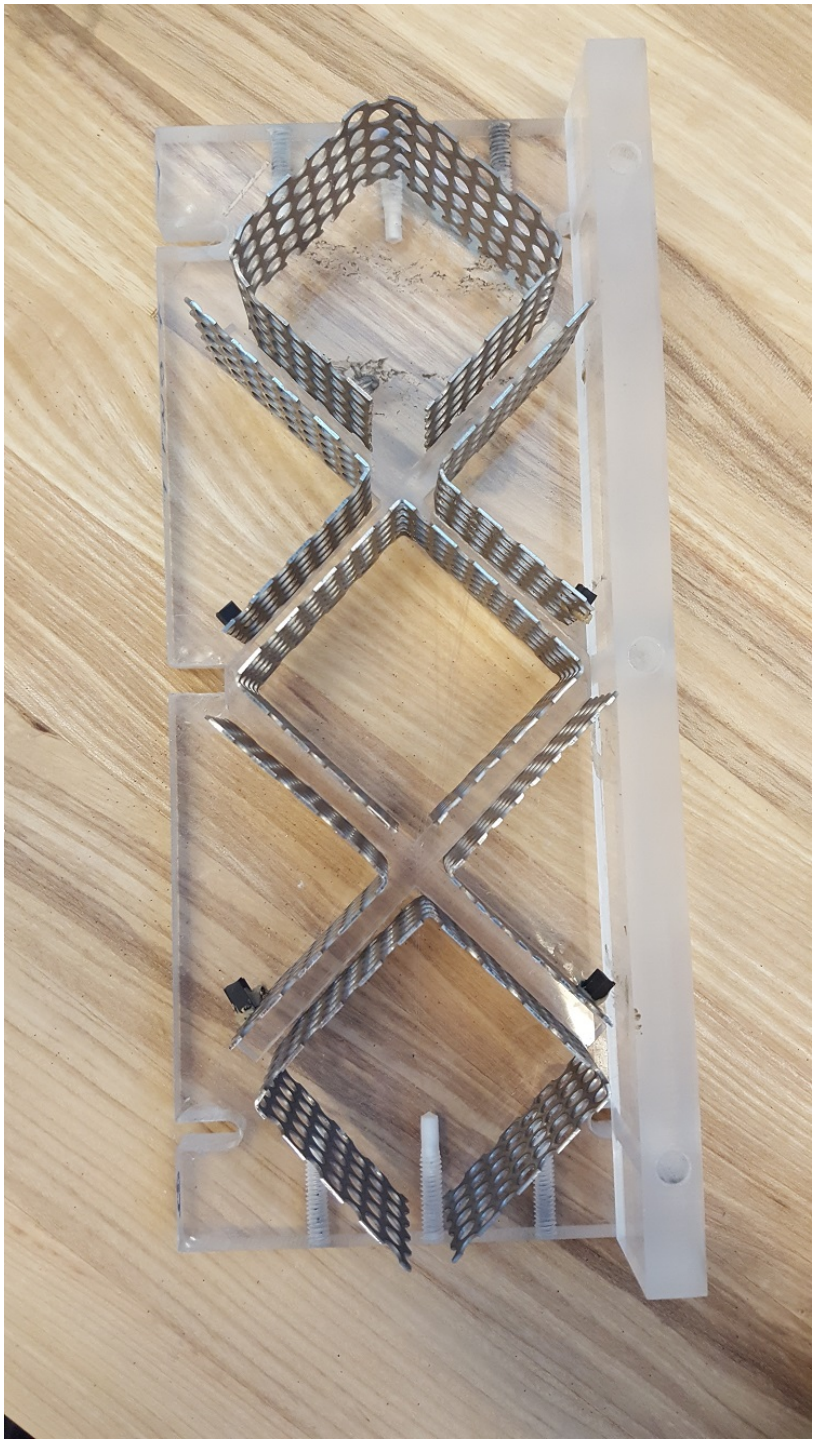

Figure 3.17: Detail of short perforated plate test section set up with 6.35 mm spacing and slotted bottoms. Indexing was not performed on the perforated plate test section, but the jagged edges of the cut squares provided sufficient friction against the front and back walls to anchor the squares in place.

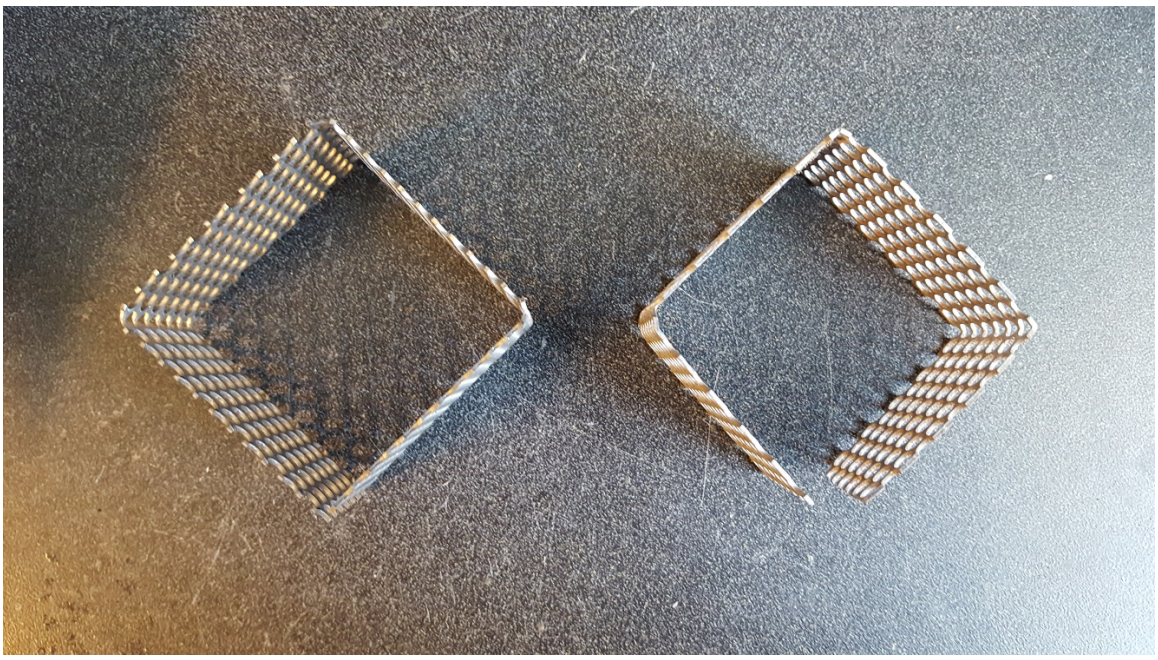

Figure 3.18: Detail of perforated plate squares. The whole square is on the left and the slotted square is on the right.

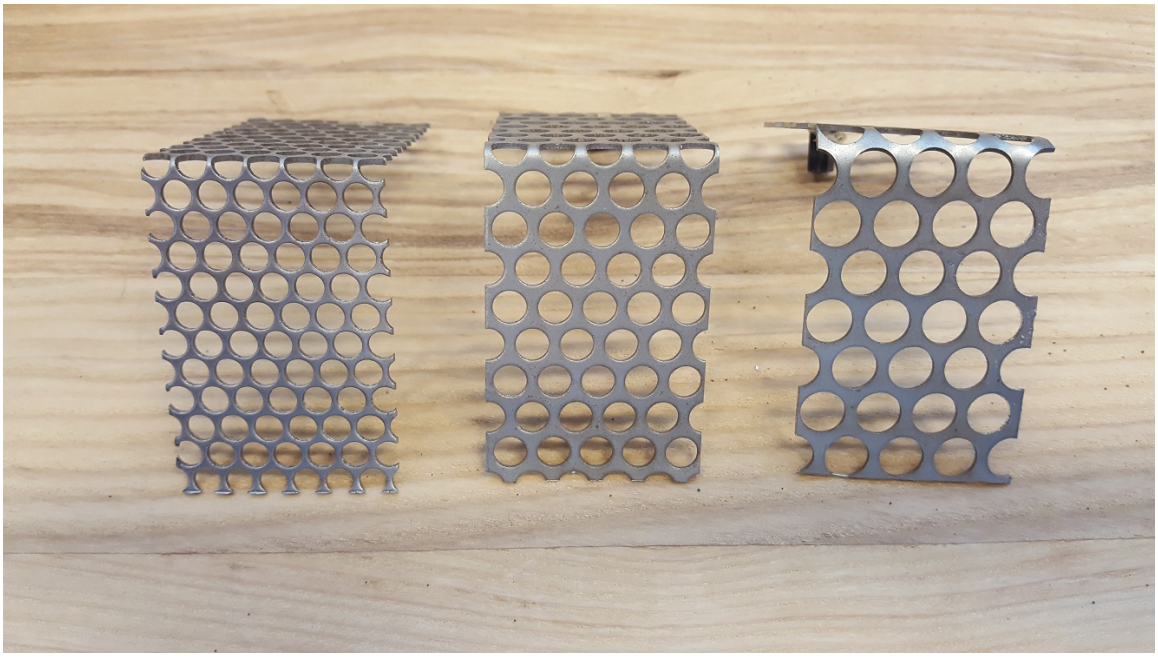

Figure 3.19: Detail of different perforated plate sizes. From left to right are 5/32 in x 3/16 in (3.97 mm x 4.76 mm), 3/16 in x 1/4 in (4.76 mm x 6.35 mm), and 1/4 in x 5/16 in (6.35 mm x 7.94 mm). Note how the difference in webbing size influences where the squares are bent.

large block of foam was approximately 30 mm deep, and that was the limit on the depth of the squares). However, this thickness would not stand up to repeated assembly and disassembly of the test section. Therefore, squares with a thickness of 12.7 mm were used during testing. The squares were cut with the same outer dimension as the aluminum tube, so the use of the 6.35 mm spacer was retained. Also due to the fragile nature of the foam, the squares could not be held in place using only the clamping force of the front and rear walls of the test section. A piece of rubber sheeting was placed along the entire back wall of the test section, including under the sidewalls. This enabled the front face to be clamped against the back face with enough pressure to hold the squares in place, while the rubber mat provided enough cushion to protect the SiC foam squares. Due to the highly porous nature of the SiC foam, large beads of construction adhesive were applied to the cut faces of the half square pieces that ran down the side of the test section. Enough was applied to attempt to discourage excess leakage from the top corner of the square, but still allow material flowing withing the porous structure itself to exit the foam via the flat face. The bead of construction adhesive also provided a small "bumper" to protect the half squares against the side faces of the test section when they were being secured into position. Figure 3.20 shows a close up of the slotted silicon carbide foam square test section.

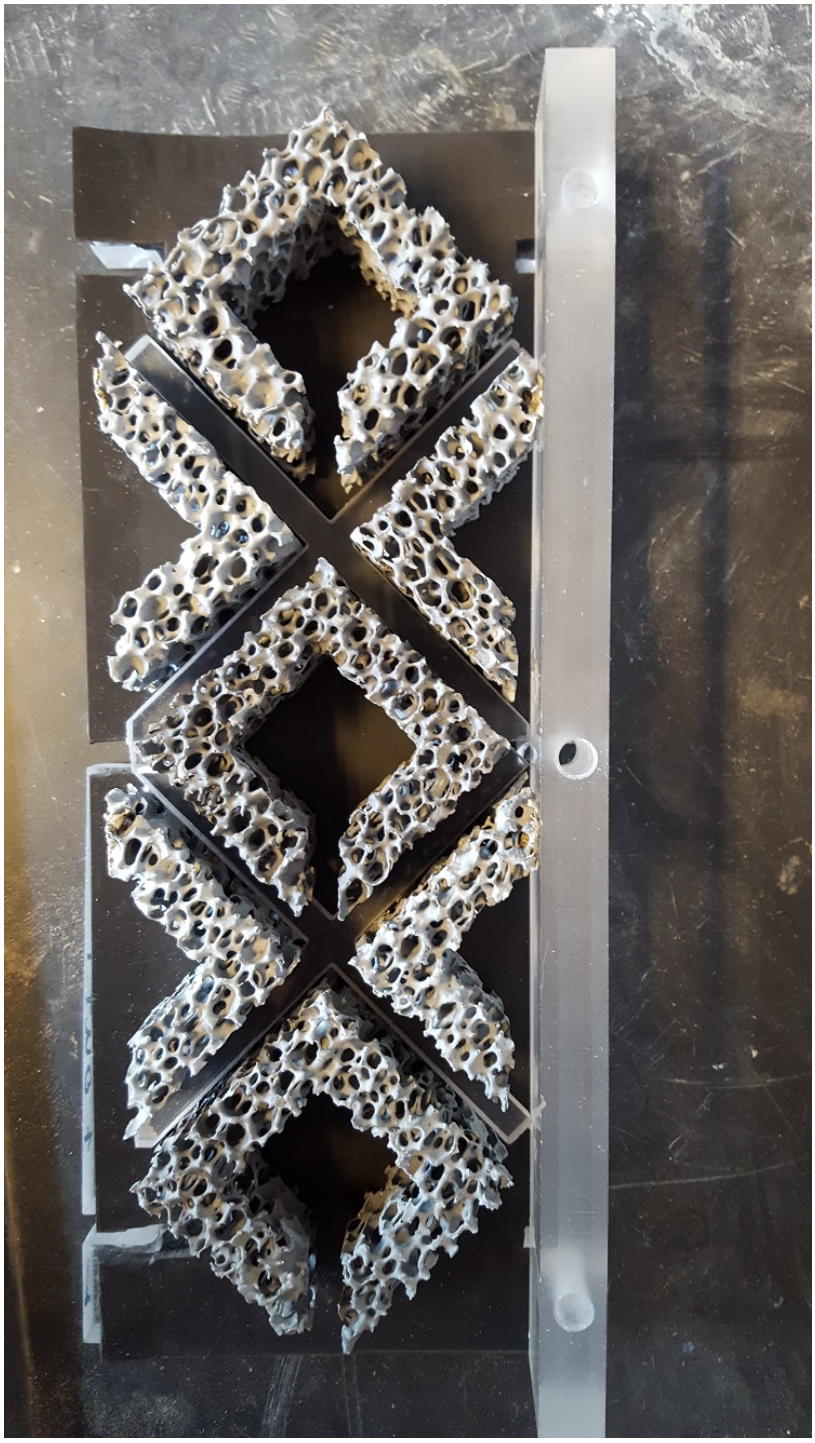

Figure 3.20: Detail of silicon carbide foam square test section, set up for slotted squares.

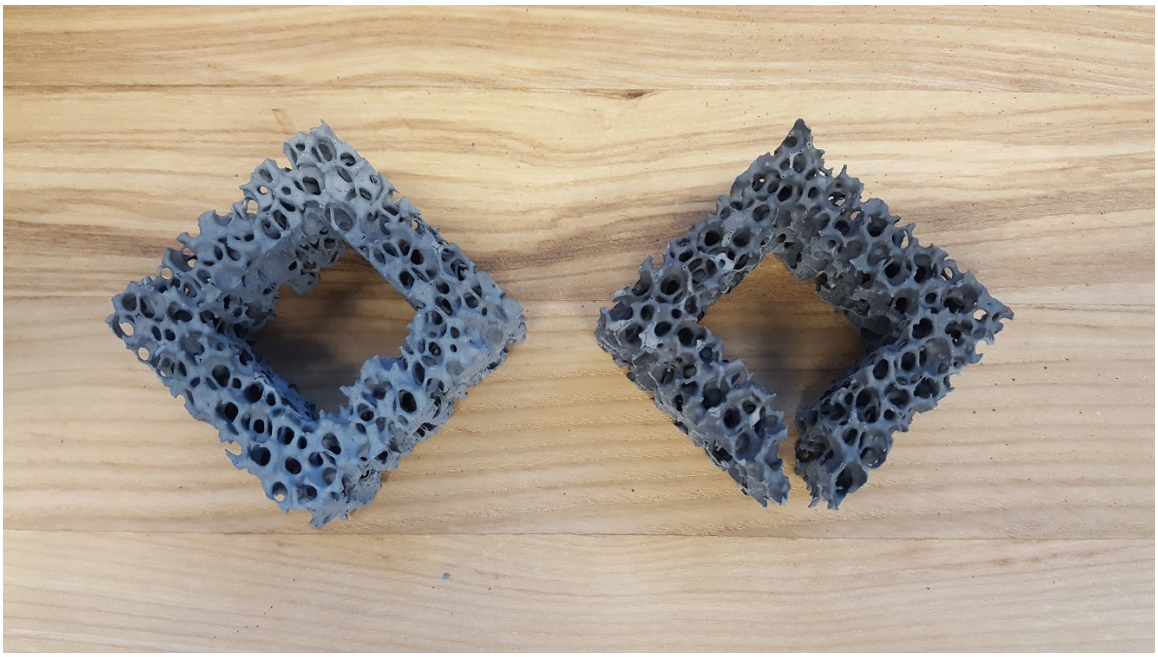

Figure 3.21: Detail of whole and slotted silicon carbide foam squares.

3.3 Experimental Procedure

This section will describe the procedure used to collect raw data for analysis. Three main types of data were collected: static mass inventory at steady state (i.e. the average volume fraction of the test section), mass flow data, and high speed video. Before data collection could begin, the load cell needed to be calibrated so that the raw voltage output could be associated with the actual weight in the collection bucket. To perform the calibration, 12 standard clay bricks were each independently weighed with the GT8000 balance. Then, the bricks were stacked in a controlled sequence on the load cell platform while collecting load cell output voltage. They were also removed in the same order to check for any hysteresis. Then, the known mass on the load cell platform at any given point could be associated with a voltage output from the load cell, and a calibration constant could be calculated.

Static mass measurements were used to determine the average volume fraction in the test section at steady state flow. To determine the volume fraction at steady state flow, both slide gate valves were open when the ball valve was opened to initiate flow. After a certain

period of time at "steady state" flow, both slide gate valves were closed simultaneously, capturing a "slice" of flowing material in the test section. While the valves were never officially timed, the estimated closing time for the entire 7.5 cm stroke was on the order of 0.1 seconds (manufacturers data are not available for valve closing time. This could be determined by video analysis, but this was not performed for this study); therefore, the time needed to cross the active flow channel was even shorter. Then, the bottom valve was opened and the test section was drained. This material was then weighed on the GT8000 balance. Using the mass of material collected in the test section, the volume that this material would occupy was calculated using the density of the given material. This was compared to the total wet volume of a given test section (i.e. total volume minus the volume occupied by flow obstacles). There is a small uncertainty in the calculation of this wet volume due to the fact that the slide gate valves were not in contact with the end faces of the test section; there was always a small gap where material was not strictly confined to the cross section of the flow channel for a particular test section geometry. Thus, for the entrance to the test section, the possibility existed that material was able to accumulate in valve bore. The volume fractions calculated in this study assumed that material was confined to the cross section of the particular test section (i.e. ignoring accumulation in the valve bore). However, using an average angle of repose of 25 degrees, the total wet volume of the horizontal mesh test section increased 6.62% on average, while the total wet volume for the angled mesh test section increased 4.55% on average.

To record mass flow data, the Agilent interface was set up to record the output of the load cell every .25 seconds. Thus, the total mass in the bucket was updated at regular time intervals. These data points were used to determine a best fit line that would determine the mass flow rate of a given test section configuration. An error analysis of the calculated mass flow rate is presented in appendix A, and for a specific flow test, is calculated to be less than 1%.

To record high speed video, a camera was set up to face directly at the front face of

the test section, near the bottom to try to prevent any entrance effects from the upper slide gate valve from introducing erroneous data. The image was typically framed so that at least two unit cells were in frame with the horizontal test section and four levels of screens in the angled test section (high speed video of the square tube, perforated plate, and SiC foam test sections was mostly used for qualitative analysis, so the framing wasn't as consistent). Two different cameras were used during the course of the experiments, and each had different sensor capabilities, so not every frame recorded was at the same resolution and frame rate. However, the minimum useful frame rate was found to be around 1000 frames per second. Due to the enormous amount of data it was possible to collect with high speed video, the typical recording lasted 20 frames for PIV analysis. Occasionally, more frames were taken for qualitative analysis.

3.4 PIV Analysis

Analysis of the high speed footage was done using particle image velocimetry, or PIV, analysis (DPIV refers to digital PIV, meaning that the images are captured digitally, rather than on film. Since this study used only digital cameras for image capture, PIV should be taken to mean DPIV). In the most basic terms, PIV analysis involves comparing images of a set of points to see if anything has moved. If a large image is broken up into several smaller parts (called iterrogation windows), a vector field can eventually be developed which describes the motion of the particles. In a typical PIV study, a fluid flow of interest is seeded with small tracer particles. These particles should be non-reactive to the fluid in question, neutrally buoyant, and have a Reynolds number of less than unity (i.e., the particles are in the Stoke's flow regime) [76]. Then, a laser shines a sheet of light through some plane of the flow field roughly parallel to the feature of interest. Finally, a camera captures successive images of the illuminated tracer particles for further analysis. Figure 3.22 shows a schematic of a typical PIV setup.

The comparison of two images to find the relative motion between them is called cross

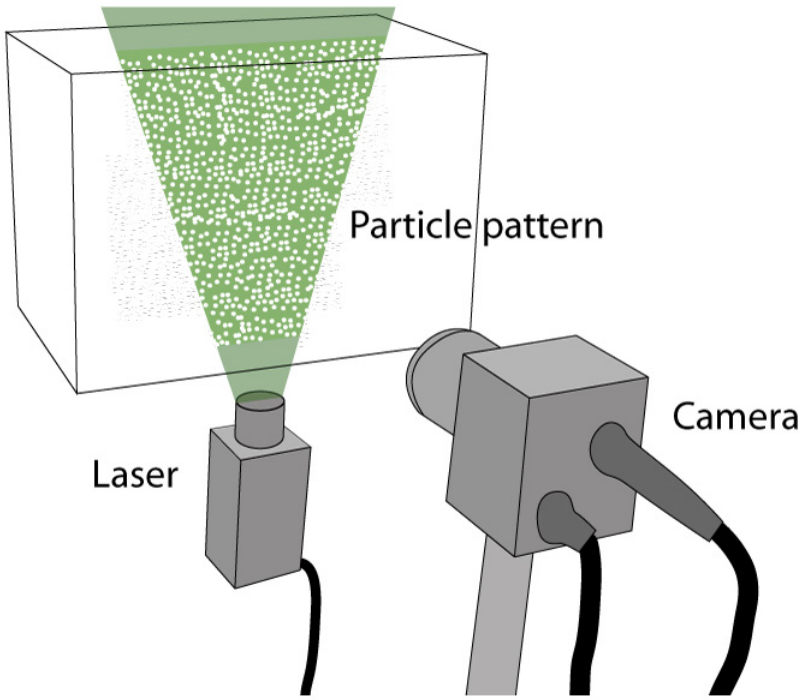

Figure 3.22: Typical PIV setup [77]

correlation. The statistical cross-correlation function is given by [77]

$$C(m,n) = \sum_i \sum_j A(i,j)B(i-m, j-n) \tag{3.3}$$

where A and B are the corresponding images. The intensity peak at $C(m,n)$ indicates the likely displacement between images A and B [78].

There are two common approaches to solving equation 3.3. The intensity matrix C can be computed directly in the spatial domain. This is known as direct cross correlation (DCC). The DCC approach can result in errors that are an order of magnitude lower than standard discrete Fourier transform methods (DFT, to be discussed next) [78]. However, the DCC approach can lead to calculation times that are at least an order of magnitude greater as well [79]. Figure 3.23 shows a schematic of how the DCC method computes the correlation matrix C.

The other approach to solving equation 3.3 is the discrete Fourier transform (DFT). The high speed at which computers are able to implement fast Fourier transform (FFT) algo-

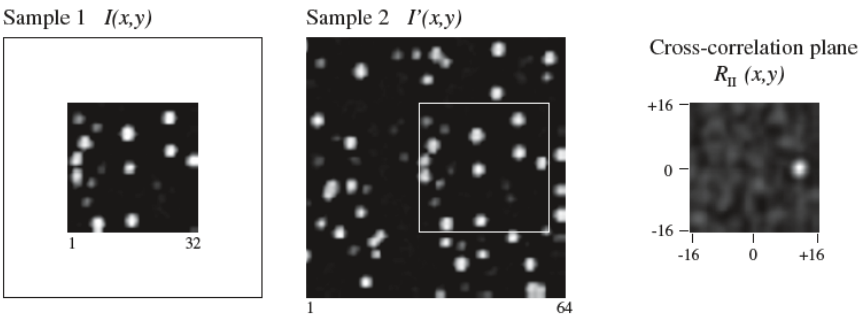

Figure 3.23: Using the DCC approach to calculate the cross correlation matrix. The smaller window I is cross correlated with the larger window I', producing the cross correlation function R_{II}, where the white dot shows the calculated displacement between the two images [80].

rithms enable this method to be much faster in general than the DCC method. However, it has a few drawbacks. One is the fact that the DFT requires interrogation windows of the same size, which induces more information loss via increased noise for any particle movement. Another drawback is that the FFT assumes its inputs are periodic, which means that as soon as a particle moves further than half of the interrogation window, the intensity peak in C moves to the other side of the matrix (a form of aliasing). As the signal to noise ratio increases with increased particle displacement, a more conservative rule saying that particle displacements should only be rougly one quarter of the interrogation window is often used [80]. This sets a minimum size on the interrogation window. Non-uniform motion (such as acceleration or shearing) tends to widen the displacement peak even further, decreasing the quality of results. However, there are several methods that can help eliminate these drawbacks. A fairly common approach uses a combination of multiple pass interrogation using window displacement, interrogation window refinement, and window deformation via local velocity gradients.

The procedure of multiple pass window displacement begins with a normal DFT interrogation and estimation of the displacement matrix. Then, the interrogation window is shifted by the integer part of this displacement, and the interrogation is performed again. This ensures that the remaining particle is less than one half of a pixel. An added feature

of this procedure is the resulting noise reduction that occurs. In the case of flows with low turbulent intensity, the noise reduction becomes

$$NR = \frac{1}{4u'^2} \tag{3.4}$$

where u' is the turbulent velocity fluctuation. For the case of flows with high turbulent intensity, the noise reduction is approximately 3 [81].

As might be expected, grid refinement uses a series of successively smaller interrogation windows to refine the local correlation matrices, and thus the local vector fields. The DFT interrogation starts on a relatively large window, and the window displacements are computed. These displacements are stored, and the windows are divided into smaller sub-regions. These sub-regions are cross correlated with the previous displacement used as a guess to limit the search parameters. The process of correlating, storing, dividing, and re-correlating can in theory be taken down to the particle level, using the displacement matrix at each step as in input into the next window division. However, one issue with this approach is that errors propagate from the top down. That is, errors during the first round of cross correlation may produce displacements that cause the sub-regions to search for particle displacements that do not exist. Thus, the size of the initial integration window must be chosen with some thought [82]. Figure 3.24 shows the cascading nature of the grid refinement method.

The final method, window deformation, is useful when dealing with non-uniform flow. As not every particle is displacing the same amount in the same direction, flows with shear, rotation, and acceleration will broaden the peak of the cross correlation matrix, and can even form more than one peak [80]. Window deformation starts with a typical DFT interrogation, which calculates displacements at the center of every window. The results at this point can be smoothed and interpolated to reduce erroneous data in further steps. Then, using bilinear interpolation, a predictor field is built up for every pixel in the image. Then, the images are deformed according to the displacement predictor field. From here, the grid

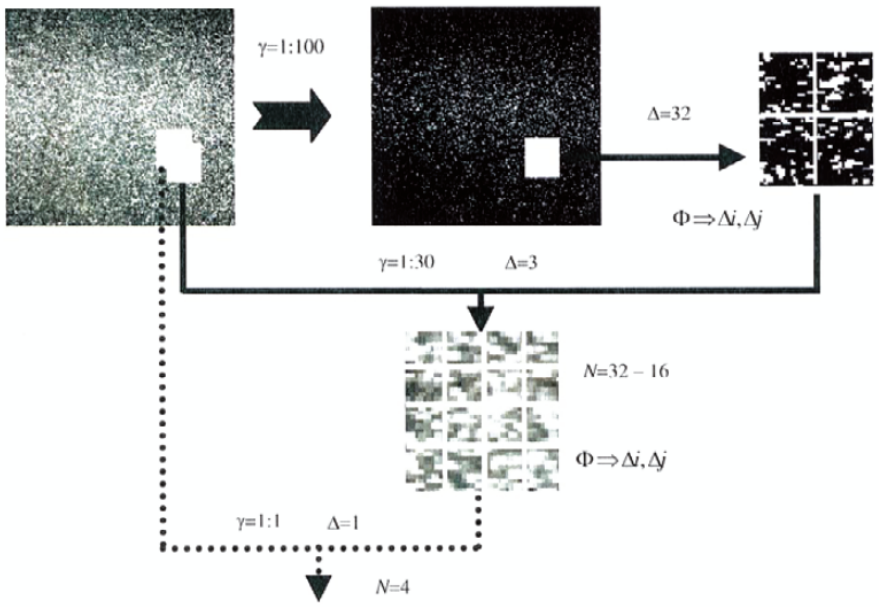

Figure 3.24: Using grid refinement with the DFT approach. Each cross correlation matrix serves as an input to the next level of refinement [82].

is refined, interrogated, and a new displacement field with finer resolution is produced. This can be used as the input to another round of deformation and grid refinement, as in a typical grid refinement approach [83]. Figure 3.25 shows a schematic of an iterative grid deformation and refinement procedure.

Similar to non-uniform flows, PIV flow fields rarely move by exact integer multiples of pixels. Thus, in order to achieve sub-pixel accuracy for the displacement vectors, a method for determining the true location of the peak of the correlation matrix is needed. The most popular methods are so called three point methods, because they involve fitting a function through three points of the pixel integer peak location. Figure 3.26 shows how a Gaussian fit over three points can be used to find the sub-pixel location of the correlation peak.

This study used the MATLAB tool PIVlab [77, 79]. PIVlab offers several different methods for image pre-processing, PIV analysis, and data validation and output. As previously stated, this study typically used 20 sequential frames to build up a large number of vectors. The images were then cropped into areas where the actual PIV analysis would

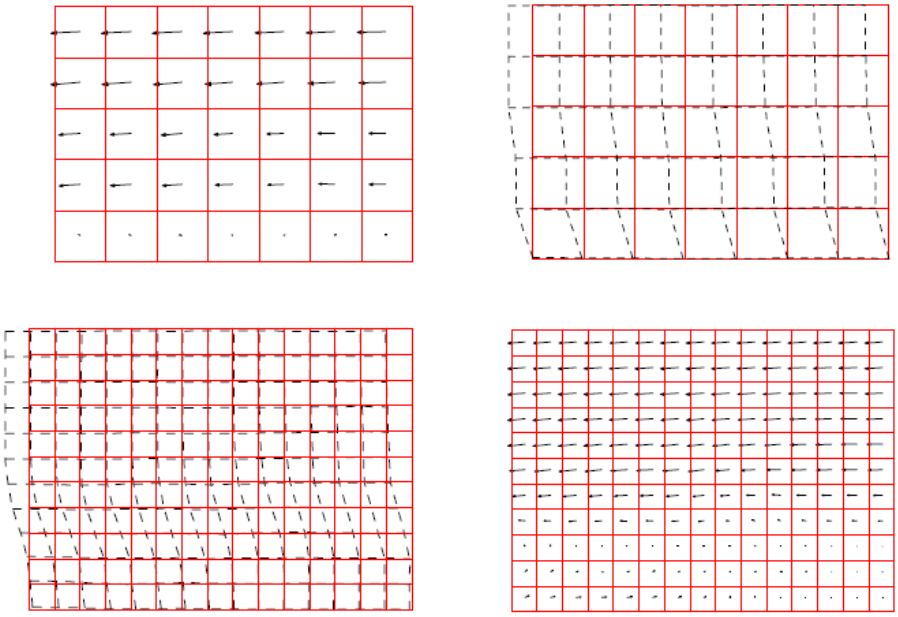

Figure 3.25: DFT using iterative deformation and grid refinement. [83].

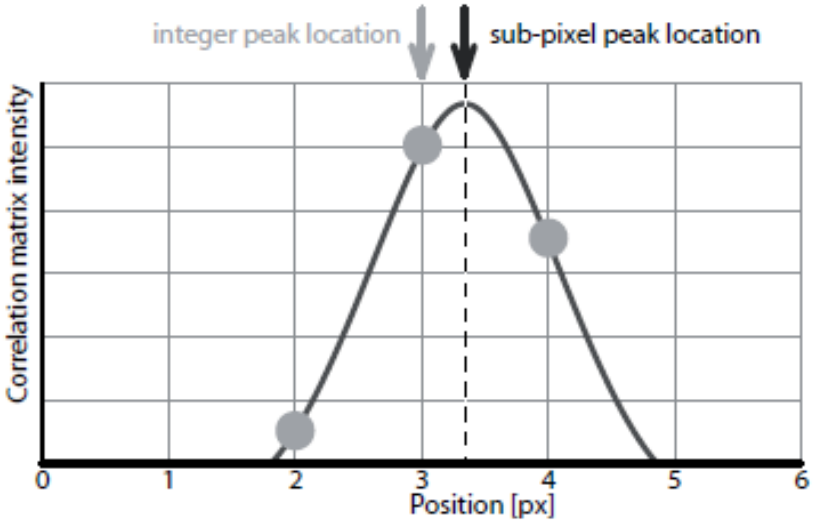

Figure 3.26: Gaussian three point method for peak finding (only one axis shown). [77].

take place (i.e. large stationary objects were ignored). All images were pre-processed using contrast limited adaptive histogram equalization (CLAHE) [84], which independently optimizes small windows of a larger image to maximize overall contrast. Due to the different resolutions used between different cameras, and even for the same camera used with different settings (typically, faster image capture requires images with less pixels), the window size for the cross correlation wasn't identical for every experimental run. However, every PIV analysis used a DFT method using the FFTW algorithm [85], a 2 pass grid refining window deformation method using splines for window interpolation, and a two dimensional (nine point) Gauss method for sub-pixel peak finding.

Once all frames were analyzed, vector validation was performed by a combination of three methods. First, a standard deviation filter was applied. This method eliminates any vectors that fall outside of

$$u = \bar{u} \pm n * \sigma \tag{3.5}$$

where $\bar{u}$ is the mean velocity and σ is the standard deviation. The value of n was typically set at 3 for the horizontal mesh configuration, while it was set to 5 for the angled mesh configuration due to the unknown non-vertical velocity components.

Then, a local median filter was applied. The local median filter uses the immediate neighbors of a vector (eight points) to calculate a median for the current position [86]. In a typical median test, the normalized residual of the central point, r'_0, is calculated by

$$r'_0 = \frac{|U_0 - U_m|}{r_m} \tag{3.6}$$

where $m = 1 - 8$ represents the surrounding points and r_m is the median of r_1 through r_8. However, in areas of low turbulence, r_m tends to zero. To compensate for this, a

fluctuation factor $epsilon$ is introduced, leading to

$$r*_0 = \frac{|U_0 - U_m|}{r_m - \epsilon} \tag{3.7}$$

A typical PIV analysis set ϵ at 0.1 (pixels), and set the threshold at 3 for the horizontal mesh configuration, and 5 for the angled mesh configuration (i.e. velocity vectors greater than 3 or $5r*_0$ away from the local median are outliers).

Finally, vector validation could be done manually, either by selecting individual vectors to delete, or by drawing appropriate velocity limits around a scatter plot of the x and y velocities. Figure 3.27 shows an example of what that might look like. This step was typically done after the application of the other two filters, as manually rejecting outliers can lead to rejecting genuine data [79].

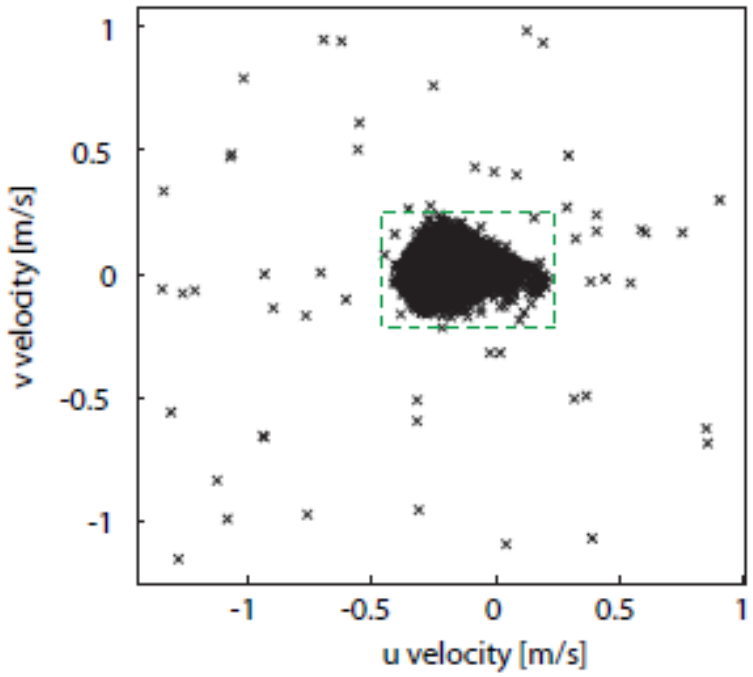

Figure 3.27: Drawing velocity limits on a scatter plot of x and y velocities. Vectors that are outside the box are discarded [79].

In a typical PIV study, there is an optimal particle size and particle image density, or

the number of particles per interrogation window. Since the particles themselves are of no interest other than for visualization purposes, there is some degree of control over the choice and seeding of the particles. In the case of this study, the particles themselves are the "fluid." This introduces a few key differences between a typical fluid flow that must be considered for a PIV analysis to be useful, or even successful [87].

One obvious difference is the lack of control over particle size. While the choice of ballotini could have been made with particle diameter in mind, the ID50-K material is under consideration for a granular heat transfer and storage medium in solar thermal power applications [64]. Therefore, the particle diameter is set by the needs of the experiment. While it is somewhat dependent on the cross correlation method used, the optimum particle diameter for a multipass DFT window deformation using splined interpolation is somewhere in the range of 2-4 pixels [77]. Bigger particles cause the correlation peak to become smaller and broader, while very small particles can cause an artifact called peak locking, where the displacement vectors tend towards integer values because three point sub-pixel interpolation can't resolve peaks smaller than one pixel. Since the particle diameter is controlled by the material being used in the experiment, the only other way to vary the particle image size is with the camera via sensor resolution and image framing. The image resolution is fixed by the sensor, while the framing is set by the user (typically a combination of lens magnification and camera placement). While those were slightly varied to suit the particular needs of a single test run, the most common image settings produced image scales that were $\sim$7.8 pixels/mm for the horizontal mesh test section, and $\sim$8.0 pixels/mm for the angled mesh test section. Thus, the ID50-K material was very near the optimal particle diameter used for the specific correlation method ($\sim$2.8 pixels). The ballotini tended to be smaller than the optimum range ($\sim$1.7 pixels/mm), but it was still very usable. A bigger challenge with the ballotini was likely tiny reflections causing very small but intense spots in the image, which in turn could produce peaks in the correlation matrix that were smaller than one pixel. These points could also not be present in a pair of interrogation windows,

leading to pair loss.

Another difference was the lack of control over particle seed rate, and therefore particle image density. The process of cross correlation is a statistical process. Therefore, interrogation windows with very few particles (less than 3) do not contain enough data in a statistically meaningful sense, leading to unsuccessful correlations [88]. However, if a window contains too many particles, it may be impossible to distinguish particle pairs from background noise (in fluid PIV experiments, extremely high particle seeding may also disturb the underlying flow patterns, giving inaccurate data). In a typical fluid flow study, there is an optimum particle loading rate for a given flow which produces particles that do not interfere with the underlying flow and provide discrete points of light for the PIV analysis. This loading rate can be effected by several variables, such as particle size, shape, and composition, fluid density and velocity, and even the type of light used [76]. In this study, the particle feed rate (i.e. the mass flux) was determined by the geometric configuration of the test section in use (which was the desired outcome). While it may be possible to calculate an average particle loading of a given video frame based on the calculated volume fraction, and thus an optimum interrogation window size, the relatively rapid acceleration of the particles throughout the test section means this interrogation window would only be optimal for certain parts of the flow. Instead, several different interrogation window sizes were tested on a video sample, and the one with the least amount of erroneous data near the theoretical maximum velocity was used.

PIV analysis of particle flows are typically either done on a free surface (as in [19]), or through a clear viewing window (as in [87, 89] and this study). When viewing particles through a window, the boundary itself may introduce artifacts into the flow, such as the introduction of extra friction, or in the reduction of a truly three dimensional flow field into a quasi-two dimensional flow field. In this study, all particle flows were viewed through a transparent window to avoid excessive particle loss, and to make the test section more rigid. It was expected that in regions of relatively low particulate loading, the presence of the front

face (or any face) would have little effect on the large scale behavior of the particle flow. However, in regions with high loading (particularly in places where there was significant particle accumulation), this assumption should be applied with some caution.

In summary, this section has provided details on the particular granular materials used, the pertinent details of the construction and instrumentation of the experimental apparatus, the procedures used to gather experimental data, and a brief overview of the PIV method and its applications to granular flows.

CHAPTER 4
NUMERICAL WORK

This section will describe the two different methods used in this study for modeling the granular flow: the discrete element method, and the finite volume method. For both methods, some initial model testing and set up was performed on personal copies of the software, but all final computations were done using the Georgia Institute of Technology's PACE high performance computing architecture. PACE provides shared high performance computing resources for a wide variety of research at Georgia Tech. Due to the shared nature of the resources and the implementation of the job scheduler, it was not practical to ask for a huge amount of computer resources for a single job. Rather, several jobs using a modest amount of computer resources were scheduled to run at once. This ensured a high rate of CPU usage, as opposed to trying to finish a single simulation as quickly as possible. While the average job used between 8 and 16 CPUs, it was noticed several times that over 500 CPUs were working on simulations for this study.

4.1 Discrete Element Models

4.1.1 Model Background

An increasingly common way to perform a numerical analysis of a group of particles is called the discrete element method, or DEM [41]. Initially formulated for two dimensional discs due to the computer limitations of the time, it has rapidly evolved in capability along with technological progress.

To understand the basic method, consider a two particle system, as seen in figure 4.1. Each particle has its own position, radius, linear velocity, and angular velocity. It is also possible for each particle to have its own set of material properties, such as density, elastic-

ity, etc., but for now it will be assumed that both particles are of the same material.

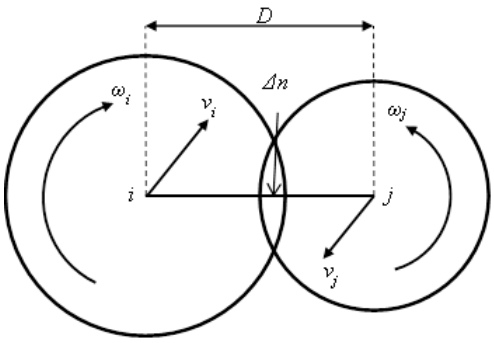

Figure 4.1: Two particle system used in DEM calculation

In real collisions, the particles deform. The crux of the discrete element method is to treat this collision as an overlap of particles. Particles are in contact if the distance between the two centers is less than the sum of the radii

$$D < R_i + R_j \tag{4.1}$$

If two particles are moving towards each other with a relative combined velocity of v, then the amount of overlap Δn will be (initially) proportional to the velocity and the time step between iterations Δt

$$\Delta n = v\Delta t \tag{4.2}$$

After this initial overlap, a normal force F_n will be exerted between the particles that will (ignoring any other attractive forces) tend to push them apart. This is modeled with a force displacement law

$$F_n = k\Delta n \tag{4.3}$$

where k can be thought of as a spring constant. According to Newton's second law of

motion, this force will begin to accelerate the particles as

$$a = \frac{\Delta F_n}{m} \tag{4.4}$$

If it is assumed that this acceleration is constant over the time step, than the resulting velocity at the beginning of the next time step is

$$v = a\Delta t. \tag{4.5}$$

Then, assuming the acceleration of the particle remains constant over the time step Δt, the velocity of the particles becomes

$$v_{t2} = \frac{F}{m}\Delta t \tag{4.6}$$

where the $t2$ subscript indicates it is for a future time step. Now, with a new velocity, particle positions and overlaps are re-calculated, and the process repeats itself for as many time steps as specified. The previous equations describe the calculation procedure for the normal direction. The same process is used for the tangential direction, substituting the necessary rotational properties into the equations. The tangential overlap describes the angular displacement (i.e. how far the particles "twist" over each other).

Several models have been proposed to model the normal and tangential contact of spherical particles. These range from simple linear spring-damper models, such as proposed in the original DEM description [41], to a very comprehensive model that includes a varying tangential force-displacement curve that depends not only on particle velocities, but the whole particle contact history as well [90, 91]. Figure 4.2 shows how the Hertz-Mindlin model computes the force on a particle at various points on force loading-unloading curve.

While the full Hertz-Mindlin model is usually taken as the most accurate model available to implement in DEM simulations, the variation of the tangential force-displacement curve requires a fairly complex algorithm to capture this behavior. Thus, a simplified no-

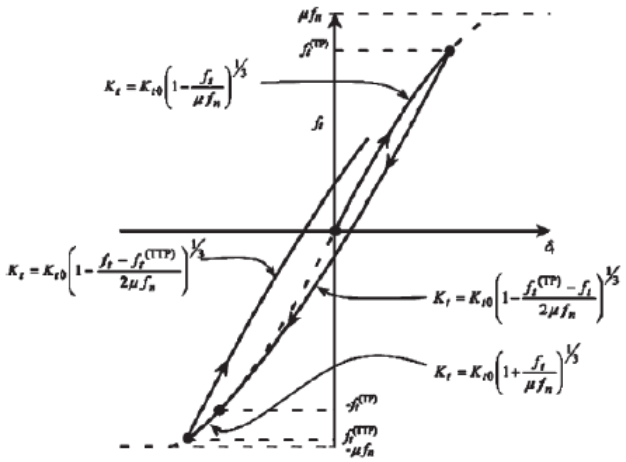

Figure 4.2: Tangential force-displacement curve for the Hertz-Mindlin particle contact model with constant normal displacement. The tangential elastic constants depend on current and previous particle loading [92]

slip version of the model is often used in which the tangential force-displacement relation is linear [92]. This is the approach used in this study.

4.1.2 Model Implementation

This section will describe how numerical simulations were built using the discrete element model, including model geometries, material parameters, and other variables needed to fully define a DEM simulation. All DEM computations were done with LIGGGHTS version 3 [93], an open source DEM code based on the molecular dynamics code LAMMPS [94]. Graphical post-processing was performed using the open source visualization program Paraview [95] on a personal computer.

LIGGGHTS implements the collision force of a particle using equation 4.7:

$$F = (k_n \delta_n - \gamma_n v_n) + (k_t \delta_t - \gamma_t v_t) \tag{4.7}$$

where k_i is the elastic contact for the given direction, γ_i is the damping constant for the given direction, δ_i is the overlap for the given direction, and v_i is the relative velocity for the given direction. Thus, the first term in parenthesis represents the normal force be-

tween particles, and the second term in parenthesis represents the tangential force between particles. The tangential overlap δ_t is truncated to ensure that

$$F_t \leq \mu_n F_n \tag{4.8}$$

where μ_n is the coefficient of normal friction. For the Hertz-Mindlin contact model, the coefficients in equation 4.7 are calculated from the following relations:

$$k_n = \frac{4}{3} Y^* \sqrt{R^* \delta_n} \tag{4.9}$$

$$\gamma_n = -2\sqrt{\frac{5}{6}} \beta \sqrt{S_n m^*} \geq 0 \tag{4.10}$$

$$k_t = 8 G^* \sqrt{R^* \delta_n} \tag{4.11}$$

$$\gamma_t = -2\sqrt{\frac{5}{6}} \beta \sqrt{S_t m^*} \geq 0 \tag{4.12}$$

$$S_n = 2 Y^* \sqrt{R^* \delta_n} \tag{4.13}$$

$$S_t = 8 G^* \sqrt{R^* \delta_n} \tag{4.14}$$

$$\beta = \frac{ln(e)}{\sqrt{ln^2(e) + \pi^2}} \tag{4.15}$$

$$\frac{1}{Y^*} = \frac{(1 - \nu_1^2)}{Y_1} + \frac{(1 - \nu_2^2)}{Y_2} \tag{4.16}$$

$$\frac{1}{G^*} = \frac{2(2-\nu_1)(1+\nu_1)}{Y_1} + \frac{2(2-\nu_2)(1+\nu_2)}{Y_2} \tag{4.17}$$

$$\frac{1}{R^*} = \frac{1}{R_1} + \frac{1}{R_2} \tag{4.18}$$

$$\frac{1}{m^*} = \frac{1}{m_1} + \frac{1}{m_2} \tag{4.19}$$

where Y is the Young's modulus, G is the shear modulus, ν is the Poisson ratio, and e is the coefficient of restitution. The equations used to describe the linear (or Hooke) model are given in appendix B.

In addition to the tangential force exerted on a particle by the friction between two particles, LIGGGHTS also allows the modeling of a separate rolling resistance torque applied to particles. This rolling resistance is often the result of plastic deformation of a surface, surface adhesion, or even the result of non-spherical particles [96]. The default model used in this study is an elastic-plastic spring-dashpot (EPSD) model which uses a similar analog to a linear normal contact model [96]. In LIGGGHTS, this model is implemented as

$$M_r = M_r^k + M_r^d \tag{4.20}$$

where M_r is the total rolling resistance torque, M_r^k is the spring torque, and M_r^d is the damping torque.

The spring torque is implemented in an incremental manner:

$$\Delta M_r^k = -k_r \Delta\theta_r \tag{4.21}$$

$$M_{r,t+\Delta t}^k = M_{r,t}^k + \Delta M_r^k \tag{4.22}$$

where k_r is the rolling stiffness, given by

$$k_r = 2.25 k_n \mu_r^2 R^{*2} \tag{4.23}$$

and μ_r is the coefficient of rolling friction. The updated rolling spring torque $M^k_{r,t+\Delta t}$ is limited by

$$|M^k_{r,t+\Delta t}| \leq M^r_m \tag{4.24}$$

where M^r_m is the limiting spring torque, given by

$$M^r_m = \mu_r F_n R^*. \tag{4.25}$$

The damping torque is assumed to be dependent on the relative rolling angular velocity, $\dot{theta}_r$, between two particles in contact, and is given by

$$M^d_r = \begin{cases} -C_r \dot{\theta}_r, & \text{if } M^k_{r,t+\Delta t} < M^r_m \\ -f C_r \dot{\theta}_r, & \text{if } M^k_{r,t+\Delta t} = M^r_m \end{cases} \tag{4.26}$$

where C_r is the damping coefficient given by

$$C_r = 2\eta_r \sqrt{I_r k_r} \tag{4.27}$$

$$I_r = \left(\frac{1}{I_i + m_i r_i^2} + \frac{1}{I_j + m_i r_j^2} \right)^{-1} \tag{4.28}$$

where I is the moment of inertia of a given particle. In the current implementation, the factor f in equation 4.26 is set to 0 to disable damping at full rolling mobilization. Setting f to 1 ensures there is always a rolling damping term present. The equations used to implement the other rolling resistance models are given in appendix B.

Table 4.1 lists the material properties used in the DEM simulations. The asterisk indi-

cates that the material property used does not correspond the the precise material used in the experiments (for instance, the properties for aluminum oxide are often substituted for the properties of ID50-K). The dagger symbol means the property had to be altered to meet the minimum requirements of a LIGGGHTS simulation.

Table 4.1: Material properties used in DEM simulations

Particles			
Material	ρ (kg/m^3)	ν	E (MPa)
ID50-K	3760 [65]	0.22* [97]	37.0* [97]
Ballotini	2500 [67]	0.245 [98]	5*† [98]
Walls			
Steel	n/a	0.30 [98]	20.0 [98]
Aluminum	n/a	0.33 [98]	7.17 [98]
Polycarbonate	n/a	0.37 [99]	5† [99]

Table 4.2 lists the interactions used for DEM simulations. Once again, the asterisk symbol means either that the material property was not available for the specific materials used in the experiments, or that the specific interaction coefficient was assumed based on other material interactions.

Table 4.2: Material interactions used in DEM simulations

Normal friction	ID50-K	Ballotini
Particle-particle	0.9* [100]	0.15 [101]
Particle-steel	0.7* [100]	0.135* [101]
Particle-aluminum	0.7*	-
Particle-polycarbonate	0.85*	0.85*
Rolling friction		
(all values)	0.1*	0.01 [102]
Coefficient of restitution		
Particle-particle	0.9*	0.9 [101]
Particle-steel	0.9* [97]	0.8 [101]
Particle-aluminum	0.9*	-
Particle-polycarbonate	0.9* [103]	0.9*

Horizontal mesh The horizontal wire mesh screen geometries were developed in the CAD program Solidworks. While the wire diameter and spacing were consistent with the parameters given by McMaster-Carr, the geometry was developed as a simple set of intersecting cylinders, instead of trying to replicate the actual wire weave that was present in the physical mesh screens. This was mostly done in an attempt to simplify the computational mesh needed for the CFD model (see the next section), but this geometry was also used in the DEM model for a more direct comparison between the two numerical methods. The native Solidworks files were converted to .stl files using the meshing software gmsh [104]. While Solidworks has the ability to generate .stl files, they often include vary narrow, high aspect ratio triangles. This leads to problems when running LIGGGHTS in parallel as there can be large numbers of triangles that can cross CPU domain boundaries, leading to collision detection issues. Thus, while gmsh .stl files are larger, they run much faster in a LIGGGHTS simulation. The element size was chosen in gmsh to balance file size against maintaining the radius of curvature in the geometry. Figure 4.3 shows the original Solidworks geometry for the 10 x 10 size mesh and the resulting .stl file produced by gmsh. Figure 4.4 shows a view of the single spaced horizontal mesh domain used in the DEM simulations. The mesh geometries represent the 10 x 10 mesh.

Due to the somewhat statistical nature of DEM simulations, the geometry was built to encompass one quarter of the flow area of the experimental test section. Two walls were given the properties of polycarbonate, while the two other walls were treated as a symmetric boundary. Strictly speaking, symmetric boundary conditions do not exist for DEM simulations, so these walls were given the same material properties as the particles for a given simulation, but they were treated as frictionless and perfectly elastic. The top and bottom surfaces of the domain were treated as periodic boundaries. For the single spaced configuration, three meshes were inserted with the appropriate spacing. For the double spaced configuration, the center mesh was not inserted.

Inserting particles was done in a sequence of batch operations in an attempt to simulate

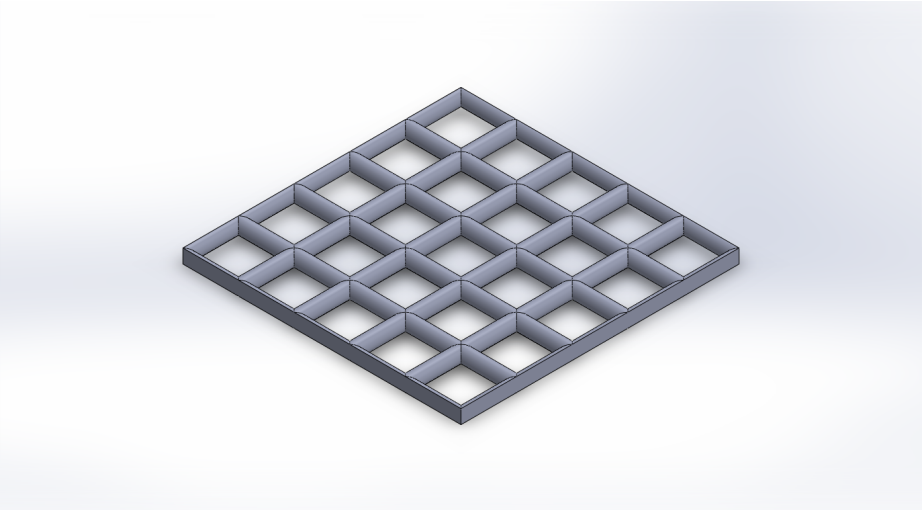

(a) 10 mesh model in Solidworks

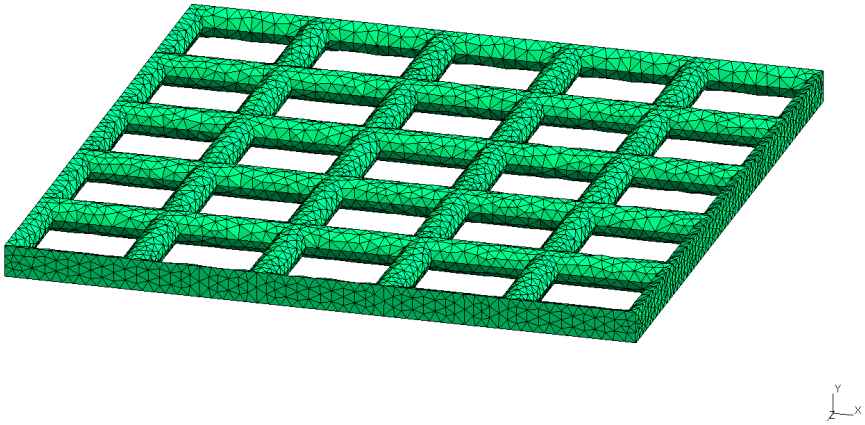

(b) 10 mesh model after .stl conversion in gmsh

Figure 4.3: 10 mesh horizontal screen geometric model.

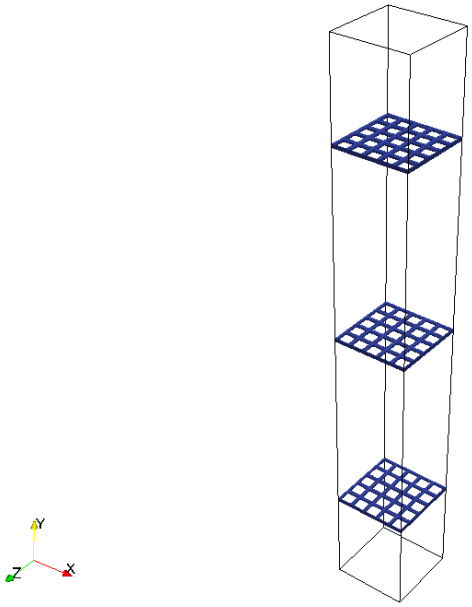

Figure 4.4: Typical view of the single spaced horizontal mesh domain for the DEM simulations. The black lines indicate the extent of the simulation bounding box.

filling the domain from a hopper located above the model. To ensure the top section of the simulation stayed filled with particles, it was calculated that approximately 100000 ID50 K particles were needed (this required 470000 ballotini particles to achieve roughly the same particle loading), inserted at evenly spaced intervals "above" the top mesh. Technically, they were inserted in the very bottom of the domain to help insure that the last few particles weren't overlapping with other particles during insertion, causing extremely large particle forces.

Mass flow measurements were taken at the plane of the central mesh. LIGGGHTS calculates mass flow by counting the number of particles that pass through a plane in the geometry. Plotting the sum of the total number of particles that cross the plane during a given time interval produces a plot that is very similar to the plots produced by the experimental data. Steady state was determined to have been reached when this plot was linear. Volume fraction measurements were taken in the space between the top and bottom mesh.

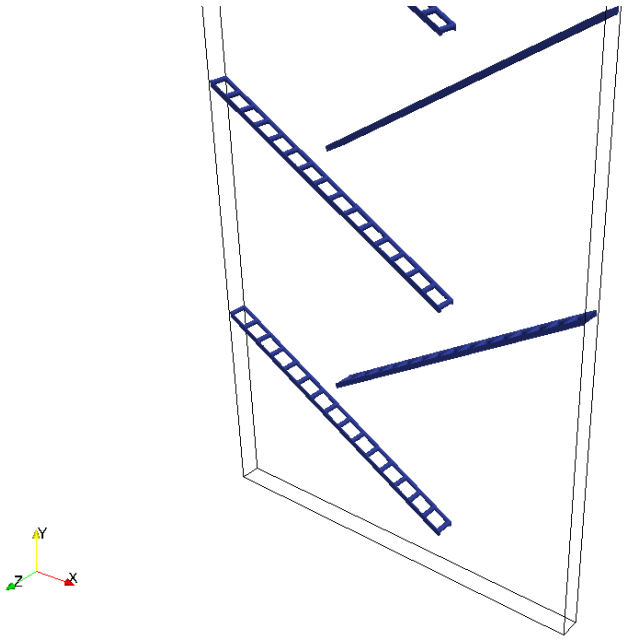

Figure 4.5: Detail of angled 10 mesh geometry in the DEM simulation, single spaced configuration. The black lines indicate the extent of the simulation bounding box. The top has been truncated.

Angled mesh The angled mesh test section was constructed in a similar fashion. For this model, the geometry was chosen so that the far left and right boundaries of the domain were at the peaks of the angled mesh structures. This enabled the geometry to maintain a constant width using various sized mesh models, and to be able to model an entire slice of the experimental test section. The depth was set at one row of holes in the wire mesh, necessitating a variable geometry depth. Three meshes were used for the single spaced model, while the double spaced mesh used only the outer two meshes. The left and right boundaries were treated as polycarbonate walls, while all other boundaries were treated as periodic. Particles were inserted near the bottom of the domain and allowed settle above the first row of angled screens. Despite the variable geometry, the angled mesh model required approximately the same number of ID50 K particles to sufficiently fill the domain (the larger meshes required the insertion of additional particles to ensure the flow was self limited). Figure 4.5 shows an image of the angled 10 mesh geometry as used in the DEM simulations.

Square tube The square tube simulation was constructed to take advantage of geometric symmetry. The left and right extents were chosen to run through the center of the adjacent columns of squares, while the front and back walls were limited to the symmetry planes running through one row of the holes on the faces of the squares. The vertical dimension was chosen to allow at least two whole squares in an attempt to allow the model to move past the entrance region (plus enough room on top for particle insertion). The top and bottom boundaries were treated as periodic, while all the side faces were treated as symmetric. Both the whole and slotted square tube models required approximately 500000 particles for sufficient filling.

Perforated plate The perforated plate test section was constructed in a similar manner to the square tube test section. In this case, the front and back walls were set at the symmetry plane than ran through two rows of adjacent cells in the perforated plate. The top and bottom boundaries were treated as periodic, while all the side faces were treated as symmetric. The whole square model required approximately 460000 particles for sufficient filling. However, when the slotted square model was filled to the same level, it was discovered that during particle insertion, some of the newly inserted particles would rebound so strongly off of particles already in the domain that they would cause the flow to back up in the bottom square. Thus, the slotted square model required the deletion of particles from the bottom of the domain to eliminate this "false accumulation." The final model contains roughly 420000 particles. Figure 4.6 shows images of the slotted square tube geometry and the non-slotted perforated plate geometry as used in the DEM simulations.

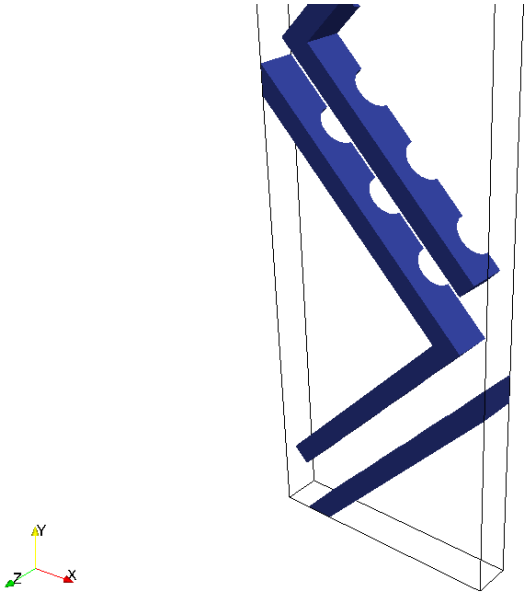

(a) Slotted square tube geometry

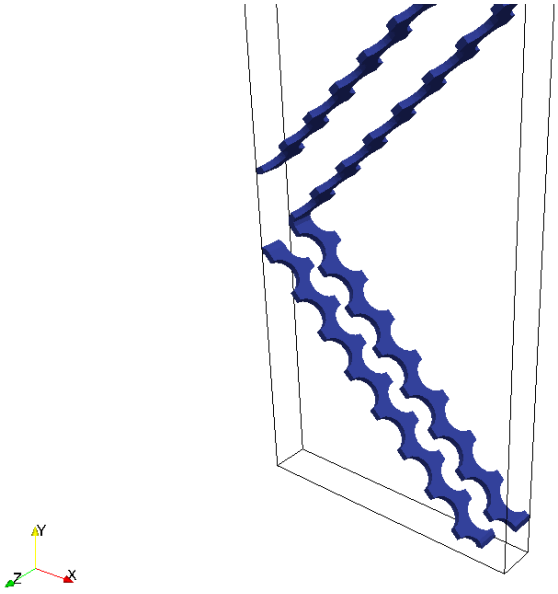

(b) Perforated plate square tube geometry

Figure 4.6: Examples of non-wire mesh geometry in DEM simulations. The black lines indicate the extents of the simulation bounding box. The top has been truncated.

4.2 Coninuum Models

4.2.1 Model Background

Continuum models, such as the one used in this study, treat a granular material as a fluid and attempt to solve modified forms of the Navier-Stokes equations. To numerically evaluate the Navier-Stokes equations, they are discretized in space and time and solved algebraically. In the case of a granular problem, a set of equations is solved for each species (i.e. the granular material and the surrounding fluid, such as air).

The three primary methods for discretizing differential equations are the finite difference method, the finite volume method, and the finite element method, with the finite volume method being used in this study. One aspect of the finite volume method that makes it particularly attractive for use in computational fluid dynamics is that the discretization method ensures continuity is preserved in each cell.

Consider the generic scalar transport equation [105]

$$\frac{\delta}{\delta t}(\rho\phi) + \nabla \cdot (\rho \mathbf{V}\phi) = \nabla \cdot \Gamma_\phi \nabla\phi + S_\phi \tag{4.29}$$

where ρ is the density, ϕ is the transported scalar, $\mathbf{V}$ is the velocity vector, Γ_ϕ is the diffusion coefficient, and S_ϕ is the source term. Thus, setting ϕ to unity returns the continuity equation, setting ϕ to $\mathbf{V}$ returns the momentum equation, and setting ϕ to T returns the energy equation. For simplicity, consider the simple rectangular domain shown in figure 4.7

In this domain, the values of ρ, ϕ, and Γ_ϕ are stored at the cell centroid P. Upper case letters refer to neighboring cell centroids, while lower case letters refer to faces of the central cell. At first, an incompressible two dimensional steady state problem is considered. To discretize equation 4.29, it is integrated over the control volume P in figure 4.7

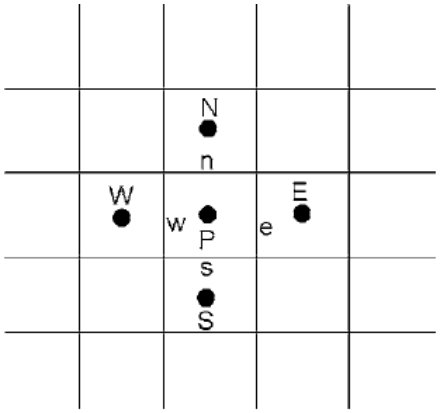

Figure 4.7: Control volume used for finite volume method [106]

$$\left(\rho u\phi - \Gamma\frac{\delta\phi}{\delta x}\right)_e - \left(\rho u\phi - \Gamma\frac{\delta\phi}{\delta x}\right)_w + \left(\rho v\phi - \Gamma\frac{\delta\phi}{\delta y}\right)_n - \left(\rho v\phi - \Gamma\frac{\delta\phi}{\delta y}\right)_s + \int SdV = 0 \quad (4.30)$$

At this point, the value of ϕ and the derivative of ϕ on the cell boundary must be determined. For the derivative of ϕ, a piecewise linear function is chosen. Then, the derivatives in equation 4.30 can be evaluated using a central differencing formula as

$$\frac{\delta\phi}{\delta x}_e = \frac{\phi_E - \phi_P}{\delta x} \quad (4.31)$$

and so on for the other neighboring cells. It can be shown that, on equidistant grids, the central difference approximation is 2nd order accurate. For non-equidistant grids, the error is proportional to the growth rate of cell sizes (see figure 4.8). While other schemes to evaluate the boundary derivatives exist, this simple evaluation is almost always used in practice [107]. Evaluating the value of ϕ on the boundary is not quite as simple. While using a central differencing scheme identical to equation 4.31 works for low Reynolds number flows, it is not acceptable in general, producing unrealistic results. For this variable, several schemes have been introduced, such as first order upwind, second order upwind,

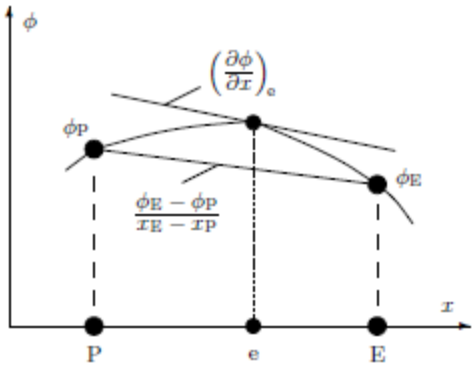

Figure 4.8: Central differencing formula for approximating boundary derivatives [107]

exponential schemes, and so on (see [105] for various examples).

In the following simple example, the first order upwind scheme has been implemented. It states that the value of ϕ on the boundary takes the value of whatever cell centroid is *upwind* of the boundary. In other words, for the eastern boundary

$$\phi_e = \phi_P, u > 0 \tag{4.32a}$$

$$\phi_e = \phi_E, u < 0 \tag{4.32b}$$

To keep the equations a bit more compact, two definitions are introduced:

$$F \equiv \phi \mathbf{V}, D \equiv \frac{\Gamma}{\delta x} \tag{4.33}$$

Now, equation 4.30 can be recast as

$$a_P \phi_P = \sum_{i=N,S,E,W} a_i \phi_i + b \tag{4.34}$$

where

$$a_{E,N} = D_{e,n} + [[-F_{e,n}, 0]] \tag{4.35a}$$

$$a_{W,S} = D_{w,s} + [[F_{w,s}, 0]] \tag{4.35b}$$

$$a_P = \sum a_i + (F_e - F_w + F_n - F_s) \tag{4.35c}$$

$$b = \bar{S}\Delta x \Delta y \tag{4.35d}$$

where the double brackets indicate that the maximum quantity is to be used. Now, the differential equation 4.29 has been transformed into an algebraic equation over the control volume P. Several iterative techniques have been used to solve equation 4.34. For the simple 2 dimension grid shown in figure 4.7, a tri-diagonal matrix algorithm (TDMA) may be employed, while more complex grids require more complex solvers [106]. If equation 4.34 is non-linear (such as containing a non-linear source term S, or a non-constant diffusion term), then the solution will have to be arrived at after several iterations.

For strongly non-linear problems, under-relaxation may be performed to limit the amount of change that occurs during each iteration. Equation 4.34 can be recast in the form

$$\phi_p = \frac{\sum a_i \phi_i + b}{a_p} \tag{4.36}$$

where the directional subscripts have been dropped for compactness. If ϕ_p^*, the value obtained at the previous iteration, is added and subtracted from the right hand side of equation 4.36, it becomes

$$\phi_p = \phi_p^* + \left(\frac{\sum a_i \phi_i + b}{a_p} - \phi_p^* \right). \tag{4.37}$$

Now the relaxation factor, α, is introduced to the second term of equation 4.37, which

now becomes

$$\phi_p = \phi_p^* + \alpha\left(\frac{\sum a_i\phi_i + b}{a_p} - \phi_p^*\right). \tag{4.38}$$

Thus, if α is equal to zero, the current iteration always maintains the same value as the previous iteration, and the solution never proceeds beyond the initial conditions. If α is equal to one, the previous iteration values cancel out, and the equations proceed normally. Any value of α less than one causes under-relaxation, causing equation 4.38 to converge more slowly (which is usually the desired result). Setting α to a value greater than one causes over-relaxation, and is not normally done (although it may be performed for very "smooth" problems where very low residuals in the solution are desired). The value of α does not need to be the same for every variable considered, every iteration, or even every grid point. However, the general goal is to pick a value large enough that will still produced a stable solution, while not slowing down convergence considerably. This must often be done through experience or the study of similar problems [105].

Now an unsteady problem is considered. To simplify the equations somewhat, only the x direction will be considered. Equation 4.29 takes the form

$$\rho\frac{\delta\phi}{\delta t} = \frac{\delta}{\delta x}\left(\Gamma\frac{\delta\phi}{\delta x}\right) \tag{4.39}$$

Once again, integrating over the cell and integrating over some time interval Δt, equation 4.39 becomes

$$\rho\int_w^e\int_t^{t+\Delta t}\frac{\delta\phi}{\delta t}\,dt\,dx = \int_t^{t+\Delta t}\int_w^e\frac{\delta}{\delta x}\left(\Gamma\frac{\delta\phi}{\delta x}\right)dx\,dt \tag{4.40}$$

To evaluate the left hand term of equation 4.40, it is assumed that the value of ϕ is constant throughout the volume, thus

$$\rho\int_w^e\int_t^{t+\Delta t}\frac{\delta\phi}{\delta t}\,dt\,dx = \rho\Delta x(\phi_P - \phi_P^0) \tag{4.41}$$

where the superscript 0 indicates the current (known) value of ϕ.

As with the steady state transport equation, the right hand side of equation 4.40 is first integrated over the volume

$$\rho\Delta x(\phi_P - \phi_P^0) = \int_t^{t+\Delta t} \left[(\phi_E - \phi_P)\left(\frac{\Gamma}{\delta x}\right)_e - (\phi_P - \phi_W)\left(\frac{\Gamma}{\delta x}\right)_w \right] dt \tag{4.42}$$

Once again, an assumption needs to be made about how the value of ϕ will vary from one time step to the next. This can be generalized by

$$\int_t^{t+\Delta t} \phi \, dt = (f\phi + (1-f)\phi^0)\Delta t \tag{4.43}$$

where f is a weighting function between zero and one. Upon performing the temporal integration given by equation 4.43 on every value of ϕ and performing the same rearranging that was done for equation 4.34, the unsteady discretization equation becomes

$$a_P\phi_P = \sum_{i=E,W} a_i(f\phi_i + (1-f)\phi_i^0) + \phi_P^0(a_P^0 - (1-f)\sum_{i=E,W} a_i) \tag{4.44a}$$

$$a_i = \left(\frac{\Gamma}{\delta}\right)_i \tag{4.44b}$$

$$a_P^0 = \frac{\rho\Delta x}{\Delta t} \tag{4.44c}$$

$$a_P = a_P^0 + f\sum_{i=E,W} a_i \tag{4.44d}$$

The value of f has a fairly large impact on how the solution of equations 4.44 proceeds. Setting f equal to zero results in a fully explicit scheme, where the updated solution values of ϕ depend *only* on previously known values. While this appears convenient, convergence

analysis shows that when using an explicit scheme, the time step is limited by

$$\frac{u\Delta t}{\Delta x} \leq 1 \tag{4.45}$$

where u is the x component of the velocity. This is known as the Courant-Friedrichs-Lewy (CFL) condition [108, 109], and the left hand side of equation 4.45 is known as the Courant number. Ensuring this condition is met keeps the fluid in a problem from moving more than one cell in a single time step.

On the other hand, setting f equal to one leads to a fully implicit scheme. In such a case, the value of ϕ depends on the updated solution values surrounding cell P. While this scheme requires iterative solution methods at each time step, it has a key advantage in that the time step requirements of equation 4.45 no longer apply. In theory, the chosen time step could be as large as desired. In practice, reasonably small time steps are used, in order to both prevent excessive iterations on a single time step, and to ensure that transient features of interest are captured. Setting the value of f equal to 0.5 results in the Crank-Nicholson scheme. For very small time steps, this scheme is more accurate than the implicit scheme, at the cost of more computations. However, for large time steps, it can result in physically unrealistic results.

4.2.2 Model Implementation

This section will describe how numerical simulations were built using the finite volume model, including model geometries, material parameters, and other variables needed to fully define a CFD simulation. All CFD meshing, computation, and post-processing was performed using Ansys v17/18 (due to difference in version between local and distributed versions). All computations were performed using Fluent v17. Equations used to describe alternate model options are given in appendix B.

In an Eulerian-Eulerian (EE) multiphase simulation, Fluent solves the following set of

general conservation equations [110]:

$$\frac{\partial}{\partial t}(\alpha_q \rho_q) + \nabla \cdot (\alpha_q \rho_q \vec{v}_q) = 0 \tag{4.46}$$

$$\frac{\partial}{\partial t}(\alpha_q \rho_q \vec{v}_q \vec{v}_q) = -\alpha_q \nabla p + \nabla \cdot \vec{\vec{\tau}}_q + \alpha_q \rho_q \vec{g} + \sum_{q=1}^{n} K_{pq}(\vec{v}_p - \vec{v}_q) \tag{4.47}$$

where q is the phase, α is the volume fraction (constrained so that $\sum \alpha_i = 1$), ρ is density, $\vec{v}$ is the velocity, p is the pressure, $\vec{\vec{\tau}}$ is the stress tensor, $\vec{g}$ is gravity, and K is the momentum exchange coefficient between phases. Thus, the Eularian-Eularian model treats the two phases as interacting fluids.

There are many ways to model turbulence in a multi-phase flow. For this study, the standard two equation $k - \epsilon$ model was chosen [111]. The $k - \epsilon$ model uses two equations to model the turbulence kinetic energy, k, and the rate of dissipation, ϵ, given by

$$\frac{\partial}{\partial t}(\rho k) + \frac{\partial}{\partial x_i}(\rho k u_i) = \frac{\partial}{\partial x_j}\left[\left(\mu + \frac{\mu_t}{\sigma_k}\right)\frac{\partial k}{\partial x_j}\right] + G_k - \rho\epsilon \tag{4.48}$$

$$\frac{\partial}{\partial t}(\rho \epsilon) + \frac{\partial}{\partial x_i}(\rho k \epsilon u_i) = \frac{\partial}{\partial x_j}\left[\left(\mu + \frac{\mu_t}{\sigma_\epsilon}\right)\frac{\partial \epsilon}{\partial x_j}\right] + C_{1\epsilon}\frac{\epsilon}{k}G_k - C_{2\epsilon}\rho\frac{\epsilon^2}{k} \tag{4.49}$$

where G_k is the production of turbulence energy, given by

$$G_g = \mu_t S^2 \tag{4.50}$$

where $S \equiv \sqrt{2 S_{ij} S_{ij}}$ is the modulus of the mean rate of strain tensor, μ_t is the turbulent

viscosity, given by

$$\mu_t = \rho C_\mu \frac{k^2}{\epsilon} \tag{4.51}$$

and C_μ, $C_{1\epsilon}$, $C_{2\epsilon}$, σ_k, and σ_ϵ are constants given by

$$C_\mu = 0.09, C_{1\epsilon} = 1.44, C_{2\epsilon} = 1.92, \sigma_k = 1.0, \sigma_\epsilon = 1.3.$$

This study solved equations 4.48 and 4.49 for both the solid and fluid phase.

The momentum exchange coefficient K in the momentum equation describes the momentum exchange between the different phases (note: while the granular flow is modeled mathematically as a fluid, it will be referred to as a solid to reduce ambiguity). In this study, the Gidaspow model [112], which is recommended for dense fluidized beds, is used for the solid-fluid exchange coefficient. The coefficient K takes the form

$$\begin{aligned} \alpha_g > 0.8 : K_{sg} &= \frac{3}{4} C_D \frac{\alpha_s \alpha_g \rho_g |\vec{v_s} - \vec{v_l}|}{d_s} \alpha_g^{2.65} \\ C_D &= \frac{24}{\alpha_g Re_s} [1 + 0.15(\alpha_g Re_s)^{0.687}] \\ \alpha_g \leq 0.8 : K_{sg} &= 150 \frac{\alpha_s (1 - \alpha_g) \mu_g}{\alpha_g d_s^2} + 1.75 \frac{\rho_g \alpha_s |\vec{v_s} - \vec{v_l}|}{d_s} \end{aligned} \tag{4.52}$$

where the s and g subscripts refer to the solid and gas phases respectively.

For the momentum exchange between the l^{th} solid particle and the s^{th} solid particle, the exchange coefficient takes the form [113]

$$K_{ls} = \frac{3(1 + e_{ls})(\frac{\pi}{2} + C_{fr,ls}\frac{\pi^2}{8})\alpha_s \rho_s \alpha_l \rho_l (d_l + d_s)^2 g_{0,ls}}{2\pi(\rho_l d_l^3 + \rho_s d_s^3)} |\vec{v_l} - \vec{v_s}| \tag{4.53}$$

where e_{ls} is the coefficient of restitution, $C_{fr,ls}$ is the coefficient of friction, d is the particle diameter, and $g_{0,ls}$ is the radial distribution function. The radial distrubution is a

correction factor that modifies the probibility of particle collisions as a granular assembly becomes more desne. It takes the form [114]

$$g_0 = \left[1 - \left(\frac{\alpha_s}{\alpha_{s,max}}\right)^{1/3}\right]^{-1} \tag{4.54}$$

Thus, as the granular assembly approaching the maximum packing fraction, the distribution function approaches infinity.

The pressure gradient term in the momentum equation requires the calculation of a solids pressure, p_s, which is calculated for granular flows which are below the maximum packing limit (i.e. a compressible flow). The solids pressure includes a granular temperature term, Θ_s, which describes the average kinetic energy of the particles. This study uses the solids pressure model of Lun et al. [115]. The solids pressure contains a kinetic term and a collision term, and is given by

$$p_s = \alpha_s \rho_s \Theta_s + 2\rho_s(1 + e_{ss})\alpha_s^2 g_{0,ss}\Theta_s \tag{4.55}$$

$$\tag{4.56}$$

The formal equation for the granular temperature accounts for the kinetic energy of particles due to random velocity fluctuations:

$$\Theta_s = \frac{1}{3}u_i u_i \tag{4.57}$$

The transport equation for granular temperature takes the form [116]

$$\frac{3}{2}\left[\frac{\partial}{\partial t}(\rho_s \alpha_s \Theta_s) + \nabla \cdot (\rho_s \alpha \vec{v_s} \Theta_s)\right] = (-p_s \bar{\bar{I}} + \bar{\bar{\tau}}_s) : \nabla \vec{v_s} + \nabla \cdot (k_{\Theta_s} \nabla \Theta_s) - \gamma_{\Theta_s} + \phi_{ls} \tag{4.58}$$

where $(-p_s\bar{\bar{I}} + \bar{\bar{\tau}}_s) : \nabla\vec{v_s}$ is the generation of energy due to the solid stress tensor (note: this term is normally seen as an energy dissipation term. However, in the case of granular flows, energy dissipation via the stress tensor includes particle collisions that will increase the granular temperature of participating particles. Thus, it is physically taken as a generation term), k_{Θ_s} is the diffusion coefficient for granular temperature, γ_{Θ_s} is the collisional dissipation of energy, and ϕ_{ls} is energy exchange between the l^{th} solid or fluid phase and the s^{th} solid phase. In the current study, the convection and diffusion terms are dropped from equation 4.58, leaving only the generation, collisional dissipation, and phase exchange terms. The collisional dissipation of energy is given by [115]

$$\gamma_{\Theta_s} = \frac{12(1-e_{ss}^2)g_{0,ss}}{d_s\sqrt{\pi}}\rho_s\alpha_s^2\Theta_s^{3/2}. \tag{4.59}$$

The energy exchange term is given by [112]

$$\phi_{ls} = -3K_{ls}\Theta_s. \tag{4.60}$$

The modeling of shear stresses is very important in dense granular flows, where collisions are frequent. To calculate the shear stresses, the stress tensor contains expressions for both shear and bulk viscosity. The shear viscosity, μ_s, consists of a collisional, kinetic, and frictional term:

$$\mu_s = \mu_{coll} + \mu_{kin} + \mu_{fric}. \tag{4.61}$$

The collisional component of the solids viscosity is the Gidaspow model [112, 117], given by

$$\mu_{coll} = \frac{4}{5}\alpha\rho d g_0(1+e)(\Theta/\pi)^{1/2}\alpha \tag{4.62}$$

where all previously defined material properties and functions pertain to the solid phase.

The kinetic component of the solids viscosity used in this study is also the Gidaspow model [112], given by

$$\mu_{kin} = \frac{10\rho d\sqrt{\Theta\pi}}{96\alpha(1+e)g_0}[1+\frac{4}{5}g_0\alpha(1+e)]^2. \tag{4.63}$$

Finally, the frictional component of the solids viscosity is the Schaeffer model [118], given by

$$\mu_{fric} = \frac{p_s \sin\phi}{2\sqrt{I_{2D}}} \tag{4.64}$$

where p_s is the solids pressure, ϕ is the angle of internal friction, and I_{2D} is the second invariant of the deviatoric sress tensor.

In addition to the shear viscosity, the stress tensor contains a bulk viscosity term, λ_s. For this study, the model of Lun et al. [115] was used, which is given by

$$\lambda_s = \frac{4}{3}\alpha^2\rho d g_0(1+e)(\Theta/\pi)^{1/2}. \tag{4.65}$$

While Fluent offers many methods for interpolation, all phase variables were interpolated using a first order upwind scheme. Spatial gradients for the horizontal mesh model were calculated using the Green-Gauss cell based theorem, which calculates variable values at the face of a cell by calculating the average of the two adjacent cell centers:

$$\phi_f = \frac{\phi_{c,0}+\phi_{c,1}}{2}. \tag{4.66}$$

While this method can be somewhat inaccurate for highly unstructured meshes, it is computationally inexpensive. For all of the other models considered, due to their more irregular computational meshes, spatial gradients were computed using the least squares cell based method. The least squares method computes derivatives for cell faces by computing a series of weights, W_{i0}^j, for each face in the cell. Then, the individual components of the

gradient can be calculated by multiplying the corresponding weight to the difference in variables in neighboring cell centers:

$$(\phi_j)_{c0} = \sum_{i=1}^{n} W_{i0}^{j}(\phi_{ci} - \phi_{c0}) \tag{4.67}$$

where $j = x, y, z$. All temporal integration was done on a fully implicit first order basis. All under-relaxation values were set at one half of the Fluent default values, as it was found that the default values would often cause a solution to diverge very quickly after the introduction of a solid phase into a simulation. During calculation, only the solid phase residuals were monitored, as the behavior of the solids phase was the primary objective of this study.

Table 4.3 shows the specific properties used in the CFD model. The common properties of particle diameter, density, and particle-particle coefficient of restitution were identical to those used in the DEM model (see table 4.1). When the granular temperature is treated as an algebraic equation (the Fluent default), the coefficient of restitution between particles and walls is not included because it is assumed that the convection and diffusion of granular temperature is zero.

Table 4.3: Material properties used in CFD simulations

Variable	ID50 k	Ballotini
Angle of internal friction	29°	25°
Friction packing limit	0.55 [17]	0.55
Maximum packing limit	0.6 [17]	0.6

Horizontal mesh The horizontal mesh models were built to enclose a single hole in the physical screen to minimize the number of elements in the final mesh. The model was cut out of the larger geometry used for the DEM model and exported from Solidworks as a .stp file, which is a common three dimensional geometry file. To actually model the wire surfaces in the model, a box with the appropriate geometrical extents was constructed in

Ansys DesignModeler, and then the wire mesh CAD geometry was subtracted from the domain via a boolean operation. This geometry could be elongated and copied to construct a model with the necessary wire spacing.

Due to the regular geometry present in the horizontal screen model, it was possible to build a structured grid using only hexahedron (hex) cells. In general, structured computational meshes are faster to solve because an explicit list of element locations does not need to be kept, reducing overhead. If the grid is aligned with the flow, a structured mesh can reduce the amount of numerical diffusion in a problem [110]. However, for very complex geometries, it may be extremely difficult, if not impossible, to construct a totally structured grid. It is also easier to locally coarsen or refine an unstructured grid. This can help reduce the number of cells overall, and thus recoup some of the computation time lost to a structured mesh.

Using a one wire unit cell as a test case, a series of grid independence tests were performed. The solution is said to be grid independent when adding elements does not change the outcome of the solution. For the grid independence study, the mass flow through the geometry was tracked with the total number of elements. Starting with a nominal mesh of 10 X 90 X 10 elements, the mesh was varied in the X/Z directions and the Y direction. Mesh elements had a uniform spacing in the X/Z direction, while they had a 5 to 1 size ratio from the ends of the domain to the face of the wire (the elements on the curvature of the wire had uniform spacing in all dimensions). Figure 4.9 shows the results of the grid independence study for the horizontal wire mesh configuration. A unit grid density of 10 X 130 X 10 elements was chosen, as varying the mesh in the X/Z direction didn't appear to have an easily definable trend. To generate the two wire domain, the 13000 element mesh was doubled in the Y direction. The final geometry used wall boundaries along the wire, symmetrical boundaries on all horizontal faces, and periodic boundaries on the top and bottom faces. Figure 4.10 shows details of the mesh for the single spaced 10 mesh geometry, and table 4.4 shows the final element counts for the different horizontal mesh

geometries.

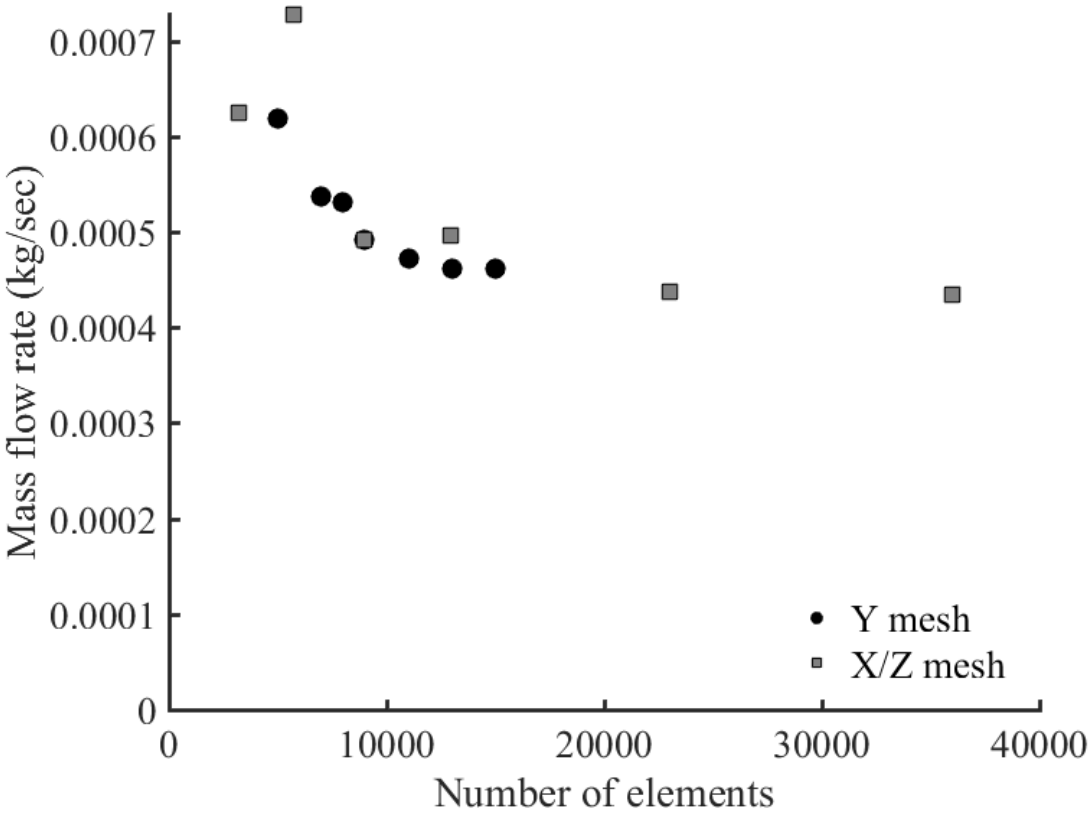

Figure 4.9: Mesh independence study for the horizontal wire mesh configuration.

Table 4.4: Horizontal mesh element counts.

Mesh size	Single spaced	Double spaced
8 x 8	37440	72000
10 x 10	26000	50000
12 x 12	16640	32000
14 x 14	12740	24500

The double spaced configuration was built by simply doubling all distances along the Y direction. The number of elements were doubled along the side faces as well, while keeping the 5 to 1 size ratio (the number of elements along the wire curvature remained constant). Therefore, the number of elements and the growth rate wasn't precisely doubled, but it was

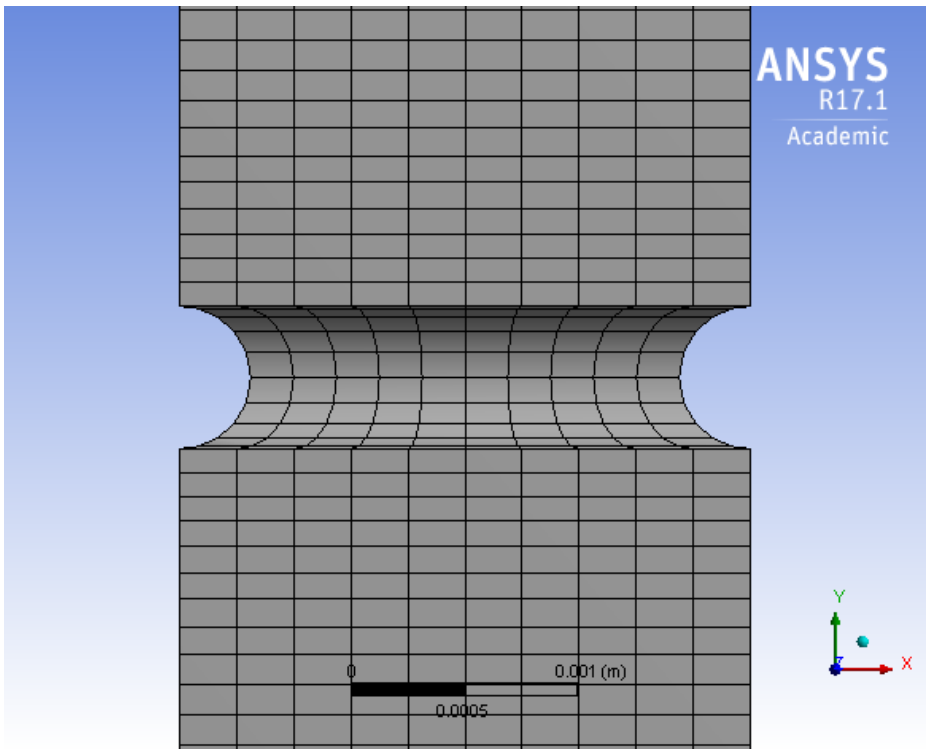

(a) Wire area

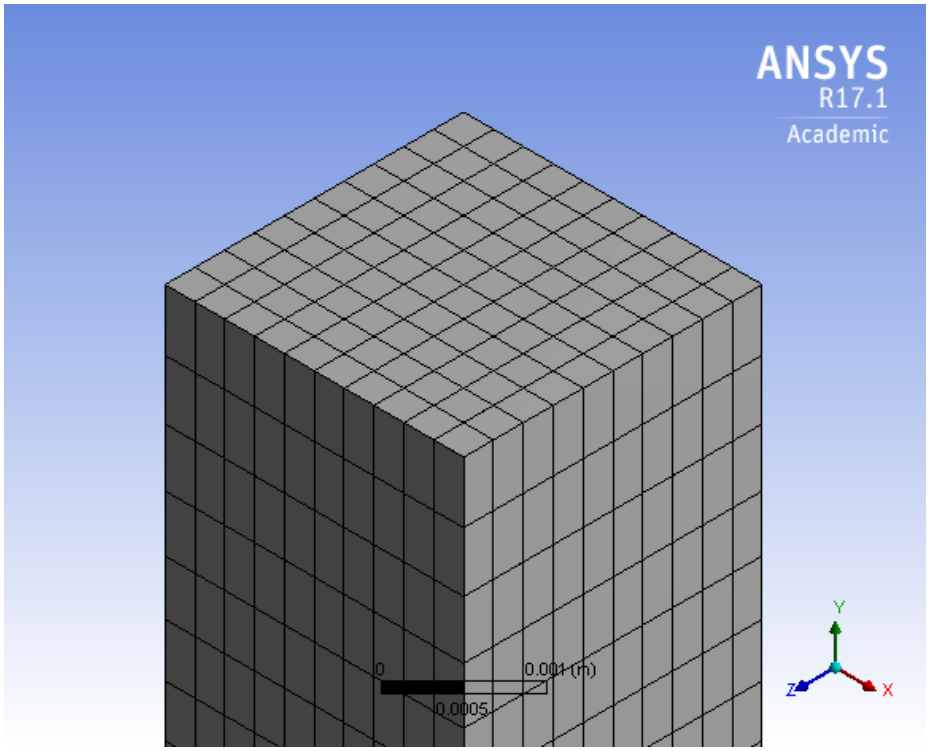

(b) Top face

Figure 4.10: Details of the 10 mesh horizontal wire mesh used in Fluent.

felt that this mesh sizing for the double spaced mesh configuration would be fairly close to grid independent as well.

For the horizontal mesh screen configuration only, particle insertion was done in a two step process. After initializing the simulation and letting it run for 20 time steps to stabilize the flow residuals to very low levels, the top, bottom, and bottom wire section of the geometry were given an initial volume fraction of 0.3. The simulation was then run for one second of flow time, which was sufficient to reach steady state. The volume fraction for this solution was then used as the initial condition for a second simulation: after the same initialization and 20 "dry" time step process, this solution was inserted into the domain, and allowed to run for a full second of flow time.

Angled mesh The angled mesh configuration was built with the same angled mesh geometry that was used in the DEM simulation, except that the wire geometry was split down the center of the holes in the wire mesh, enabling the use of symmetry. In an attempt to enable rapid geometry modification for the different sized wire screens, and to possibly enable enough geometric decomposition to aid in mesh generation, the wire geometries were inserted into a parallelepiped that was embedded into a larger rectangular geometry. The overall goal was to enable a hybrid mesh so that relatively rapid mesh generation could occur in the geometry near the wires, while the rest of the mesh could be as structured as possible. The top section, above the uppermost mesh, was able to be completely mapped, but the rest of the domain would need much further domain decomposition to enable a fully mapped mesh. This hybrid mesh did not enable as much fine control over the element size as was possible with the horizontal mesh geometry. However, it was possible to control the number of elements that spanned the thickness of the geometry, as well as general element sizes throughout the domain.

Because this mesh proved to be rather large and complex, a grid independence study was performed on a slice of the 14 mesh geometry (the smallest geometry available) con-

sisting of the height of a single wire mesh spacing. The global mesh control allowed the mesh spacing to maintain the same approximate element size that was used in the horizontal mesh configuration. It was found that similarly sized elements approached grid independence for the angled geometry as well. Figure 4.11 shows the results of the angled mesh grid independence study.

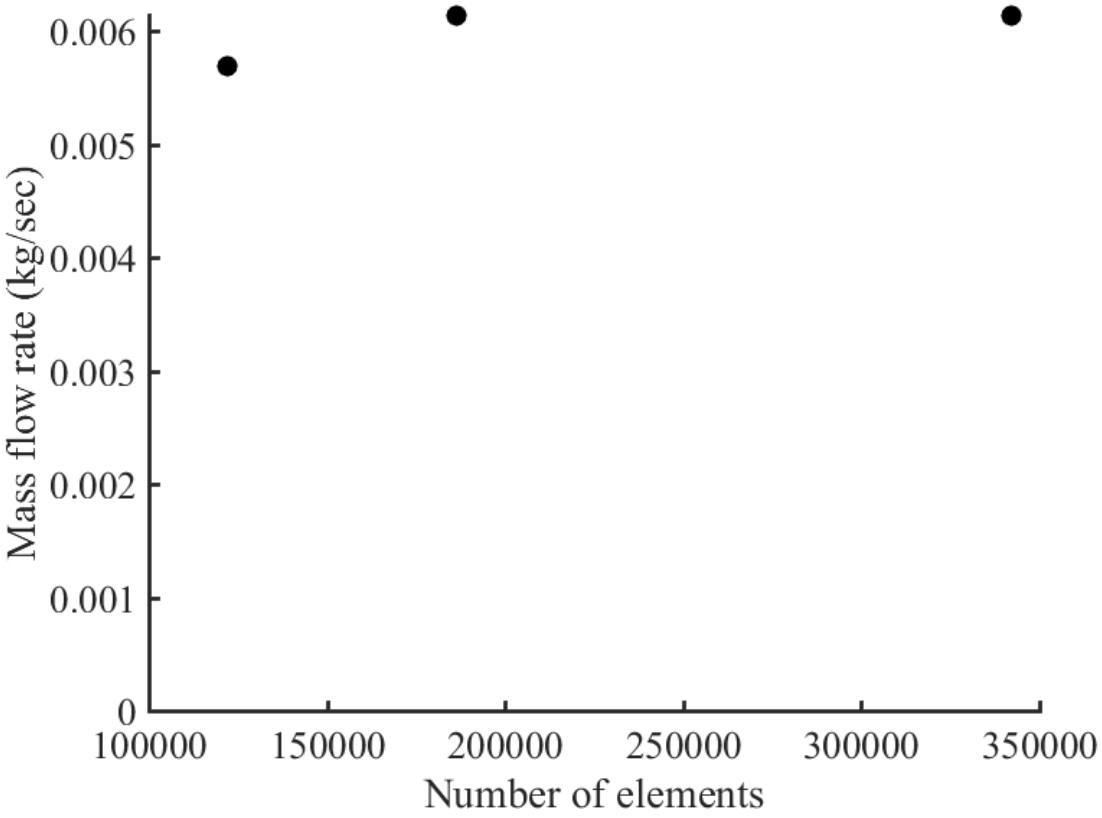

Figure 4.11: Mesh independence study for the angled wire mesh configuration.

Thus, the final angled mesh models had mesh element sizes on the same order as the horizontal mesh models. To generate the double spaced configuration, only the space between the angled mesh geometries was doubled to keep the element count to a minimum. The left and right boundaries were treated as walls, while the front and back boundaries were given a symmetric boundary condition. The top and bottom faces were treated as periodic. Particle insertion was accomplished by periodically setting the volume fraction

of the top portion of the domain to 0.3, thereby partially simulating the effect of filling the domain from the top. It was discovered that setting the volume fraction higher than 0.3 would eventually lead to a diverging solution due to issues with calculating the turbulence, so this meant that simulations had to run a fairly long time (2-3 seconds flow time) to become filled enough to be self limiting and reach steady state. Figure 4.12 shows details of the mesh size for the single spaced angled 10 mesh geometry. The grey volume is the top insertion volume, the brown volume surrounds the wires, and the green volume is the fluid space between the wire meshes. Table 4.5 shows the final element counts for the different angled mesh geometries. Curiously, for larger mesh sizes, the single spaced geometries had a higher mesh count that the double spaced geometries, despite being lower in overall volume. This was likely due to the mesher being able to rapidly inflate element sizes when not near small geometric features such as the wire.

Table 4.5: Angled mesh element counts.

Mesh size	Single spaced	Double spaced
8 x 8	1402177	1182493
10 x 10	1097923	909297
12 x 12	649710	664053
14 x 14	369650	386868

Square tube The square tube configuration used the same geometry as the DEM simulations, again taking the step of subtracting the geometry from a larger rectangular domain. In addition, an upper "loading" zone and a very small bottom outlet zone were included to enable particle loading and tracking from top to bottom. Despite being fairly simple in geometric terms, the many combinations of flat and curved elements in the geometry has the potential to lead to a fairly complicated mesh. Although Fluent has the ability to calculated the flow between non-conforming mesh faces (that is, boundaries where elements on either side do not match up exactly), it was decided to keep these areas conforming so that the results wouldn't depend on some sort of flow tracking algorithm that might not be present

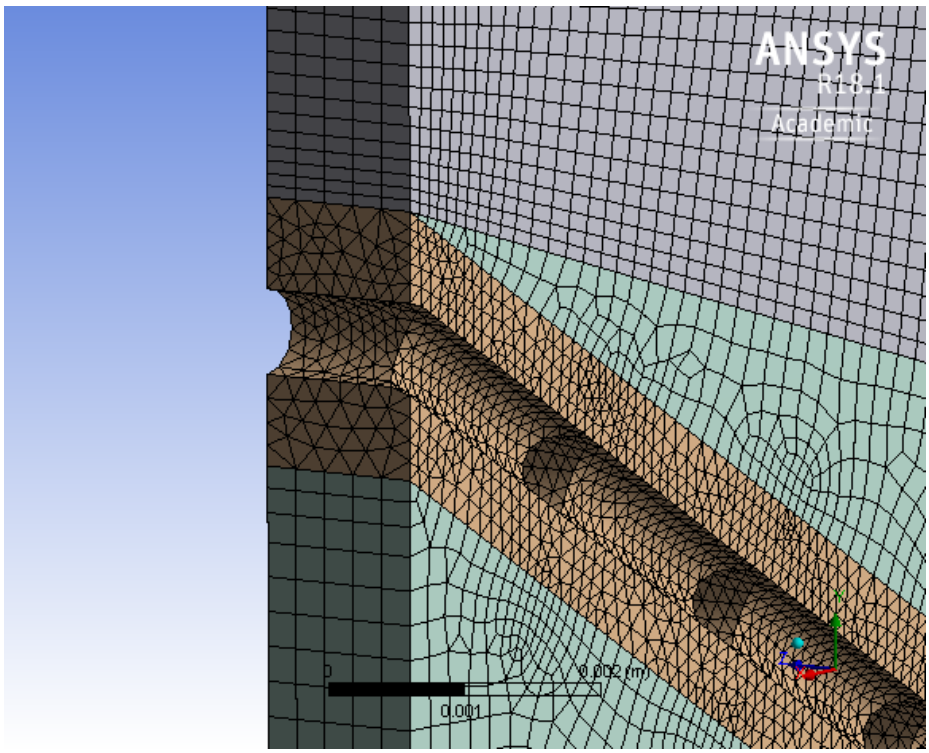

(a) View of wire cut out

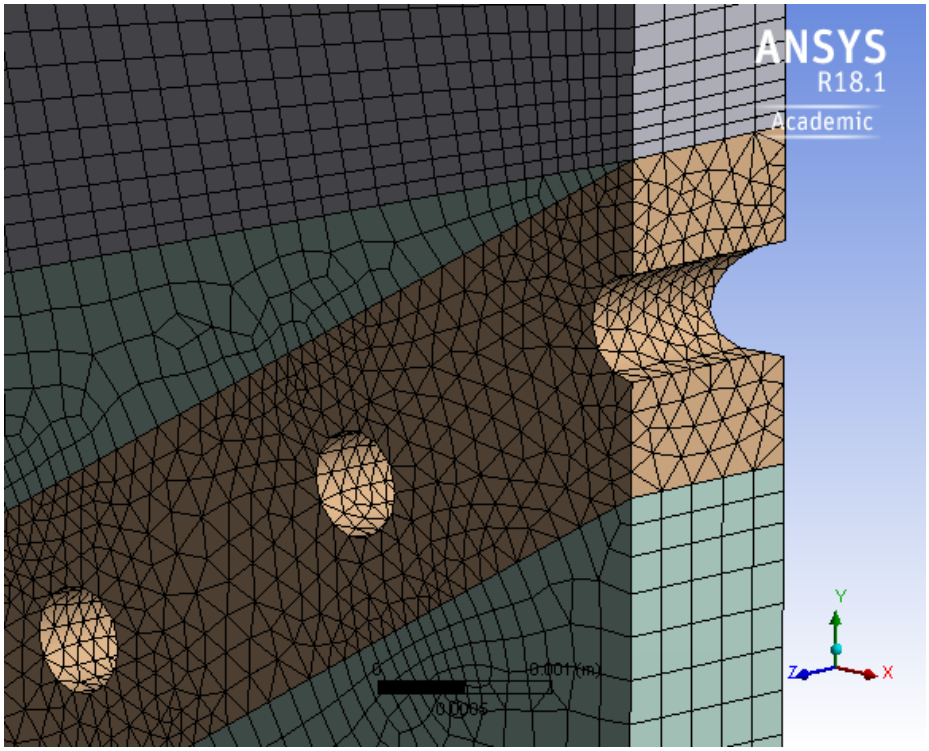

(b) View of mid-plane

Figure 4.12: Details of the 10 mesh angled wire mesh used in Fluent.

in other solvers.

The square tube geometry did not have a mesh independence study performed for it, and mesh sizing was only done using global size parameters. Despite the relatively large domain in geometric terms, the relatively large radius of curvature of the square tube geometry kept the total number of elements relatively small (the average size per element was much larger than for either wire mesh geometry). Similar to the angled mesh model, the square tube model was filled by setting the volume fraction of the upper section to 0.3 at a specified interval, to simulate filling the domain from a filled hopper. Figure 4.14 shows a detail of the whole and slotted square meshes. The holes in the faces of the squares and the slot in the latter geometry are clearly visible. Table 4.6 shows the final mesh size of the default mesh density used, and a denser model that was created after initial simulations were performed (more details will be given in the results section). The discrepancy in element counts between the default whole and slotted meshes was rather surprising, and both geometries used the same global size controls. Figure 4.13 shows a close view of the whole square tube model that is also shown in figure 4.14. It can be seen in figure 4.14 that the slotted mesh appears maintain a larger element size in the body of the square tube due to the lack of a sharp corner in the bottom where the slot is. That advantage begins to shrink as the mesh count goes up, as seen in table 4.6.

Table 4.6: Square tube element counts.

	Whole	Slotted
Default	451079	216209
Dense	2212896	2046910

Perforated plate The perforated plate grids were built in an identical manner to the square tube grids. However, due to the much larger number of curved faces, and the small thickness of the perforated plate itself, these meshes contained many more elements than their square tube cousins. Again, a grid independence study was not performed for the

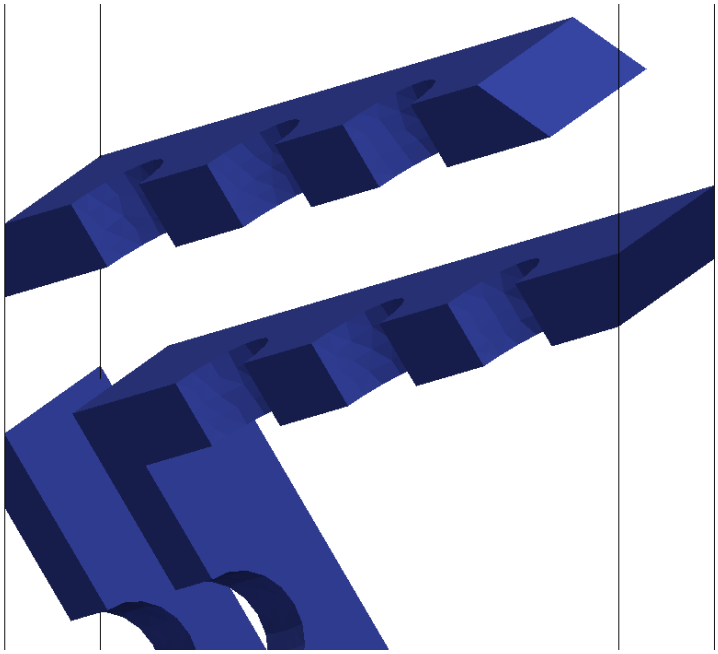

Figure 4.13: Detail of slotted aluminum tube square geometry (from the DEM simulation). Compare to the detailed mesh view seen in figure 4.14.

perforated plate mesh. The top and bottom faces were given periodic boundary conditions, while all side faces were treated as symmetric. Particles were inserted by setting the volume fraction of the top section to 0.3 at specified intervals, to simulate filling the domain from a filled hopper. Figure 4.15 shows a detail of the perforated plate mesh used. Table 4.7 shows the final element counts used in the Fluent simulations.

Table 4.7: Perforated plate element counts.

Whole	Slotted
945766	907915

In summary, this section has described the theoretical and mathematical backgrounds of the discrete element method and the finite volume method, provided details of their actual implementation, and described the numerical model and procedures used to generate data from the computer simulations.

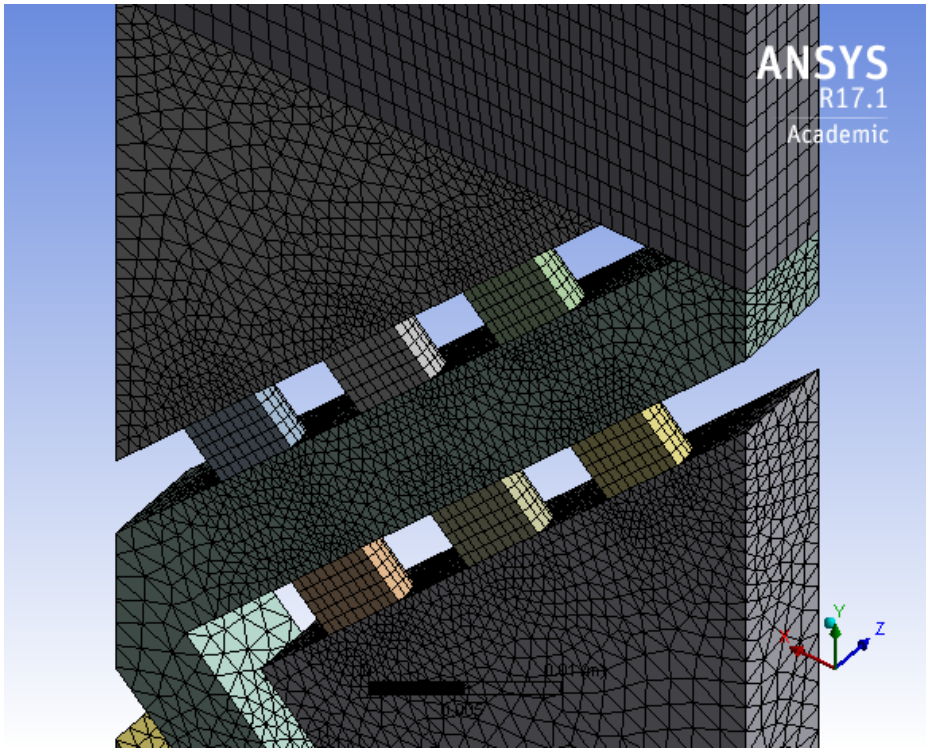

(a) Whole square tube geometry

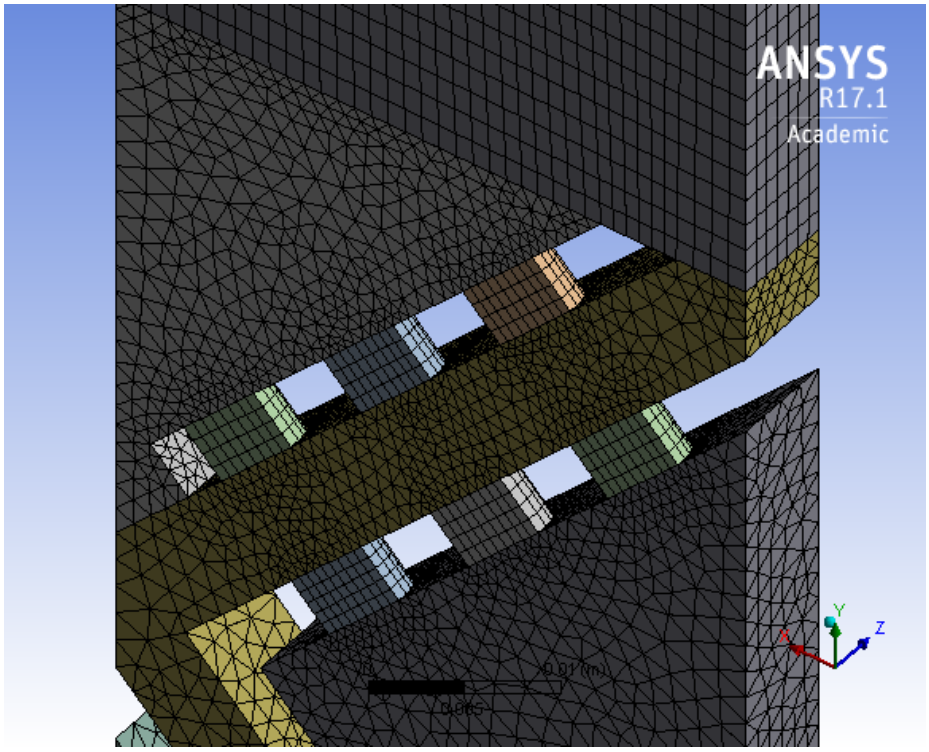

(b) Slotted square tube geometry

Figure 4.14: Details of the square tube mesh used in Fluent.

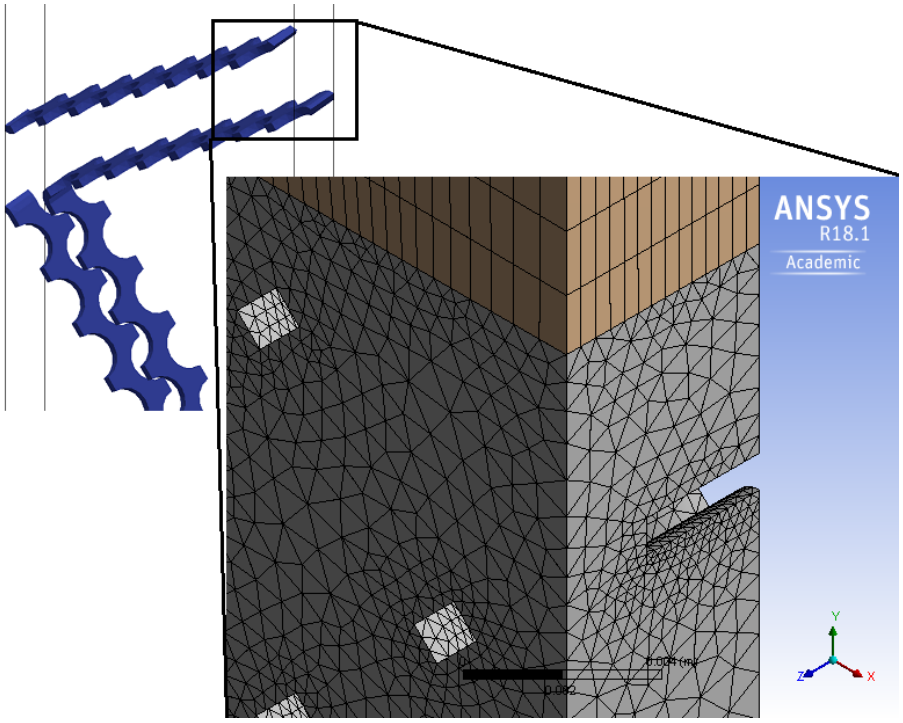

Figure 4.15: Detail of the perforated plate mesh. The DEM model is used to show the approximate location of the detailed view.

CHAPTER 5
RESULTS

The following sections will present the results from the experiments, the DEM simulations, and the CFD simulations. The results are grouped by test section geometry: horizontal wire mesh, angled wire mesh, square aluminum tube, and perforated plate. Results from the silicon carbide foam squares are reported in appendix E.

5.1 Horizontal mesh

5.1.1 Experimental Data

One of the critical variables measured in the lab was the raw mass flow rate of each configuration and granular material. To measure the mass flow rate, the accumulated mass of material flowing through the test section was weighed in a collection bucket placed on a load cell at known, regular intervals. Plotting these data over time resulted in a plot of the mass flow rate. The results shown in this section have been converted to a mass flux basis by multiplying the raw mass flow by the appropriate area ratio. Thus, the data show the equivalent mass flux per square meter. In every case measured, the mass flow rate was constant (i.e. the accumulated mass increased linearly with time) despite the amount of material remaining the upper hopper (above a critical level), which agrees with previous observations.

Figure 5.1 shows the mass flux results obtained with the ID50-K material using four different mesh sizes in the horizontal configuration. Absent an obvious variable against which to plot the mass flux data, the published hole size for an individual mesh opening was used. This was done to see if there was a similar relationship between mass flow rate and "orifice size" (obviously, a mesh screen is made of of many orifices that are quite close

together) as was found in other studies (such as a $D^{5/2}$ law [22, 27] or a general power law formula [26, 29]). The data were fitted with both a linear regression of the form $y = mx+b$, and a power law regression of the form $y = a^x + b$, as no fit featuring a $D^{5/2}$ term was applicable. The error bars represent a confidence interval of $\pm 2\sigma$, where σ is the standard deviation of the measured mass flux. For the single spaced configuration using ID50-K, the regressions are $y = 50750x - 28.7$ and $y = 8640x^{0.648} - 79.9$, while for the double spaced case, the regressions are $y = 47760x - 23.41$ and $y = 1.273e^6x^{1.184} - 9.73$. In this case, both regressions do a good job of describing the data. While the measured uncertainty is slightly higher for the double spaced configuration, the data are still reasonably represented by either a linear fit or a power law fit. The measured mass flux rates are roughly identical between the single and double mesh spacings. This is expected for a test section where the orifice (i.e. a wire mesh screen) covers the entire flow path. As these flow tests (like all presented in this study) were self limiting (i.e. there was not a flow control valve upstream of the test section), these mass flux values and regressions should be seen as the maximum mass flux of a given mesh size and geometry. These equations could aide designers of particle heating receiver who need to attain a certain thermal performance benchmark, or perhaps need to include a safety factor in their design.

Figure 5.2 shows the experimental results for the ballotini 8 mil material using the single spaced horizontal mesh test section. The same linear and power law fits were applied. The single spaced regressions are $y = 79000x - 35.88$ and $y = 2811x^{0.242} - 500$, while for the double spaced configuration they are $y = 49700x+9.841$ and $y = -3.58e^{-3}x^{-1.542}+167.6$. Once again, both the linear and power law fits do a reasonable job of representing the data. However, there is significantly more uncertainty associated with the data point for the largest mesh hole size for the double spaced configuration; the power law fit appears to do a better job of describing that data than the linear fit (the linear fit still has a fairly high R^2 value). It is unclear why this particular configuration produced a more strongly curved trend than the other three material-mesh combinations. It is also unclear what caused the

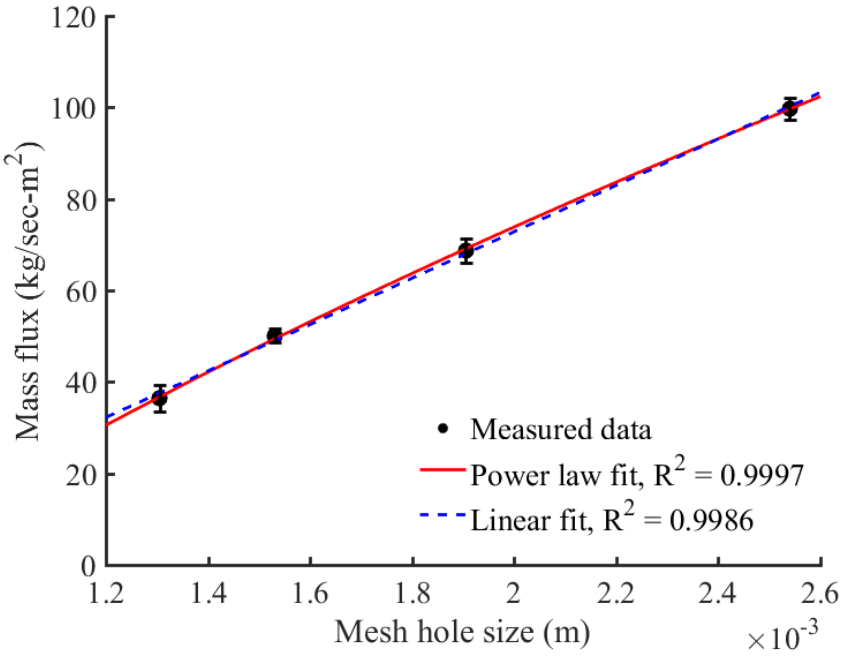

(a) Single spaced horizontal meshes

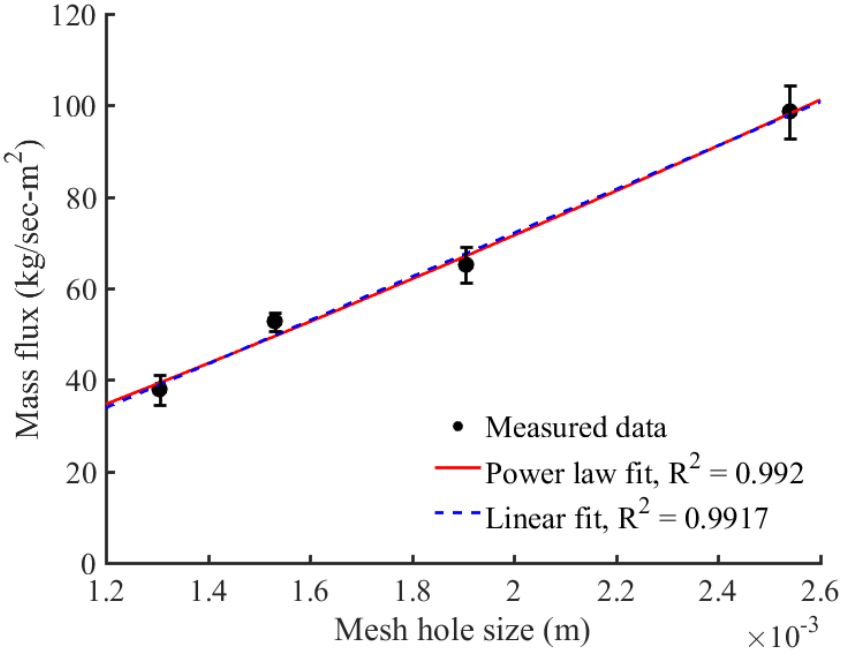

(b) Double spaced horizontal meshes

Figure 5.1: Experimental mass flux results for the ID50-K material, horizontal mesh configuration. The error bars represent 2σ.

large amount of uncertainty in that data point. Further measurements could be made to shrink the amount of error.

Another measurement performed on the experimental section was to measure the particle velocities using PIV analysis. Using high speed cameras, particle velocities could be calculated by comparing scaled images of particle flow fields. While this is technically the image of a flow field against the wall of the test section and not a true free field, these data can still be used to identify trends between the different mesh configurations and particle materials. If the ratio of particles colliding with the test section wall to free flow particles is fairly low, then these data could be used to estimate velocities within a free flow stream. Figure 5.4 shows a single frame of an example velocity vector field obtained with the ID50-K material using the single spaced horizontal mesh configuration. Figure 5.5 shows a velocity histogram of the vertical component of 20 frames of film. In this histogram, downward velocity is positive. Thus, this gives an estimated upper velocity limit of approximately 0.9 m/s. While there are populated bars with a higher velocity, they have very low counts and could be seen as outliers.

Figure 5.6 shows the same histogram for the double spaced horizontal meshes using the ID50-K material. The vertical velocity histogram peaks further to the right, which is expected. The velocity histogram also has more vectors that are to the right of the theoretical $\sqrt{4gh}$ velocity. This is expected because there are always some particles that enter the top of a unit cell with a non-zero velocity, having passed through the previous mesh screen layer(s) without colliding with them. As the mesh spacing increases, this entrance velocity should also increase, therefore increasing the exit velocity.

A direct comparison of the two velocity histograms, as seen in figure 5.7, shows the expected trends: the single spaced histogram has a taller but slower peak than the double spaced histogram.

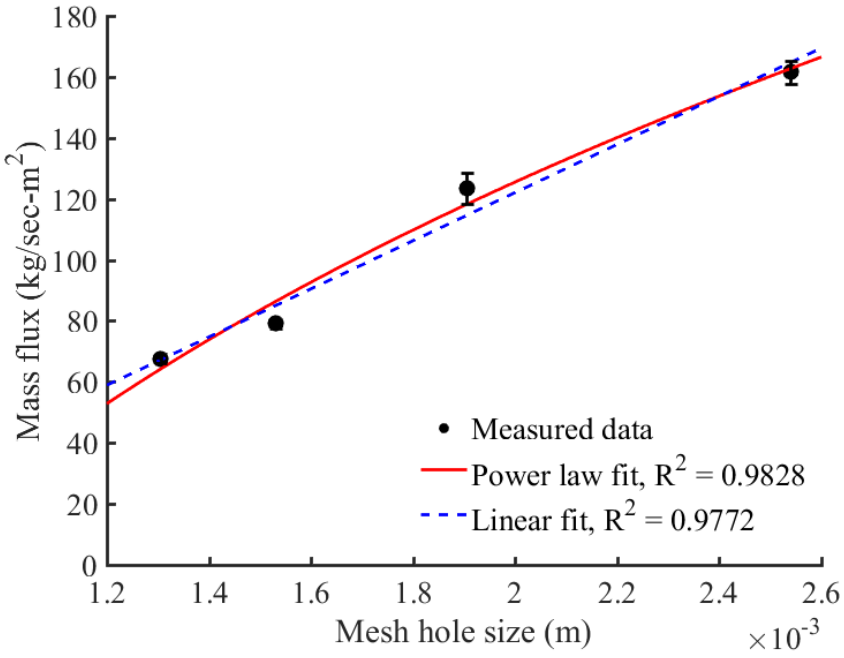

(a) Single spaced horizontal meshes

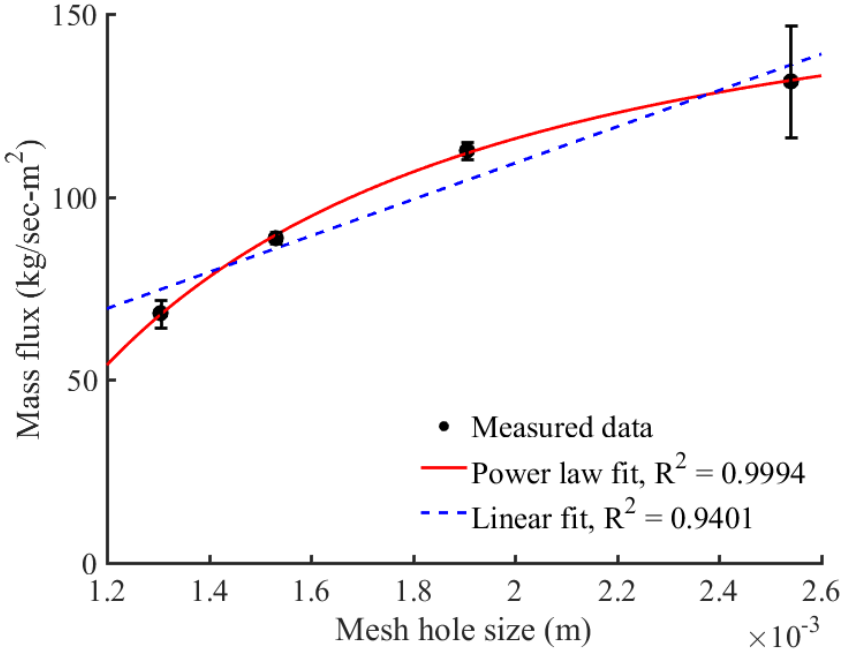

(b) Double spaced horizontal meshes

Figure 5.2: Experimental mass flux results for the ballotini material, horizontal mesh configuration. The error bars represent 2σ.

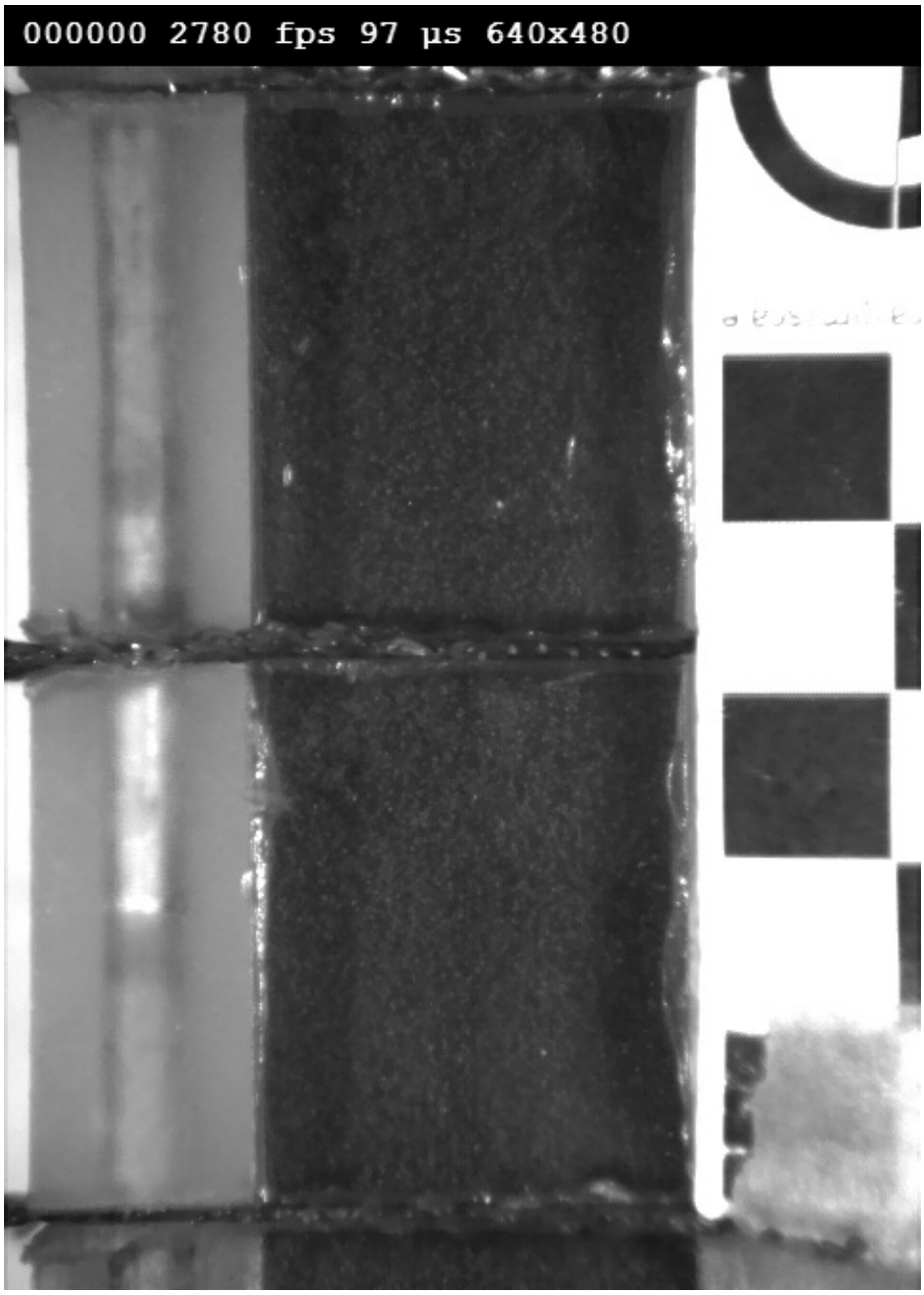

Figure 5.3: Raw video frame, ID50-K material, single spaced horizontal meshes. As indicated at the top, the camera was shooting 2780 frames per second, with an exposure time of 97 microseconds, capturing an image that was 640 by 480 pixels in size. The camera has been turned on its side to capture two whole unit cells in the frame. The black squares in the right of the frame are 1 cm by 1 cm, and are used to calibrate the image against a known distance.

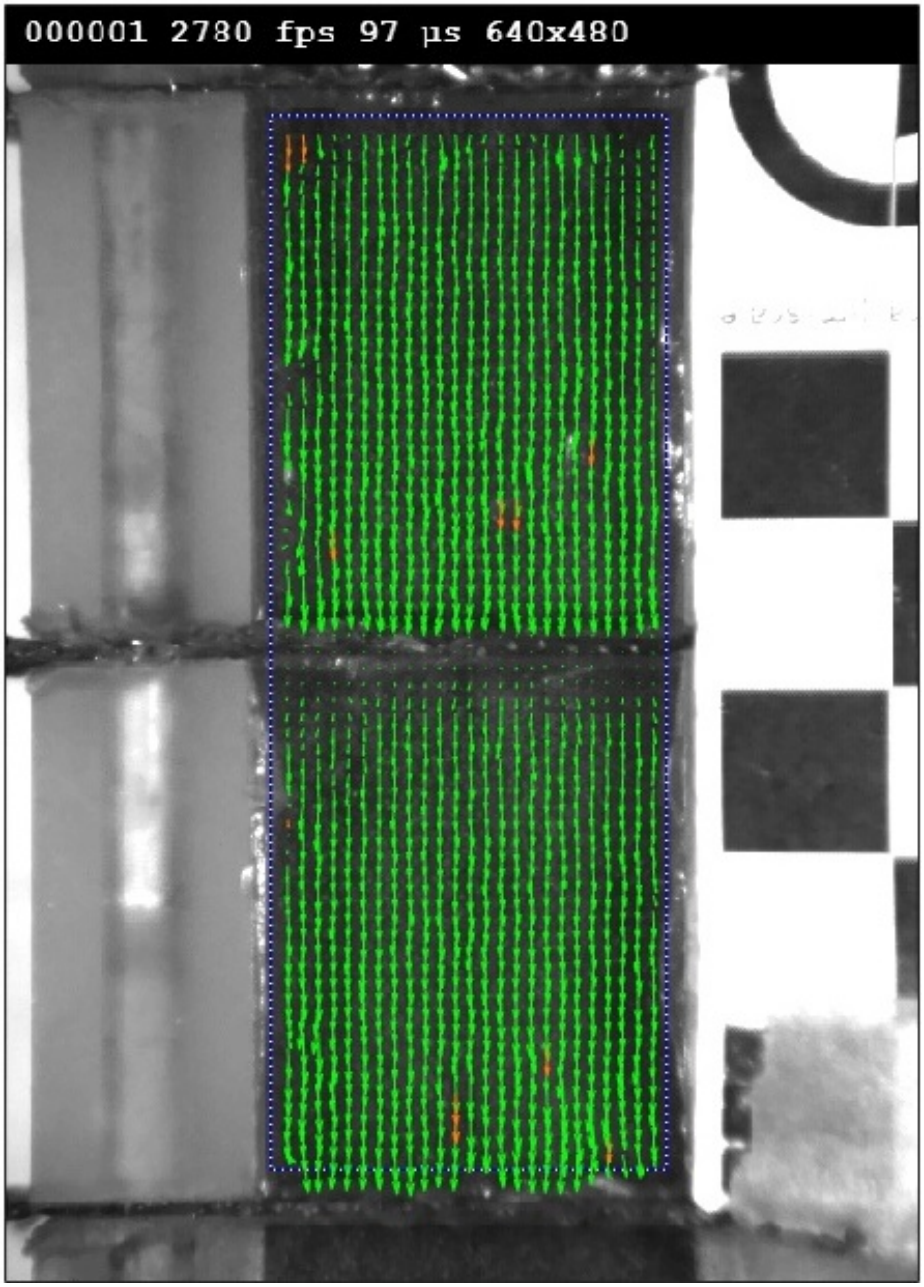

Figure 5.4: PIV vector field, ID50-K material, single spaced horizontal meshes. The dotted blue lined box indicates the extent of the frame used for PIV calculations. Each arrow originates in one of the interrogation areas used for the PIV calculation, and their length corresponds the velocity associated with that area. Green arrows are raw velocity vectors, and orange arrows indicate they have been interpolated from surrounding data.

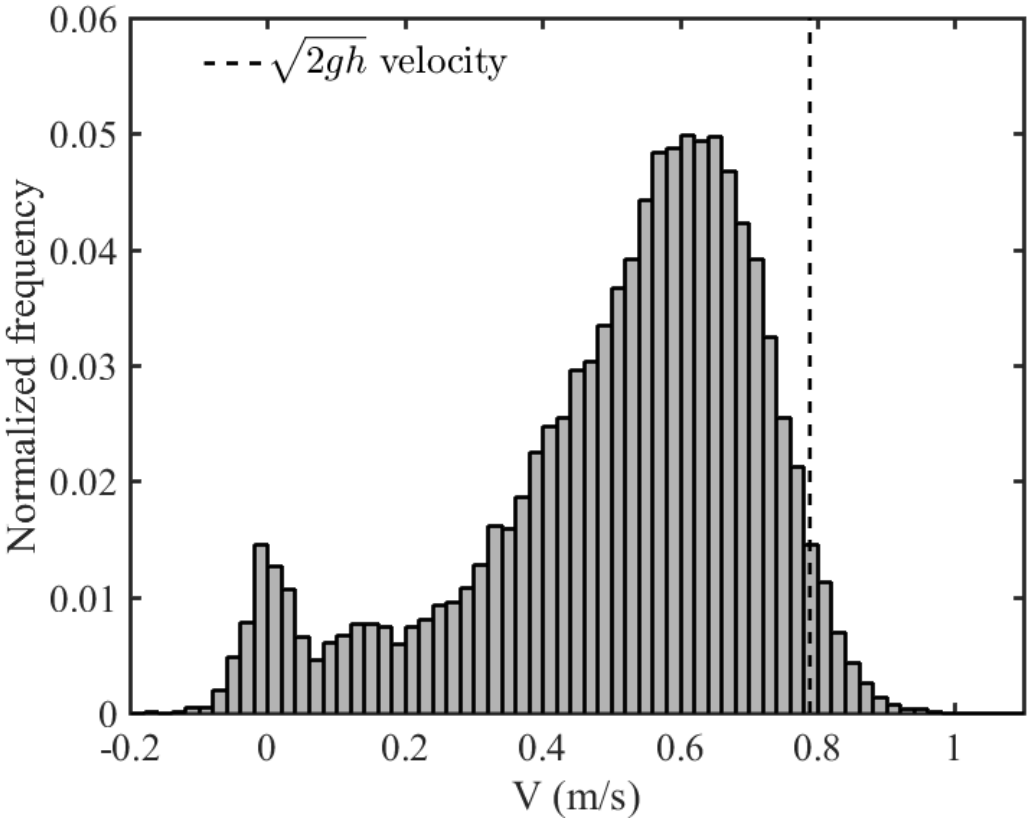

Figure 5.5: A vertical velocity histogram, ID50-K material, single spaced horizontal meshes. The vertical dashed line indicates the theoretical velocity of a particle released from a height of $\sqrt{2gh}$, where h is the mesh spacing. The small peak near zero is caused by the joint in the test section running through the middle of the frame, producing many zero and near-zero vectors. Down is positive.

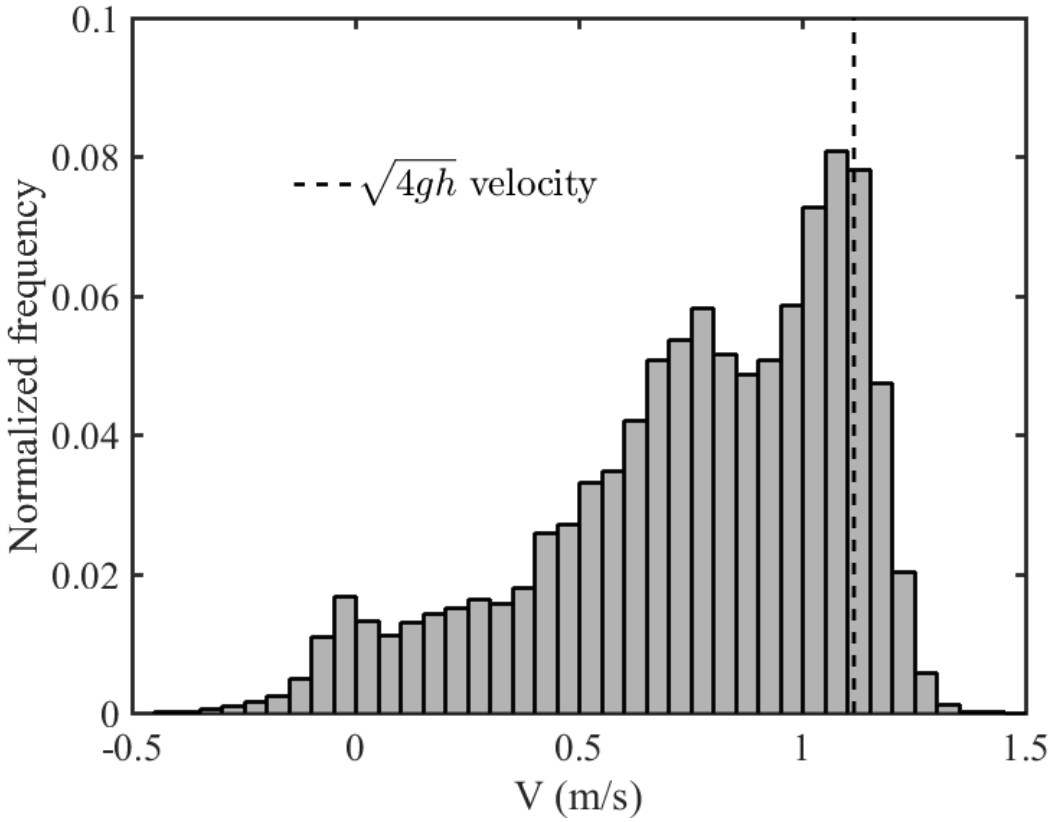

Figure 5.6: A vertical velocity histogram, ID50-K material, double spaced horizontal meshes. The vertical dashed line indicates the theoretical velocity of a particle released from a height of $\sqrt{4gh}$, where h is the mesh spacing. Down is positive.

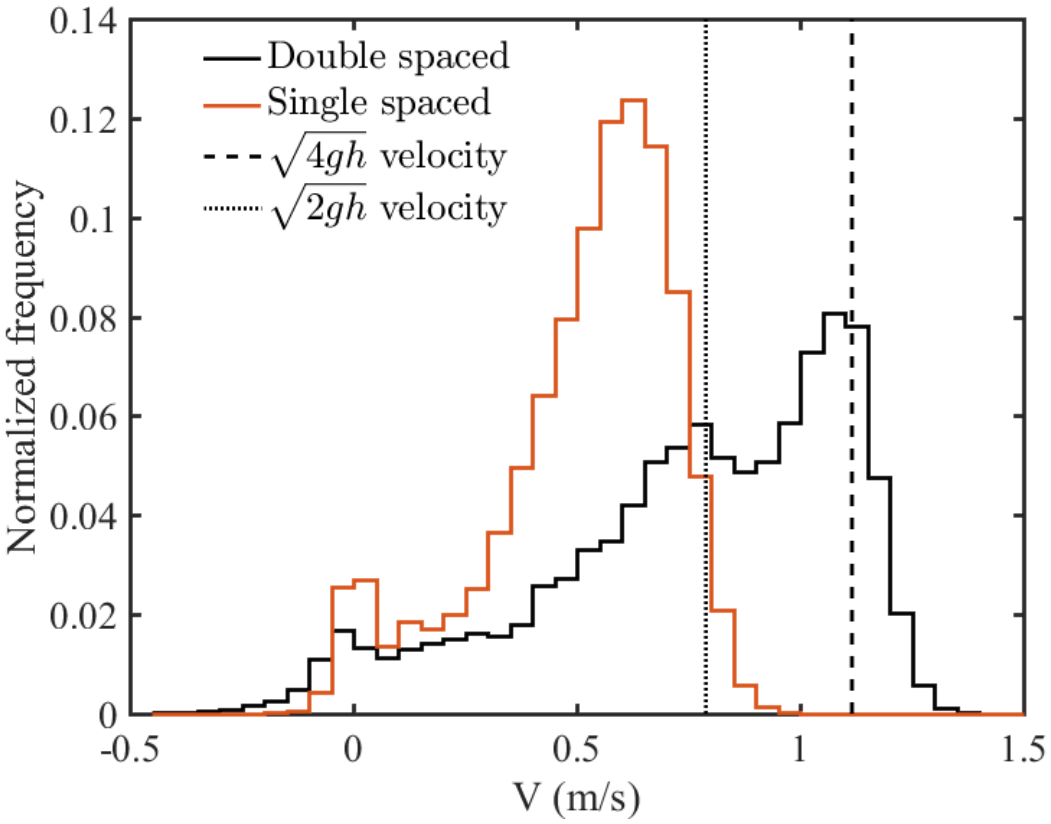

Figure 5.7: A comparison of the single spaced and double spaced velocity histograms.

Finally, the steady state volume fraction of each mesh configuration was measured. By closing both slide gate valves simultaneously, a "slice" of flowing material was captured in the test section. Using the density, the volume of this material was calculated and compared with the overall volume of the test section between the slide gate valves. Figure 5.8 shows the results of both the single spaced and double spaced horizontal mesh test sections for the ID50-K material. The single space test section has a higher steady state volume fraction than the double mesh test section, which is expected: the double spaced test section shows higher particle velocities, but the overall mass flow rates are roughly the same.

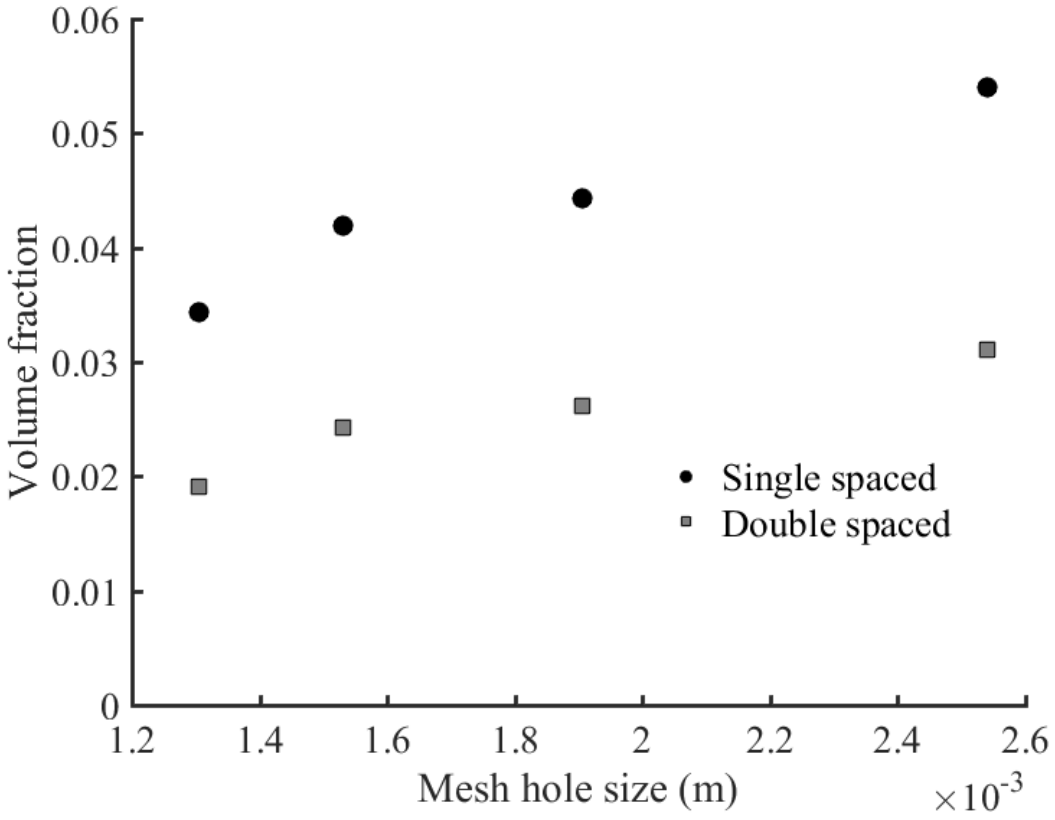

Figure 5.8: Steady state volume fraction of both horizontal mesh test sections, ID50-K material. The single spaced mesh test section contains more material than the double spaced test section.

Figure 5.9 shows the same results for the ballotini 8 mil material. Again, a higher volume fraction is observed in the single spaced test section than the double spaced test

section. The ballotini 8 mil material had overall higher levels of loading than the ID50-K material, and a larger spread between the single and double spaced test sections. This is likely due to the Ballotini's smaller diameter and smoother surface profile, allowing more individual particles to be flowing faster at any given time.

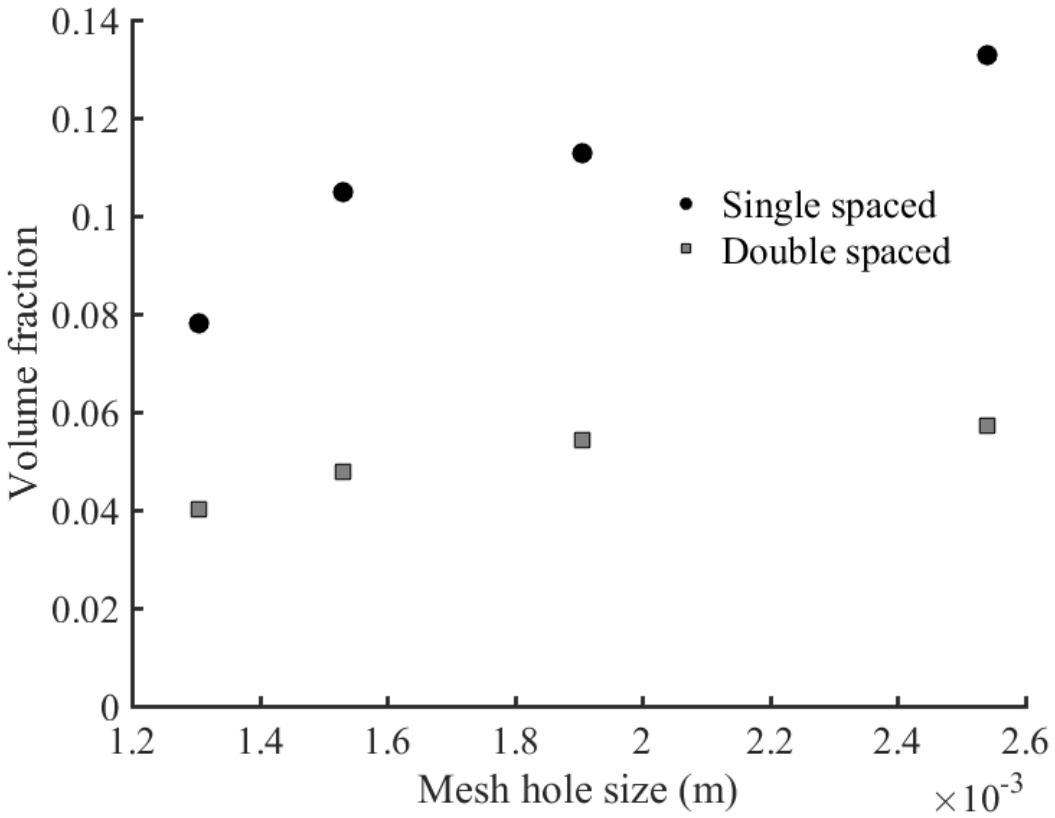

Figure 5.9: Steady state volume fraction of both horizontal mesh test sections, ballotini 8 mil material. The single spaced mesh test section contains more material than the double spaced test section.

5.1.2 Numerical Models

Numerical modeling of each mesh configuration and both materials was performed using both a discrete element model (DEM) and a computational fluid dynamics model (CFD). This allowed the direct comparison of the same variables that were measured in the lab. The material properties used in the models were from experimental data when possible, and published data when needed.

The DEM model calculates the mass flow rate in much the same way as the experimental apparatus. It counts the number of particles that cross an imaginary plane in the model over time. By saving the total accumulation over time, a plot can be generated of mass per time, and the slope of the trend line gives the mass flow rate. As with the experimental data, the trend is linear. Particles are initially inserted into the model using a random number seed. Thus, it is conceivable that models beginning with different seeds will have slightly different results from each other, as was observed in the experimental apparatus. However, this seeding was only performed once, so the extent of this statistical difference was not determined.

The CFD model calculates the mass flow directly from the cell centroid values of volume fraction, cell face velocity normal values, and cell face areas. Therefore, models using the same mesh and same initial conditions should calculate the very same values, up to the limit of machine precision.

In both simulations, small representative domains were used to speed up the calculation process. These results have been corrected in the same way as the experimental results to give a mass flux per square meter.

Figure 5.10 shows the mass flux for the horizontal mesh test section using the ID50-K material. Both models predict the experimental mass flux fairly well. The CFD model shows a slightly higher over-predicted mass flux for the double spaced model than the single spaced model. This could be due to the lack of wall boundary conditions on the horizontal faces of the geometry.

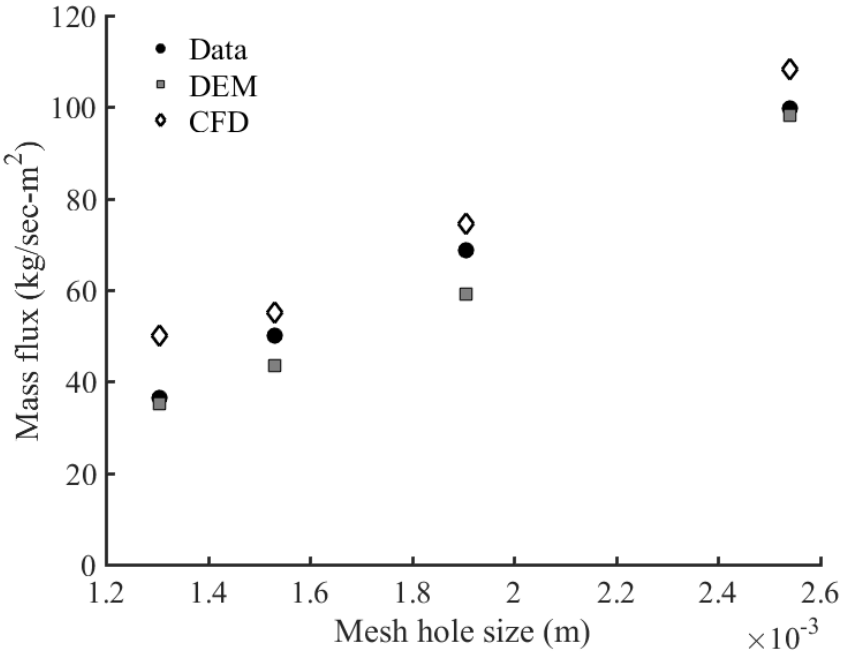

(a) Single spaced horizontal meshes

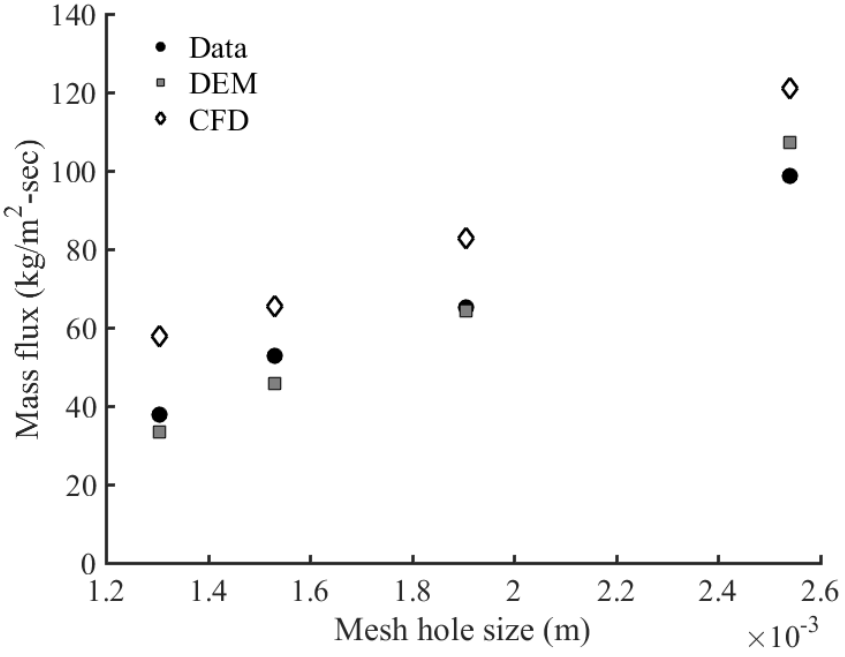

(b) Double spaced horizontal meshes

Figure 5.10: Experimental and numerical mass flux for the ID50-K material, horizontal mesh configuration.

Figure 5.11 shows the mass flux of the ballontini material for the horizontal mesh configuration. Compared to the ID50-K material, the numerical models switch, with the DEM model over-predicting the mass flux while the CFD model generally under-predicts the mass flux. Both models appear to fail to predict the concave down trend seen in the experimental data.

Another way to visualize these data is to plot the mass flux ratio between the single and double spaced configurations. If the main influences on mass flux are the particle size and the hole size, then the ratio of the two different mass fluxes should be fairly close to unity. Figures 5.12 show this to be generally the case for the experiments and both numerical models.

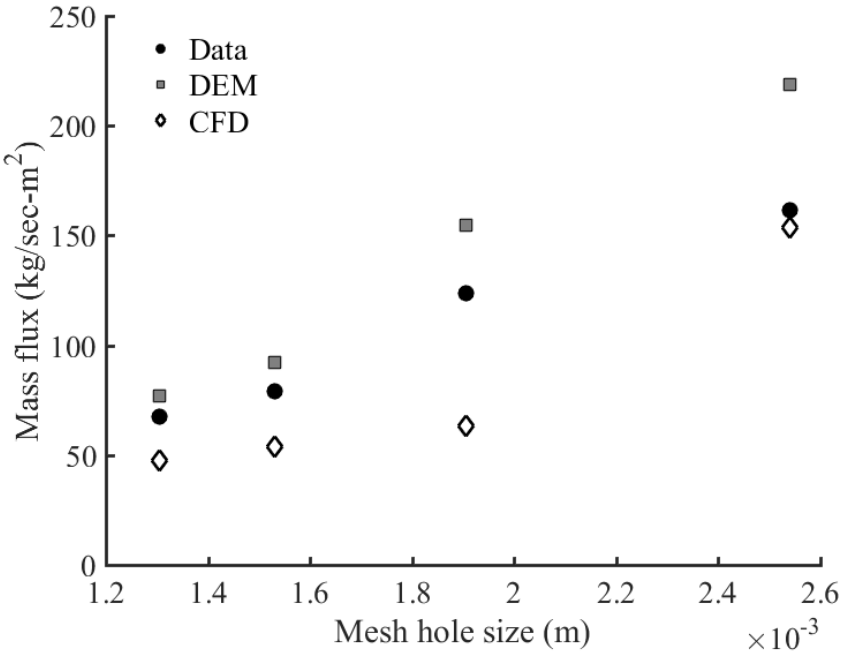

(a) Single spaced horizontal meshes

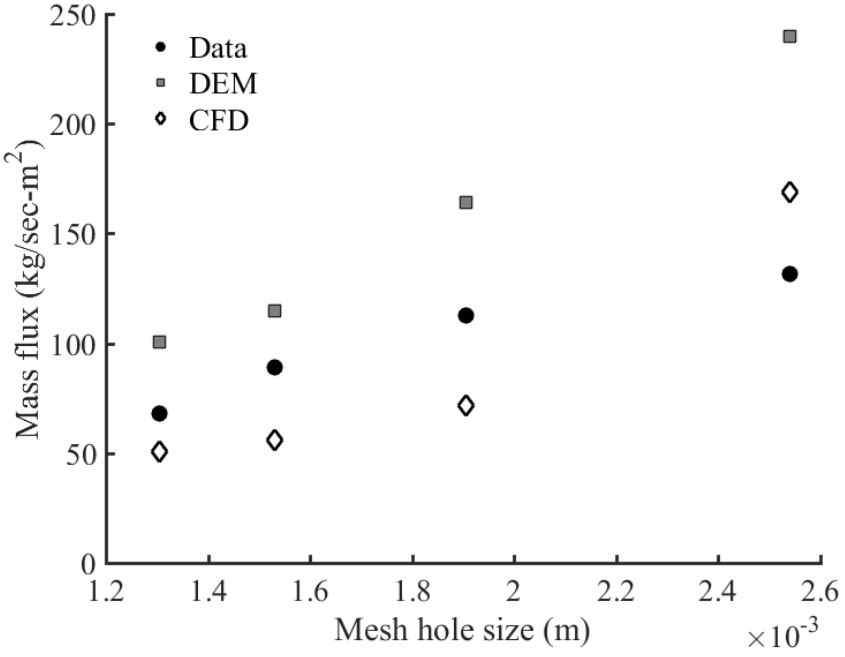

(b) Double spaced horizontal meshes

Figure 5.11: Experimental and numerical mass flux for the ballotini material, horizontal mesh configuration.

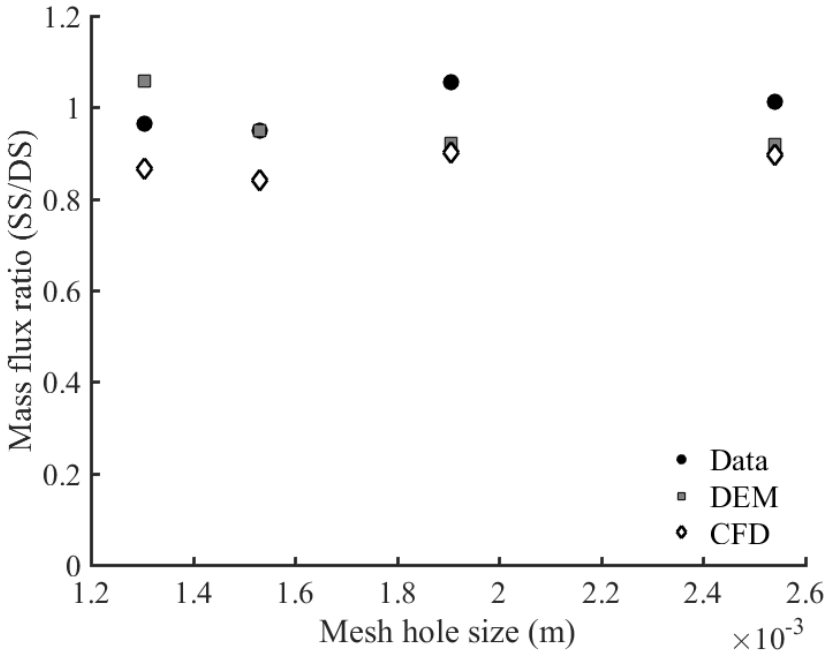

(a) ID50-K material

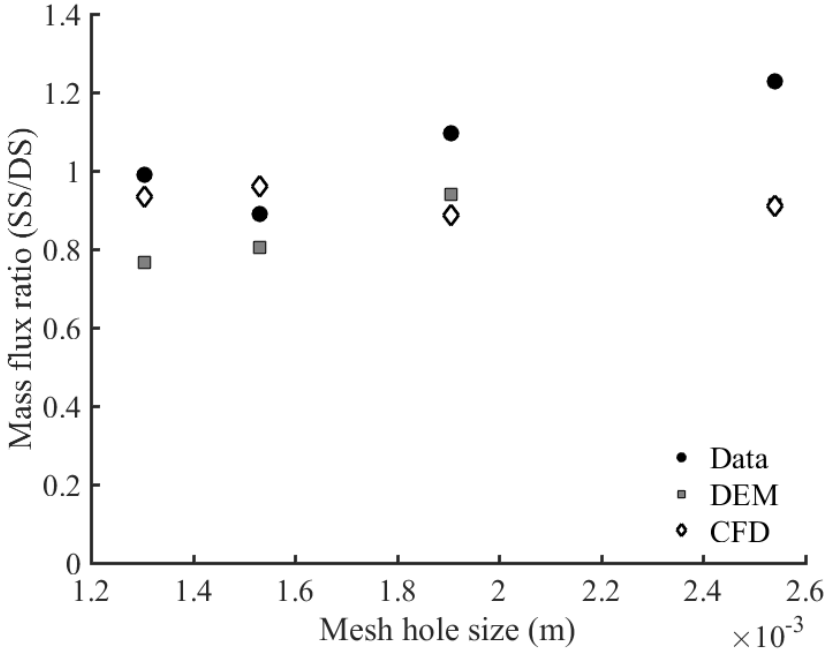

(b) Ballotini material

Figure 5.12: Experimental and numerical mass flux ratio for the horizontal mesh configuration.

The average volume fraction was also calculated from the numerical models. For the DEM model, the volume comprised the height of 2 mesh spacings, and thus includes a mesh in the center of the domain for the single spaced case. For the CFD model, the domain was the center section between two wire screens, and the small volume comprising the flow channel of the lower wire screen. Figure 5.13 shows the steady state volume fractions for the ID50-K material for the horizontal mesh configuration. In the single spaced configuration, the DEM model results agree fairly well with the experimental data except for the largest mesh size, while the CFD model appears to get better with increasing mesh size. For the double spaced configuration, both numerical models trend together fairly closely, getting better with larger mesh sizes. The likely cause for the discrepancies was the short vertical dimension of the numerical models compared to the experimental test section. The models are thus not able to advance beyond the entrance region of the geometric domain, where there was still considerable accumulation on the screens in the test section. Simulating a longer model may be able to verify this, but would require either more particles or more cells, thus requiring more simulation time. Another factor could be the use of a relatively large single spherical particle model, as opposed to a distribution of non-spherical particles. While the maximum packing fraction tends to increase for poly-disperse groups of spheres, this behavior could be different for non-spherical particles undergoing shear deformation. Another feature of these plots is the large variance in the size of the error bars for the experimental data. While each error bar represents a 95% confidence interval, the reason for the large discrepancy between the single and double spaced meshes is unknown. A cause of this could be that the double spaced test section has fewer meshes for material to accumulate on. This, coupled with the higher average velocities in the double spaced test section, could lead to less of a chance for particles to accumulate, leading to an overall emptier test section. Note that the error bars pertain only to the random error of the measurement. The systematic error from the uncertainty in the total wet volume of the test section was calculated to be typically the same order of magnitude as twice the standard

deviation of the volume fraction calculations (although the error would only add or subtract in a single direction from the nominal volume fraction calculation).

Figure 5.14 shows the steady state volume fractions for the ballotini material for the horizontal mesh configuration. The DEM model does a better job predicting the volume fraction for the single spaced configuration, while the CFD model appears to do a little better at the double spaced configuration. As opposed to the ID50-K material, the numerical models appear to make generally worse predictions as the mesh sizes get larger. Again, there is not a good explanation for the wide variation in error in the experimental data points, but further measurements could be made to reduce the discrepancies.

Similar to the mass flux, the ratio of single spaced to double spaced volume fraction can be plotted. Since the mass flux is roughly the same between configurations, but the average velocity increases with mesh spacing, the volume fraction should decrease with increasing mesh spacing. Figure 5.15 shows the ratio of single spaced to double spaced volume fraction for the experimental and numerical data for both materials. The experimental data behave rather consistently, with the ballotini material showing a slightly higher volume fraction ratio. However, nearly every numerical data point falls well below the experimental data, with some of the DEM models predicting a ratio even less than unity. Once again, this is likely due to the small vertical dimension of the numerical models as compared to the experimental test section, meaning the numerical models are still within the entrance region of the domain.

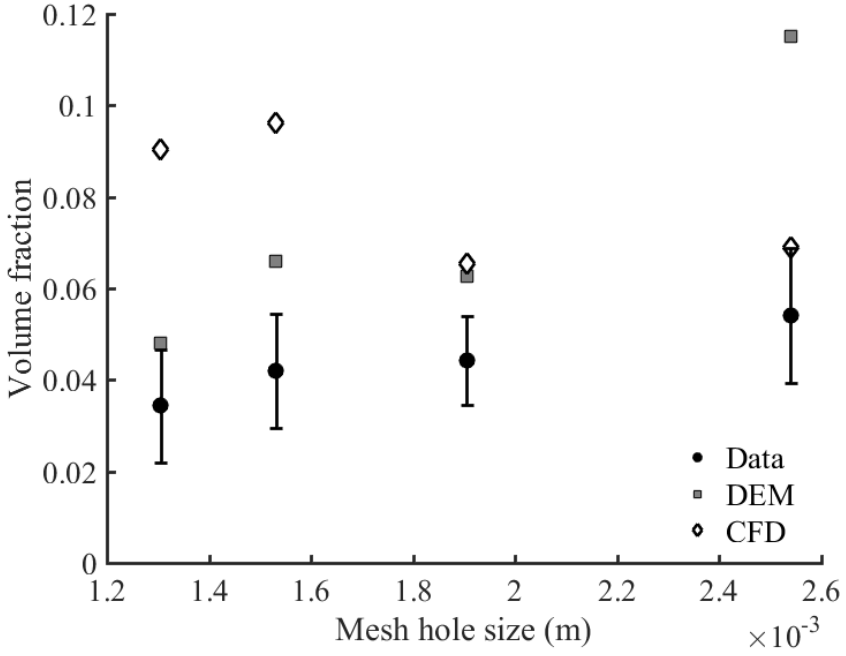

(a) Single spaced horizontal meshes

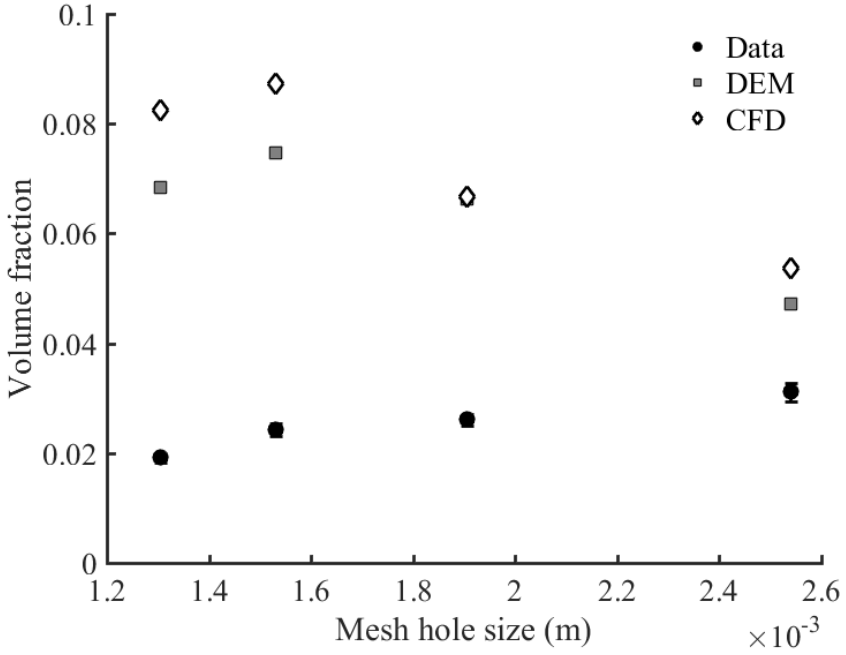

(b) Double spaced horizontal meshes

Figure 5.13: Experimental and numerical volume fraction for the ID50-K material, horizontal mesh configuration. The error bars represent 2σ of the random error associated with the measurement.

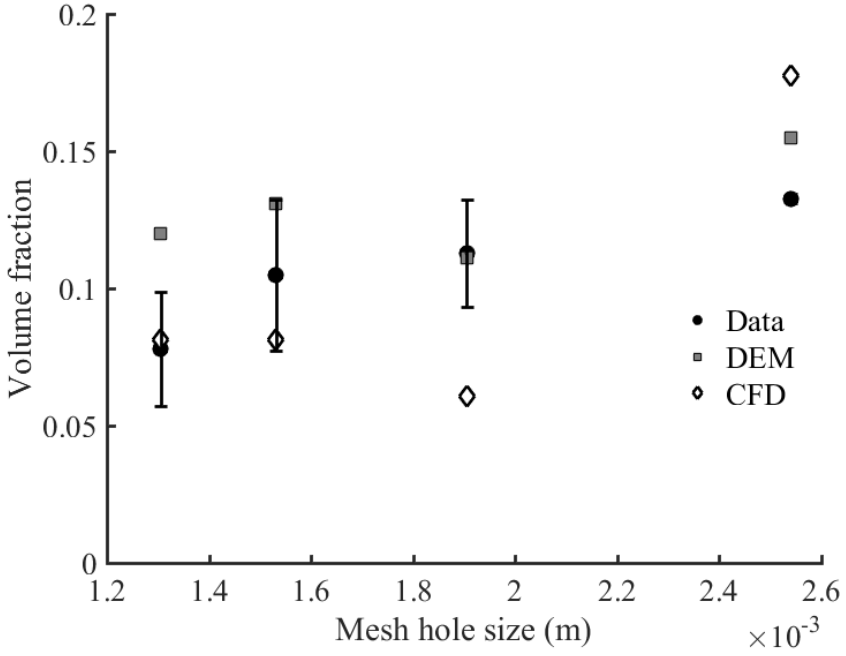

(a) Single spaced horizontal meshes

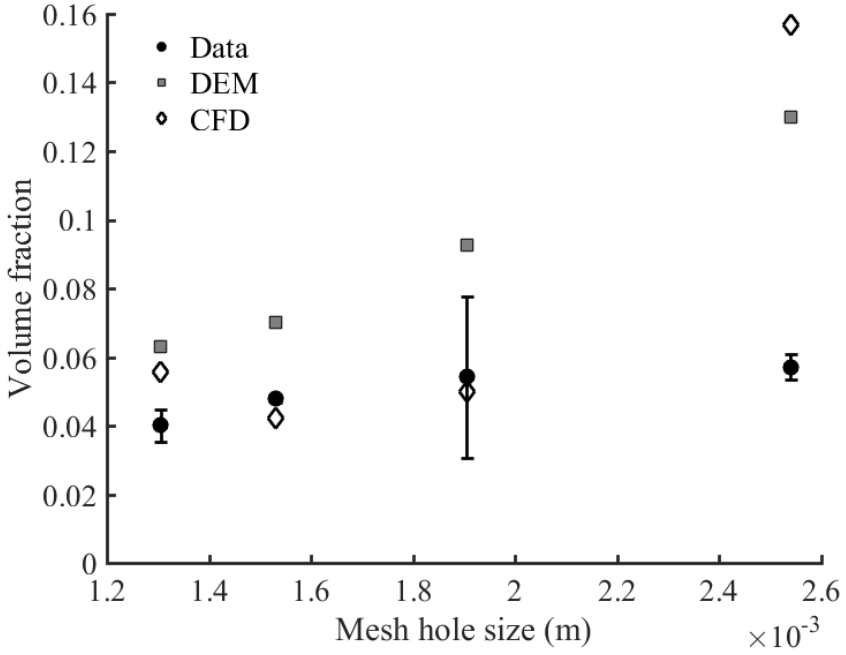

(b) Double spaced horizontal meshes

Figure 5.14: Experimental and numerical volume fraction for the ballotini material, horizontal mesh configuration. The error bars represent 2σ of the random error associated with the measurement.

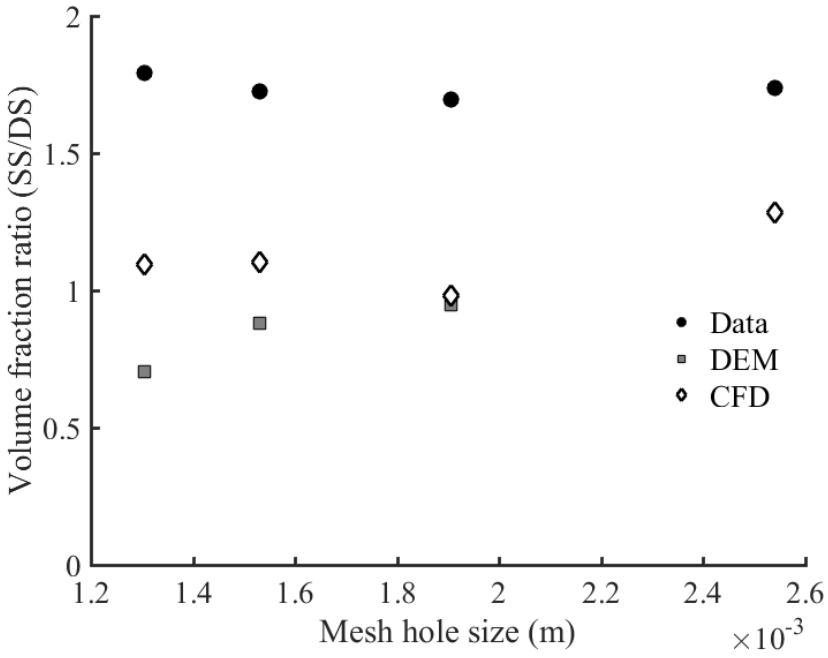

(a) ID50-K material

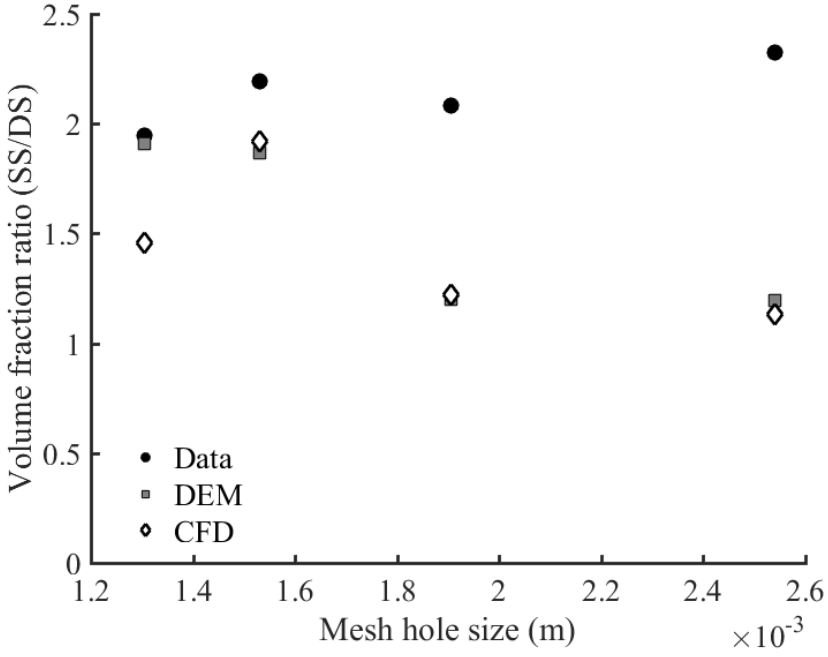

(b) Ballotini material

Figure 5.15: Experimental and numerical volume fraction ratios for the horizontal mesh configuration.

A velocity analysis was also performed on both numerical models. The DEM model outputs a velocity vector for every particle it tracks, while the CFD model computes an average cell velocity based on the normal velocity at the cell faces.

Figure 5.16 shows a snapshot of the DEM model for the single spaced case using the ID50-K material. The picture clearly shows the accumulation of particles on the uppermost screen, and the increase in velocity as the particles fall through the wire mesh.

Figure 5.17 shows a snapshot of the CFD model for the single spaced case using the ID50-K material. The left image is colored by volume fraction, while the right image is colored by velocity magnitude. The accumulation is harder to visualize due to the large spread in volume fractions in the image. The velocity begins decreasing relatively far away from the bottom mesh.

Figure 5.18 shows a comparison of the vertical velocity components of the experimental PIV, DEM, and CFD results for the ID50-K material with the horizontal mesh configuration for the size 10 mesh. The vertical line shows the limiting terminal velocity based on the spacing between the meshes. The DEM model appears to taper off to roughly the theoretical upper velocity limit. The large peak near zero in the DEM data for the single spaced case is due to particles accumulating on one of the wire meshes in the model. The PIV analysis of the experimental flow has trouble tracking these very slow moving particles, leading to a smaller peak around zero. This also explains why the PIV data have an upward trend until near the theoretical maximum velocity, while both the DEM and CFD histograms are relatively flat, as the higher velocities were better optimized for the interrogation windows used in the PIV analysis. The sharp cliffs at the minimum and maximum velocities in the CFD data are an artifact of the model itself. For instance, without individual particles to collide with each other and with the walls, there are no negative (i.e. upwards) vertical velocity vectors. It also shows a smaller terminal velocity than the other two data. This is also likely caused by the continuity maintained by the finite volume model, as there are no individual particles that still have a chance of falling through an area of increasing volume

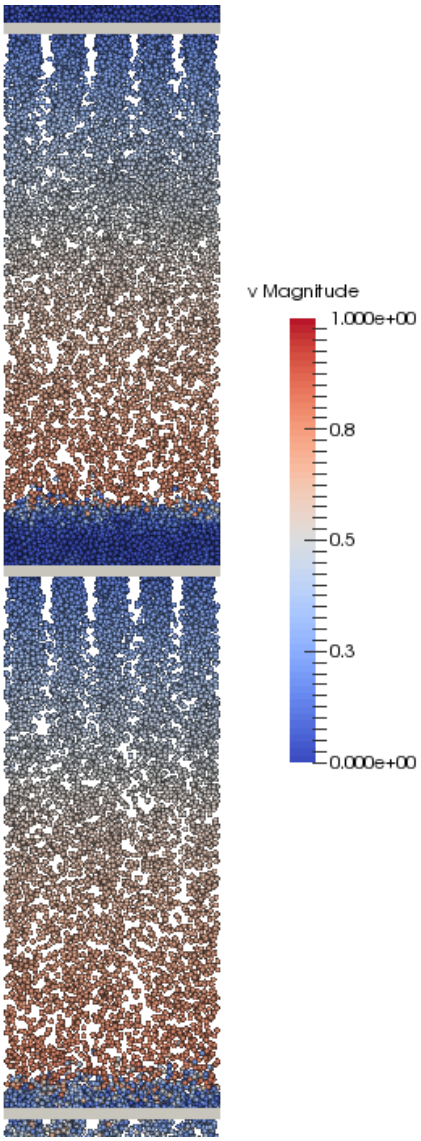

Figure 5.16: Snapshot of the DEM model for the ID50-K material with the single spaced mesh. The particles are displayed with the same diameter used in the calculations, enabling a direct visualization of particle accumulation. The particles are colored by overall velocity magnitude. The upper mesh screen represents the "top" screen in the model.

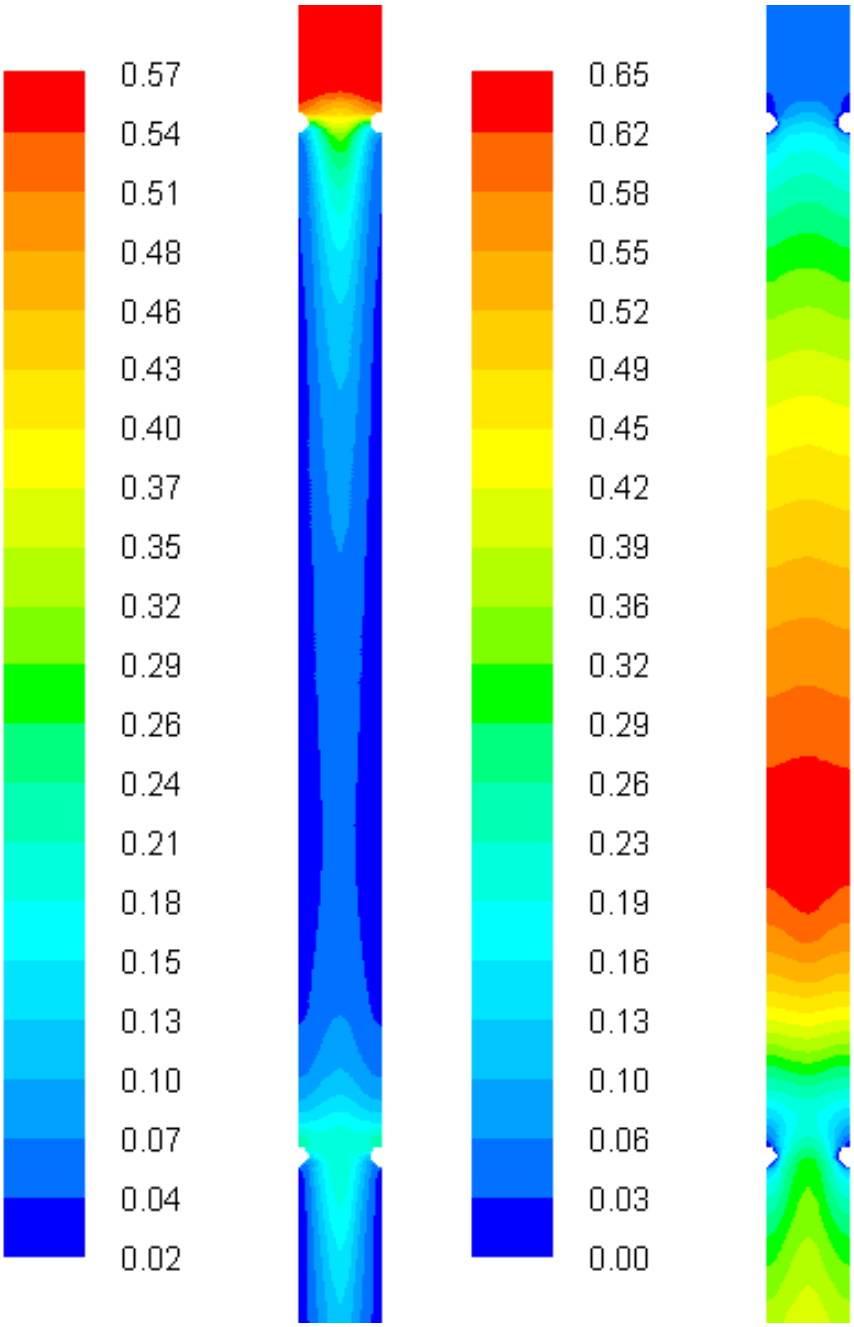

(a) Contours of volume fraction (b) Contours of velocity magnitude

Figure 5.17: Snapshot of the DEM model for the ID50-K material with the single spaced mesh. The CFD model shows much smoother transitions when approaching the lower mesh.

fraction, leading to a lower overall maximum velocity.

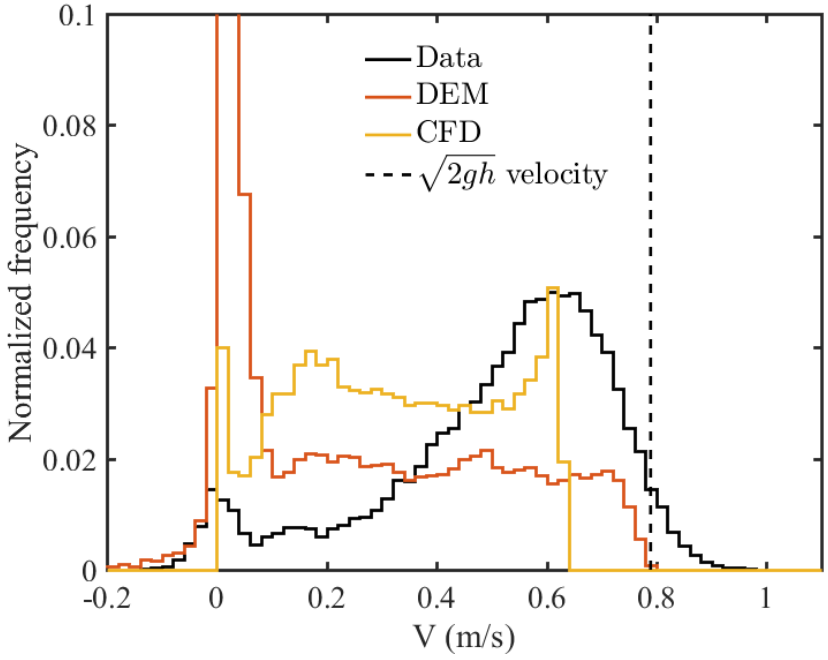

(a) Single spaced horizontal meshes

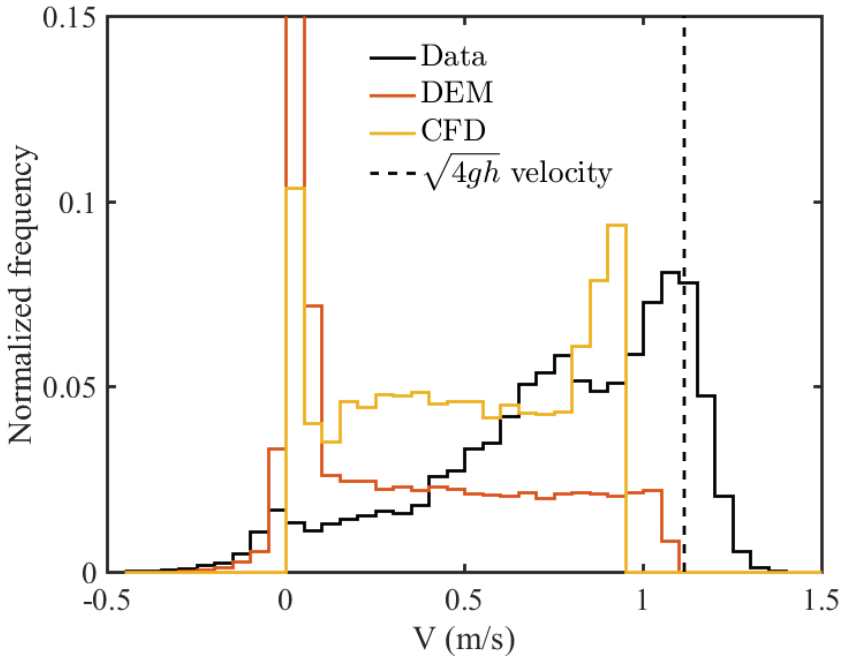

(b) Double spaced horizontal meshes

Figure 5.18: Experimental and numerical volume vertical velocity histograms for the ID50-K material, horizontal mesh configuration, size 10 mesh.

5.1.3 Parametric studies

This section presents the results of parametric studies done on different variables and modeling options in both the DEM and CFD models. There was some uncertainty in the material properties used to build the models themselves, as well as differences between the options available in the models to resolve the flow. To see how some of these parameters effect the results, several parameters were altered and the effects on the mass flux were recorded. Unless otherwise noted, all parametric studies have been performed on a horizontal single spaced 10 mesh geometry using the ID50-K material.

DEM friction coefficients

In DEM simulations, two critical parameters that govern particle motion are the coefficients of normal and rolling friction. While the values for normal friction are typically well known for a given material, the values for rolling friction aren't as straight forward. For "hard" spherical particles, values for the coefficient of rolling friction are typically on the order of 10^{-2} against a flat surface, and 10^{-3} against another particle. These values also depend on several factors, such as shape, surface roughness, and even the size of the particle, with rolling friction decreasing as particle size increases [102]. In this study, the value of normal friction for particle-particle contact for the ID50-K material was altered between a low, medium, and high value. As is expected, higher normal friction values produced lower mass flow rates. The particle-particle friction was the only value that was altered, because it was assumed that particle-particle contacts would dominate the macroscopic flow behavior. The coefficient of rolling friction was altered in a similar fashion (the highest value is high in a relative sense). Due to the irregular size, shape, and surface condition of the ID50-K particles, it was difficult to estimate an appropriate value for rolling friction a priori. It was decided that a relatively high value of 0.1 would be appropriate to attempt to capture the effect these particle irregularities might have on the actual value of rolling friction. As expected, the mass flux decreases with higher values of rolling friction, with relatively large

changes noted at small values. These values are plotted in figure 5.19.

Ballotini friction coefficients While the ballotini used in the experiments were much more uniform in size, shape, and surface roughness (and thus, their behavior should be better predicted by the DEM code than the ID50-K material), there is a considerable difference in the literature pertaining to the coefficient of normal friction that could be used for this material. Previous authors have found that the coefficient of normal friction for small glass beads to be fairly low, on the order of 0.1-0.2 [101, 119], but a "textbook" value for glass-glass friction is usually around 0.9 (for clean glass plates [120]). Values of both 0.15 and 0.9 were tested on the single spaced horizontal 10 mesh simulation, along with several values for the coefficient for rolling friction. Due to the nature of the ballotini, it was expected that they would offer much less rolling resistance than the ID50-K material, so the values of rolling friction tested were all less than 0.1, as shown in figure 5.20. At higher levels of normal friction, the effect of different rolling friction appears to be larger than with lower values of normal friction. While most of the combinations produce mass fluxes that are different from the lab value by relatively the same amount, it was decided to use the lower value of normal friction since that was the value obtained by experiments on glass spheres.

DEM normal contact models

The DEM code provides two different models for calculating the normal and forces involved in particle collisions. For the normal direction, the collision models used were "Hertz" and "Hooke." The Hertz model is based on the work of Hertz [90] and Mindlin and Deresiewicz [91], while the Hooke model first appeared in the original DEM model description by Cundall and Strack [41]. One important difference between the two models as implemented in LIGGGHTS is that the Hooke model requires the selection of a characteristic impact velocity. A velocity of 1 mm/sec was chosen as it was thought that the low

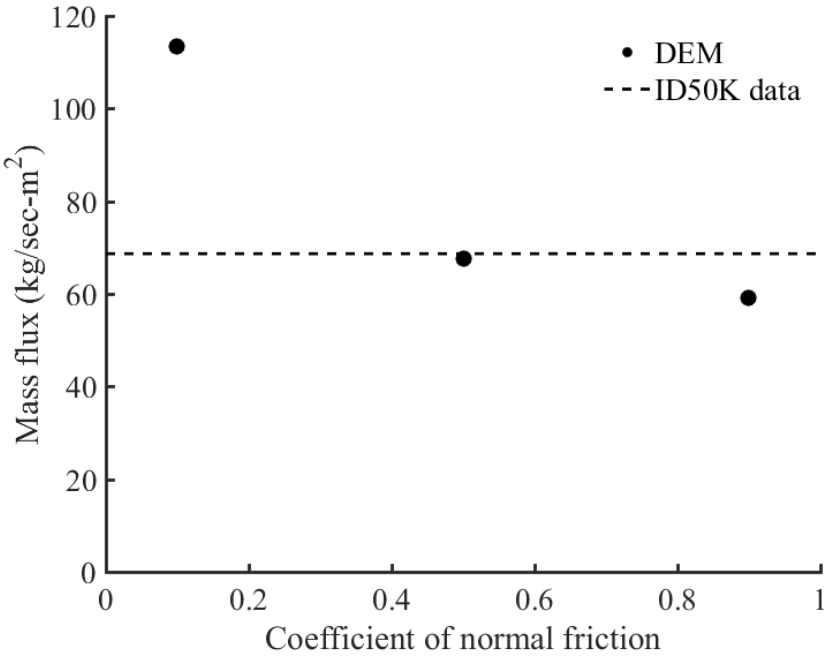

(a) Normal friction

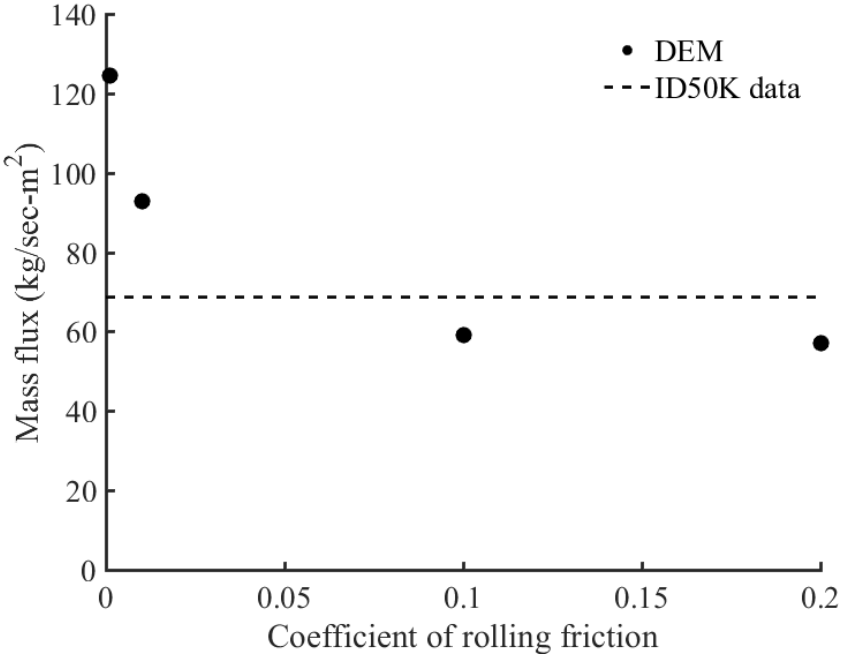

(b) Rolling friction

Figure 5.19: Effect of normal and rolling friction on mass flux, DEM model.

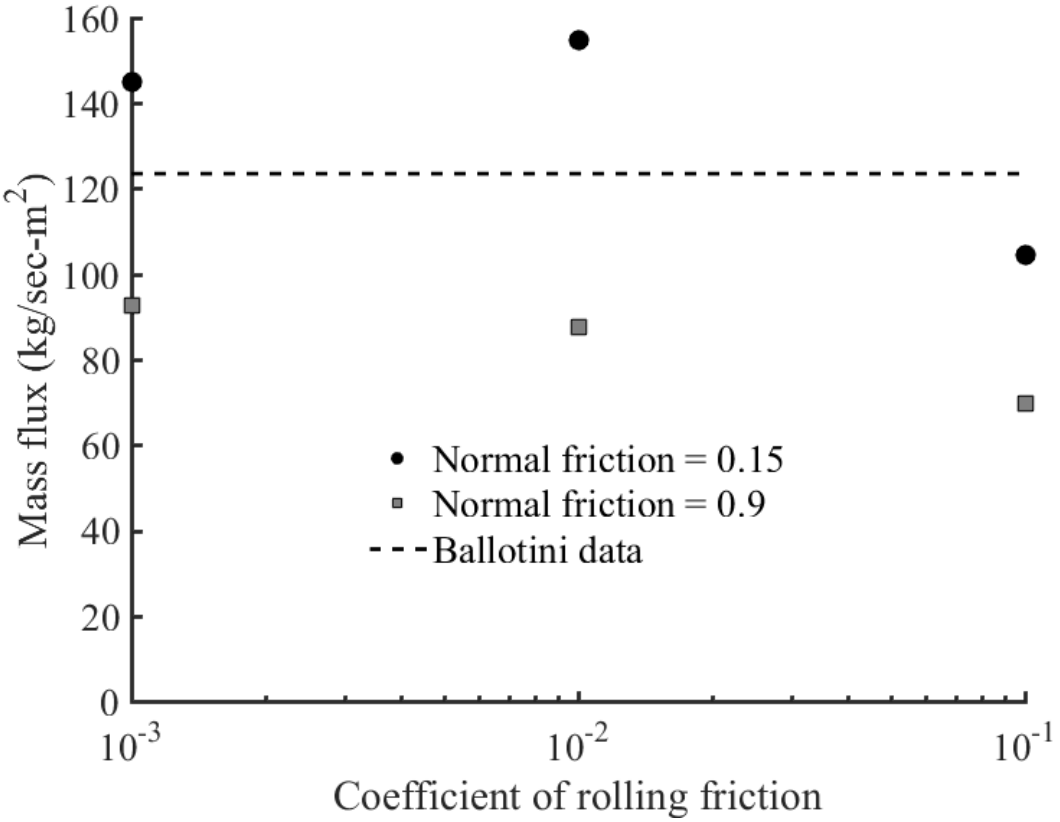

Figure 5.20: Effect of different combinations of normal and rolling friction on mass flux, ballotini, DEM model. The dashed line represents the value obtained by experiment. Note that the x axis is on a logarithmic scale.

speed, highly loaded areas of the model were more important for determining the overall behavior rather than relatively higher velocity impacts from free fall. As the Hertz model does not require such an input variable, it was used as the default normal collision model. Both models are in reasonable agreement, as seen in figure 5.21. The equations for the Hooke contact model are given in appendix B.

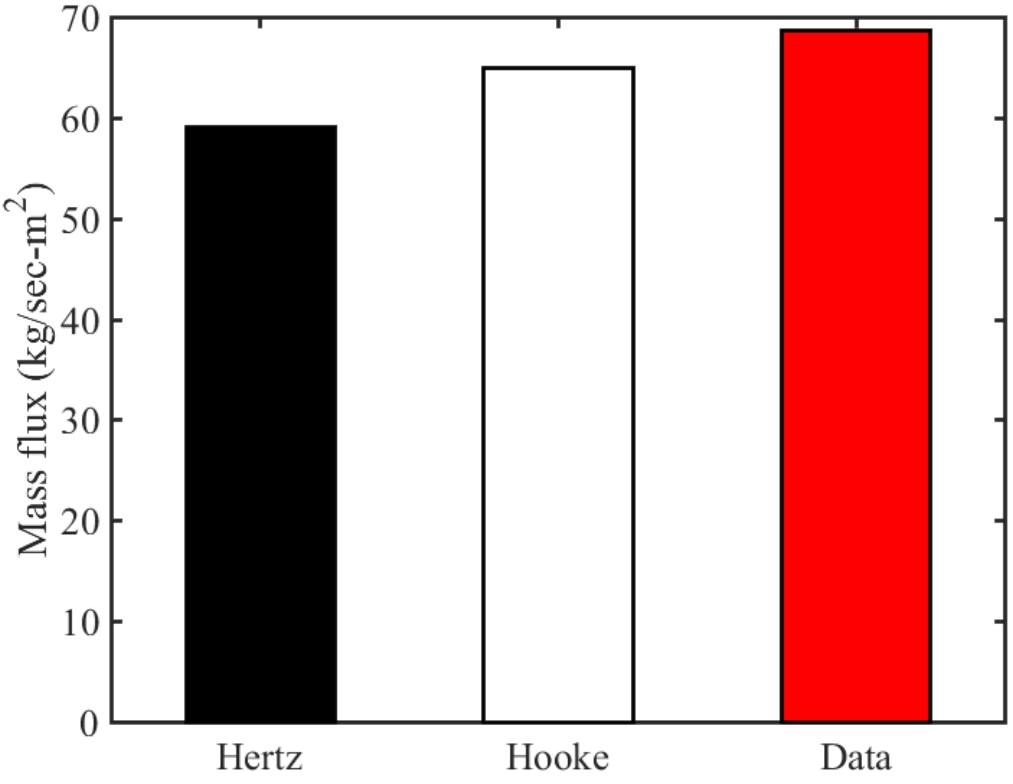

Figure 5.21: Effect of normal contact model on the DEM mass flux.

DEM rolling resistance models

The DEM code also provides several differen methods to model the rolling resistance of particles. Figure 5.22 shows the effect of using different rolling friction models. EPSD stands for elastic-plastic spring-dashpot, while CDT stands for constant directional torque. The EPSD models are the rolling analog of the Hooke linear spring-dashpot model for normal contact, while the CDT model applies a rolling resistance that is proportional to the

relative difference in rotational velocities between particles [96]. In addition, the EPSD and EPSD2 models differ in how the tangential stiffness and viscous damping torque are treated, as the EPSD2 model ignores the latter. While the EPSD model required the selection of a variable relating to the coefficient of viscous rolling damping (chosen to be the same as in [96] and not altered), it was the default model used in this study. The equations for the different rolling contact models are given in appendix B.

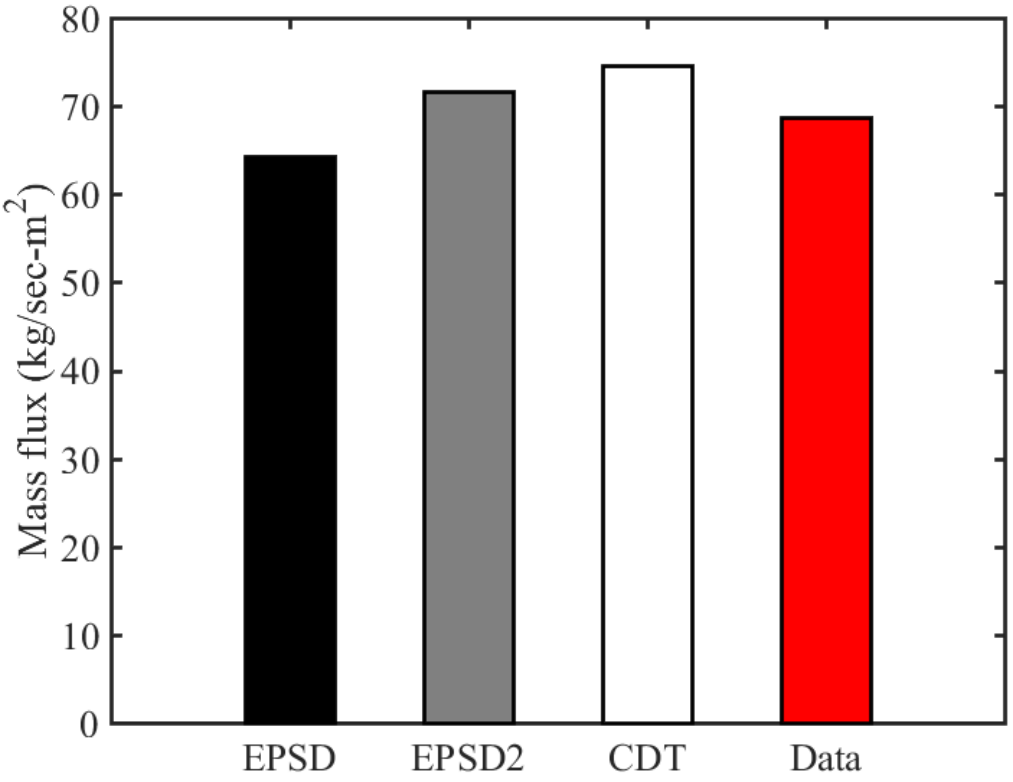

Figure 5.22: Effect of rolling contact model on the DEM mass flux.

Overall, the choice of rolling contact model appears to have a larger impact on the final result than the normal contact model, but this could be model dependent: a very dense flow might show different sensitivity characteristics than a very diffuse flow. There may also be a difference in the contribution of rolling resistance in a mostly horizontal geometry as opposed to a geometry with many oblique surfaces (i.e. horizontal mesh versus angled mesh or square tubes). These parameters were only altered for a single horizontal mesh

configuration in this study, but could be the subject of future numerical investigations.

DEM time step

The size of time step in the DEM model was also studied. In a typical DEM simulation, the goal is often to use as large a time step that will produce a stable solution. There has been quite a bit of study related to finding this maximum value, and one good estimate has been determined to be 0.1 times the critical time step for a given model [121]. A common method to determine the critical time step in many body DEM simulations is to use the Rayleigh time step, given by

$$T_R = \frac{\pi R \sqrt{\rho/G}}{0.1631\nu + 0.8766} \tag{5.1}$$

where ρ is the particle density, G is the particle shear modulus, and ν is the particle Poisson's ratio. Thus, the maximum stable time step in DEM simulation might be around 10% of equation 5.1. It was found during particle insertion that particles could attain relatively high velocities that could cause them to penetrate extremely deeply into walls and other particles due to the large time step (despite being below the 10% threshold), so a much more conservative factor of 1% was often used during filling. This was often raised to 5% once the domain was full of particles to speed up a simulation, but was reduced back to 1% to produce stable results. Figure 5.23 shows the results of the DEM time step on the mass flux. The differences are quite small, indicating that once the domain is full of particles, this particular simulation does not suffer greatly from using the largest practical time step allowed by the simulation parameters.

Figures 5.24 and 5.25 show what can happen if the time step is too large to handle high particle velocities in a simulation, even if the time step is below 10% of the Rayleigh criteria. With the solid surfaces in place, the simulation appears normal (the velocity scale has been truncated to enhance the color contrast between slow and fast moving particles). When the solid surfaces are removed, it can been seen that the spaces where the upper

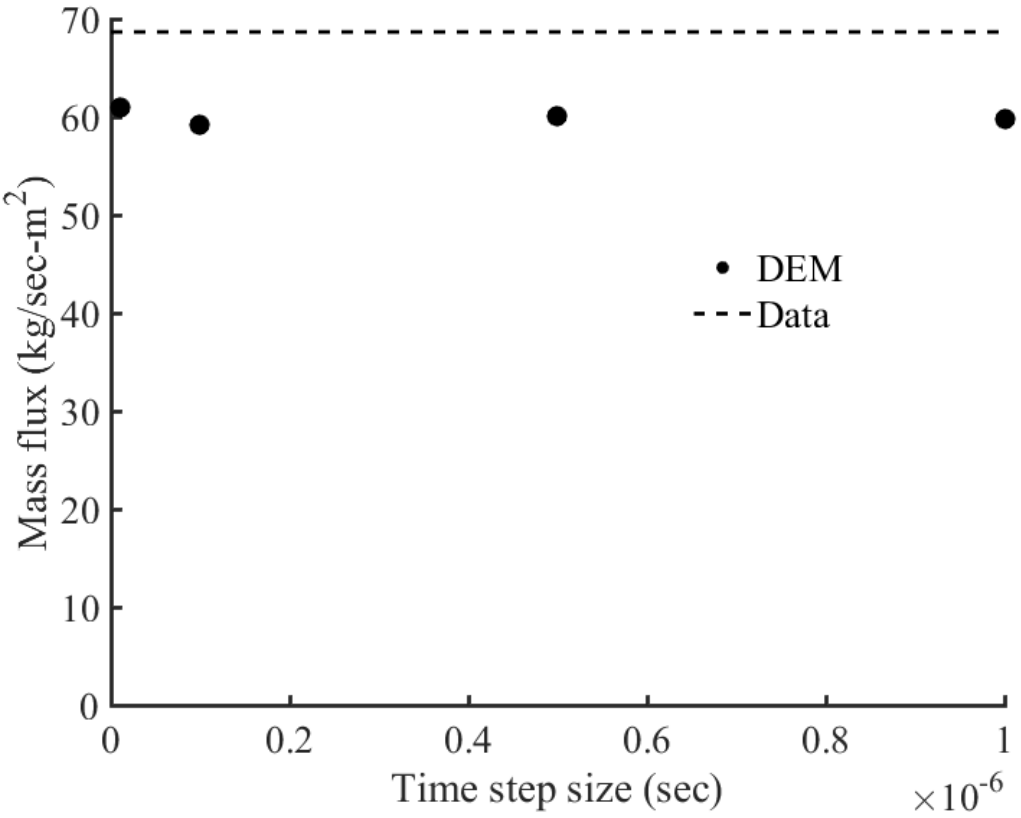

Figure 5.23: Effect of time step on DEM mass flux. The largest time step is approximately 10% of the Rayleigh time step.

surfaces were are completely filled with particles. This was due to the relatively high velocities attained during particle insertion. Using smaller time steps prevents this from occurring, but does cause the simulation to spend more time attaining a filled state.

DEM Young's modulus

Due to the constraints of a small time step on DEM simulations using real material properties (particularly, a very large K value for a particle-particle collision), a very common method to speed up DEM simulations is to lower the Young's modulus of materials in a simulations by several orders of magnitude [43], enabling a much larger minimum time step. While this approach might not be appropriate for all types of simulations, it has been reported that lowering the particle Young's modulus by a factor of 10000 had no effect on the discharge rate, particle velocities, or angle of repose of particles released from a flat bottomed hopper and allowed to form a pile on a flat surface below [44]. Thus, the Young's modulus of every material in the DEM simulation was initially lowered by a factor of 10000. LIGGGHTS has a built in minimum of 5 MPa for the Young's modulus when using SI units, so this factor was chosen to enable the Young's modulus of the polycarbonate walls to maintain the same order of magnitude difference with the other materials in the simulation (polycarbonate has a Young's modulus around 2.4 GPa [99]). Figure 5.26 shows the effect of the Young's modulus on the mass flux. The higher Young's modulus produces a slightly lower mass flux, but the difference is not very large. Citing figure 5.23, the fact that the higher Young's modulus required the use of a smaller time step likely had a negligible effect on the outcome.

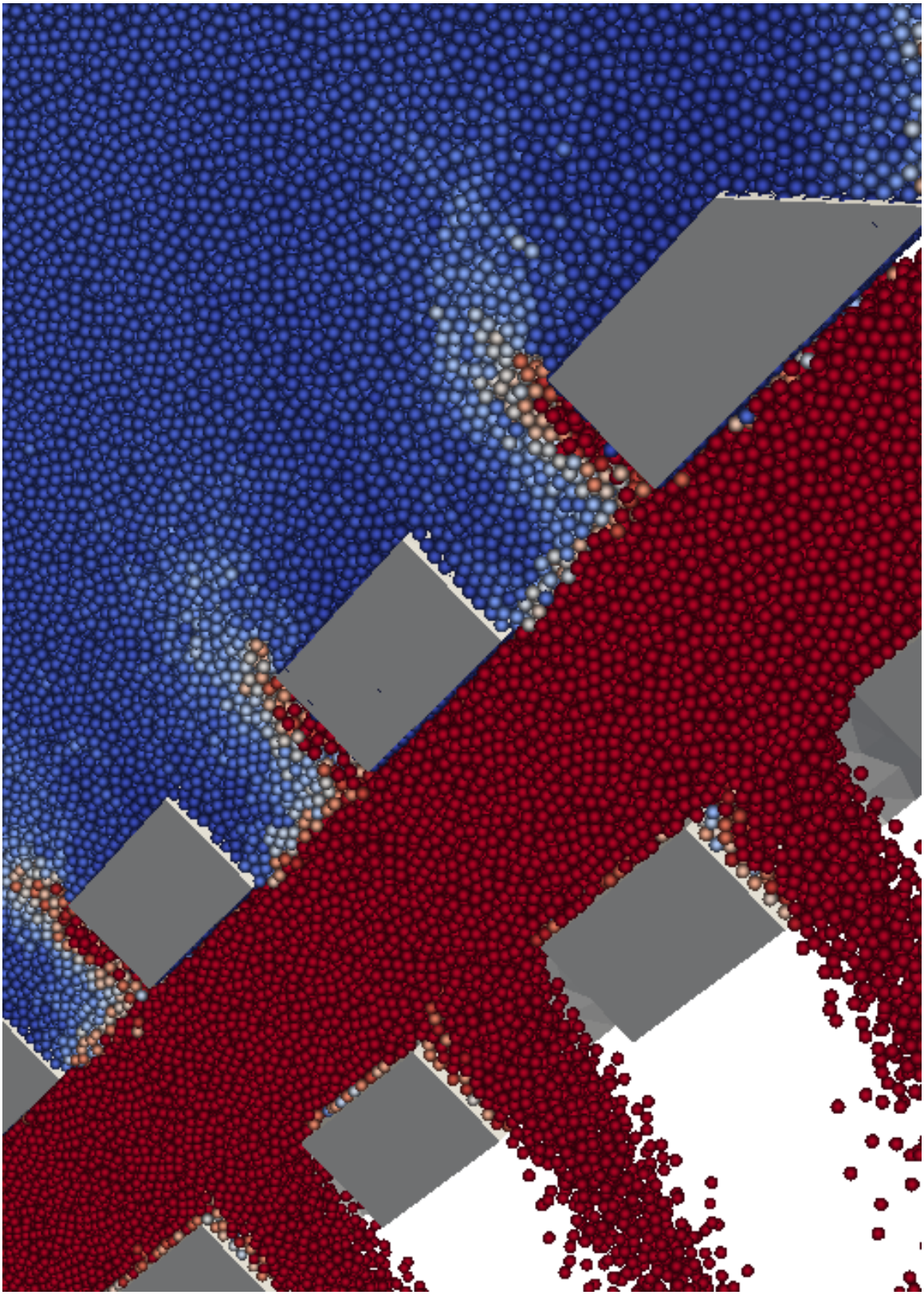

Figure 5.24: Snapshot of a DEM simulation where particles became stuck inside solid surfaces.

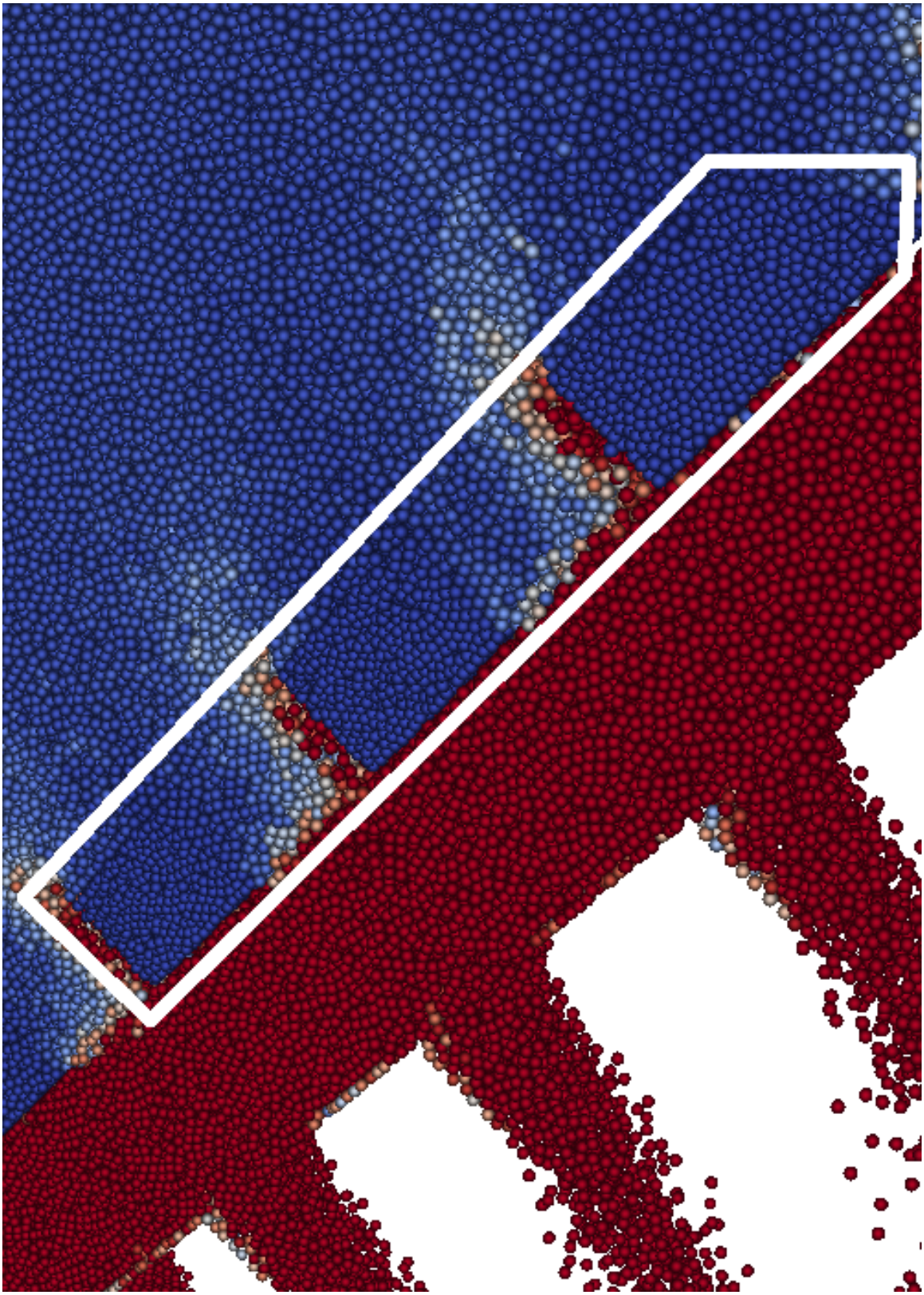

Figure 5.25: Snapshot of a DEM simulation where particles became stuck inside solid surfaces (surfaces have been removed).

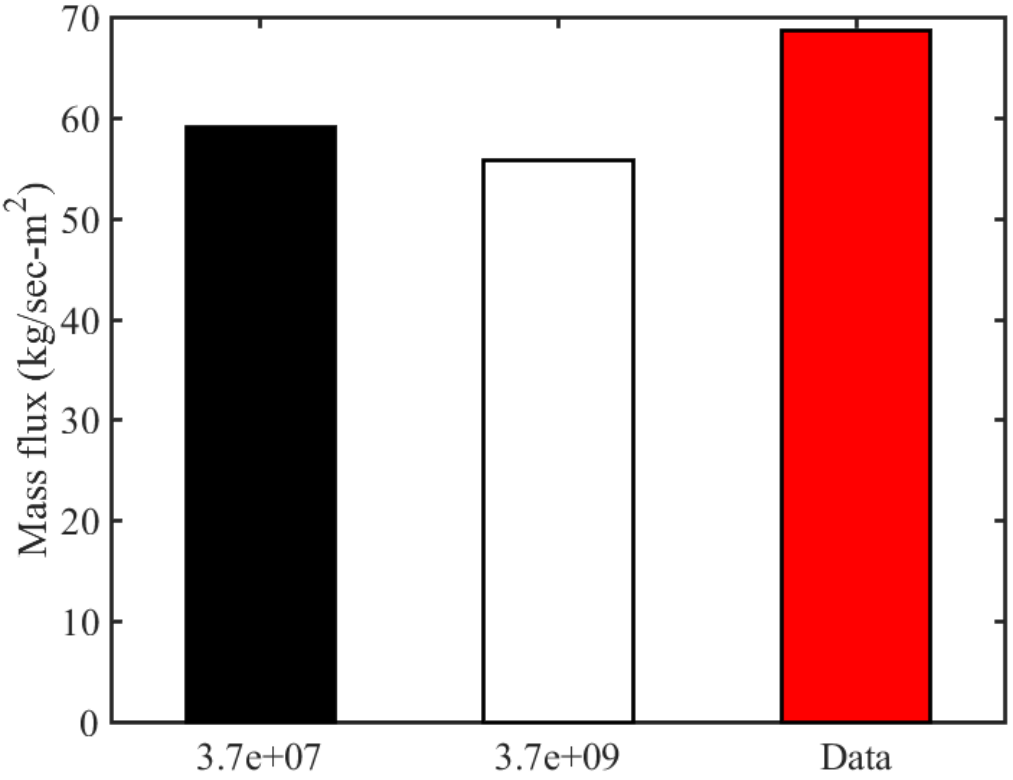

Figure 5.26: Effect of Young's modulus on mass flux.

CFD angle of internal friction

The CFD model, due to treating the granular flow as a continua, is potentially better suited to handle macroscopic properties of a granular assembly. One important parameter that is widely used in granular studies is the angle of internal friction. The angle of internal friction is determined by plotting the normal and shear stress acting on a granular material before it fails. These values were measured in the lab using a Jenike shear cell. By plotting several different combinations of normal and shear stress, a rough linear relationship between the two stresses can be developed and the angle of internal friction directly calculated as the inverse tangent of the slope of the stress-stress curve. For the ID05 K material, an angle of 29 degrees was determined from the Jenike shear cell, as seen in figure 5.27. Two other points - 24 and 34 degrees - were used to find a relationship between internal friction and mass flow rate. As shown in figure 5.28, higher angles of internal friction lead to lower mass fluxes, as these materials are more resistant to shear failure. However, the effect is relatively small. All three values used are in the typical range for natural materials [73].

CFD maximum packing fraction

The maximum packing fraction is another macroscopic parameter that was varied. The packing fraction is simply the amount of space taken up by particles in a region. The maximum packing fraction of a collection of monodisperse spheres is usally given as approximately 0.63 [122], while the maximum packing density of polydisperse spheres can reach into the 0.75 range, depending on the exact particle size distribution [123]. A default value of 0.6 was used as the maximum packing fraction, with additional values of 0.55 and 0.65 used. The results, as seen in figure 5.29, show that higher packing fractions allow higher mass flow rates, which is expected.

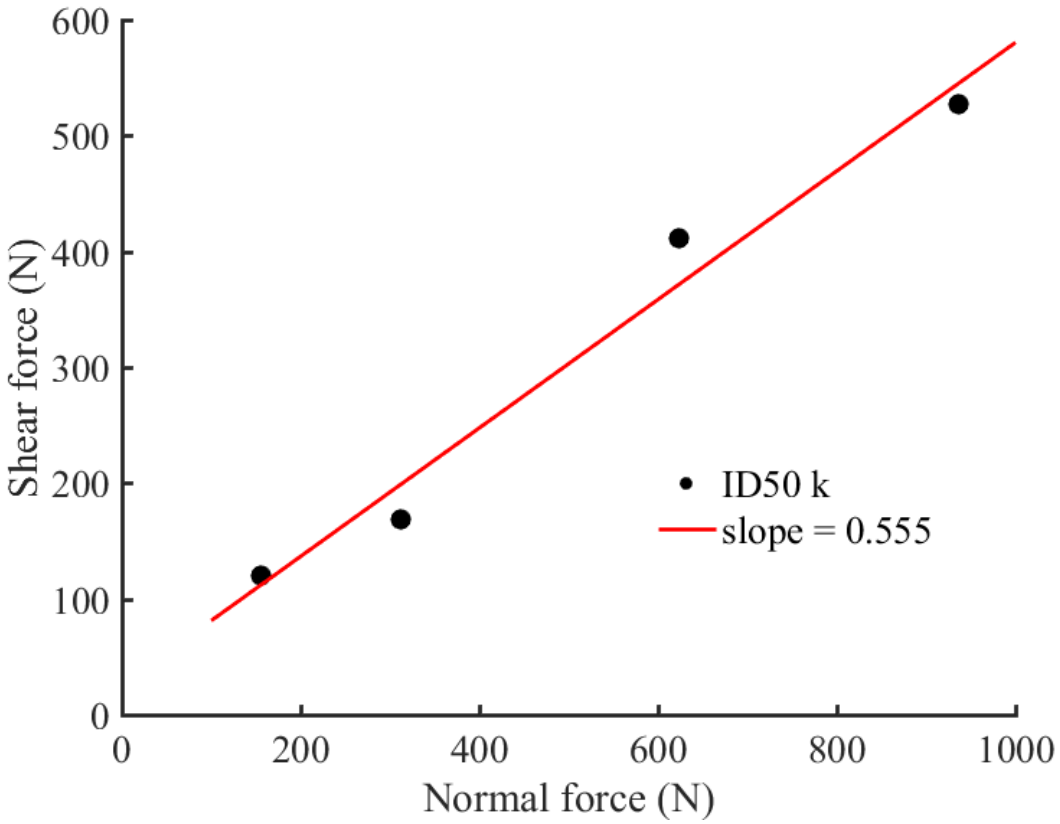

Figure 5.27: Plot of normal versus shear force produced by Jenike shear cell, ID50-K. The inverse tangent of the slope gives the angle of internal friction.

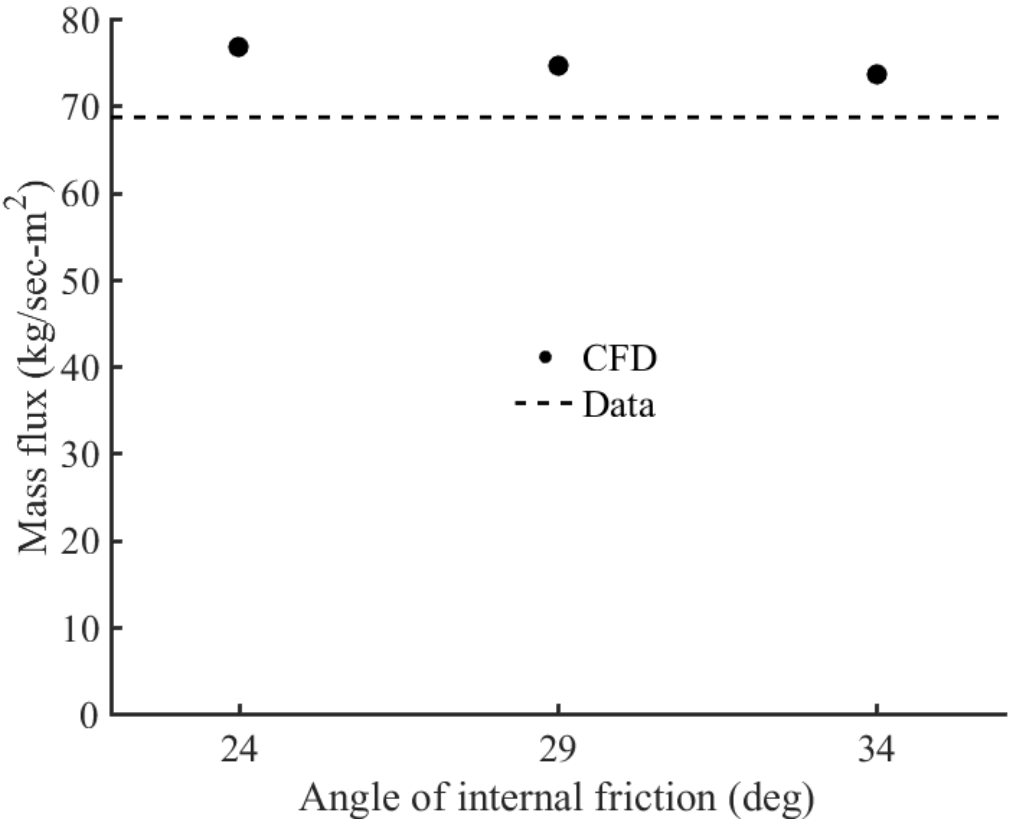

Figure 5.28: Effect of the angle of internal friction on the mass flux, CFD model.

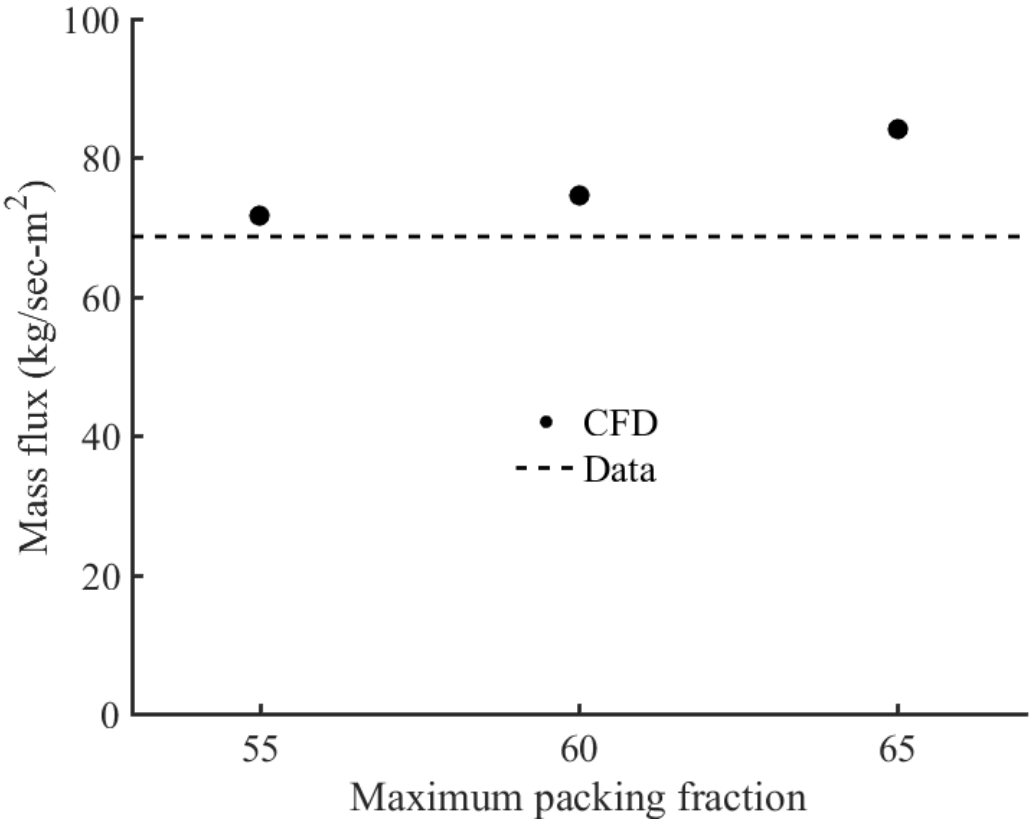

Figure 5.29: Effect of the maximum packing fraction on the mass flux, CFD model.

CFD frictional packing fraction

The friction models available in Fluent also allow the specification of so called friction packing limit. This is defined as the packing fraction where frictional effects start to dominate [110]. For the default value of 0.6 for the maximum packing fraction, a value of 0.55 was used for the friction packing limit. The separation of 0.05 was maintained for each value of the maximum packing fraction tested in figure 5.29. In figure 5.30, the maximum packing fraction was held constant at 0.6 while the frictional packing limit was varied. In contrast to the maximum packing fraction, there appears to be some sort of maximum max flux for the friction packing limit that isn't simply the largest number. It is likely very difficult to experimentally determine the relationship between maximum packing fraction and this frictional packing fraction, but it may be related to the dilation or contraction a granular assembly experiences as it undergoes shear failure.

CFD initial conditions

Since the computational cost of the CFD model is not impacted by particulate loading, the initial conditions were varied in Fluent to study their effect on mass flux. Figure 5.31 shows the outcome of three different initial conditions. IC1 refers to setting the volume fraction of half of the domain (specifically, the top, bottom, and lower wire sections of the mesh) to 0.3. IC2 refers to using only the volume fraction from the steady state solution produced by IC1 as the initial condition. IC3 refers to taking volume averaged volume fractions in the different model sections produced by IC2, and using them as the initial volume fractions. Due to the relatively small size of the domain, all of the results for the CFD model using the horizontal mesh test section have been produced using IC2. However, this was not done for other configurations because it requires that the simulation be run twice (they were essentially produced using IC1). The plot shows that decent values for the initial volume fractions (IC3) produce results that are fairly close to the results from using the "best case" initial conditions (IC2). Thus, if these values can be determined, it may be possible to get

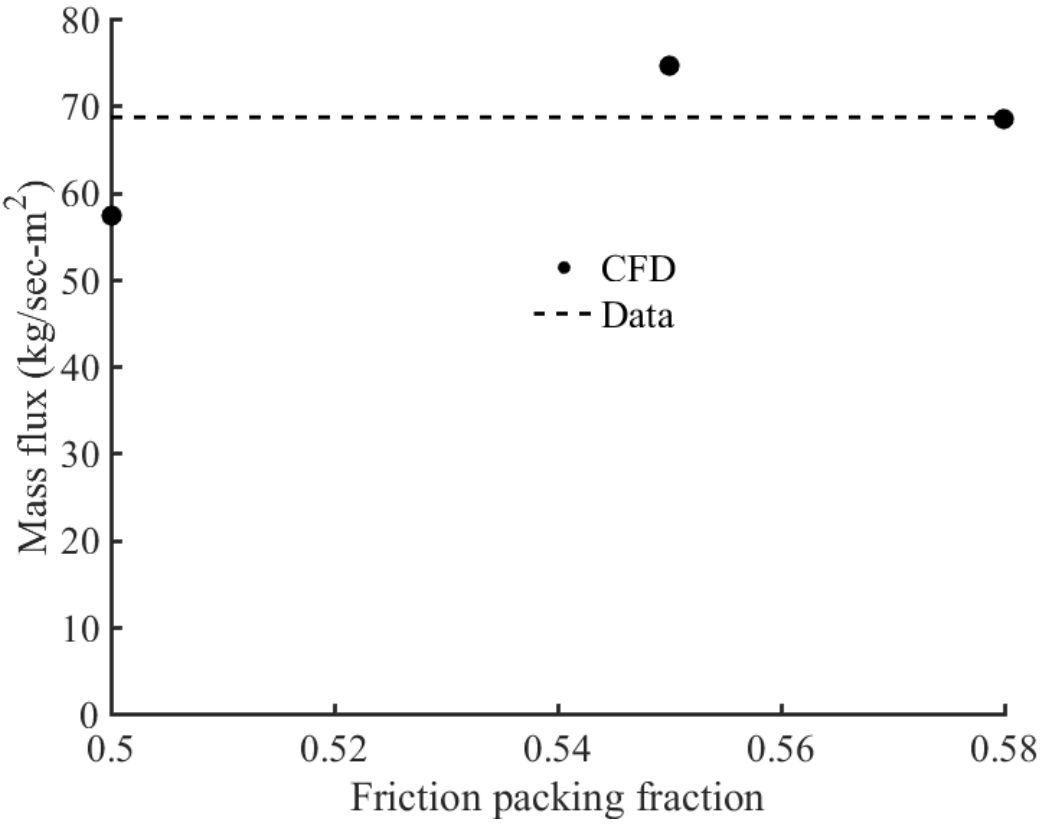

Figure 5.30: Effect of the friction packing limit on the mass flux, CFD model.

better results than with IC1, but in a much shorter time frame than with IC2.

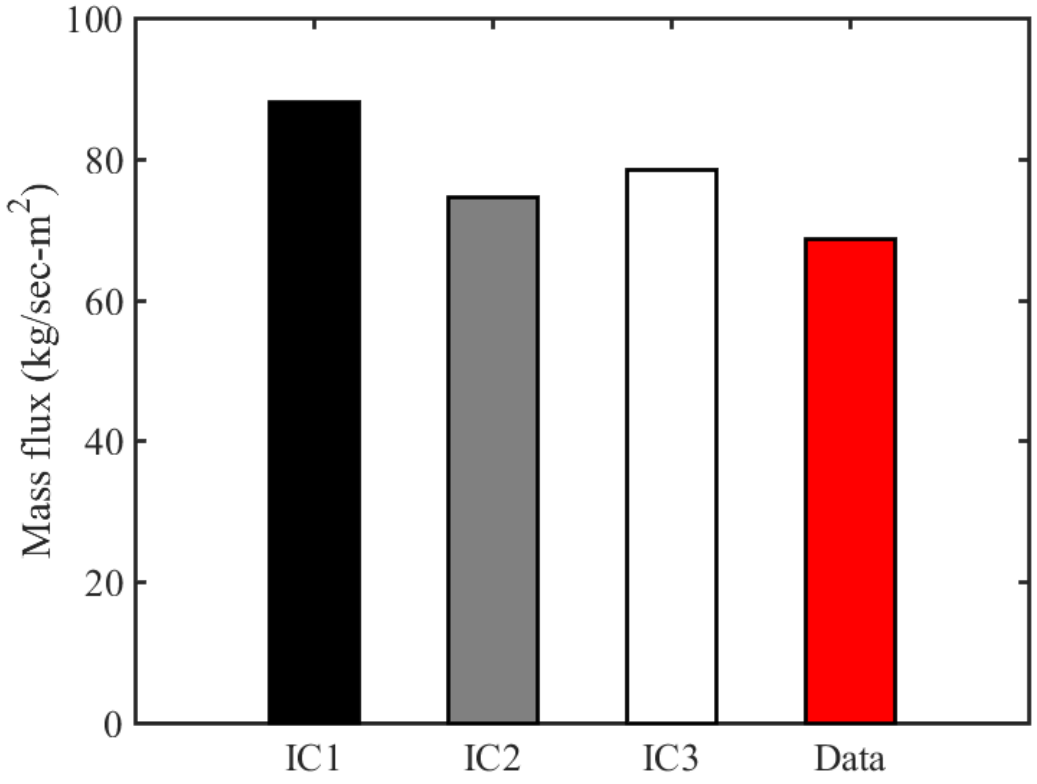

Figure 5.31: Effect of initial conditions on the mass flux, CFD model.

CFD drag models

The CFD model offers several different models to represent the drag exerted on the solid phase by the fluid phase. Figure 5.32 shows how different models available in Fluent effect the observed mass flux. As can be seen, the results are nearly identical (to three significant figures in four of the models) no matter what drag model is used. This is not unexpected, given the large ratio of fluid densities (on the order of 10^3) and the relatively short distance traveled by the solid phase in free fall (i.e. low Reynolds number). If the fluid phase used in the model were much more dense or viscous, or the screens were far enough apart that the particles could be expected to approach terminal velocity, the differences in the drag model

formulations might become more important. This is also a somewhat desirable result, as one of the goals of an impeded flow design is to reduce the influence of air currents within the receiver cavity. The equations for the other drag models are presented in appendix B.

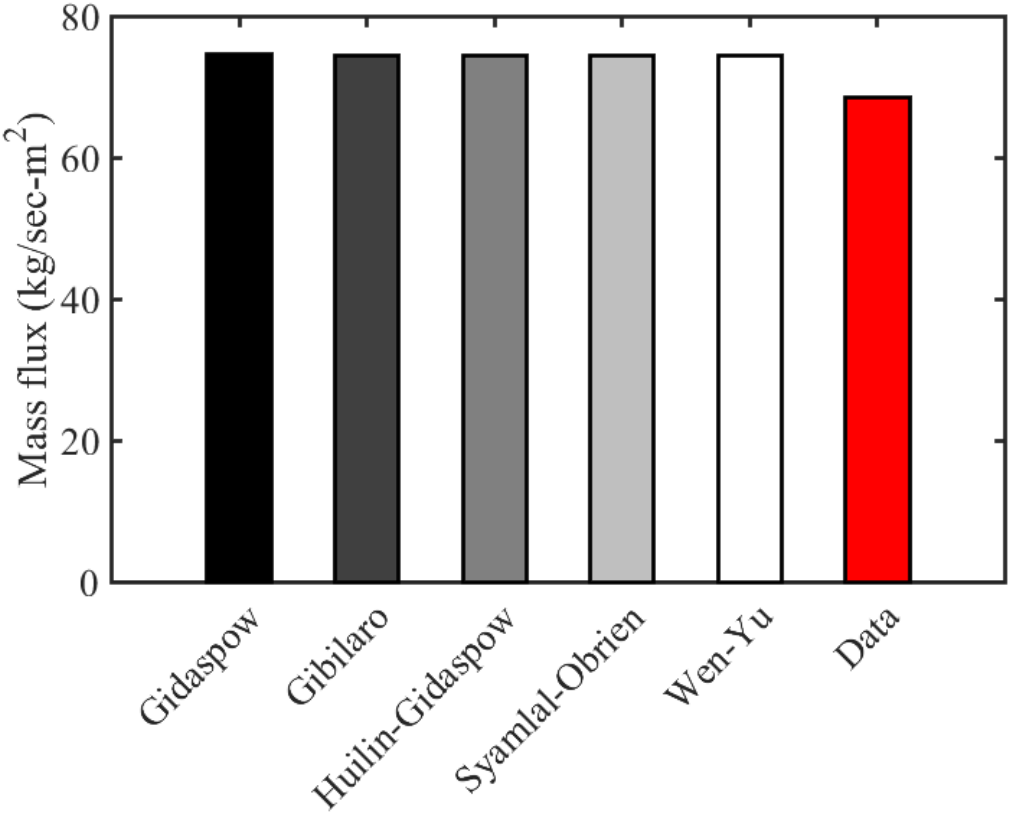

Figure 5.32: Effects of solid-fluid drag model on mass flux

CFD friction pressure-viscosity models

Another important parameter used in the CFD models was the approach to modeling the effects of frictional pressure and viscosity. The frictional viscosity models chosen were from Schaeffer [118], and from Johnson and Jackson [124]. The frictional pressure models chosen were from Johnson and Jackson, Syamlal et al. [117], and a model based on the kinetic theory of granular flow (KTGF) from Ding and Gidaspow [116]. As seen in figure 5.33, only 2 of the model combinations were able to approach steady state after the specified flow time (2 seconds). The Scheaffer-KGTF model experienced a relatively large transient

flow feature shortly before 2 seconds was reached; the value in the figure represents the steady state value the was achieved before this upset. The Johnson-Syamlal combination was experiencing a small oscillation in flow at 2 seconds; the value in the figure represents the mean value of this oscillation. 2 other combinations were possible (Schaeffer-Syamlal and Johnson-Johnson), but those simulations diverged, and are not plotted. The equations for the different frictional pressure and viscosity relations are presented in appendix B.

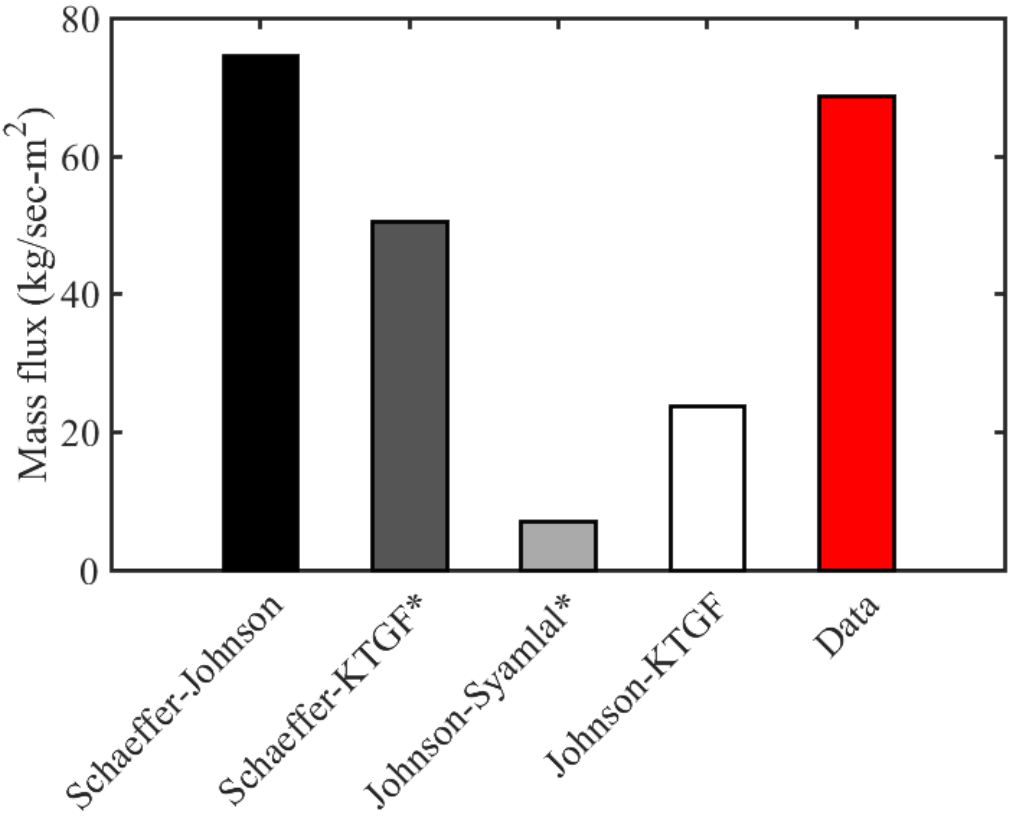

Figure 5.33: Effect of friction pressure-viscosity model combinations on mass flux. The asterisks indicate that the particular model was not able to approach steady state even after unrealisticly long simulated times. The values indicated show an estimated steady state value for the mass flux.

CFD machine precision

Fluent also gives users the option of running a simulation in single or double precision, which essentially controls the number of significant digits used in a calculation. While the default Fluent solver is a single precision solver, Fluent recommends the double precision solver for several types of problems, including multiphase problems [110]. Figure 5.34 shows the effect of machine precision on mass flux, which is quite small. While modern high performance computing architecture is able to handle the double precision solver without any issues, using a single precision solver could be an option for someone using consumer grade hardware, especially if storage or memory are limited.

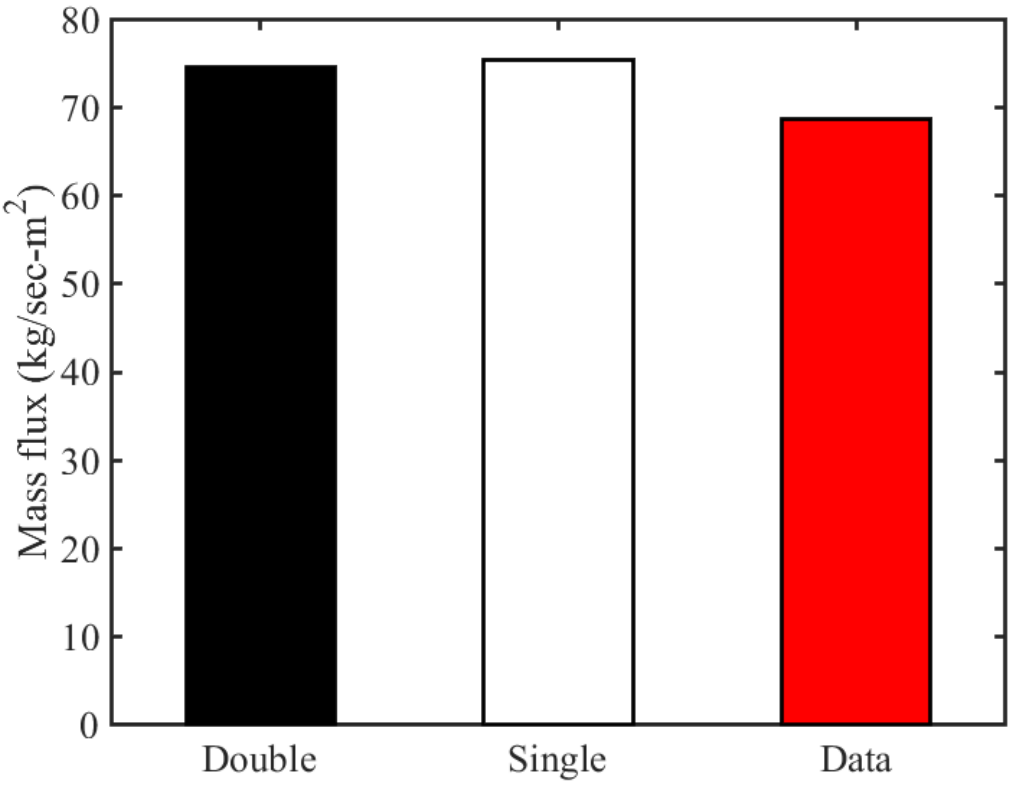

Figure 5.34: Effect of machine precision mass flux.

CFD wall boundary conditions

In many CFD simulations, wall boundaries are treated with a no slip boundary condition. There is another way to specify the solids phase wall boundary condition when modeling granular flow using CFD: specularity. The specularity coefficient is a way to model shear stress between the wall and the solids phase [124] and is similar in principle to the specularity coefficient used in electromagnetic reflections. In Fluent, the shear stress is modeled with the specularity coefficient by

$$\tau = -\frac{\pi}{6}\sqrt{3}\phi\frac{\alpha_s}{\alpha_{s,max}}\rho_s g_0 \sqrt{\Theta_s} U_s \tag{5.2}$$

were ϕ is the specularity coefficient, α_s is the solids volume fraction, ρ is the particle density, g_0 is the (model dependent) radial distribution function, Θ_s is the granular temperature, and U_s is the particle slip velocity. Thus, a specularity coefficient of 0 is essentially a free slip condition. While many authors state that a specularity coefficient of 1 is equal to a no slip boundary condition, this claim may not be completely general [125]. To see the effects of the different boundary conditions, the wall boundaries were given different values for the specularity coefficient and compared against a no slip boundary condition, as seen in figure 5.35. As expected, the lower values of specularity coefficient lead to a higher mass flux. However, there is still a significant difference between the unity specularity coefficient and the no slip boundary condition. Nearly all of the literature on the influence of the specularity coefficient on granular behavior has been done on fluidized beds or other geometries with no particle scale features (and in many cases, those studies were carried out in two dimensions). Therefore, it is difficult to directly compare those results to this study, or even conclude if they are applicable. However, even in a simulation domain with a relatively small amount of wall boundary conditions, the effects of slip on that boundary condition are quite clear.

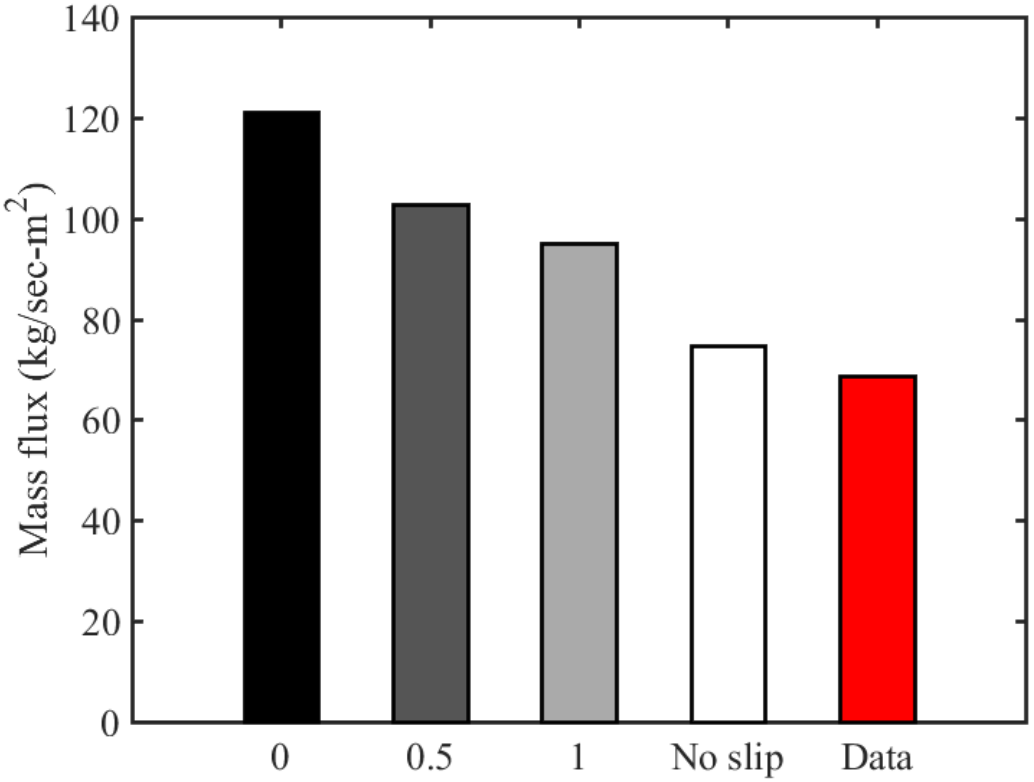

Figure 5.35: Effect of specularity coefficient on mass flux.

CFD granular temperature transport models

Another way Fluent handles particle-wall interactions is in the computation of granular temperature. In the algebraic model (the default used for this study), it is assumed that granular temperature is a highly local feature, and the convection and diffusion terms are dropped from the convection-diffusion equation for granular temperature. While this may be appropriate for dense flows, it also means that the coefficient of restitution between particles and walls is not taken into account. Figure 5.36 shows the effect of treating the granular temperature as an algebraic phase property (the default) and as a partial differential equation using the Syamlal-Obrien option [117] for the granular temperature diffusion coefficient (this model also enables the convective term in the granular temperature equation). Particle-wall restitution was set at 0.9 when using the PDE option. The PDE option tends to increase the mass flux. However, as mentioned previously, the importance of wall interactions in dense granular flows should be considered before using the more complicated PDE transport model.

CFD time step

Similarly to grid size, the CFD time step can be altered to ensure that the model has achieved temporal independence. While an implicit solver does not place an absolute limit on the size of time step used, care should be taken to ensure the Courant number does not grow too large in the model, and any transient flow features of interest are resolved. Figure 5.37 shows the results of different time steps for the chosen mesh size. The shape of this plot is the opposite of what was expected. It was thought that larger time steps would produce diverging results. However, the results are clearly changing as the time step gets smaller (each simulation was run for the same total flow time). There is currently not a good explanation for this trend. It might be possible that there is an optimal Courant number for a given simulation, but these time steps were all used on the same mesh, so that was not investigated in this study.

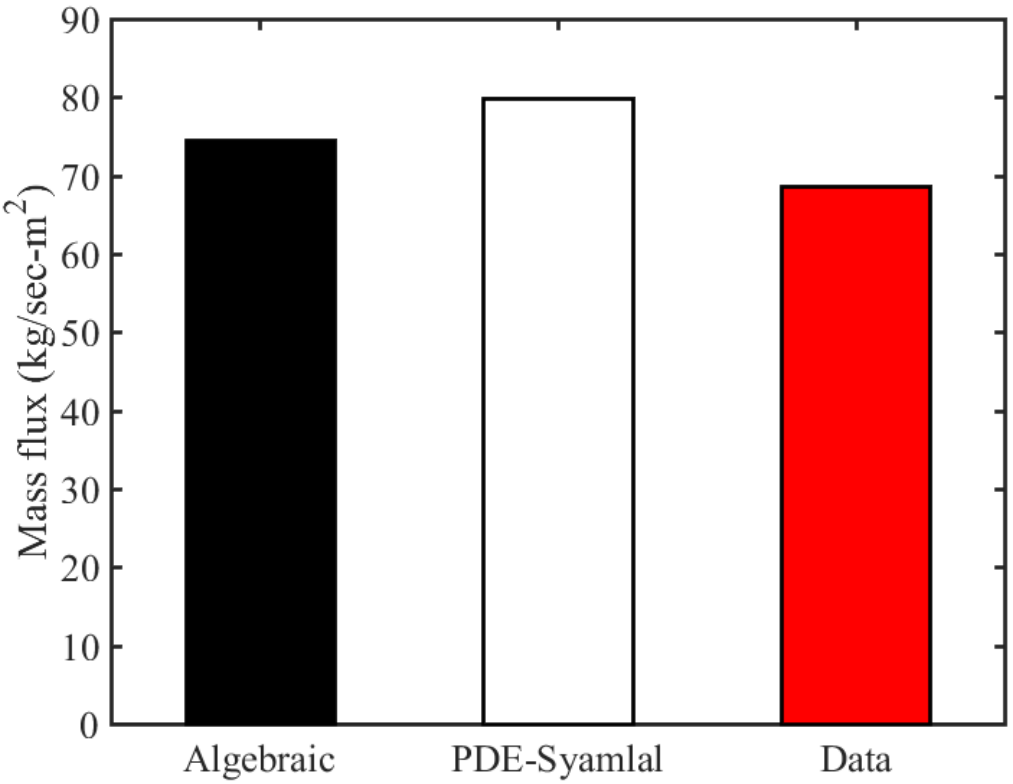

Figure 5.36: Effect of using different granular temperature transport models on mass flux.

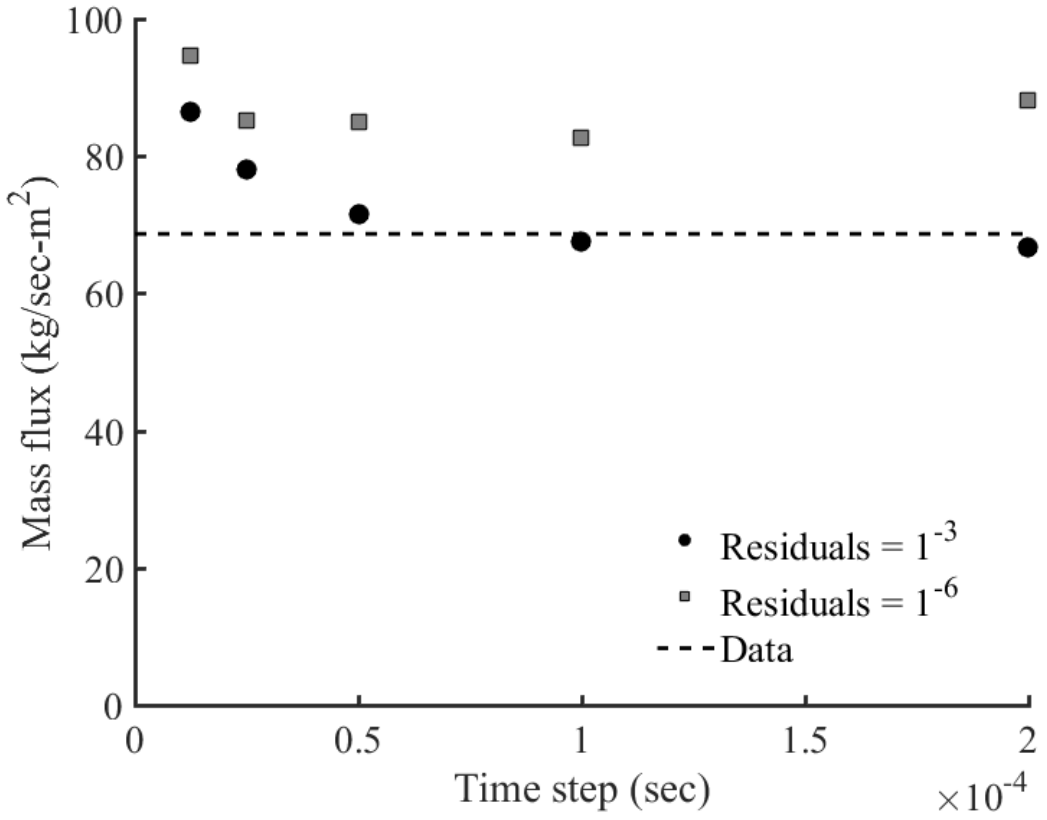

Figure 5.37: Effect of CFD time step on mass flux at different residual levels

Particle diameter

Finally, one other parameter that was modeled in both the DEM and CFD simulations was the particle diameter. The ID50-K material has a particle size distribution that spans an order of magnitude for particle radius. While both DEM and CFD offer methods to model a poly-disperse group of particles, a single particle diameter was used in this study to greatly ease the computational requirements. The particle diameter was chosen based on an average particle size calculated from a series of photomicrographs of the different materials. While the ballotini are fairly uniform in their size and roundness, the ID50-K material shows a relatively large variance in size, shape, and smoothness. While the CFD model is better able to accommodate these differences by the use of previously mentioned macroscopic properties, particle diameter is a key variable in the DEM models. The use of monosized perfect spheres to model "real" particles should be carefully scrutinized to ensure it is a reasonable assumption. Figure 5.38 shows the effect of particle diameter on mass flow rate for both the DEM and CFD models, along with the experimental data for comparison.

Figure 5.39 shows the same data presented a slightly different way. The x axis is the ratio of particle diameter to mesh hole size. The flux values for the 8 mesh are slightly higher than the general trend; this is likely due to the fact that the 8 mesh used had a higher open area percentage than the other 3 meshes. Overall, both figure 5.38 and figure 5.39 show that the mass flux obtained in the lab is captured within the range produced by altering the size of the particles in both the DEM and CFD simulations.

With the previous differences outlined, it is possible to plot an "area of effect" for different model parameters. Much like plotting confidence intervals for measured data, these would be regions where the specified dependent variable could lie. In the case of the DEM model, the particle diameter has the largest effect on the mass flow rate of the ID50-K material. The particle diameter also likely has a fairly large uncertainty associated with it, given the small sample size used to obtain the measurement. As shown in figure 5.40, the

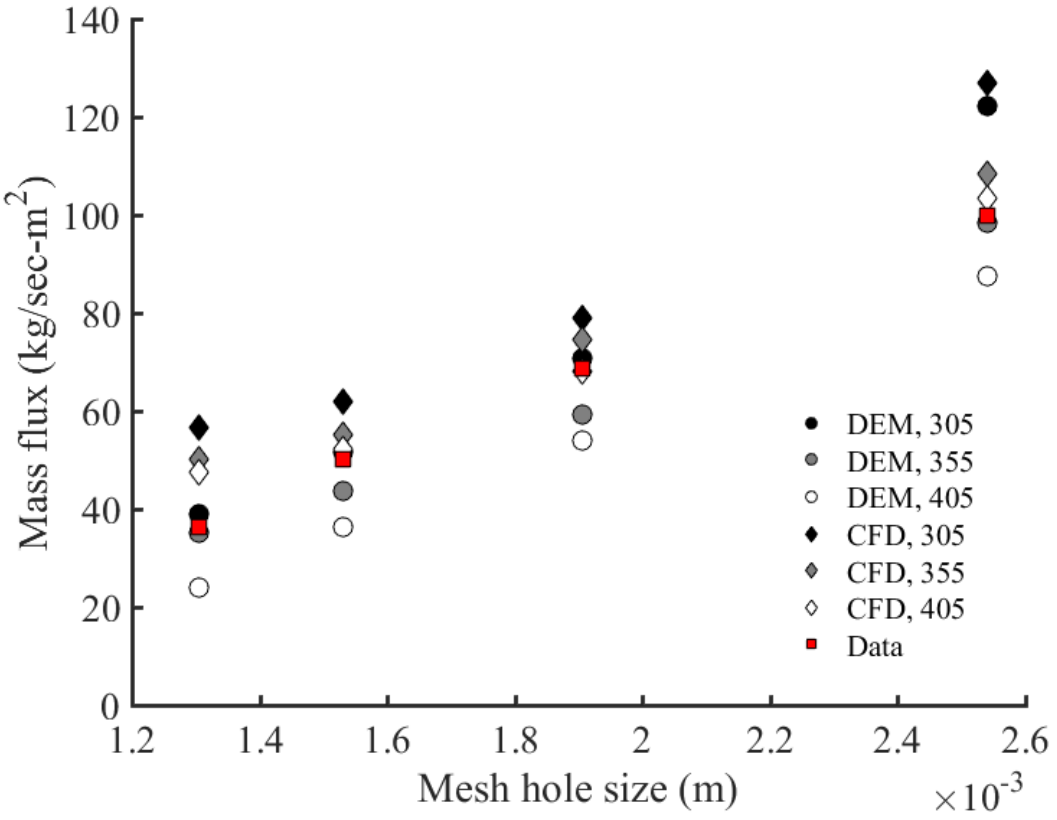

Figure 5.38: Effect of particle diameter on mass flux.

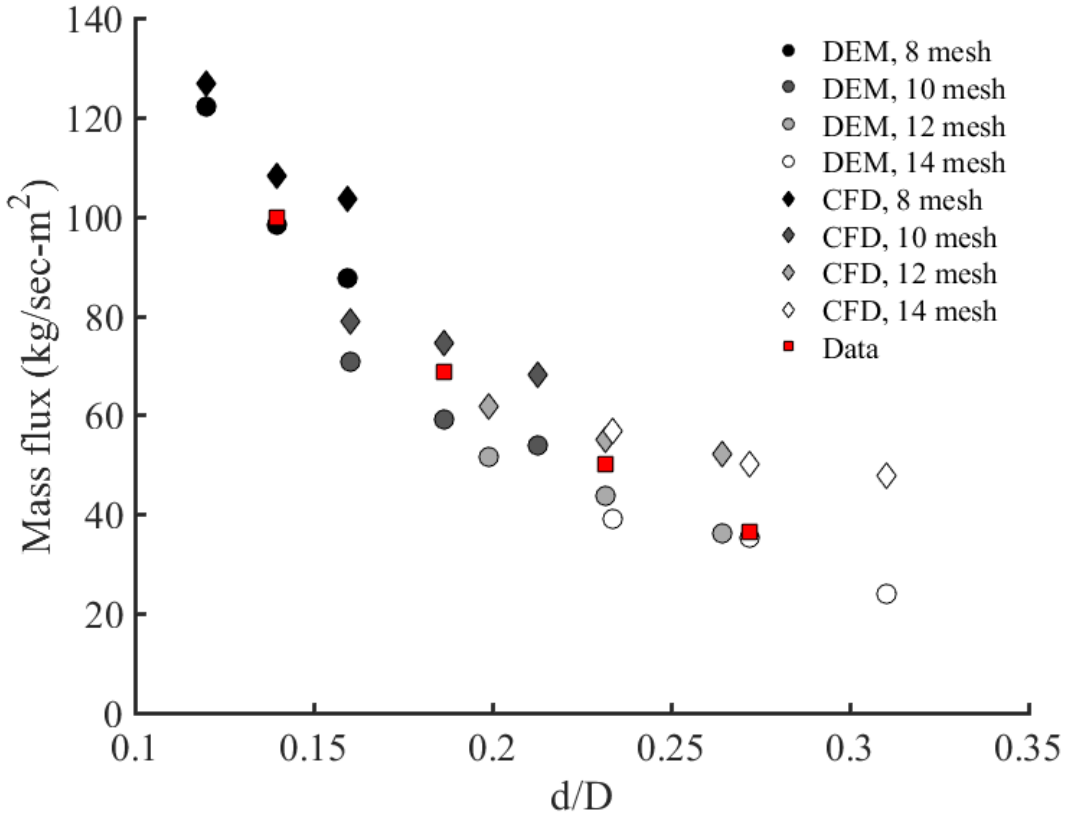

Figure 5.39: Effect of particle diameter/mesh hole size ratio on mass flux.

experimental data falls within the shaded region, which indicates the range of mass flux values based on different particle diameters.

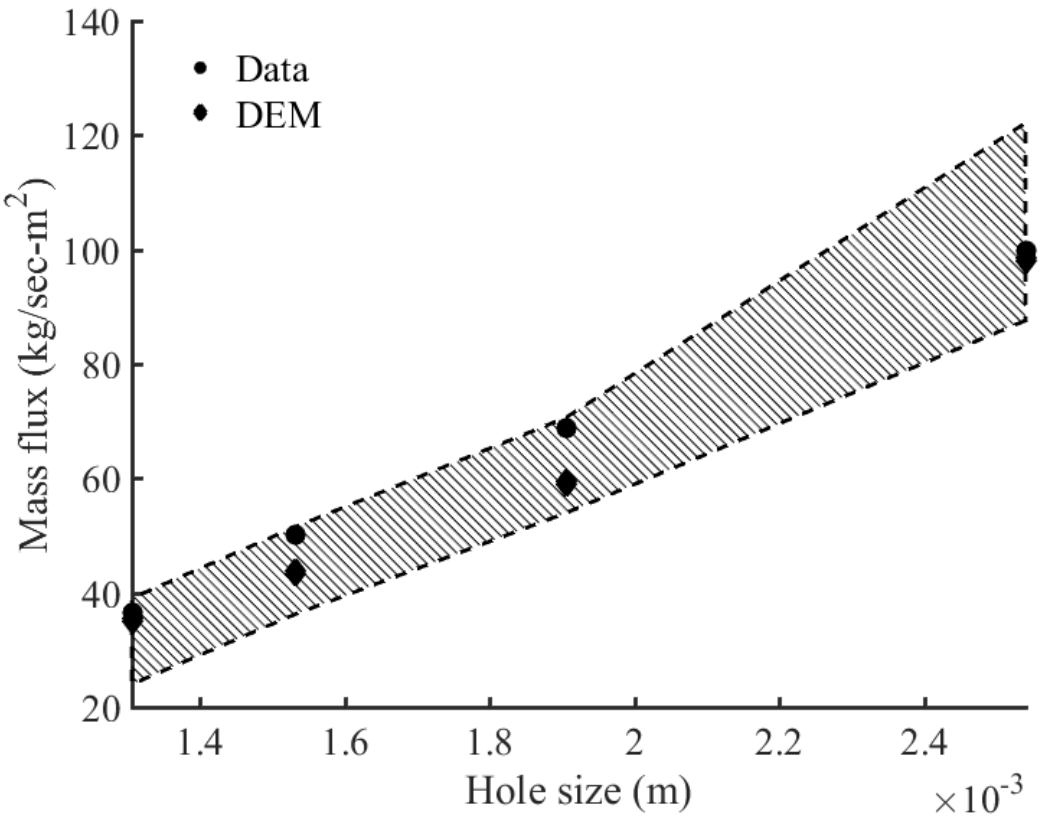

Figure 5.40: Sensitivity of mass flow rate on particle diameter

In the case of the CFD simulation, the particle diameter was also used to generate the shaded region. Figure 5.41 shows the area of influence the same particle diameter variance has on the mass flux. The hatched area shows that the CFD model appears to be less sensitive to the particle diameter than the DEM model. In particular, the 14 mesh experimental data point still lies well outside the shaded area. Other variables, such as packing fraction or angle of internal friction, could be used to widen the shaded area, but these studies were only performed on a single particle diameter. Adding a wall boundary condition to a larger simulation domain could help reduce the mass flux somewhat. The model parameter that had the largest effect on simulation outcomes was the frictional pressure-viscosity coupling used. However, since two out of the six combinations produced oscillating results, and two

others produced simulations that didn't converge at all, the choice of method used in a simulation should be carefully studied to determine if it is generally applicable to the flow in question.

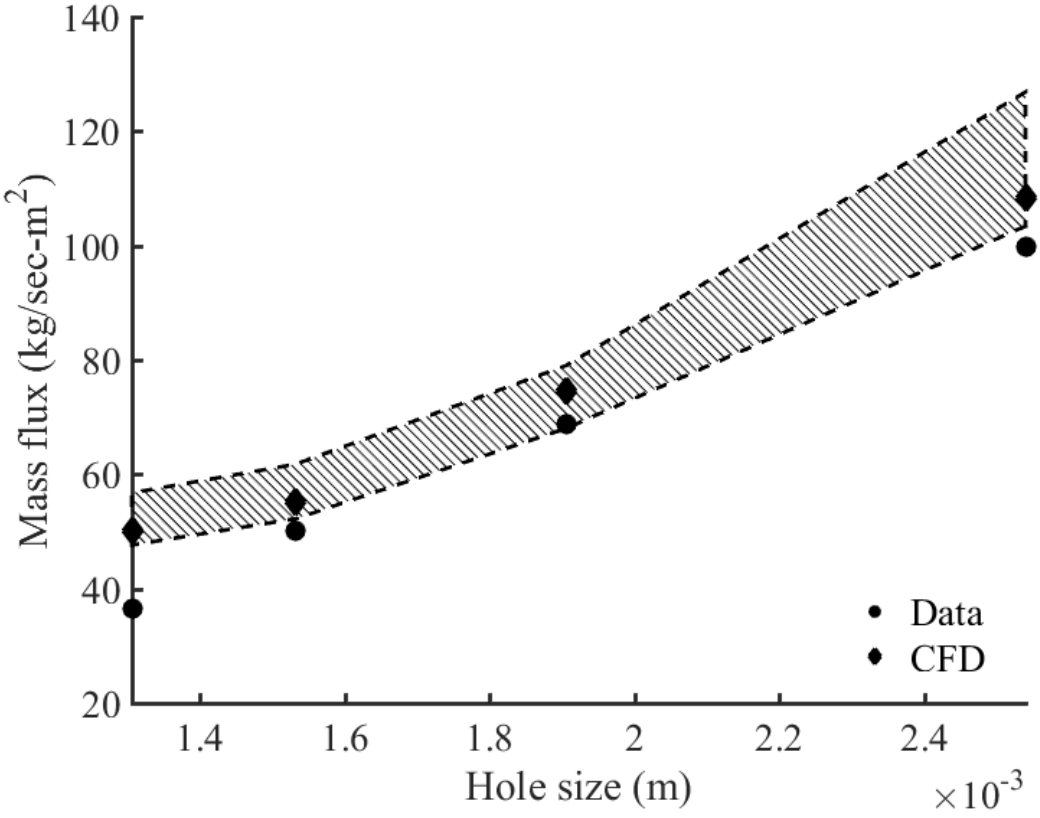

Figure 5.41: Sensitivity of mass flow rate on frictional pressure-viscosity model

5.2 Angled Mesh

5.2.1 Experimental Data

Similar to the horizontal mesh test section, the angle mesh test section was tested in a single spaced and double spaced configuration. Both ID50-K and ballotini 8 mil were used. The same configurations and materials were also modeled using DEM and CFD.

Figure 5.42 shows the mass flux results for the single and double spaced angled meshes using the ID50-K material. The error bars represent two times the standard deviation of the measured mass flux. The horizontal line represents the mass flux when solid metal plates were inserted in place of wire mesh screens. In this case, particles were only allowed to flow through the gaps between plates. These plates were relatively smooth pieces of steel, so the mass flux might be different when compared to a much rougher surface, such as a blinded mesh, or a plate made of a ceramic material. However, it could still be used to compare the relative amounts of flow that goes through an angled mesh as opposed to around it. Clearly, even the smallest mesh allows a relatively large amount of material to flow through it as opposed to around it, which is useful for developing a fairly uniform particle curtain in particle heating receivers for concentrated solar power applications. Compared to the mass flux plot for the horizontal mesh screens (see figure 5.1, it is clear that the error bars are generally wider. Despite the fact that the angled mesh sections do not span the entire width of the flow path, a linear and power law fit were again applied to the angled mesh test section. For the angled mesh configuration, the linear fit was $y = 35000x + 18.15$ and the power law fit was $y = -2.83e^{-6}x^{-2.53} + 113.6$. For the double mesh configuration, the linear fit is $y = 42000x + 2.83$ and the power law fit is $y = -9.93e^{-7}x^{-2.71} + 114.3$ The linear fit does not capture the drop off in flow as the mesh hole size decreases; the power law fit provides a much better relationship over the entire range.

Figure 5.43 shows the experimental mass flux for the single and double spaced angled mesh configuration using the ballotini material. Once again, a power law fit does a better

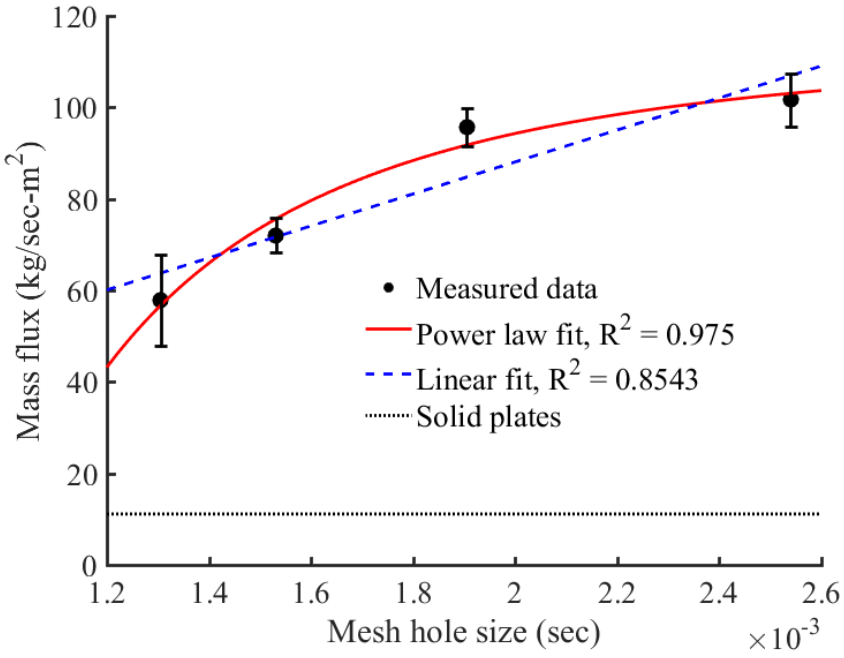

(a) Single spaced configuration

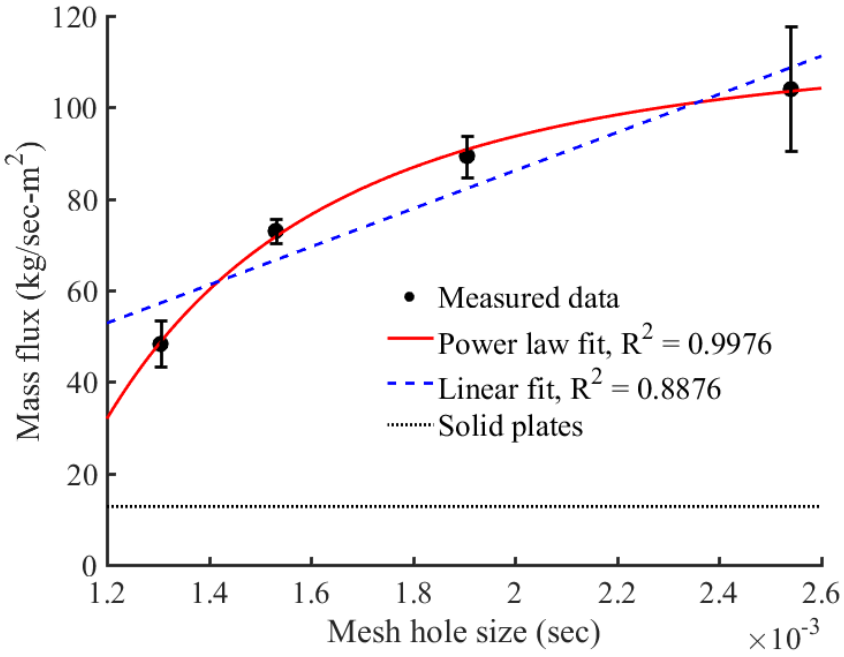

(b) Double spaced configuration

Figure 5.42: Experimental mass flux rates for the ID50-K material, angled mesh configuration. The horizontal line represents the mass flux when solid plates are inserted in place of the wire meshes.

job of describing the data than a linear fit, although the curvature isn't as strong as with the ID50-K material. This is likely due to the smoother, smaller diameter particles being able to more easily flow through a given mesh hole size. The solid plate mass flux is nearly the same for both materials (approximately 10 kg/sec-m^2). For the single spaced configuration, the linear fit is $y = 63800x + 20.8$ and the power law fit is $y = -11.67x^{-0.485} + 391.1$. For the double spaced configuration, the linear fit is $y = 90700x + 6.02$ and the power law fit is $y = -376x^{-0.1628} + 1227$. It is unknown why the error bar associated with the 8 mesh single spaced data point is so much larger than the other points, as nothing strange was noted during the experiment.

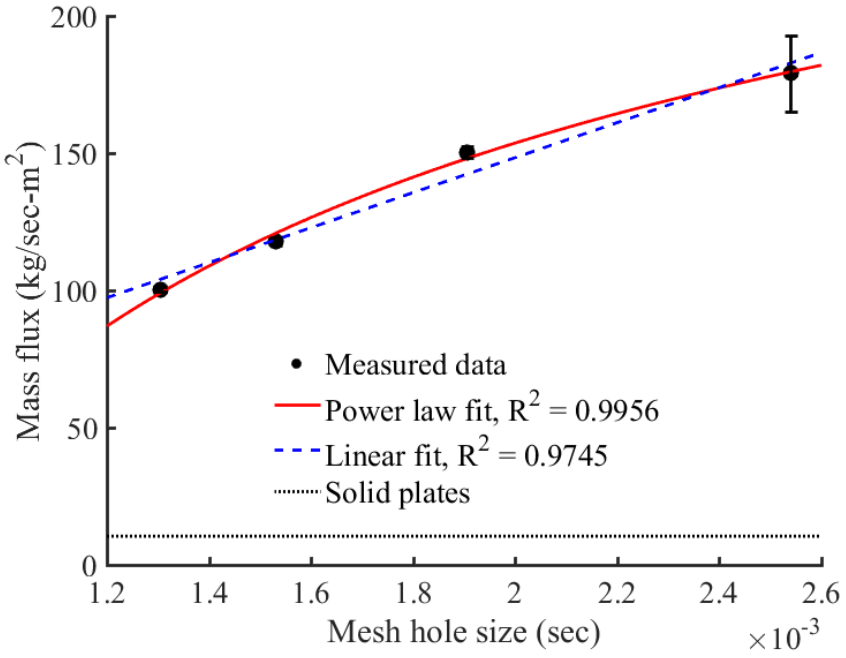

(a) Single spaced configuration

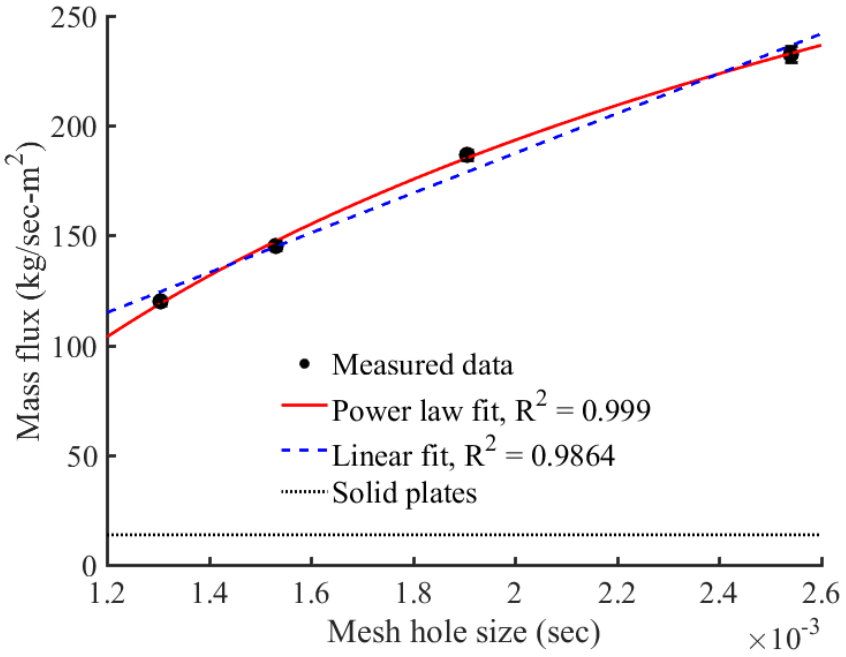

(b) Double spaced configuration

Figure 5.43: Experimental mass flux rates for the ballotini material, angled mesh configuration. The horizontal line represents the mass flux when solid plates are inserted in place of the wire meshes.

Figure 5.44 shows the steady state volume fraction of the single and double spaced angled mesh test sections for the ID50-K and ballotini materials. While there does not appear to be any significant trends for a given configuration, the trends for different spacings appear to match up fairly well. The ballotini material exhibits a much larger volume fraction than the ID50-K material. This is likely due to the better flow properties of the material, as it can more easily flow through a given size mesh opening.

Figure 5.45 shows a raw video frame from the single spaced angled mesh test section, and figure 5.46 shows the vector field from the PIV analysis of this frame. The red areas represent areas that were excluded from the PIV analysis. Due to the large slots in the face of the test section that were in the image frame, it was likely that these areas would produce excess amounts of zero vectors.

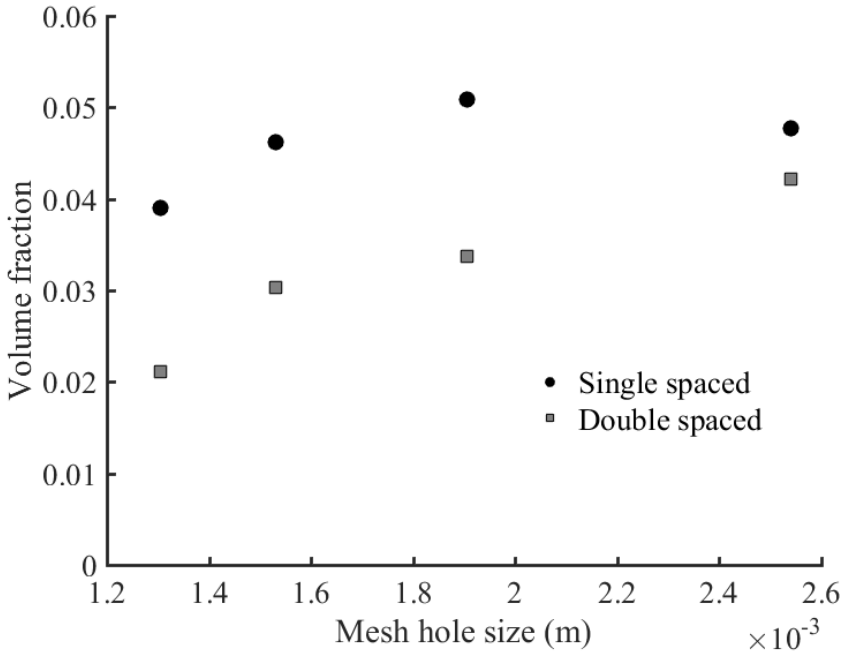

(a) ID50-K material

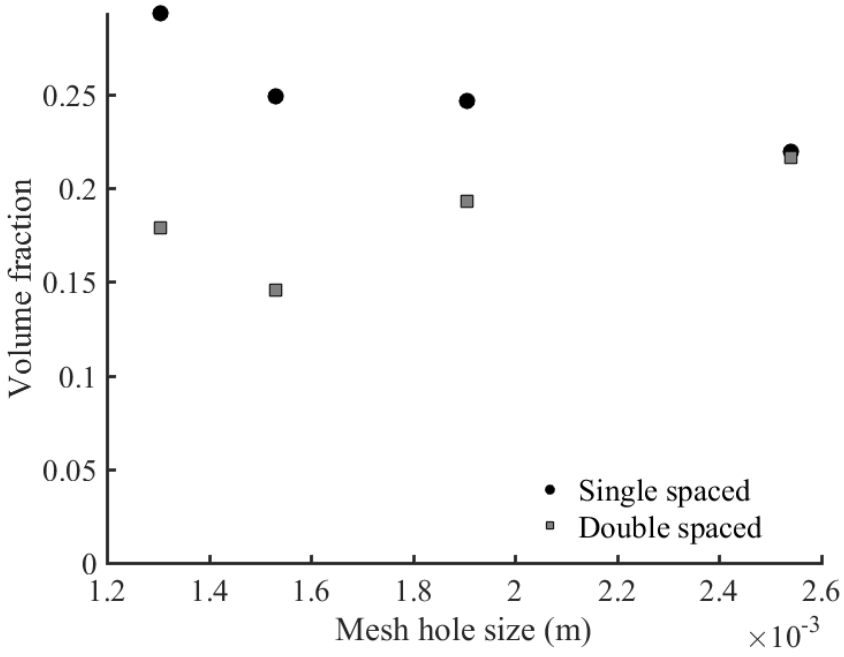

(b) Ballotini material

Figure 5.44: Experimental volume fraction for the angled mesh configuration.

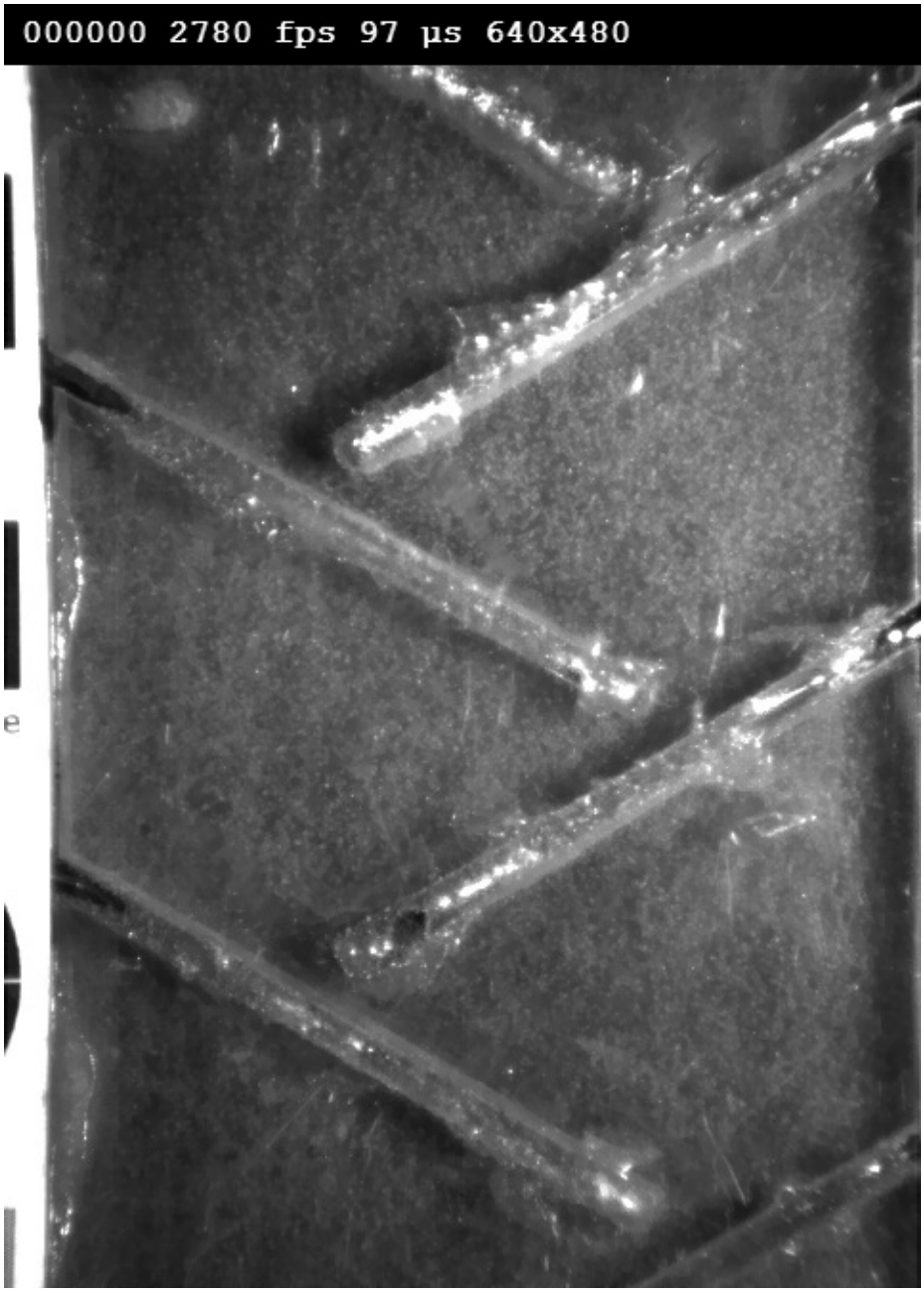

Figure 5.45: Raw video frame, ID50-K material, single spaced angled meshes. As indicated at the top, the camera was shooting 2780 frames per second, with an exposure time of 97 microseconds, capturing an image that was 640 by 480 pixels in size.

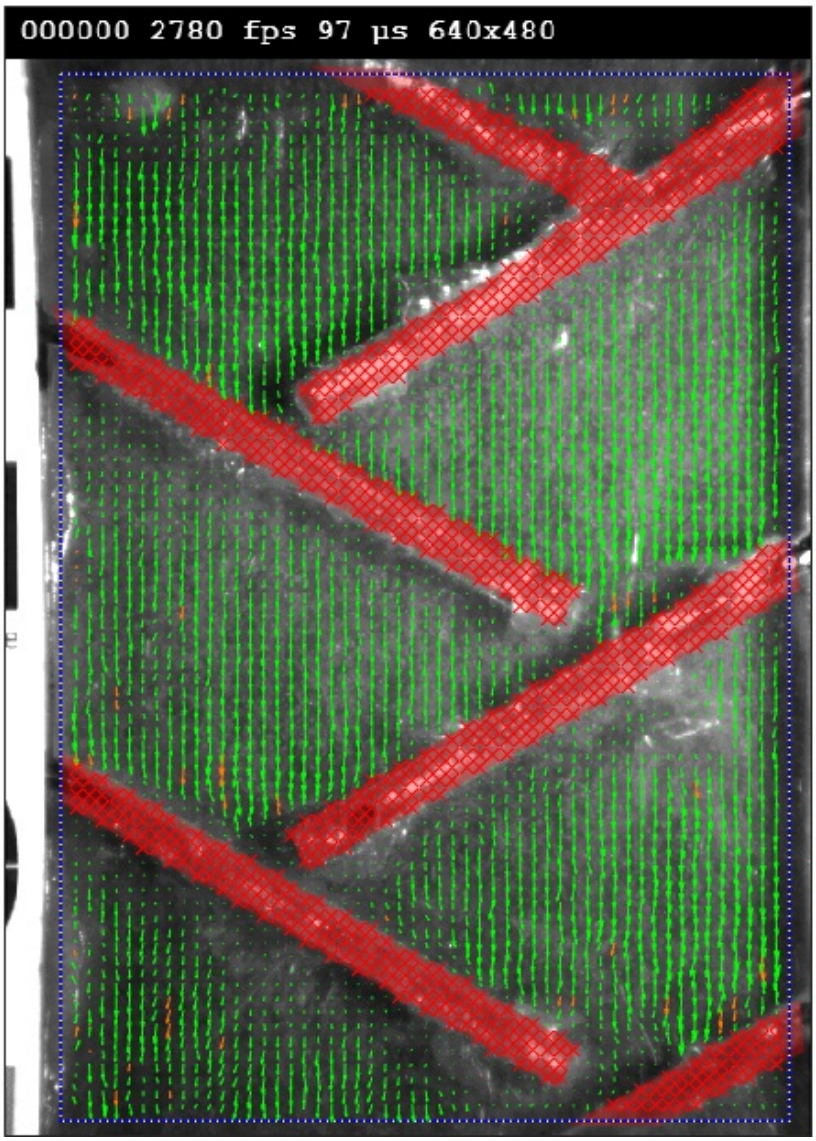

Figure 5.46: Vector field from PIV analysis of single spaced angled mesh configuration, ID50-K material. The red represents areas that aren't used in the PIV analysis as they contain large stationary features that would produce excess zero vectors.

Figure 5.47 shows a comparison of the single spaced and double spaced PIV data for the vertical velocity component, compared to the theoretical maximum velocity for a given mesh spacing. These histograms have a much more gentle slope to the right hand side when compared to the same histogram for the horizontal mesh test section as seen in figure 5.7. This is likely due to the larger viewing area of the angled mesh test section allowing a larger PIV analysis window, and thus enabling more velocity vectors at different locations to be calculated. Both histograms trail off very close to their respective theoretical maximum velocities.

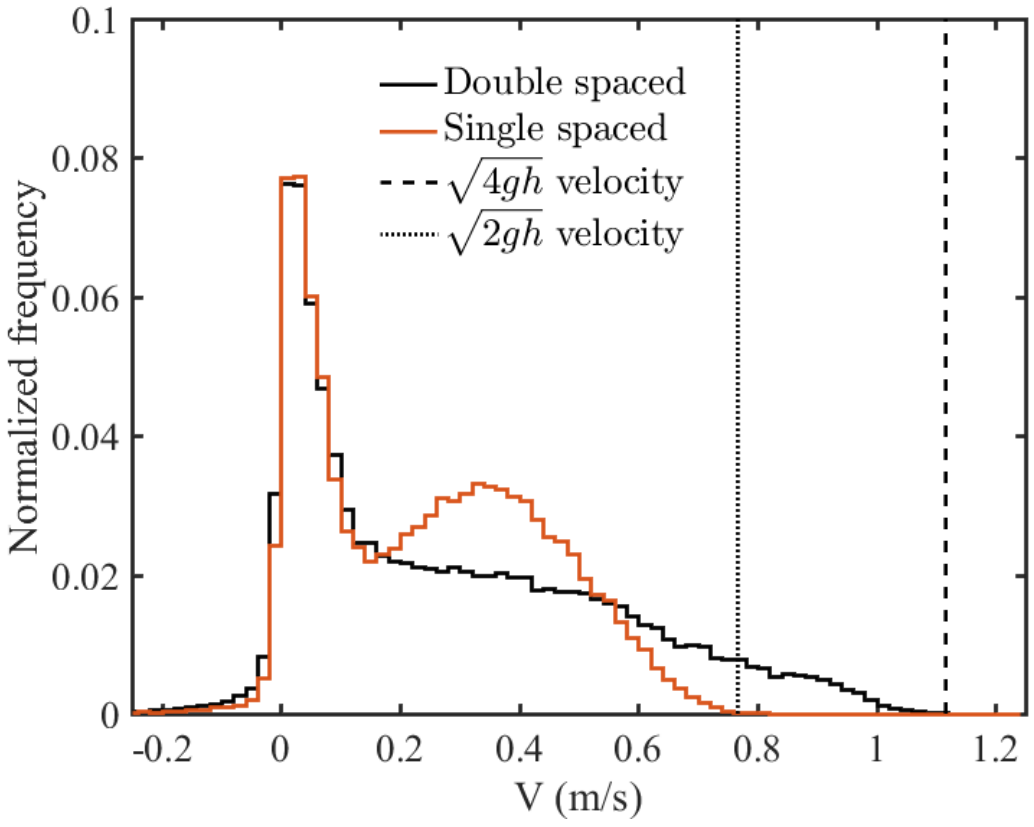

Figure 5.47: A comparison of the single spaced and double spaced vertical velocity histograms, angled mesh test section. Downward velocity is positive.

5.2.2 Numerical Models

Figure 5.48 shows the experimental and numerical mass flux for single spaced and double spaced angled mesh configuration using the ID50-K material. The DEM model does a better job of predicting the mass flux compared to the CFD model. Both models appear to fail to recreate the concave down nature of the experimental data. This could be an artifact of using a mono-dispersed particle in the numerical models.

Figures 5.49 shows the experimental and numerical mass flux for the single and double spaced angled mesh configuration using the ballotini material. In contrast to figure 5.48, the CFD model appears to better predict the mass flux than the DEM model. Curiously, the 14 mesh geometry has a higher mass flux than the 12 mesh geometry. While the exact cause of this discrepancy is unknown, a contributing factor could be the end separation between successive screens. The geometry used in the numerical models always has a closed cell at the end of a given mesh, which is always the same distance away from the next nearest wire screen. Due to the different mesh sizes, none of the angled mesh arms are exactly the same length in the numerical models. The separation between the end of one mesh and the face of the next mesh for the 14 mesh section is 4.87 mm, while it is 4.66 mm for the 12 mesh geometry. As the hole sizes get smaller, these end gaps start to contribute more to the overall mass flux. This level of geometric control was not possible using hand cut wire mesh screens in the experimental test section, and so any effect this had on the experimental test section is impossible to determine. This flow feature was not duplicated in the DEM model. The DEM model also appears to maintain the overall curvature of the experimental data better.

As with the horizontal test section, the average volume fraction was measured for the angled mesh test section, and compared to the volume fractions obtained in the numerical models. Figure 5.50 shows the volume fraction for the single and double spaced angled mesh geometry for the ID50-K material. Both numerical models show a higher volume fraction than the experimental values. This is again likely due to the numerical models

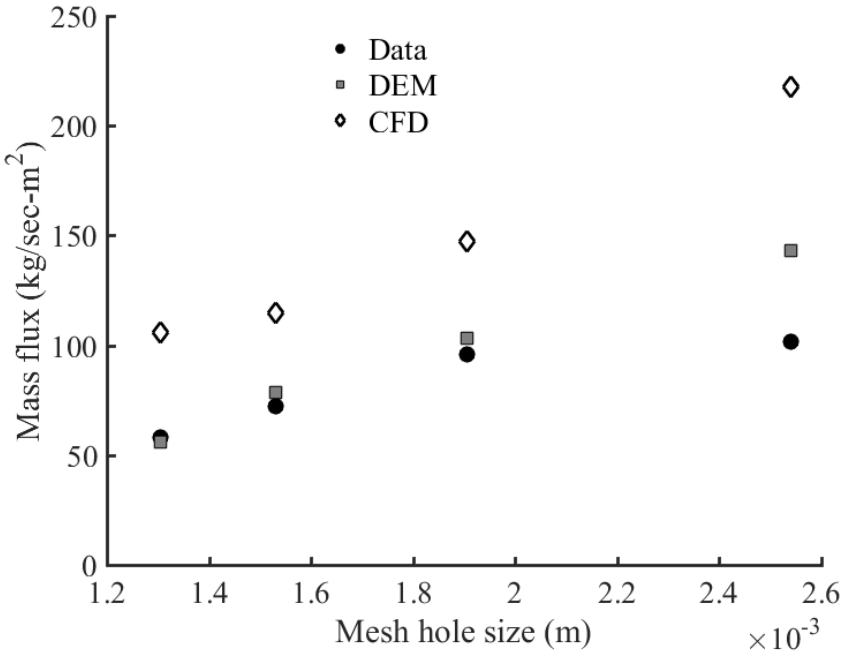

(a) Single spaced configuration

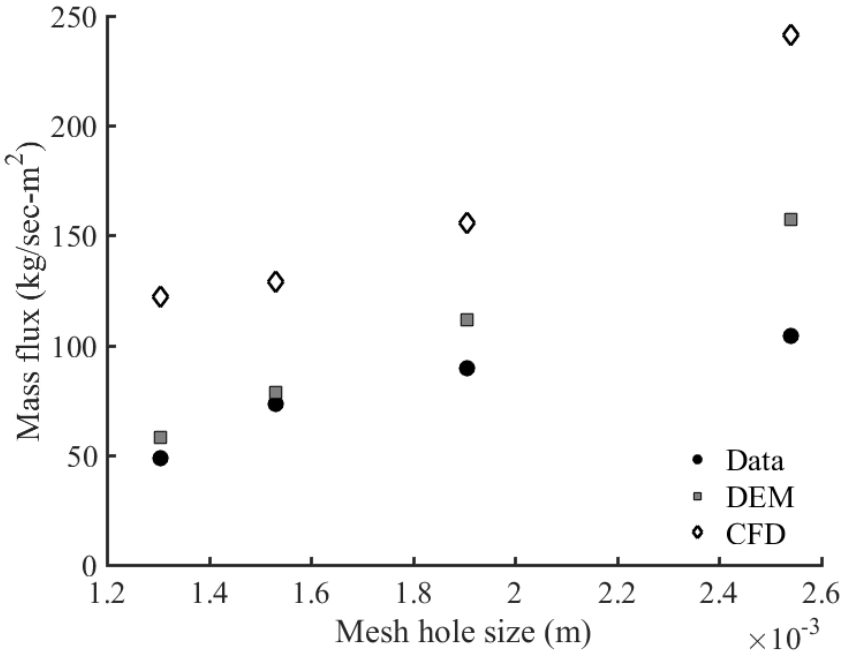

(b) Double spaced configuration

Figure 5.48: Experimental and numerical mass flux for the angled mesh configuration, ID50-K material.

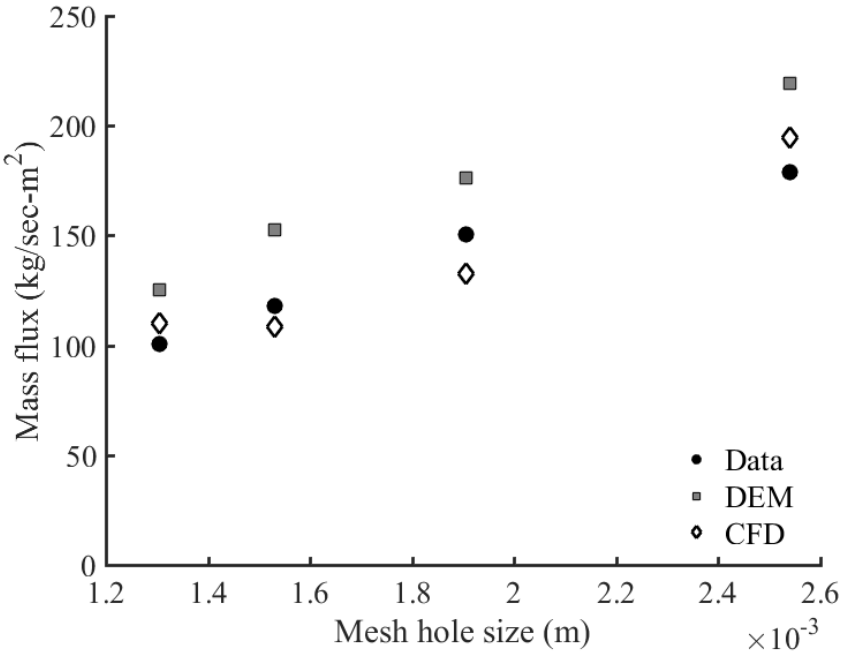

(a) Single spaced configuration

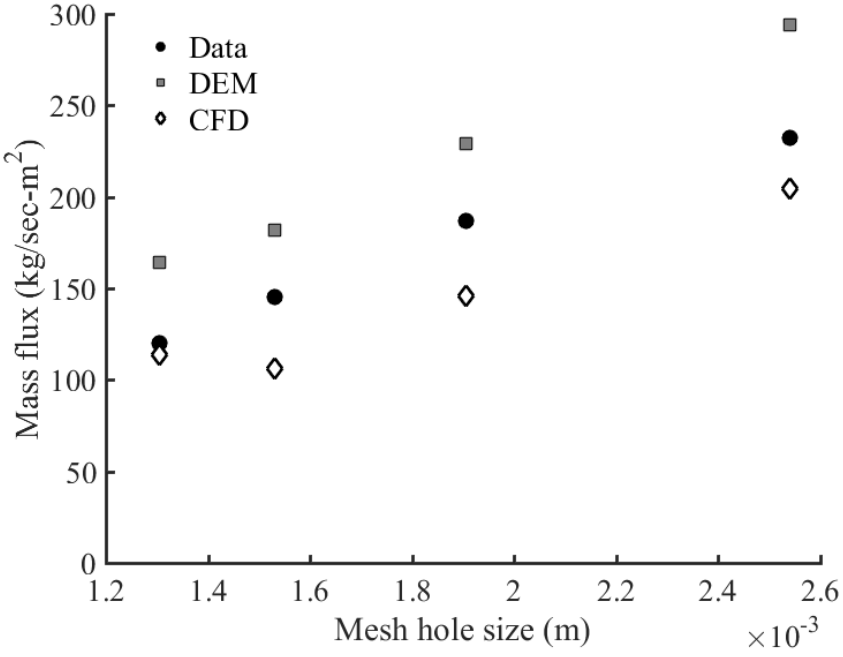

(b) Double spaced configuration

Figure 5.49: Experimental and numerical mass flux for the angled mesh configuration, ballotini material.

being much shorter in the vertical direction than the experimental test section. Because of this, the numerical models were much closer to the entrance region of the geometry than the test section. While this could be tested, it would require a larger number of particles for the DEM model, and a much larger number of cells for the CFD model, resulting in larger computational times. The DEM model appears to better predict the raw number for most cases, while the CFD model appears to better predict the overall trend of the experimental data. As with the horizontal mesh data, the error bars represent a 95% confidence interval for the measured data. The systematic uncertainty from the discrepancy in the total wet volume of the test section is again typically the same order of magnitude as the random error present in the measurement.

Figures 5.51 through 5.54 show snapshots of the DEM and CFD models for the single and double spaced angled mesh test section using the ID50-K material. The single spaced models show a gradual decrease of accumulation on the wire mesh screens, which was observed in the experimental test section. There likely aren't enough screens in the double spaced models to observe a similar decrease.

Finally, experimental PIV data was compared to the numerical models. Figure 5.55 shows a comparison of the vertical velocities of the experimental and numerical models for both the single and double spaced configurations using the ID50-K material. The difference in clustering around the zero peak is likely due to the PIV analysis being unable to fully resolve the small displacements associated with low velocities, making the peak narrower. It could also be due to more accumulation on meshes in the numerical models than in the experimental results, resulting in wider peaks. All three histograms trail off to about the same maximum velocity.

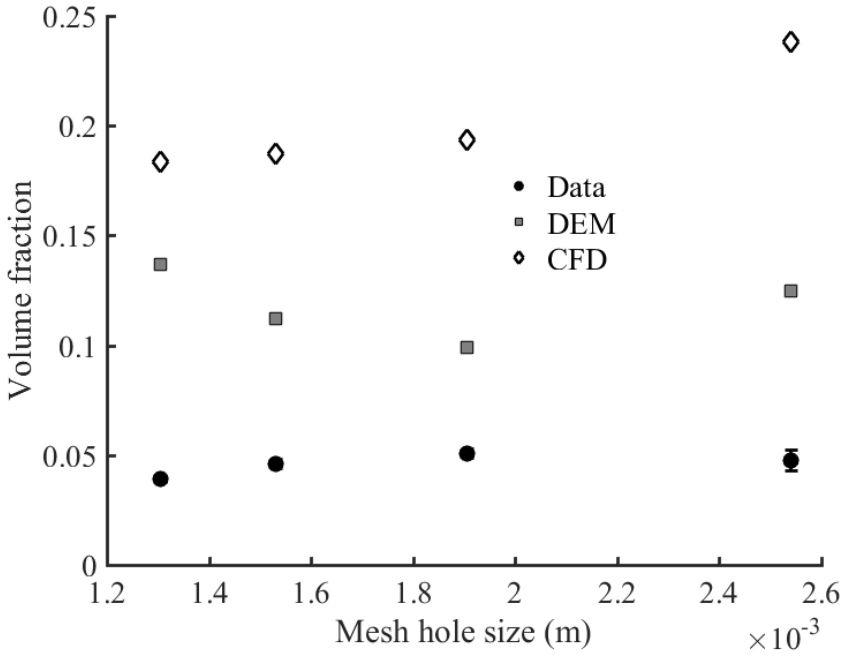

(a) Single spaced configuration

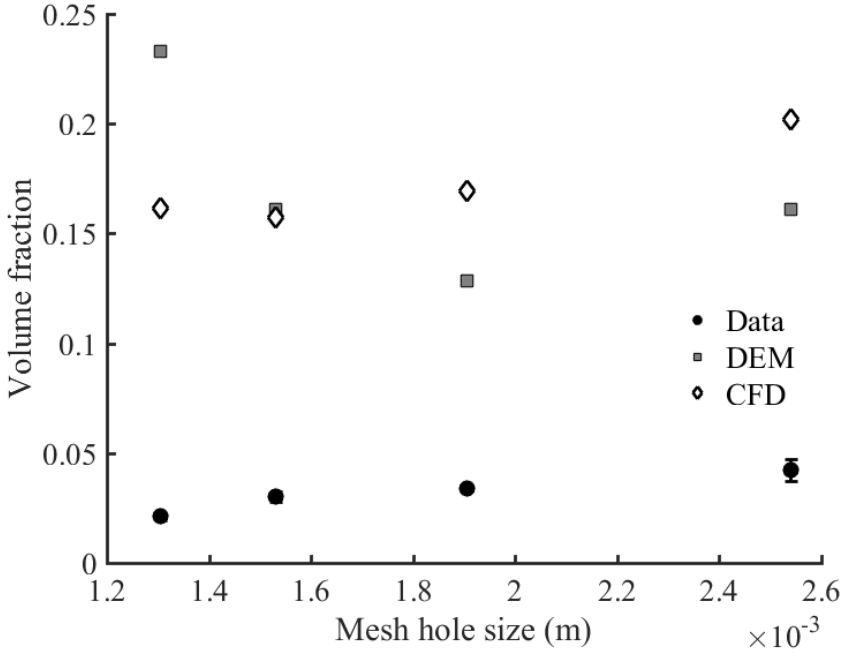

(b) Double spaced configuration

Figure 5.50: Experimental and numerical mass flux for the angled mesh configuration, ID50-K material.

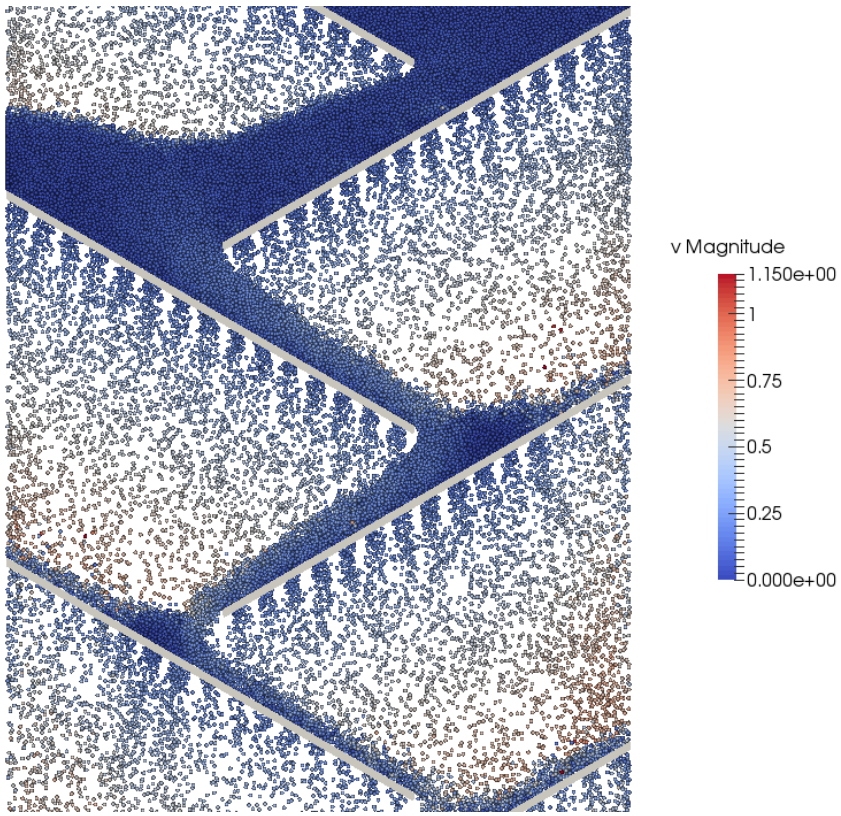

Figure 5.51: DEM model of single spaced angled mesh configuration, ID50-K material. The particles are colored by overall velocity magnitude.

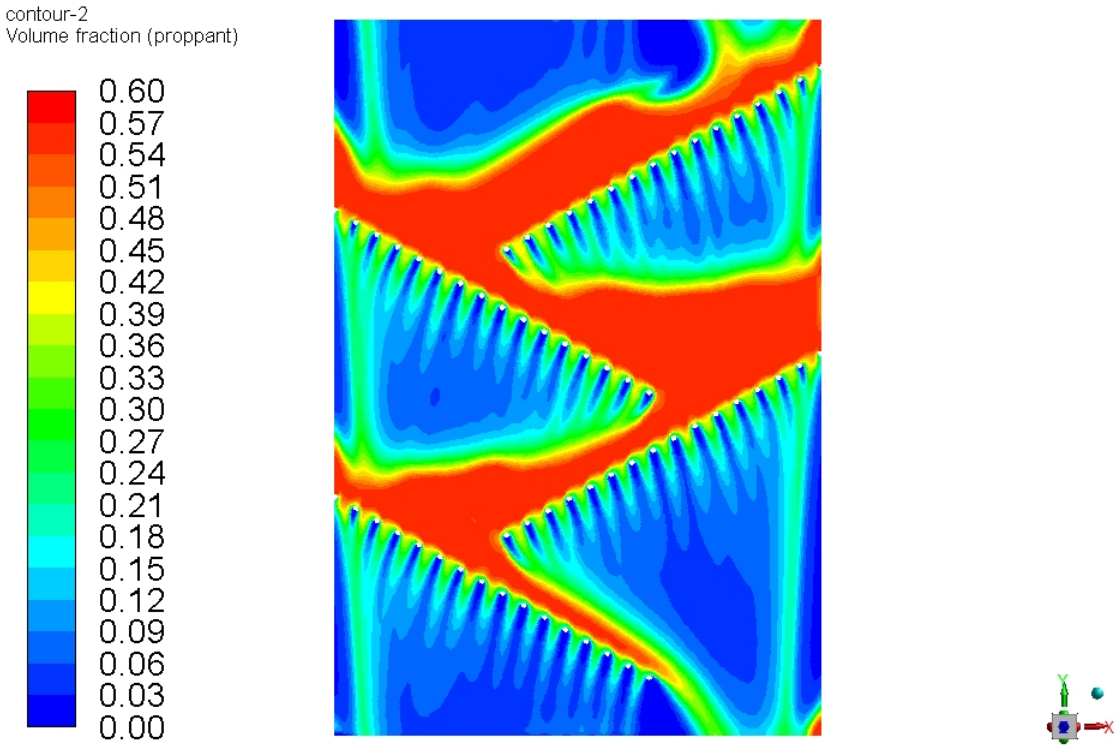

Figure 5.52: CFD model of single spaced angled mesh configuration, ID50-K material. The geometry is colored by overall volume fraction.

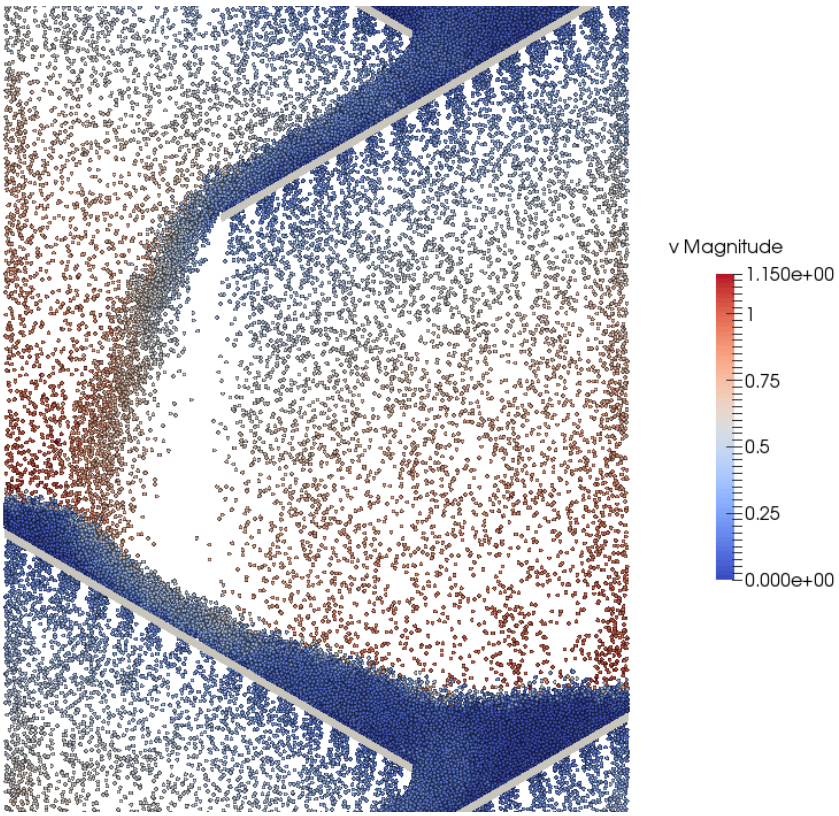

Figure 5.53: DEM model of double spaced angled mesh configuration, ID50-K material. The particles are colored by solids velocity magnitude.

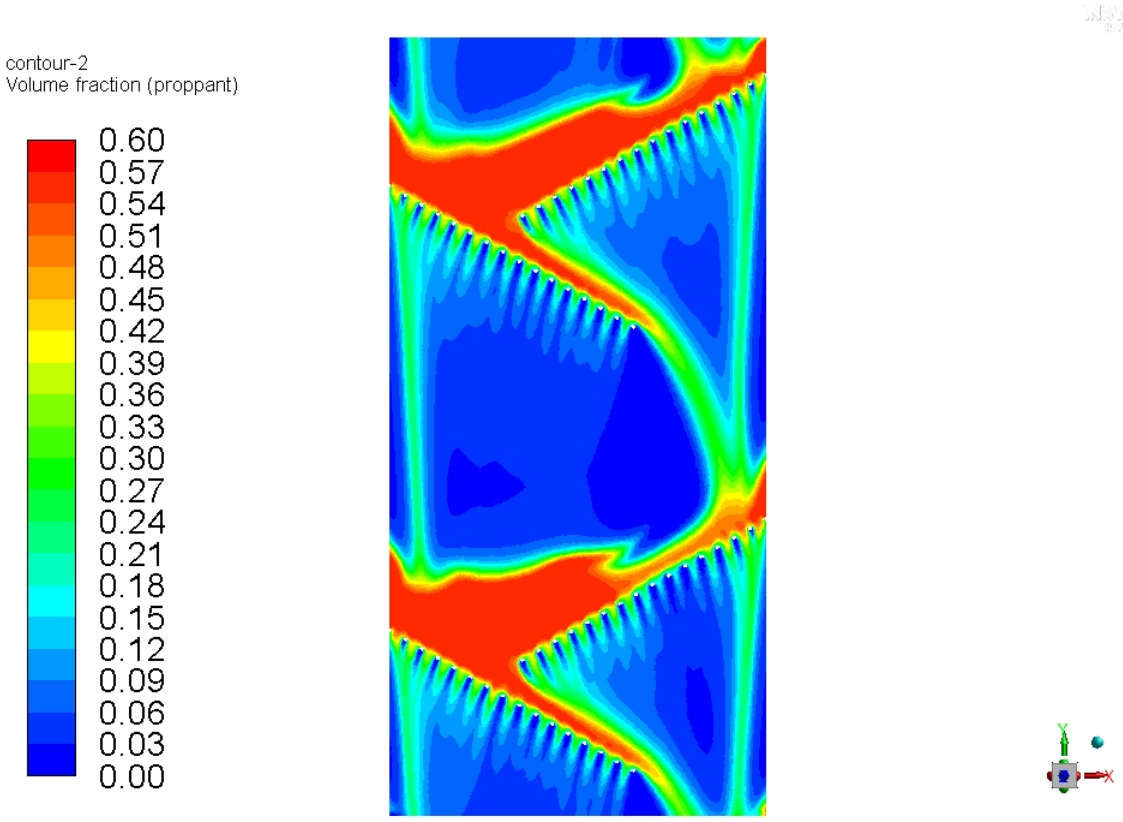

Figure 5.54: CFD model of double spaced angled mesh configuration, ID50-K material. The geometry is colored by solids volume fraction.

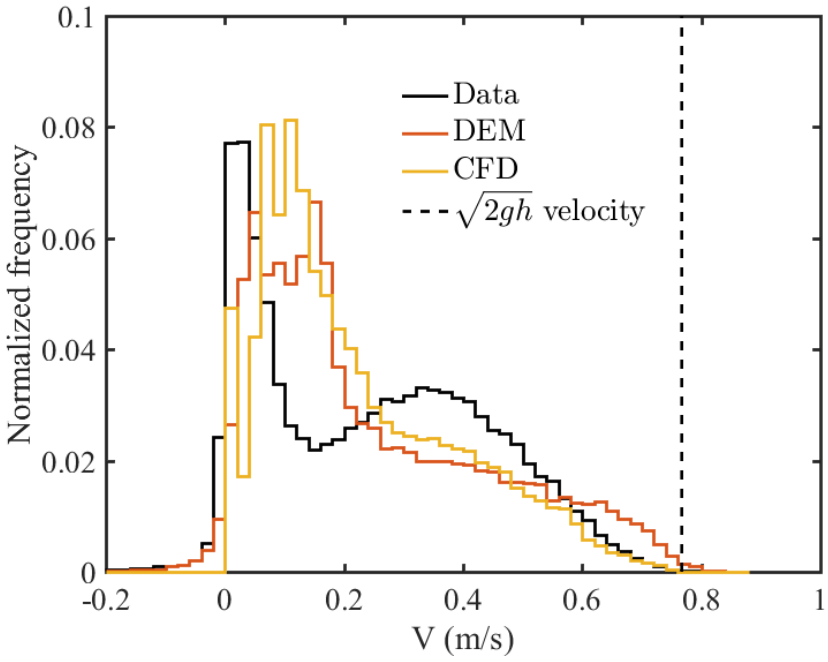

(a) Single spaced configuration

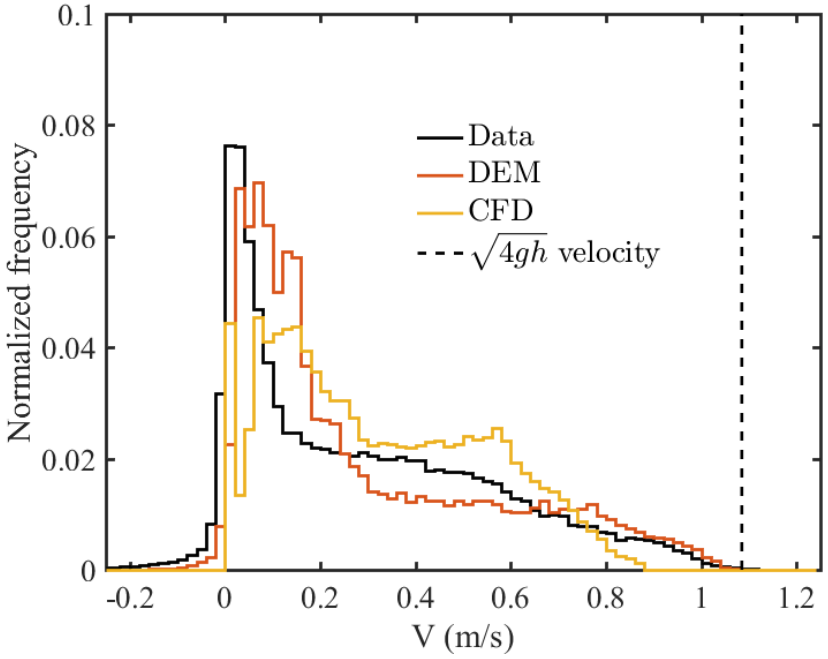

(b) Double spaced configuration

Figure 5.55: Experimental and numerical volume vertical velocity histograms for the ID50-K material, angled mesh configuration.

5.3 Square Tube

5.3.1 Experimental Data

For the square tube test section, there were two basic variables (apart from the different materials): the spacing between the squares, and whether the squares were whole or had a slot cut in the bottom of them. Figure 5.56 shows the mass flux through the square tube test section with various spacings through both whole and slotted squares. The relative similarity of the mass flux between whole and slotted squares hints at fact that the mass flux is mostly determined by the first "orifice" the granular flow encounters. The slots help prevent particle accumulation inside the squares, but since they are underneath the top face of the squares, they are only redistributing the flow they receive from above, rather than adding to it. Topologically, the slotted squares are identical to the angled meshes. It is unknown why the smallest whole square configuration flowed more than the next largest spacing with the ID50-K material. This could be due to poor geometric control of the test section. There is also the possibility that if the squares get close enough, the flow through the holes of one square into the next is enhanced because it does not have to fight through as much flow through the gaps between the squares, thus leading to a higher flow. While this might be hard to verify experimentally, the gaps between the squares could be eliminated, leading to flow only through the holes in the faces of the squares. Another method might be to somehow isolate the flow in the channels as compared to through the holes. Taping over the holes would test the former; the latter might be accomplished by blocking the slots in the first row of squares, and then using washers, straws, or some other means to contain the flow between squares to only what flows through the holes.

One of the primary motivations to testing the square tube configuration was to see if the holes would produce well defined jets within the square tubes. If this could be accomplished, it would be conceivable to essentially create a uniform curtain of particles within each square, enabling fairly uniform heating of the particles while being able to use a stur-

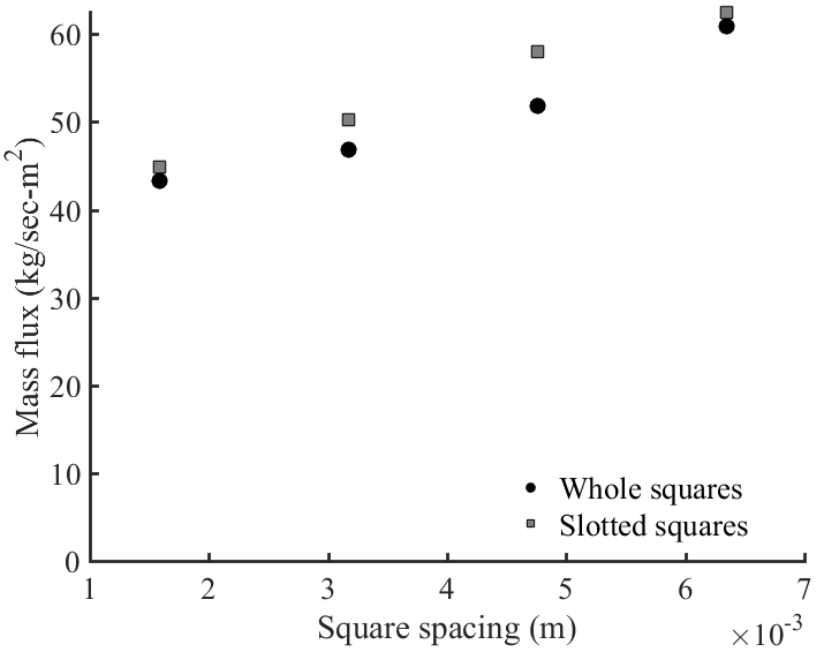

(a) ID50-K material

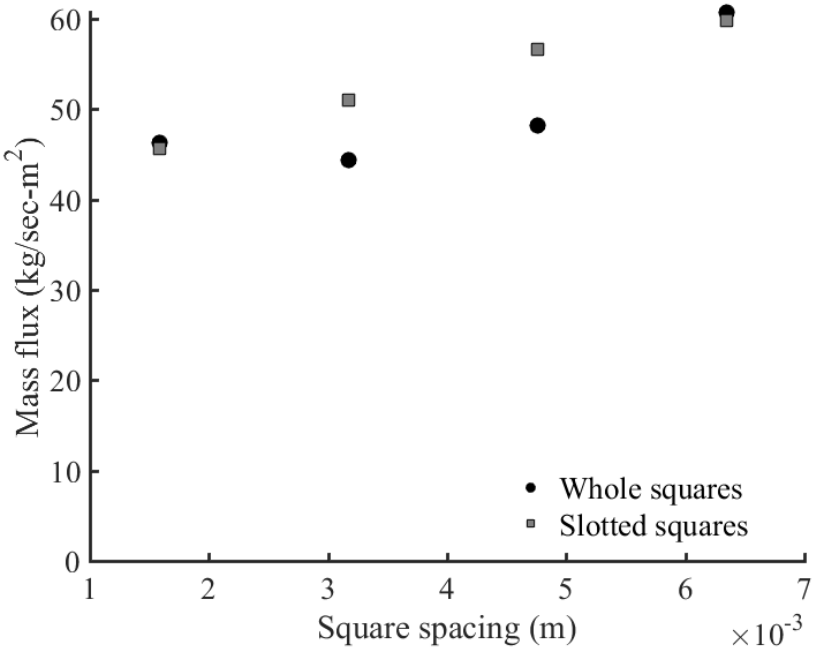

(b) Ballotini material

Figure 5.56: Experimental mass flux for the square tube test section.

dier flow obstruction than wire mesh screens. Figures 5.57 and 5.58 show video frames using ID50-K for both the whole and slotted square tube test sections respectively. Not only are there clearly defined jets of material for each hole, but the difference in particle accumulation is easily visible. There is also a visible difference in the amount of flow between squares. This is likely due to the slotted squares having less material with in them to contribute to the flow between the squares. Due to the highly non-uniform flow through the square tube test section, coupled with large areas of stagnant material for the whole squares, PIV analysis was not performed for this test section. Similarly, average volume fractions were measured, but due to the very non-uniform flow through the test section, this data not as useful as the data obtained with the wire mesh screens, and is not reported here.

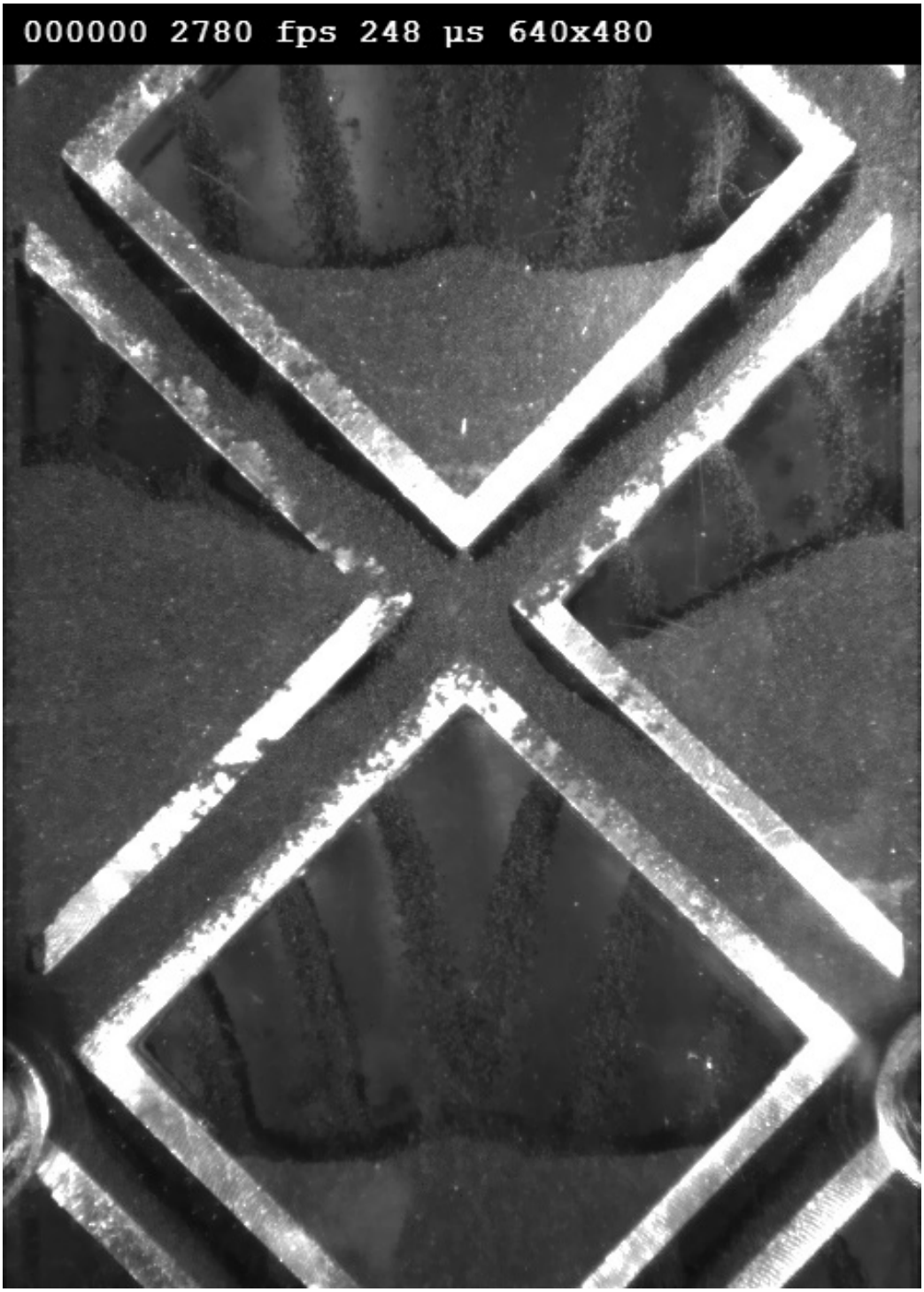

Figure 5.57: Raw video frame, square tube test section, 6.35 mm spacing, ID50-K material.

Figure 5.58: Raw video frame, slotted square tube test section, 6.35 mm spacing, ID50-K material.

5.3.2 Numerical Models

Numerical models were only developed for the 6.35 mm spacing configuration using the ID50-K material, as the DEM model would have required a relatively large number of particles for the ballotini material. Thus, trends for different spacings and materials were not developed for this study. Figure 5.60 shows the comparison of mass flux for the experimental and numerical models. While both numerical models over-predict the mass flux, the most striking feature of the plot is the difference between the whole and slotted tube mass flux for the CFD model. This lead to the creation of the "CFD dense" model. Starting with the results from the grid independence study of the horizontal wire mesh screens, it was assumed that the default mesh used for the square tube CFD model was not quite grid independent, and that a denser mesh would lead to a lower mass flux. To keep the element count reasonable, the mesh density was increased in the holes, the channel between the squares, and the slots in the case of the slotted tube model, as it thought that these higher velocity areas would influence the flow more. Similarly to the wire mesh models, the mesh density was increased until the individual cells were around the same size as the individual particles. Figure 5.59 shows the change in the mesh density between the default and the dense models. As seen in figure 5.60, this had very little effect on the mass flux. While this could indicate that the default mesh density is already fairly close to grid independence, it still does not offer an explanation to the increased mass flux. The overall element size in the default model is much larger than in the wire mesh models, likely owing to the larger geometric features present in the square tubes.

Figures 5.61 through 5.64 show snapshots of the DEM and CFD models of the whole and slotted square tubes. Both models exhibit good qualitative agreement with the experimental test section, with clearly defined jets below the holes, varying levels of flow between the squares, and much less accumulation in the slotted squares compared to the whole squares.

A velocity analysis and volume fraction comparison were not performed for the numeri-

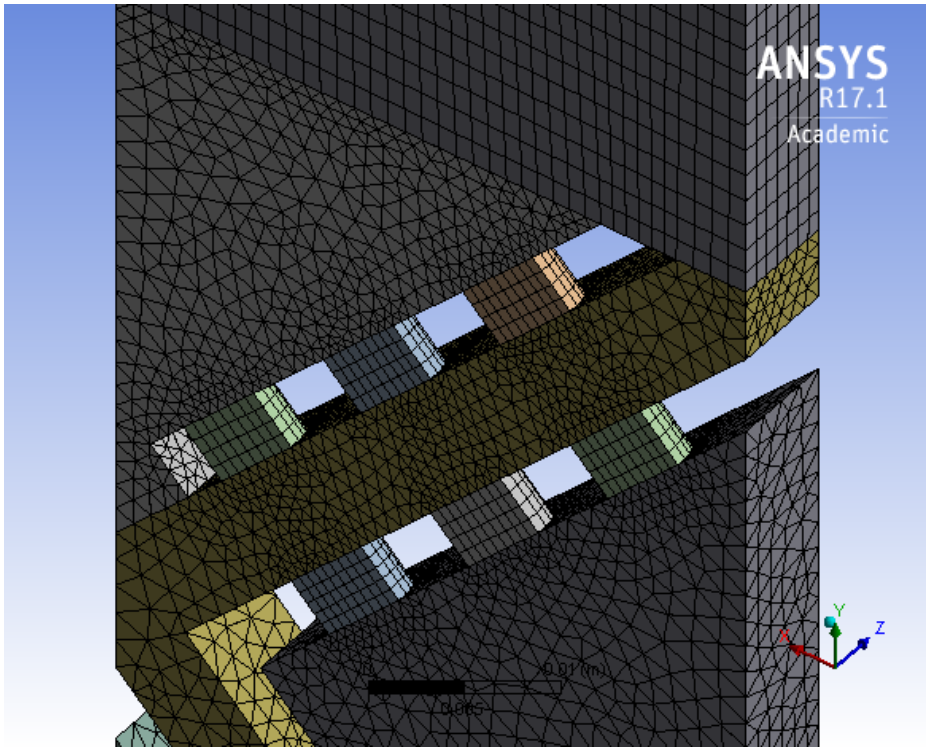

(a) Default slotted square tube mesh

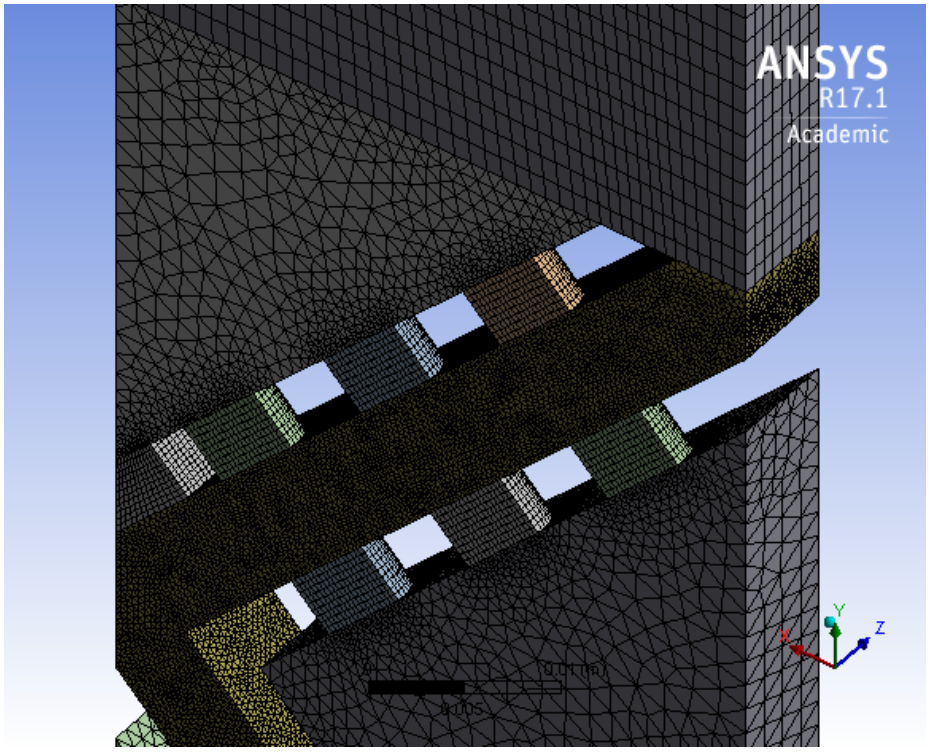

(b) Dense slotted square tube mesh

Figure 5.59: Detail of default and dense slotted square tube mesh used in CFD simulation.

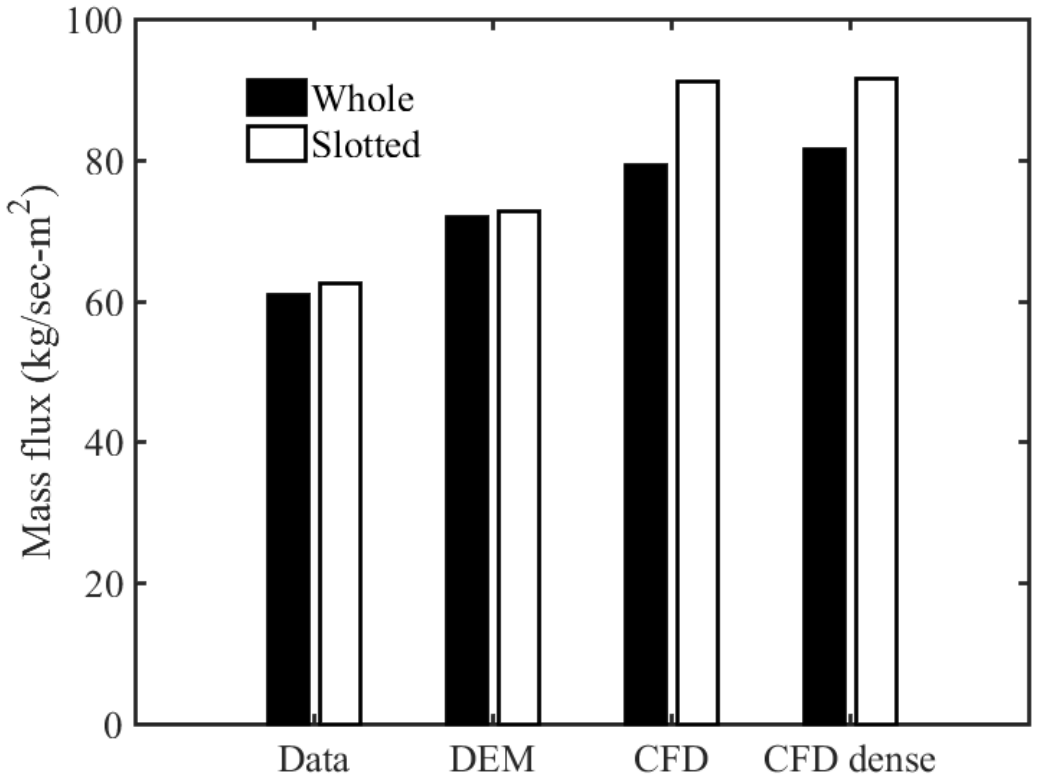

Figure 5.60: Comparison of mass flux of square tube test section, 6.35 mm spacing, ID50-K material.

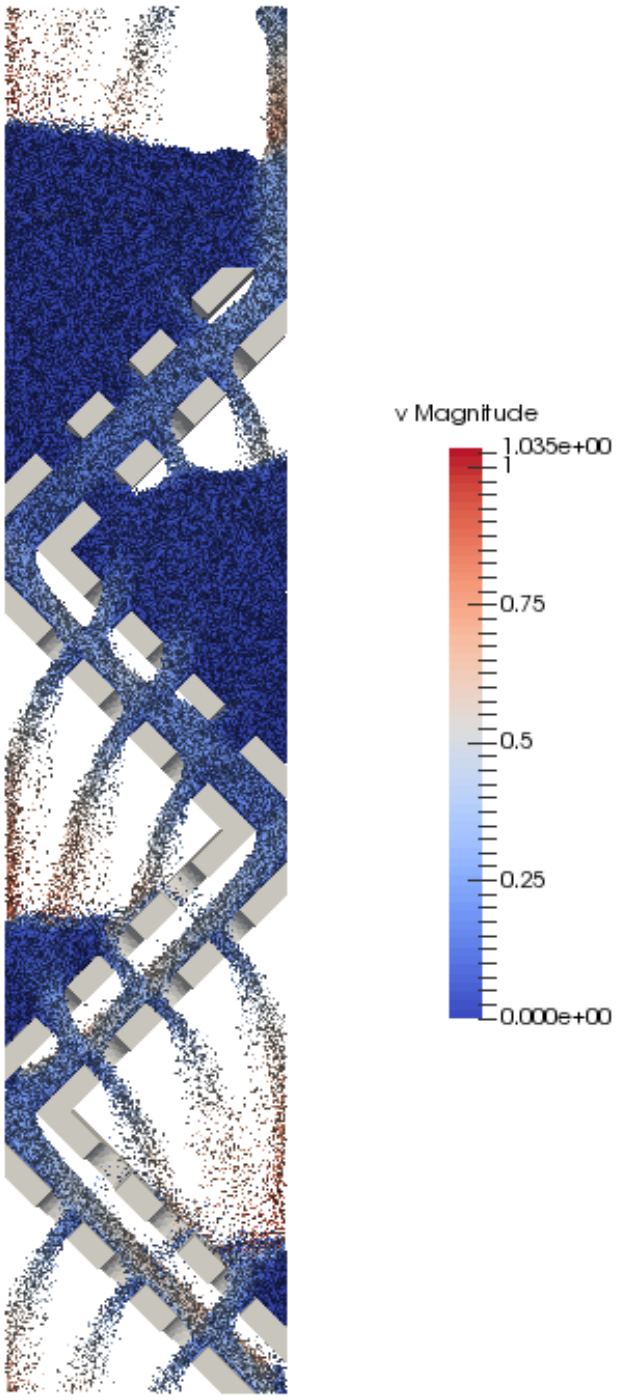

Figure 5.61: DEM model of square tube test section, 6.35 mm spacing, ID50-K material. The particles are colored by velocity magnitude.

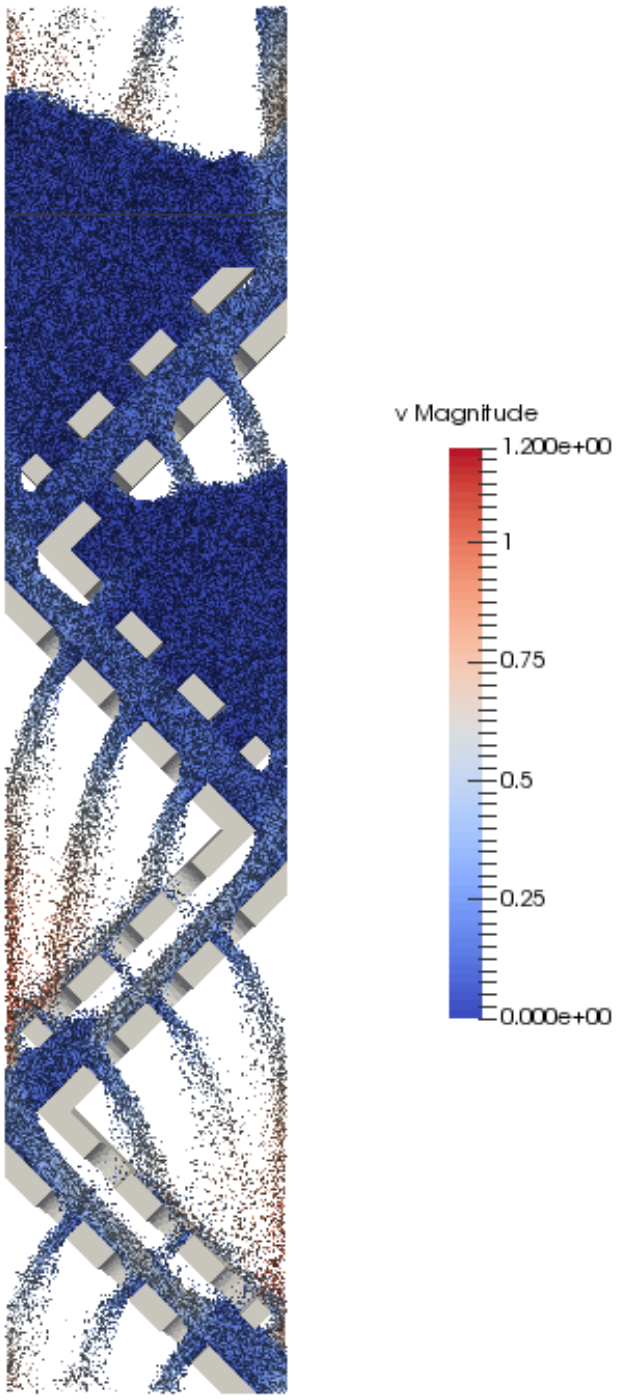

Figure 5.62: DEM model of slotted square tube test section, 6.35 mm spacing, ID50-K material. The particles are colored by velocity magnitude.

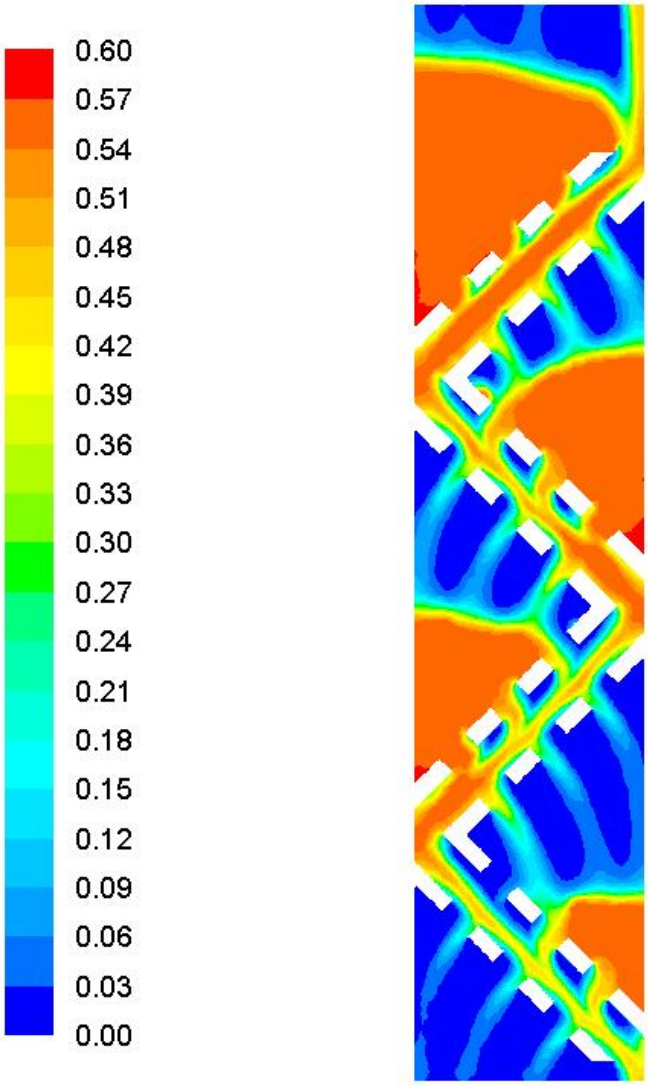

Figure 5.63: CFD model of square tube test section, 6.35 mm spacing, ID50-K material. The geometry is colored by volume fraction.

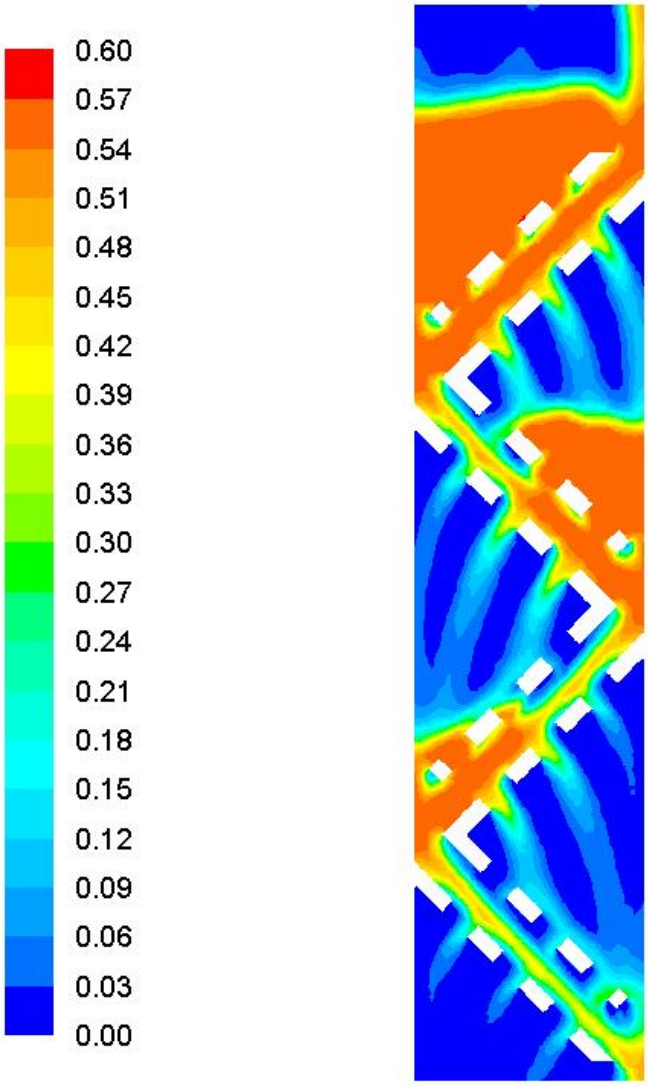

Figure 5.64: CFD model of slotted square tube test section, 6.35 mm spacing, ID50-K material. The geometry is colored by volume fraction.

cal models due to the highly non-uniform flow within the models. These may be performed in a future study. However, due to the results from the wire mesh test sections, it is assumed that a velocity analysis would agree fairly well to the experimental data, while the volume fraction comparison would likely suffer from a short test section.

5.4 Perforated Plate

5.4.1 Experimental Data

Owing to the qualitative success of the square tube test section, pieces of perforated plate were bent into squares to see if the idea of creating jets would carry over onto a material with a much larger total open area (in other words, the perforated plate may be seen as the limit when many holes are drilled in the face of a square tube). Three different sized perforated plates were used, but only the 6.35 mm spacing was tested. Once again, whole and slotted squares were used. Figure 5.65 shows the mass flux results for the ID50-K and ballotini material respectively. Despite the 5/32 in plate having the highest open area, it did not have the highest mass flux. In this case, the mass flux is likely a function of hole size and percent open area. As with the square tube test section, the slotted perforated plate squares had roughly the same mass flux as the hole squares, although the slotted square configuration consistently allows the ballotini material to have a higher mass flux.

Figures 5.66 and 5.67 show video frames of the whole and slotted perforated plate test section. As with the squares, the jets of material and different levels of accumulation are easily noticeable.

An interesting feature of the slotted perforated plate squares was the increase in entrance length as opposed to the solid aluminum squares. Figures 5.68 and 5.69 show wide shots of the slotted square tube and perforated plate test sections respectively. While the slotted aluminum squares become empty relatively quickly in the test section, the slotted perforated plate squares maintain a high level of material until near the bottom of the test section. There is the possibility that the perforated plate squares only become empty due

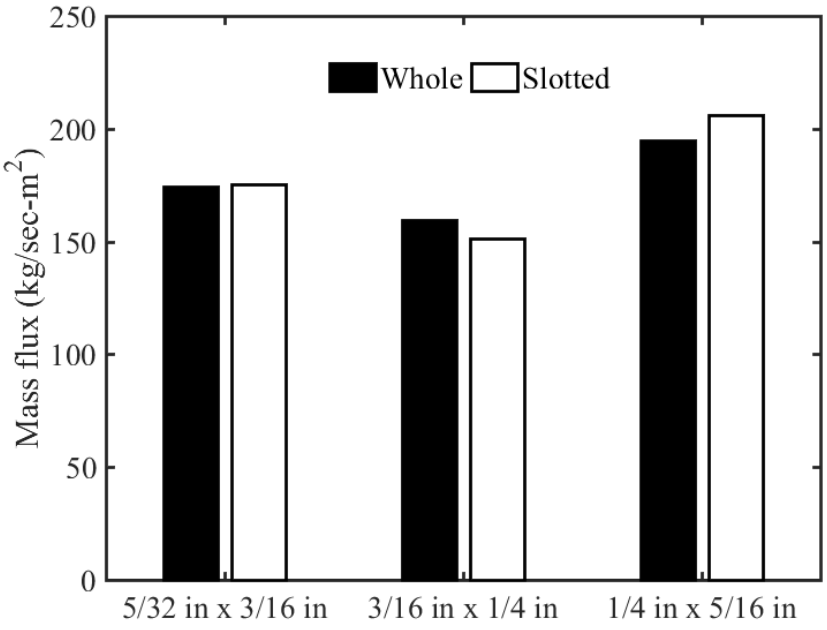

(a) ID50-K material

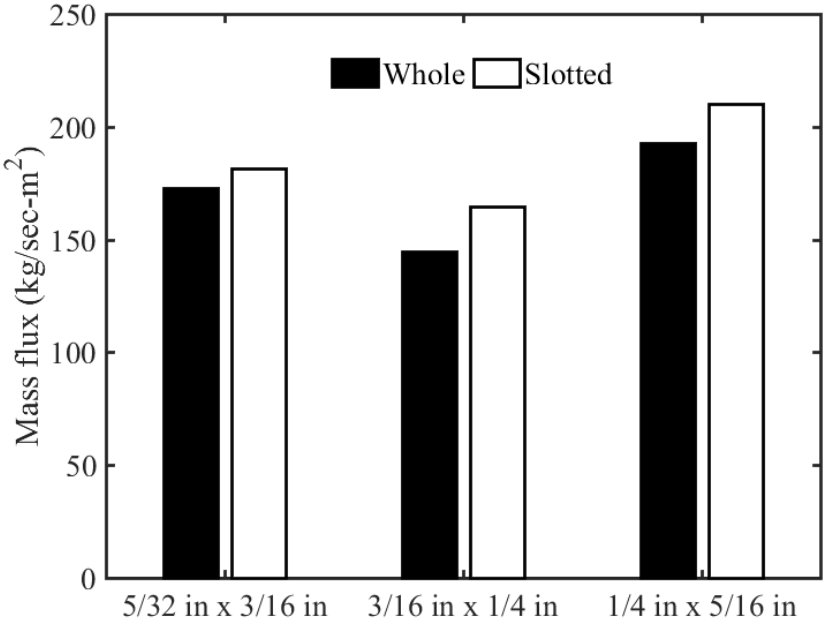

(b) Ballotini material

Figure 5.65: Experimental mass flux results for the perforated plate test section.

to their proximity to the outlet of the test section, but it would take a longer test section to study this.

5.4.2 Numerical Models

Figures 5.70 through 5.73 show the DEM and CFD models of the whole and slotted perforated plate test sections respectively. Both models show good qualitative agreement with the experimental results, with the whole squares retaining a small amount of material throughout the length of the geometry, and the slotted squares eventually becoming empty (at least near the outlet of the domain).

Figure 5.74 shows a comparison of the mass flux for the experimental and numerical data for the 3/16 in x 1/4 in perforated plate test section using the 6.35 mm spacing. Although the CFD model over-predicts the mass flux rate compared to the experimental and DEM data, it does not show the large difference between the whole and slotted geometries as it does with the square tube model. A denser mesh was not created for the CFD perforated plate model as it was assumed, after the experience with the square tube model, it was near grid independence. The CFD model does predict the slightly lower flux rate for the slotted square, where the DEM model does not.

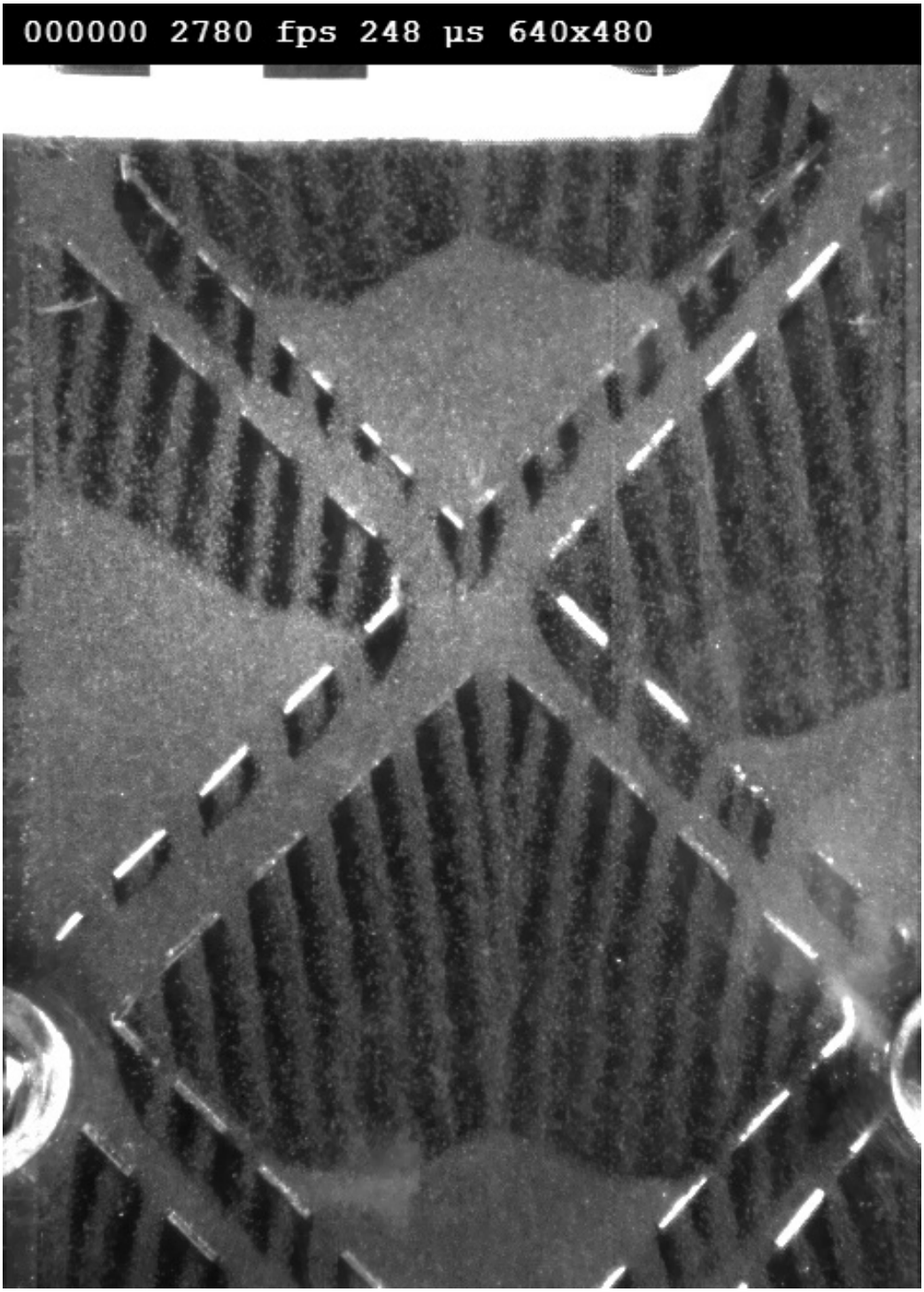

Figure 5.66: Raw video frame, perforated plate test section, 6.35 mm spacing, ID50-K material.

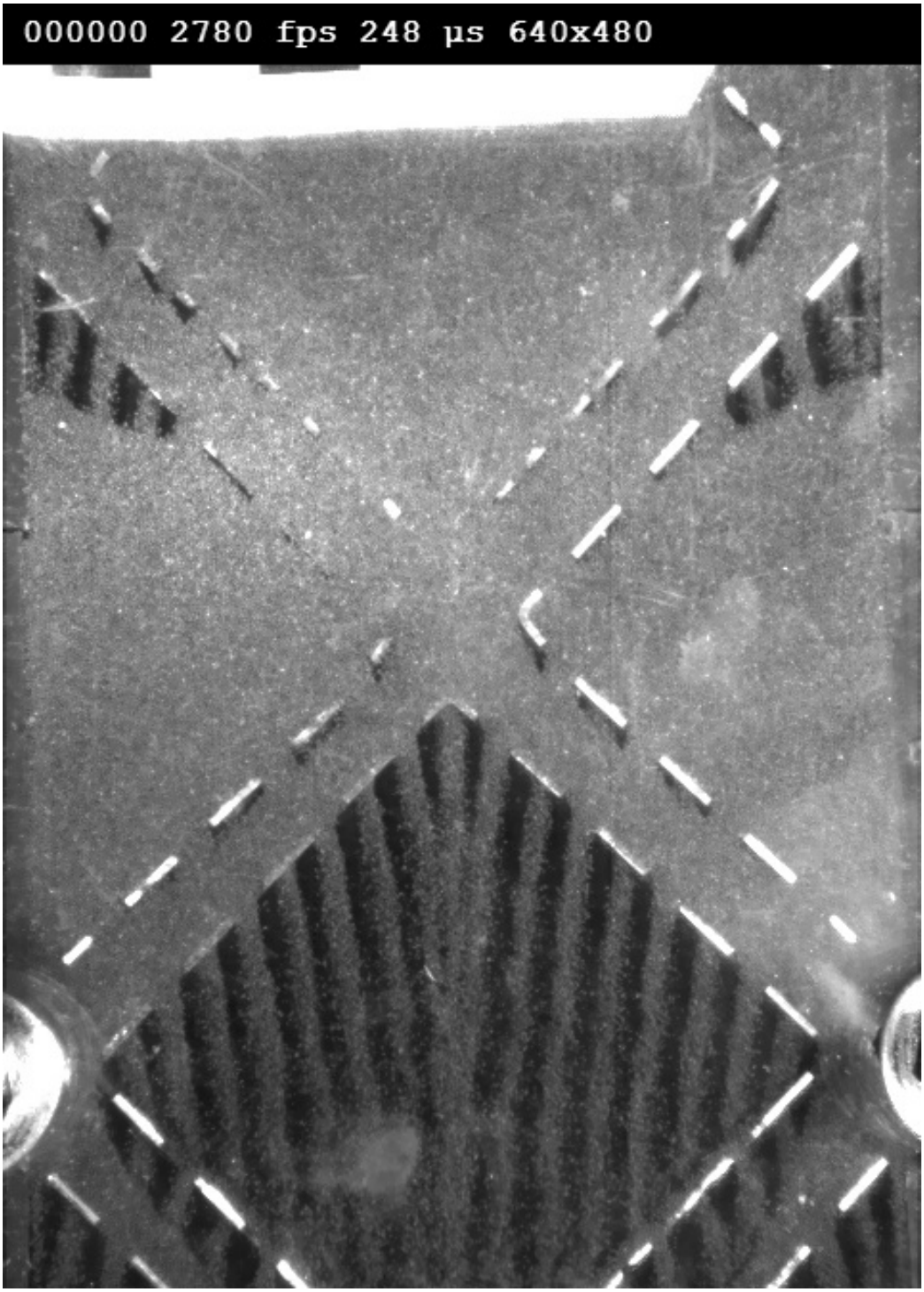

Figure 5.67: Raw video frame, slotted perforated plate test section, 6.35 mm spacing, ID50-K material.

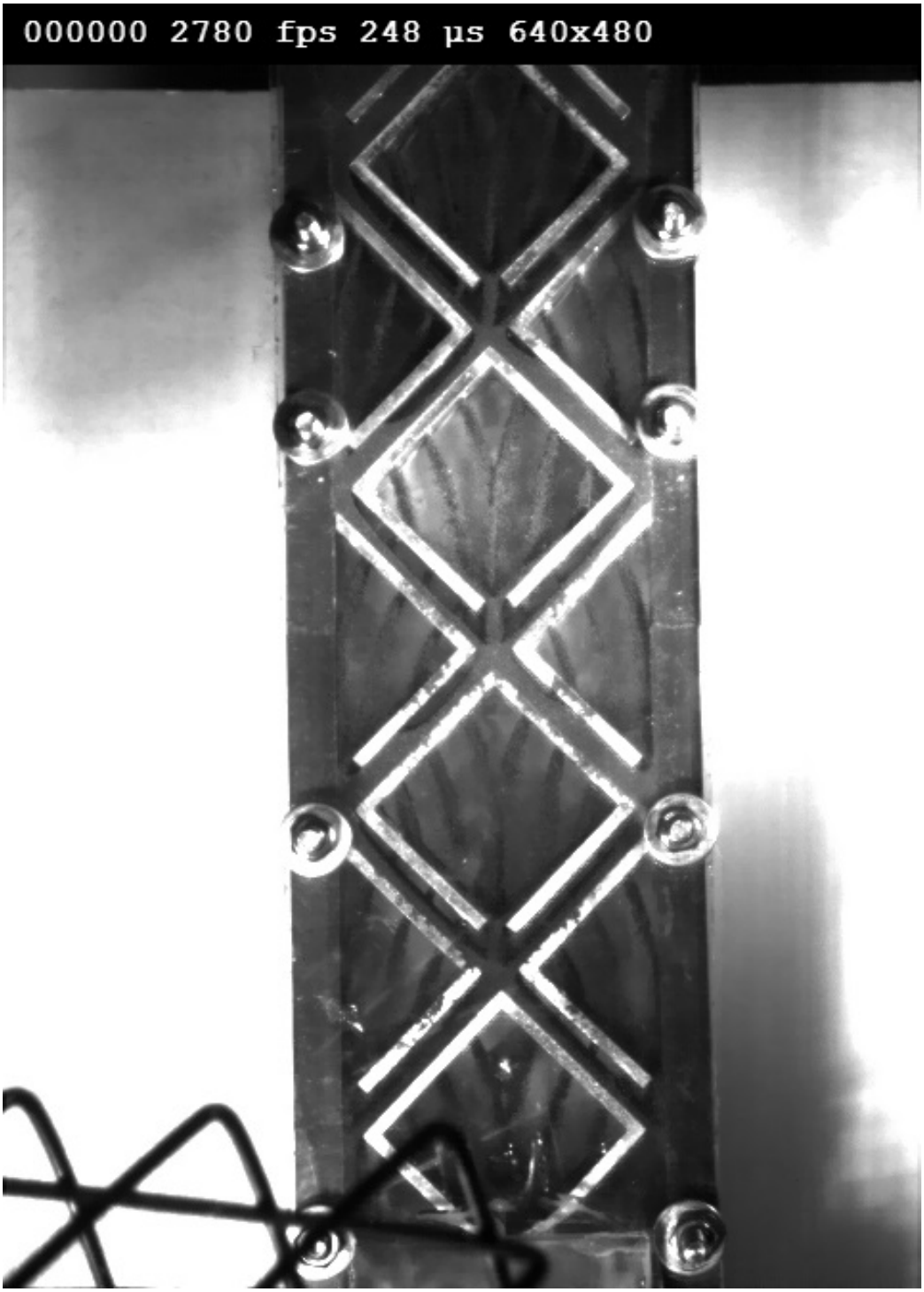

Figure 5.68: Wide shot of slotted square tube test section, 6.35 mm spacing, ID50-K material. Every square in the frame is essentially devoid of accumulated material.

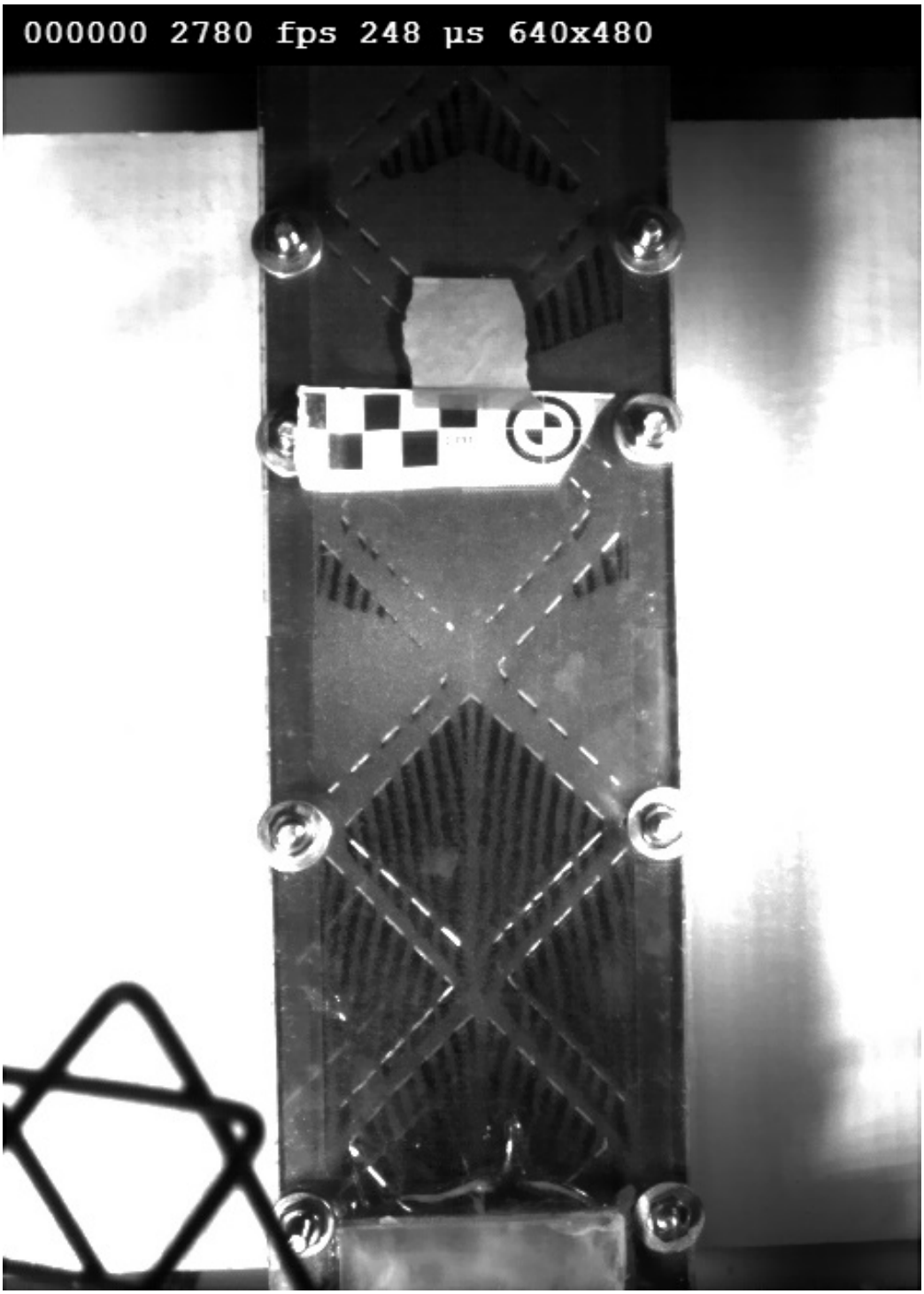

Figure 5.69: Wide shot of slotted perforated plate test section, 6.35 mm spacing, ID50-K material. There is a very sharp transition between filled squares and empty squares near the bottom of the test section.

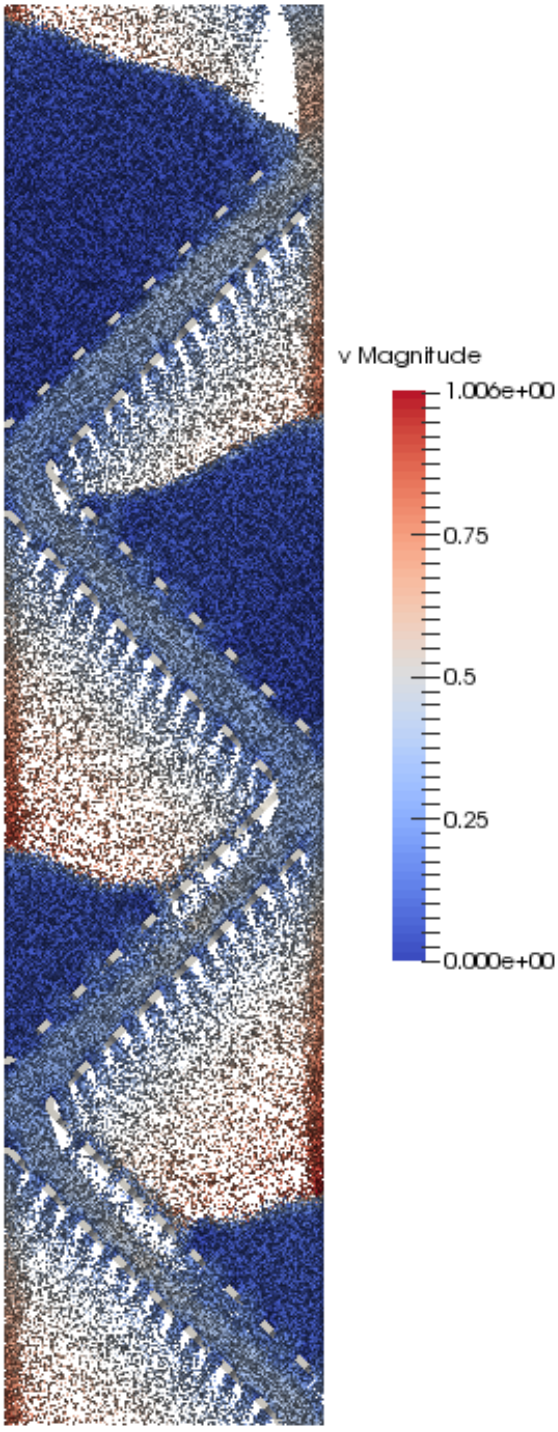

Figure 5.70: DEM model of perforated plate test section, 6.35 mm spacing, ID50-K material. The particles are colored by velocity magnitude.

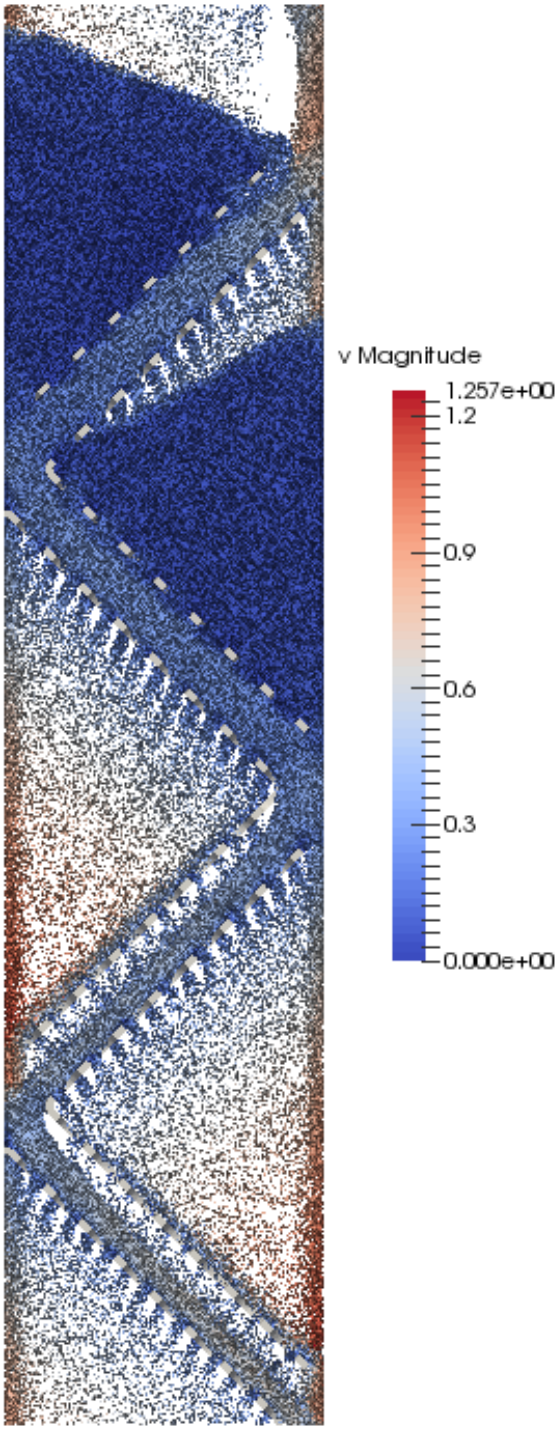

Figure 5.71: DEM model of slotted perforated plate test section, 6.35 mm spacing, ID50-K material. The particles are colored by velocity magnitude.

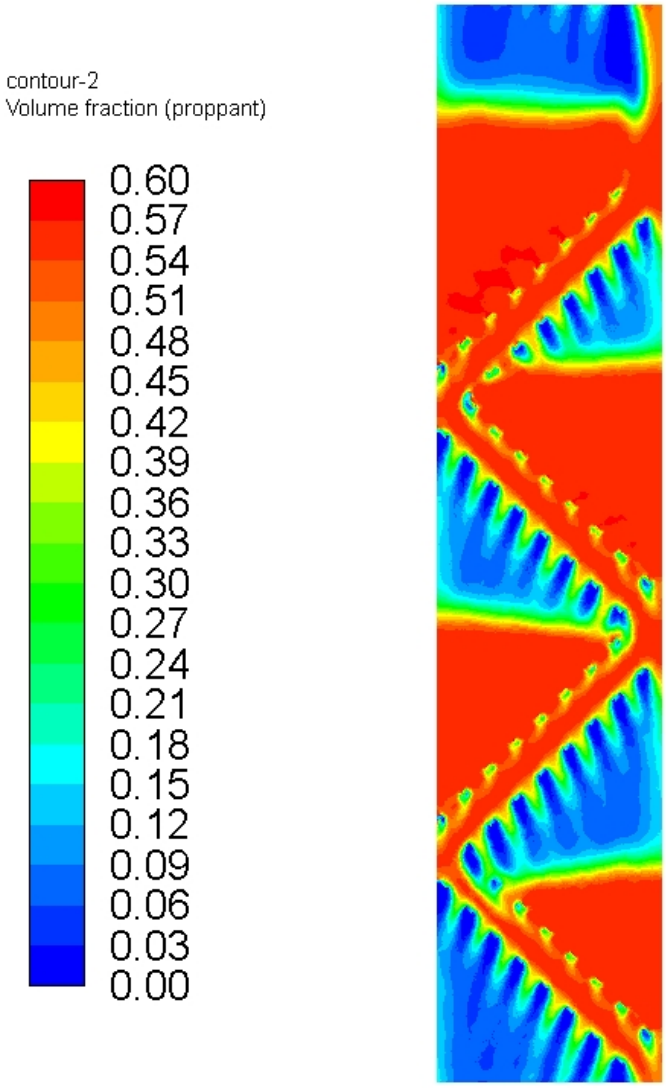

Figure 5.72: CFD model of perforated plate test section, 6.35 mm spacing, ID50-K material. The geometry is colored by volume fraction.

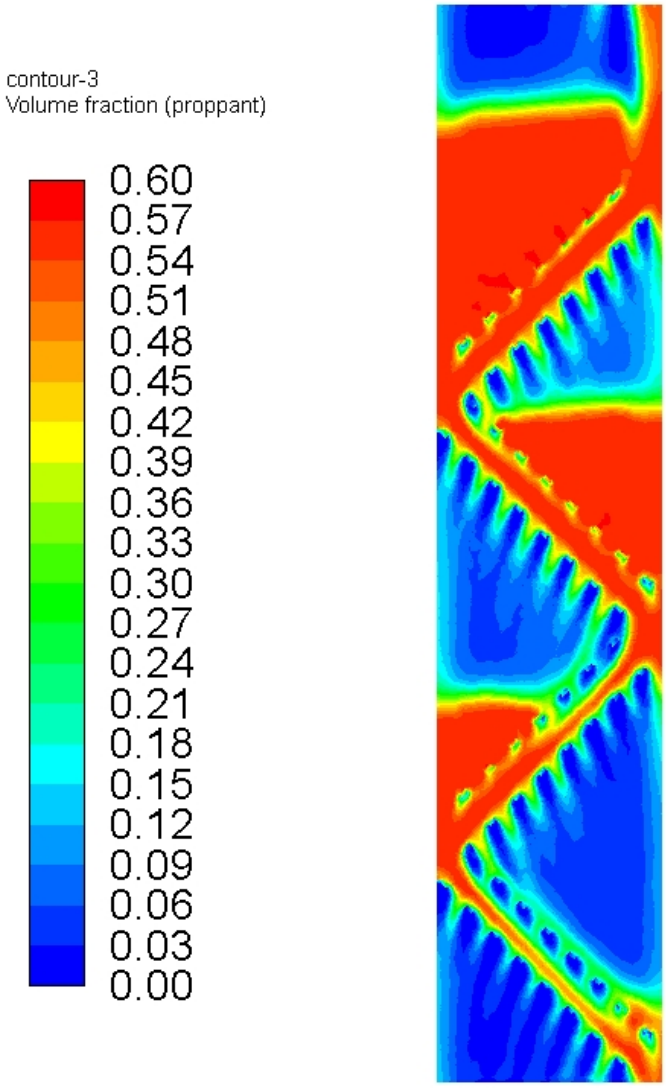

Figure 5.73: CFD model of slotted perforated plate test section, 6.35 mm spacing, ID50-K material. The geometry is colored by volume fraction.

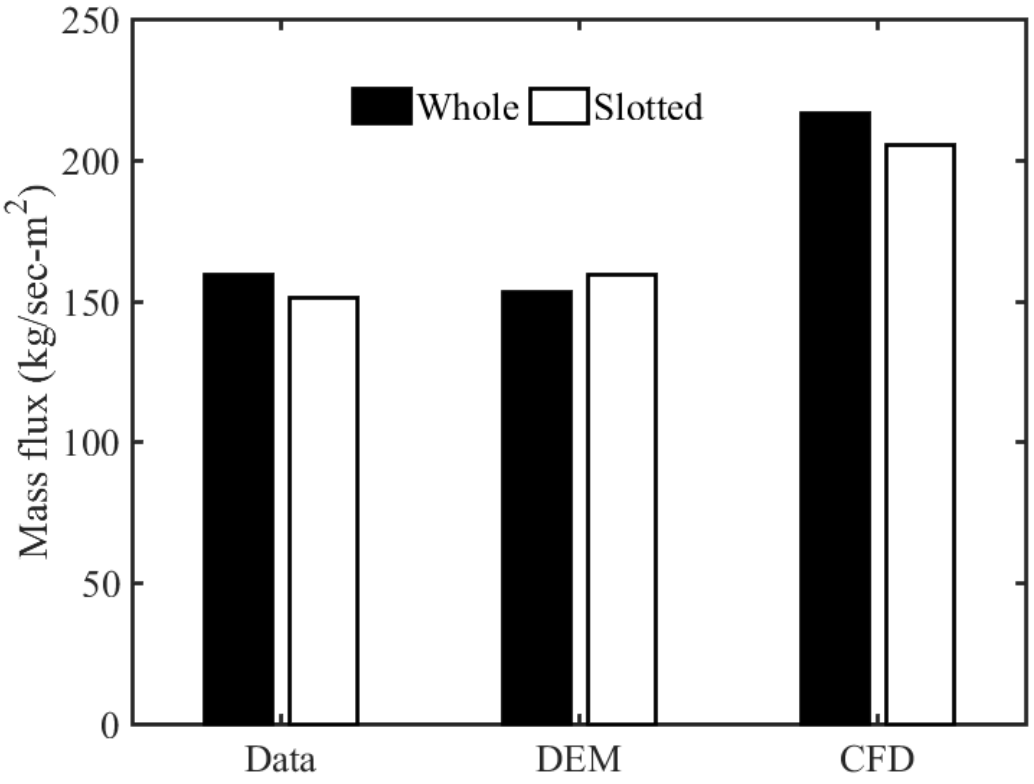

Figure 5.74: Mass flux of perforated plate test section, 6.35 mm spacing, ID50-K material.

In summary, this section has presented the results of the mass flux, steady state volume fraction, and PIV velocity analysis of two different materials running through different representative models of a hypothetical heated particle solar receiver. For horizontal wire mesh configuration, there does not appear to be a clear $D^{5/2}$ relationship found in many other granular flow studies. The mass flux of the horizontal mesh test section may be described by a linear model for the range of mesh sizes chosen, but a linear relationship no longer holds as the complexity of the test section increases. Indeed, the mass flux of any of these test sections likely depends on a combination of orifice sizes and percent open area (most notable for the perforated plate test section). Altering wire mesh spacing in both the horizontal and angled mesh test sections produced expected results: while the mass flux remains constant, particle velocities scale by about a factor of $\sqrt{2gh}$, while the steady state volume fraction scales by about the same factor in the opposite direction (i.e. as velocities increase, volume fraction decreases).

The experimental results were then compared to two different numerical models: a discrete element model, and a computational fluid dynamics model. Both models are able to achieve reasonable agreement for both mass flux and particle velocity. However, due to the smaller geometric size of the numerical domains as compared to the experimental test section, it is difficult to compare the results for the steady state volume fraction. The numerical models also differ from the experimental data because they use a mono-dispersed spherical particle model, and because they are able to achieve geometric tolerance control that is not possible in the test section.

For the 10 mesh single spaced horizontal case, a series of parametric studies were performed with both the DEM and CFD models to judge the relative effect that various model parameters had on the mass flux. The DEM model appears to be greatly influenced by the values of normal and rolling friction. The choice of the rolling friction model also had a relatively large effect on the outcome. The CFD model appears to be most influenced by the parameters that control the modeling of granular friction in the system: wall bound-

ary conditions, frictional packing, and the frictional pressure-viscosity model combination used. Indeed, the choice of frictional pressure-viscosity model itself seems to have a large role to play in whether a CFD simulation will even converge. The initial conditions also have a relatively large effect on the mass flux of the CFD model.

Two parameters in common with both models were altered: simulation time step and particle size. The DEM model seems to be nearly unaffected by the choice of time step size, up to a certain maximum limit dictated by material properties and particle velocities. However, the CFD model exhibited very unexpected behavior when altering the time step, as smaller time steps produced diverging results. It is currently unclear what produced this effect. The DEM model appears to be more sensitive to particle diameter than the CFD model, but both models behaved as expected when altering this variable.

CHAPTER 6
CONCLUSIONS AND FUTURE WORK

This section will summarize the results of this study and provide avenues for future research using the methods used.

A series of experimental investigations of potential impeded flow particle heating receiver designs was performed using small representative sections of the geometry of interest: horizontal wire mesh screens at specified spacing that span the entire flow channel, inverted chevron-shaped wire mesh screens at specified spacing that leave end gaps between successive rows, square tubes oriented at 45 degrees from the horizontal with six holes drilled into each face (both whole squares and squares with a slot cut into the bottom corner), perforated plate squares oriented at 45 degrees from the vertical which can be thought of as a limiting case when many holes are drilled into the faces of the squares (again using whole and slotted square sections), and squares cut out of silicon carbide foam oriented at 45 degrees from the vertical (again using whole and slotted square sections). Two different granular materials were used for flow testing: a ceramic casting material that is fairly polydisperse in size and irregular in shape and surface roughness, and small glass ballotini that were much more uniform in size, shape, and smoothness. For all geometries, mass flux values were recorded and high speed video was recorded for qualitative analysis. For both wire mesh geometries, steady state volume fractions were calculated and the video was also analyzed using particle image velocimetry (PIV). Then, numerical models were constructed of the experimental models using the discrete element method (DEM) and the finite volume method (CFD), and the results were compared to the experimental data for all models except the silicon carbide foam geometry. In addition, parametric studies of various model parameters were conducted for one of the horizontal mesh geometries to study the effect of numerical model inputs on the results of the different methods.

The experimental mass flow results do not appear to conform to any previously established model of granular flow; previous empirical and analytical models of granular flow were usually conducted for a single orifice, while all of the experimental designs examined here contained much more complicated outlet geometries. However, mass flux relations as a function of mesh hole size were developed for both wire mesh geometries. For the size of the meshes tested, a simple linear model may suffice, while the chevron mesh geometry is better fitted by a power law model. In addition, the PIV analysis produced velocity results that were in reasonable agreement with simple theoretical calculations of maximum particle velocity for a given mesh spacing, indicating that this analysis tool may be valid for investigating granular flows through complex geometries.

The DEM method modeled both materials as monodisperse and perfectly spherical. The particle diameter was calculated by from photomicrographs of particle samples and calculating the equivalent particle diameter that would have the same area as the two dimensional projection of the particle with the same area. When material properties of the exact compound could not be located, reasonable substitutions were made. Using small geometric domains to limit the total number of particles, the DEM model appears to be able to predict mass flux and particle velocities reasonably well, but does not predict the steady state volume fraction with the same accuracy. This is likely due to differences between the numerical and experimental geometry, and possibly also due to the difference in particle size distribution used. The DEM model appears to be most sensitive to particle diameter and friction coefficients in determining the mass flux.

The CFD model used the same monodispersed particle diameter as the DEM model, as well as lab measured values for the angle of internal friction. A reasonable estimate was used for the maximum packing fraction, and appropriate closure models were used for modeling granular pressure, friction, and turbulence. Again, using small representative geometries to limit the total number of computational cells in a given model, the CFD model was also able to reasonably predict mass flux and particle velocities, while having the same

shortcomings when predicting the steady state volume fraction. The reasons are likely the same as the DEM model. Grid independence studies may indicate that the optimum element size is dependent on local geometric size, rather than particle size. However, temporal independence studies showed diverging results as time steps shrank, which was the opposite of the expected result. The CFD model appears to be most sensitive to variations in initial and boundary conditions, as well as the specific models chosen for granular pressure and viscosity, as some models do not converge.

Overall, the DEM model appears to be better at predicting mass flux and particle velocities (neither model is clearly better at predicting steady state volume fractions). In practical terms, running times were typically faster with DEM simulations than with CFD simulations using the ceramic material (the square tube model ran faster using the CFD model). However, the CFD model is much better at comparing varying particle sizes as it does not depend on the actual number of particles being simulated.

Going forward, there are several modifications that can be made to both the experimental and numerical work to enhance the utility of the data.

6.1 Improvements to current work

6.1.1 Experimental Work

The easiest way to obtain better data from the experimental work would be to make the test sections bigger. A larger cross sectional area should enable better estimates of mass flux as wall effects are reduced. Longer test sections should enable better estimates of steady state volume fraction and overall qualitative analysis as more of the test section would be further away from any entrance region effects caused by valve transition regions.

The results from the PIV analysis are within reasonable agreement with theoretical predictions of particle velocity. It turned out that the high speed footage provided images that were within very useful ranges with regards to particle size and expected velocity. However, several aspects could be improved to enhance the reliability of these measurements.

All of the changes could be achieved with more lighting. Lighting affects not only the actual image quality recorded by the camera, but effects the choices of lens and camera placement as well. This study used consumer grade shop lighting for the majority of light output. While that may be suitable for a dark work space, the light requirements when shooting at shutter speeds measured in μs are quite high. While the light levels were high enough to ensure shutter speeds high enough where motion blur did not appear to be an issue, it necessitated compromises in camera placement and lens choice. Lens choice typically involves choosing a focal length and aperture setting. The focal length of a lens has an effect of depth of focus and usually the maximum aperture size, as long focal length lenses typically have smaller maximum apertures available than wide angle lenses. The aperture size effects maximum light levels and the depth of focus as well. In general, long focal lengths create shorter depths of focus, while short focal lengths enhance it. For the aperture, large openings decrease the depth of focus while small openings increase it (obviously at lower light inputs). Due to the available light levels, fairly wide lenses were used to achieve the necessary aperture openings. This had two main drawbacks: it produced a relatively shallow depth of focus due to the large aperture required, and it required setting the camera fairly close to the test section, requiring care to make sure the camera itself didn't case a shadow in the frame. Higher light levels could potentially allow for longer lenses to be used, allowing better camera placement or smaller apertures. This could be extended to on-sun testing or testing in a solar simulator, as there would likely be ample light levels for any shutter speed or lens choice.

Because of the varying image widths needed for the different sized test sections, the camera was placed and focused manually each time a video was recorded. Ideally, the entire experiment would be placed on an optical table and focus distances could be accurately calculated for a given focal length. If that were unfeasible, the camera could be set far enough away from the experiment so that it would not interfere with the lighting or other measurements.

6.1.2 DEM Work

The main difference between the experimental work and the DEM work was the use of monosized spheres as particles. DEM in general, and LIGGGHTS in particular, has the capability to model both particle distributions and non-spherical particles, with some caveats.

LIGGGHTS allows the insertion of a discrete size distribution of particles; by modifying the number of bins used for particle diameter, a continuous particle distribution can be approximated to any desired accuracy. However, this can degrade performance for widely dispersed systems. Attempting to calculate the interaction between every single particle in a system is a very expensive operation, so many DEM codes use some sort of detection algorithm to calculate potential interactions only for particles that are a certain distance from each other (it should also be possible to program a continuous distribution function in LIGGGHTS, as it is open source). LIGGGHTS uses a concept called Verlet neighbor lists [93]. Originally developed for Lennard-Jones molecules [126], the idea is to build up lists of potential contacts every certain number of time steps. These neighbor lists are made up of (spherical) particles that satisfy

$$||x_i + x_j|| < r_i + r_j + s \tag{6.1}$$

where s is a skin distance that can be used to enlarge the search area for neighbors (for instance, for fast moving particles that move a significant fraction of a particle diameter every time step). If this skin distance is large enough, these neighbor lists are valid for several time steps, saving computation time. While the optimum size for this skin distance is simulation (and even hardware) dependent [93], a skin distance the size of the particle radius was found to offer a good performance increase for this study. For bi- or polydisperse systems (especially systems with a wide disparity in particle size), the choice of a skin distance based on the largest particle diameter leads to bigger neighbor lists which increase computation time (see figure 6.1). Skin distances based on the smallest particle diameter

lead to constant list updates, also degrading performance. The current public version of LIGGGHTS does not support dynamic skin distances.

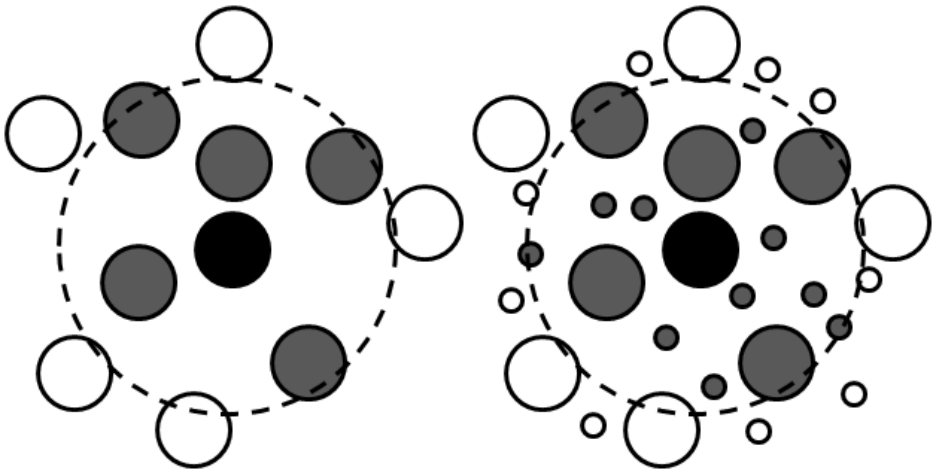

(a) Monodisperse (b) Bidisperse

Figure 6.1: Contact detection using Verlet lists. Grey particles are in the neighbor list of the black particle.

Other problems related to using a wide polydisperse model include the large increase in the number of particles for a given volume fraction, the scaling of the time step with the smallest particle, and, in an issue similar in nature to the contact detection issue describe above, the increase in communication overhead when running in parallel. While the issues dealing with increased particle counts and communication issues can be negated somewhat by improved parallization and memory sharing schemes, the decrease in time step is a feature of the DEM model itself [127].

Particles encountered in practice are almost never perfect spheres. While there are several methods for creating non-spherical particles, one of the most common methods for modeling natural materials (seeds, rock aggregate, etc.) is by building particles from a clump of smaller spheres [43]. Figure 6.2 shows an example of building complex shapes from different numbers of spheres. Multiple spheres are locked together to form a rigid body, and the resulting linear and angular velocity are computed from the sums on all of the individual spheres.

One advantage of clumped sphere method is that it can use the relatively simple contact

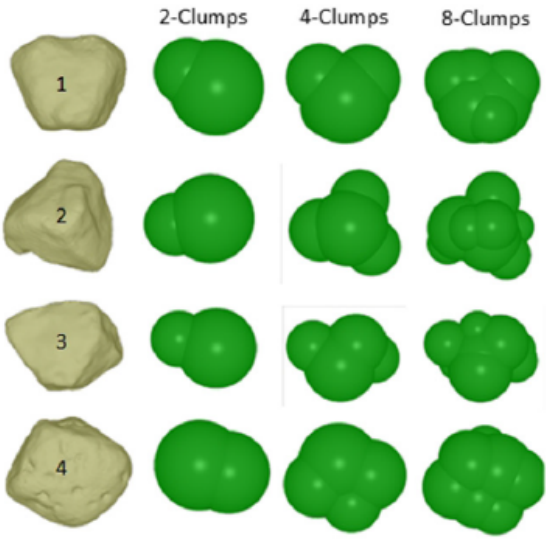

Figure 6.2: Building complex shapes from multiple spheres [43].

detection algorithm previously described for spherical particles. However, the possibility of multiple contacts per particle can lead to unphysical behavior at the particle scale [128]. As a practical matter, the current public version of LIGGGHTS does not support simulations using a multisphere model in parallel, which would place limits on the number of particles for reasonable simulation times. The non-free version of LIGGGHTS offers multisphere simulations in parallel.

As with the experimental work, the size of the DEM simulations could be increased. The wire mesh models containing the ceramic material have particle counts on the order of 100000, which is not a very large number for modern computational hardware. By taking advantage of periodic boundary conditions all around, the computational domain could be extended to match (or exceed) the depth of the experimental test section. This might enable more accurate volume fraction calculations to be obtained. The square tube and perforated plate models could also be extended, although they would use far greater particle counts. One issue this might present would be the issue of CPU load balancing. When running in parallel, the current public version of LIGGGHTS typically divides the computational domain in an attempt to minimize the surface area to volume ratio for each CPU sub-domain to decrease inter-CPU communication overhead. LIGGGHTS also allows for the

parallel sub-domain grid to be set manually, but both methods have the restriction that the CPU grid must be an evenly spaced rectangular mapping. For systems with widely varying particle loads, such as this study, running in parallel usually means either sub-optimal CPU loads, or excessive CPU communication. LIGGGHTS does offer non-free version of the DEM code that offer dynamic load balancing capabilities. Figure 6.3 shows the benefits of load balancing on a highly non-homogeneous system.

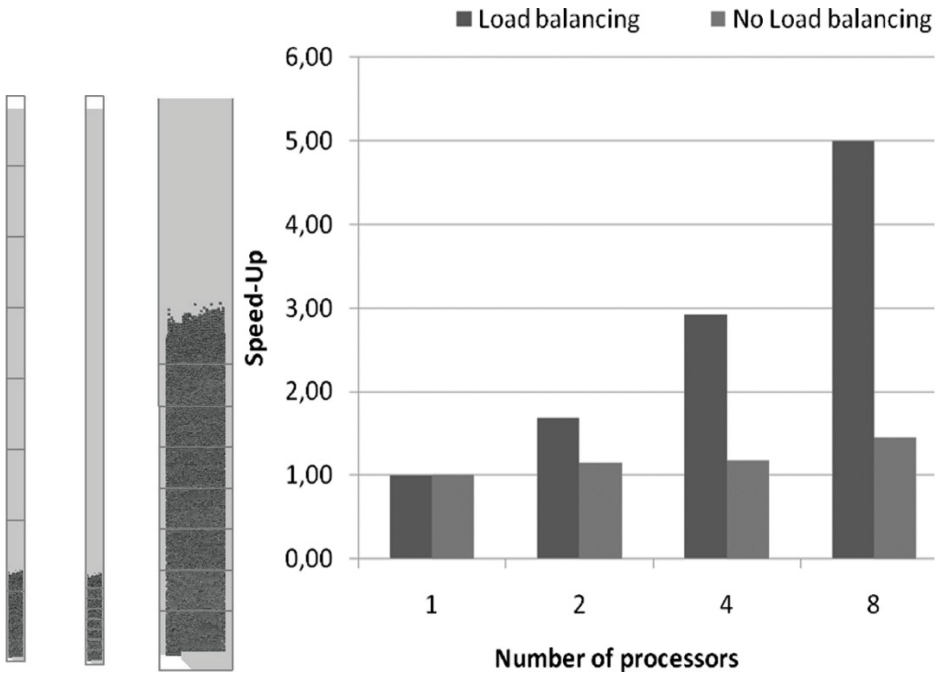

Figure 6.3: Benefits of dynamic load balancing in DEM, showing improved CPU load balance and better scalability [93].

6.1.3 CFD Work

The effect of non-spherical particles (and to some extent, the particle size distribution) are accounted for in CFD simulations by the angle of internal friction and the maximum packing and friction packing limits. However, each granular phase only has one particle size. Attempting to simulate a particle size distribution by adding different phases quickly leads to simulations with an enormous number equations being solved.

Modeling a polydisperse system can be accomplished by population balance models.

Population balance models use "external" coordinates r to describe the position of a particle, and "internal" coordinates x to describe particle properties (mass, temperature, etc.). Thus, a number density function $f(x, r, t)$ describes the expected number of particles at a specific location, state, and time. The total number of particles in a system is given by

$$N(t) = \int_{\Omega_x} dV_x \int_{\Omega_r} dV_x f(x, r, t). \tag{6.2}$$

If the particles are distributed evenly in space, then the number density becomes independent of the external coordinate. Consider a one dimensional case were the x coordinate is the particle size. If $\dot{X}(x, t)$ represents the change in size of a particle, then the conservation equation for particle size (the population balance equation) is given by

$$\frac{\partial f(x,t)}{\partial t} + \frac{\partial}{\partial x}(\dot{X}(x,t) f(x,t)) = 0. \tag{6.3}$$

Additional source terms can be added to account for particle birth or death due to aggregation and breakage [129].

Different methods are available to solve equation 6.3, such as discrete methods [129], the standard method of moments [130], the quadrature method of moments [131], and the direct quadrature method of moments [132], each with their own advantages and disadvantages. More research needs to be done in this area to determine if the potential benefits of accounting for a polydisperse system outweighs the added computational complexity.

The most pressing issue with the current CFD models are related to grid size. Previous studies of two dimensional fluidized beds have indicated that grid independence can be obtained with cell sizes that are several times larger than the particle size [133]. However, the current study may indicate that grid independence is also correlated with local geometry size (the previously cited study by [133] was for a fluidized bed; there were no geometric features on the same scale as the particle size). If this is the case, CFD models using wire mesh screens will be severely constrained on overall domain size. The situation could be

helped somewhat for the angled mesh models by doing a rather large amount of geometric decomposition to enable a larger portion of the domain to be occupied by a mapped mesh.

Another option could be to replace the wire mesh geometry with some sort of equivalent computational element(s). Fluent can create porous cell zones that act as a sink on the momentum equation, creating a drop in pressure and velocity (it may also be possible to create custom cells by the use of user defined functions in Fluent, or equivalent methods in other CFD codes). This could eliminate the small curved geometry features present in the wire mesh screen geometry, while still allowing overall flow characteristics to be preserved. This would require the characterization of the wire meshes in terms of pressure and velocity losses, which could be accomplished by more detailed experimental and PIV analysis, or by examining the flows obtained in the current study.

One more area for improvement could be in the modeling of turbulence. Using the standard $k-\epsilon$ model for turbulent flows, it was discovered that the CFD models could only be run using a first order upwind discretization scheme for the two turbulence variables; running higher order schemes resulted in diverging solutions due to the turbulence variable ϵ diverging for the solid phase. This also put limits on how fast particles could be loaded into the system using the previously described batch process, as suddenly introducing a relatively large volume fraction into certain areas would also cause the solution to diverge. It is currently unknown if this was related to grid issues, or if a different turbulence model would help. The realizeable $k-\epsilon$ model contains a different transport equation for ϵ, and the eddy viscosity has a non-constant coefficient C_μ to ensure that the normal stress is never negative . The model is claimed to be more numerically stable than the standard model due to the different equation for turbulent dissipation [134], and offers superior performance for a wide range of flows, including those within a solid particle receiver [7]. This may also not be an issue for models with an inlet and an outlet (i.e. a pre-determined mass flux) using low flow rates, as they wouldn't be subjected to such rapid swings in solids fraction when inserting particles.

Finally, for modeling the flow through the ceramic foam structure, Lee et al. [17] has shown that, with an appropriately chosen simplified geometry substitute for the foam structure, good qualitative agreement can be achieved (and quantitative trends can be predicted). Further research into the geometric substitution could result in a complete model for the complex structure present in the ceramic foam. This simplified geometry could also be tested in a DEM simulation, and the hydrodynamics could be compared between the two models to determine the suitability for future research.

6.2 Future Work

The ultimate goal of the numerical models would be to add a heat transfer model, thus building a complete model of a particle heating receiver. In this case, the CFD model has a slight edge going forward. As the DEM model is purely a granular simulation tool, it can only model heat transfer via particle conduction (and the particle softening procedure used to speed up simulation times can adversely effect the calculation of conductive heat transfer via the increased contact area [135]).

The CFD model is capable of including both convection and radiation heat transfer models along side the current two fluid simulation. To model convection, the energy equation is solved, given by [110]

$$\frac{\partial}{\partial t}(\rho E) + \nabla \cdot (\vec{v}(\rho E + p)) = \nabla \cdot \left(k_{eff} \nabla T - \sum_j h_j \vec{J}_j + (\bar{\bar{\tau}}_{eff} \cdot \vec{v}) \right) + S \qquad (6.4)$$

where k_{eff} is the sum of the normal and turbulent thermal conductivities, $\vec{J}_j$ is the diffusion flux of species j, and S is a source term. While several studies performing convective heat transfer in granular flows have been performed for fluidized bed applications [136] and drying processes [137], those studies are heavily dependent on the hydrodynamics of the processes under investigation, while this study seems to indicate that particle aerodynamics

has little effect on the outcome (this is also a desired outcome of an impeded flow particle heating receiver).

Due to its non-linearity, modeling radiation heat transfer is usually done seperately. To solve for radiation heat transfer in a participating madium (such as a particle curtain), the radiative transfer equation (RTE) is solved, given by [110]

$$\frac{dI(\vec{r},\vec{s})}{ds} + (a+\sigma_s)I(\vec{r},\vec{s}) = an^2\frac{\sigma T^4}{\pi} + \frac{\sigma_s}{4\pi}\int_0^{4\pi} I(\vec{r},\vec{s'})\Phi(\vec{s}\cdot\vec{s'})d\Omega' \tag{6.5}$$

where I is the radiation intensity, $\vec{r}$ is the position vector, $\vec{s}$ is the direction vector, $\vec{s'}$ is the scattering direction vector, s is the path length, a is the absorption coefficient, σ_s is the scattering coefficient, n is the refractive index, σ is the Stefan-Boltzmann constant, T is the local temperature, Φ is the phase function, and Ω' is the solid angle. There are a few ways to numerically solve equation 6.5, but a common approach is the discrete ordinates (DO) method. The DO method allows for different values of scattering and absorption of radiation for different directions and wavelengths of radiation [138].

The inclusion of a radiation model typically depends on the nature of the simulation. In simulations of a falling particle curtain, the effects of radiation are critical to the analysis of the overall model. However, more complex flow geometries can be a challenge. A recent study assessing the heat transfer between heated surfaces and particle flow revealed that a two fluid model may not be able to capture flow instabilities that occur near walls, leading to an under-prediction of convective heat transfer coefficients [55]. To overcome this problem, DEM models of granular flow are being used to develop better closer equations for the continuum models [56, 57].

Another approach to this issue is to model granular flows using a combined Euler-Lagrangian approach. In this method, individual particles are tracked in a Lagrangian frame as they move through a typical CFD fluid domain. This potentially allows for very accurate modeling of hydrodynamic and heat transfer effects at the particle scale, at the cost of increased computational requirements.

There appear to be two general approaches for this. One is called the discrete phase model (DPM). In the discrete phase model, particles are inserted and tracked in a similar way to the DEM model. However, one of the major assumptions is that the volume fraction of particles is low enough (typically less than 10%) that there is only one way coupling of momentum: the particles are influenced by the local pressure and velocity gradients, but the flow field is not effected by the presence of particles. Furthermore, particle interactions are often neglected [139] (models that employ two way coupling, particle interactions, and other phenomena are available, but the application of such additional interactions does not appear to be very consistent). While this method has been used to model the hydrodynamic and thermodynamic performance of falling particle curtains (for example, [7, 10, 12, 13]), the volume fraction limitation means it could not be implemented in this study as is. It is also unclear how the effect of a relatively large amount of particle-wall interactions would effect the hydrodynamics of such a model. As a practical matter, the previous studies have also used a prescribed particle flow rate with an entrance and exit zone, rather than periodic entrance and exit zones; the ability of the DPM method to handle periodic boundary conditions is not understood at this time. A dense discrete phase model reports to overcome some of the limitations of the standard model, allowing for higher volume fractions to be obtained [140], but it does not appear to have seen much application in solar heating particle receivers. Figure 6.4 shows the results of a DPM simulation of a falling curtain particle heating receiver. Different sized particles were released from a slot in the top of the geometry, and both hydro- and thermodynamic performance was studied.

The other approach is the combined CFD-DEM method. In this approach, a DEM simulation takes place inside of a CFD simulation. In the unresolved approach, CFD cells are many times the size of an individual particle, while a fully resolved approach uses DEM particles that span several CFD cells. Due to the nature of DEM modeling, the DEM time step is typically an order of magnitude lower than the CFD time step. Different time steps to account for effects such as radiation or chemical reactions can also be included that are a

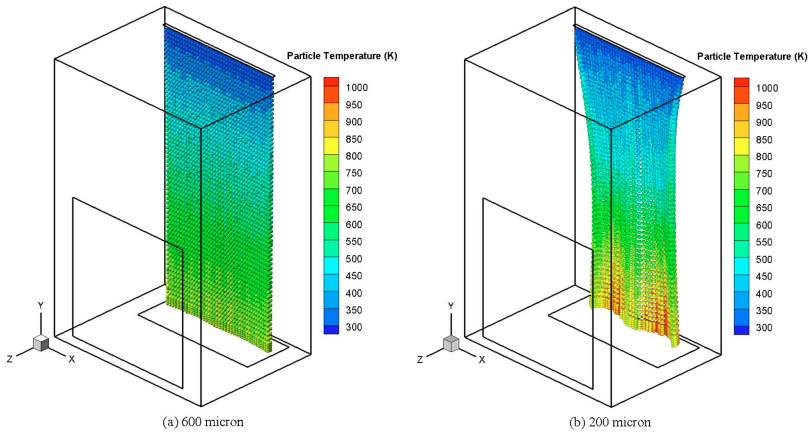

Figure 6.4: Particle flow path lines in a DPM simulation for a particle heating receiver, colored by temperature [7].

different size again that the coupling time step [93]. While this method is computationally expensive, it has the potential for superior accuracy due to the fully resolved granular flow simulation.

Once again, owing to the complex hydrodynamics of the process, and on the increasing computational power available, the CFD-DEM approach has seen use for modeling processes such as fluidized beds [141] and fluid catalytic cracking risers [142]. However, the addition of a radiation heat transfer model to a simulation with potentially millions of surfaces likely adds significant computational cost, thus slowing its adoption for modeling of particle heating receivers. However, work is ongoing to include radiation heat transfer models in granular systems [143, 144].

Finally, there is ongoing research on how to make numerical simulations (especially DEM simulations, owing to the small time step constraint) run faster, including better parallelization techniques [145, 146] and the use of graphics processing units (GPUs) [147, 148]. While the development of such tools is beyond the scope of this study, progress in such areas should be monitored to ensure that the latest parallelization methods are used. This information could also guide future hardware purchases, should the use of dedicated (rather than shared, as in this study) computing resources be desired.

Appendices

APPENDIX A

ERROR ANALYSIS

This appendix will present an analysis of the error present in measuring the raw mass flow data from the experimental test section, including an example of a single case.

In general, an experimental measurement will have two sources of error [149]: bias error (or systematic error), and random error. Bias errors, B, reflect errors that do not vary between measurements and can not be reduced by repeated measurements (such as calibration errors). Random errors, P, are statistical in nature and reflect the inherent noise in a measurement. The total uncertainty in a measurement, U, can be calculated by

$$U^2 = B^2 + P^2. \tag{A.1}$$

Three variables were measured in this study: mass, voltage, and time. The calculation of a mass flow rate, $\dot{m}$, was done by measuring the change in voltage from a load cell over a certain time interval, $\dot{V}$, and then multiplying the result by a calibration factor, b_{cal}, that related the voltage output with a known mass

$$\dot{m} = \dot{V} b_{cal}. \tag{A.2}$$

The uncertainty of any measurement, w_R, can be estimated as the root sum square (RSS) of the uncertainties of the different variables that make up a measurement by

$$w_R^2 = \sum_i \left(w_{x_i} \frac{\partial R}{\partial x_i} \right)^2 \tag{A.3}$$

Thus, the bias error present in the measurement of the mass flow rate can be estimated

as

$$B_{\dot{m}}^2 = (\dot{V}U_{b_{cal}})^2 + (b_{cal}U_{\dot{V}})^2 + \left(\frac{\dot{m}}{\bar{m}}U_m\right)^2 \tag{A.4}$$

where the final term, $\frac{\dot{m}}{\bar{m}}U_m$, is included to represent the uncertainty in the measurement of mass on the lab scale. U_m is taken as plus or minus the least significant digit of the OHAUS scale output.

$\dot{V}$ is obtained by performing a linear regression on a set of experimental data, while b_{cal} is obtained from the previously described calibration procedure (see chapter 3).

As the generation of the calibration curve is statistical in nature, $U_{b_{cal}}$ can be calculated by

$$U_{b_{cal}} = tS_{cal} \tag{A.5}$$

where t is the student's t variable (taken as 2 in this study to correspond with a 95% confidence level) and S_{cal} is the standard error of the b_{cal} measurement.

The uncertainty in $\dot{V}$ can be calculated as

$$U_{\dot{V}}^2 = \left(\frac{\dot{V}}{\bar{V}}U_V\right)^2 + \left(\frac{\dot{V}}{\bar{t}}U_t\right)^2 \tag{A.6}$$

where U_V and U_t represent the uncertainties in the measurement of voltage and time respectively. The uncertainty in time is simply plus or minus the least significant digit in the output of the Agilent data acquisition switch. The uncertainty in the voltage has contributions from both the Agilent switch and the Keli load cell. The Agilent switch produces errors in the voltage reading that are both a function of the reading itself and of the scale used on the switch (in this case, 100 mV) [150]. The Keli load cell has uncertainty contributions from non-linearity, hysteresis, and non-repeatability [151]. For a conservative

estimate, the total uncertainty in the voltage is the sum of each device,

$$U_V = U_{V_{Agilent}} + U_{V_{Keli}} \tag{A.7}$$

The random error of the mass flow measurement is given by

$$P_{\dot{m}} = tS_{\dot{m}}. \tag{A.8}$$

where t is again 2 and $S_{\dot{m}}$ is the standard error in the mass flow calculation.

Figure A.1 shows an example of flow test data and the calibration curve that was used for that particular data set. The flow test was performed with the ID50-K material using the single spaced horizontal mesh configuration with size 10 mesh screens.

Calculating all of the terms in equations A.1 through A.8, the uncertainty in the mass flow measurement presented in figure A.1 is $9.47 * 10^{-5}$ kg/sec, or 0.214% of the measured mass flux. The error is fairly evenly split between the bias error and the random error, which are calculated as $6.13 * 10^{-5}$ kg/sec and $7.22 * 10^{-5}$ kg/sec respectively. More observations (i.e. letting a flow test run longer) would reduce the random error. The largest term in the calculation of the bias error (by several orders of magnitude) was the $b_{cal}U_{\dot{V}}$ term. A more precise load cell would have the largest impact on this term. Table A.1 shows the uncertainties in the individual variables used in calculating the error in the mass flow rate measurement.

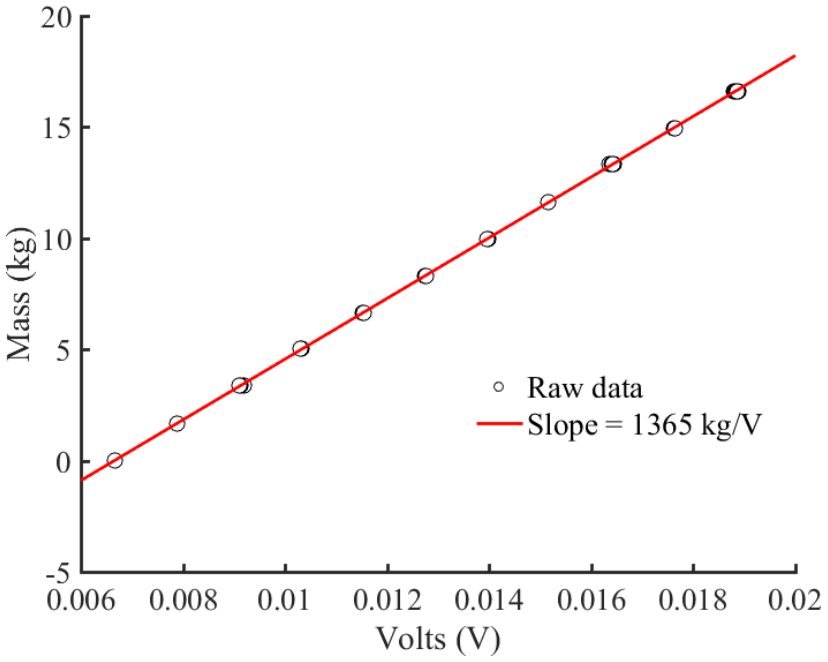

(a) Calibration curve

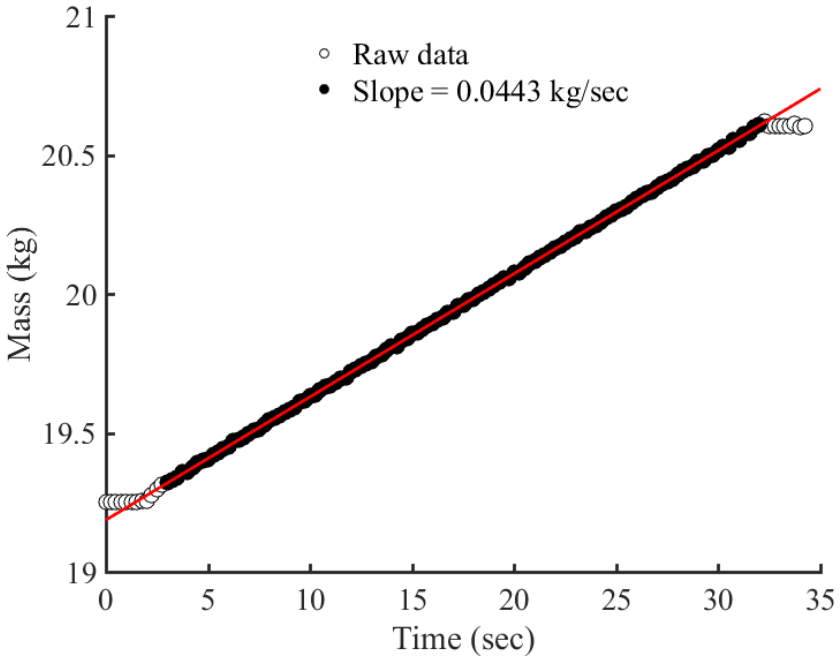

(b) Flow test data

Figure A.1: Calibration curve and flow test data using the ID50-K material and single spaced horizontal 10 mesh screens.

Table A.1: Uncertainties in individual variables.

	Relative uncertainty	Absolute uncertainty
Time		0.001 sec
Mass		1^{-4} kg
Voltage		
Keli DEFY100 load cell [151]		
Non-linearity	0.03% of full scale	$9.89 * 10^{-6}$ V
Hysteresis	0.03% of full scale	$9.89 * 10^{-6}$ V
Non-repeatability	0.02% of full scale	$6.60 * 10^{-6}$ V
Agilent 34970 data acquisition switch [150]		
Reading	0.005% of reading	$7.31 * 10^{-7}$ V
Range	0.004% of scale	$4 * 10^{-6}$ V

APPENDIX B

ALTERNATE EQUATIONS

This appendix will provide the equations used for the alternate modeling options in both the DEM and CFD simulations.

B.1 DEM models

Normal contact The "Hooke" normal contact model is given by [41]

$$F = (k_n \delta_n - \gamma_n v_n) + (k_t \delta_t - \gamma_t v_t) \tag{B.1}$$

$$F_t \leq \mu_n F_n \tag{B.2}$$

$$k_n = \frac{16}{15}\sqrt{R^*}Y^*\left(\frac{15 m^* V^2}{16\sqrt{R^*}Y^*}\right)^{1/5} \tag{B.3}$$

$$\gamma_n = \sqrt{\frac{4 m^* k_n}{1 + \left(\frac{\pi}{ln(e)}\right)^2}} \geq 0 \tag{B.4}$$

$$k_t = k_n \tag{B.5}$$

$$\gamma_t = \gamma_n \tag{B.6}$$

$$S_n = 2Y^*\sqrt{R^*\delta_n} \tag{B.7}$$

$$S_t = 8G^* \sqrt{R^* \delta_n} \tag{B.8}$$

$$\beta = \frac{ln(e)}{\sqrt{ln^2(e) + \pi^2}} \tag{B.9}$$

$$\frac{1}{Y^*} = \frac{(1-\nu_1^2)}{Y_1} + \frac{(1-\nu_2^2)}{Y_2} \tag{B.10}$$

$$\frac{1}{G^*} = \frac{2(2-\nu_1)(1+\nu_1)}{Y_1} + \frac{2(2-\nu_2)(1+\nu_2)}{Y_2} \tag{B.11}$$

$$\frac{1}{R^*} = \frac{1}{R_1} + \frac{1}{R_2} \tag{B.12}$$

$$\frac{1}{m^*} = \frac{1}{m_1} + \frac{1}{m_2} \tag{B.13}$$

where V is a characteristic impact velocity.

Rolling resistance The constant directional torque (CDT) rolling resistance model is given by [96]

$$M = -\frac{\omega_{rel}}{|\omega_{rel}|} \mu_r k_n \delta_n R^* \tag{B.14}$$

$$\omega_{rel} = \omega_i - \omega_j \tag{B.15}$$

where ω is the angular velocity of a particle.

The alternative elastic-plastic spring-dashpot (EPSD2) model is identical to the normal EPSD model except in the treatment of the rolling stiffness, k_r and the damping torque,

M_r^r [152]. In the EPSD2 model, the rolling stiffness is given by

$$k_r = k_t R^{*2} \tag{B.16}$$

where k_t is the tangential stiffness defined for normal contact. The damping torque, M_d^r is completely ignored for this model.

B.2 CFD models

Solid-fluid momentum exchange coefficient The Syamlal-O'Brien model is given by [153]

$$K_{sl} = \frac{3\alpha_s \alpha_l \rho_l}{4 v_{r,s}^2 d_s} C_D\big(\frac{Re_s}{v_{r,s}}\big)|\vec{v_s} - \vec{v_l}| \tag{B.17}$$

where C_D is given by

$$C_D = \big(0.63 + \frac{4.8}{\sqrt{Re_s/v_{r,s}}}\big)^2 \tag{B.18}$$

and $v_{r,s}$ is given by

$$v_{r,s} = 0.5(A - 0.06Re_s + \sqrt{(0.06Re_s)^2 + 0.12Re_s(2B - A) + A^2}) \tag{B.19}$$

where

$$A = \alpha_l^{4.14} \tag{B.20}$$

and

$$B = \begin{cases} 0.8\alpha_l^{1.28}, \alpha_l \leq 0.85 \\ \alpha_l^{2.65}, \alpha_l > 0.85 \end{cases} \tag{B.21}$$

The Gibilaro drag model is given by [154]

$$K_{sl} = \big(\frac{18}{Re} + 0.33\big)\frac{\rho_f |v_s - v_l|}{d_p}\alpha_s \alpha_l^{-1.8} \tag{B.22}$$

where the Reynolds number, Re, is given by

$$Re = \frac{\alpha_l \rho_l d_p |v_s - v_l|}{\mu_l} \tag{B.23}$$

The Wen-Yu drag model is given by [155]

$$K_{sl} = \frac{3}{4} C_D \frac{\alpha_s \alpha_l \rho_l |\vec{v_s} - \vec{v_l}}{d_s} \alpha_l^{-2.65} \tag{B.24}$$

where

$$C_D = \frac{24}{\alpha_l Re_s}[1 + 0.15(\alpha_l Re_s)^{0.687}] \tag{B.25}$$

The Huilin-Gidaspow model [156] is a combination of the Wen-Yu model [155] and the Ergun equation [157]. It is given by

$$K_{sl} = \Phi K_{sl,Ergun} + (1 - \Phi) K_{sl,Wen-Yu} \tag{B.26}$$

where $K_{sl,Ergun}$ is given by [157]

$$K_{sl,Ergun} = 150\frac{\alpha_s(1 - \alpha_l)\mu_l}{\alpha_l d_l^2} + 1.75\frac{\rho_l \alpha_s |\vec{v_s} - \vec{v_l}}{d_s} \tag{B.27}$$

and $K_{sl,Wen-Yu}$ is given by equation B.24. The stitching function, Φ, is given by

$$\Phi = 0.5 + \frac{\arctan(262.5(\alpha_s - 0.2))}{\pi} \tag{B.28}$$

Frictional pressure-viscosity model The Johnson frictional viscosity model is given by [124]

$$\mu_{fric} = P_{fric} \sin(\phi) \tag{B.29}$$

where P_{fric} is the frictional pressure, given by

$$P_{fric} = 0.1\alpha_s \frac{(\alpha_s - \alpha_{s,min})^2}{(\alpha_{s,max} - \alpha_s)^5} \tag{B.30}$$

The Syamlal frictional pressure model is given by [117]

$$P_{fric} = A(\alpha_l - \alpha_{l,min})^n \tag{B.31}$$

where A and n are constants.

The specific form for the fictional pressure based on kinetic theory is not given in the Fluent manual. However, kinetic theory usually gives the pressure as a function of particle velocity, i.e. [117, 158]

$$P \propto \Theta \tag{B.32}$$

where Θ is the granular temperature.

Granular temperature transport If the granular temperature is modeled with a partial differential equation, the convection and diffusion terms are included in the transport cal-

culation. In this case, the granular conductivity, k_{Θ_s}, is given by [117]

$$k_{\Theta_s} = \frac{15 d_s \rho_s \alpha_s \sqrt{\Theta \pi}}{4(41 - 33\eta} [1 + \frac{12}{5}\eta^2(4\eta - 3)\alpha_s g_{0,ss} + \frac{16}{15\pi}(41 - 33\eta)\eta\alpha_s g_{0,ss})] \tag{B.33}$$

where

$$\eta = \frac{1}{2}(1 + e_{ss}) \tag{B.34}$$

APPENDIX C

TABULATED DATA

This appendix will present the mass flux and volume fraction results from chapter 5 in tabular form.

Table C.1: Mass flux results for the ID50-K material, horizontal mesh configuration.

Hole size (mm)	2.54	1.905	1.532	1.306	
Mesh number (ppi)	8	10	12	14	
	Single spaced				
Mass flux (kg/sec-m^2)	99.7	68.7	50.1	36.4	Data
	98.3	59.1	43.6	35.2	DEM
	108.3	74.6	5.1	50.1	CFD
	Double spaced				
	98.6	65.1	52.7	37.8	Data
	107.1	64.2	45.9	33.3	DEM
	121.0	82.8	65.5	57.8	CFD

Table C.2: Mass flux results for the ballotini material, horizontal mesh configuration.

Hole size (mm)	2.54	1.905	1.532	1.306	
Mesh number (ppi)	8	10	12	14	
	Single spaced				
Mass flux (kg/sec-m^2)	161.5	123.5	79.1	67.6	Data
	218.9	154.7	92.3	77.2	DEM
	153.7	63.5	54.0	47.5	CFD
	Double spaced				
	131.6	112.7	88.8	68.2	Data
	240	164.4	114.8	100.8	DEM
	168.6	71.5	56.2	50.9	CFD

Table C.3: Mass flux results for the ID50-K material, angled mesh configuration.

Hole size (mm)	2.54	1.905	1.532	1.306	
Mesh number (ppi)	8	10	12	14	
	Single spaced				
Mass flux (kg/sec-m^2)	101.6	95.6	72.1	57.9	Data
	143.1	103.1	78.3	55.9	DEM
	218	147.4	114.5	105.9	CFD
	Double spaced				
	104.1	89.4	73.1	48.4	Data
	157.4	111.5	78.3	58.3	DEM
	241	115.8	129.1	122.1	CFD

Table C.4: Mass flux results for the ballotini material, angled mesh configuration.

Hole size (mm)	2.54	1.905	1.532	1.306	
Mesh number (ppi)	8	10	12	14	
	Single spaced				
Mass flux (kg/sec-m^2)	179.0	150.4	118.0	100.4	Data
	219	176.1	152.5	125.1	DEM
	194.6	132.8	108.4	110.0	CFD
	Double spaced				
	233	186.8	145.5	120.0	Data
	294	229	181.2	163.9	DEM
	205	145.9	106.2	113.6	CFD

Table C.5: Mass flux results for the ID50-K material, square tube configuration.

Spacing (mm)	1.588	3.18	4.76	6.35	
			Whole squares		
Mass flux (kg/sec-m^2)	43.2	46.9	51.8	60.9	Data
				72.0	DEM
				79.3	CFD
				81.6	CFD dense
			Slotted squares		
	44.9	50.3	58.1	62.5	Data
				72.8	DEM
				91.2	CFD
				91.6	CFD dense

Table C.6: Mass flux results for the ballotini material, square tube configuration.

Spacing (mm)	1.588	3.18	4.76	6.35	
			Whole squares		
Mass flux (kg/sec-m^2)	46.3	44.3	48.3	60.8	Data
			Slotted squares		
	45.6	51.1	56.7	59.8	Data

Table C.7: Mass flux results for the ID50-K material, perforated plate configuration.

Plate dimensions (in)	5/32 x 3/16	3/16 x 1/4	1/4 x 5/16	
		Whole squares		
Mass flux (kg/sec-m^2)	174.6	159.8	194.6	Data
		153.3		DEM
		217		CFD
		Slotted squares		
	175.6	151.3	206	Data
		159.6		DEM
		206		CFD

Table C.8: Mass flux results for the ballotini material, perforated plate configuration.

Plate dimensions (in)	5/32 x 3/16	3/16 x 1/4	1/4 x 5/16	
	Whole squares			
Mass flux (kg/sec-m^2)	172.6	144.6	192.9	Data
	Slotted squares			
	181.3	164.6	210	Data

Table C.9: Volume fraction results for the ID50-K material, horizontal mesh configuration. To calculate the experimental volume fraction by including the volume in the upper slide gate valve bore that is larger than the cross sectional area, multiply these results by 0.929.

Hole size (mm)	2.54	1.905	1.532	1.306	
Mesh number (ppi)	8	10	12	14	
	Single spaced				
Volume fraction	0.0540	0.0442	0.0419	0.0343	Data
	0.1150	0.0627	0.0659	0.0481	DEM
	0.0689	0.0653	0.0963	0.0903	CFD
	Double spaced				
	0.0311	0.0261	0.0243	0.0191	Data
	0.0471	0.0662	0.0747	0.0684	DEM
	0.0537	0.0666	0.0872	0.0825	CFD

Table C.10: Volume fraction results for the ballotini material, horizontal mesh configuration. To calculate the experimental volume fraction by including the volume in the upper slide gate valve bore that is larger than the cross sectional area, multiply these results by 0.929.

Hole size (mm)	2.54	1.905	1.532	1.306	
Mesh number (ppi)	8	10	12	14	
		Single spaced			
Volume fraction	0.1327	0.1128	0.1049	0.0780	Data
	0.1546	0.1112	0.1307	0.1201	DEM
	0.1777	0.0609	0.0811	0.0812	CFD
		Double spaced			
	0.0571	0.0542	0.0478	0.0401	Data
	0.1299	0.0927	0.0701	0.0629	DEM
	0.1569	0.0499	0.0423	0.0557	CFD

Table C.11: Volume fraction results for the ID50-K material, angled mesh configuration. To calculate the experimental volume fraction by including the volume in the upper slide gate valve bore that is larger than the cross sectional area, multiply these results by 0.952.

Hole size (mm)	2.54	1.905	1.532	1.306	
Mesh number (ppi)	8	10	12	14	
		Single spaced			
Volume fraction	0.0478	0.0508	0.0461	0.0390	Data
	0.1246	0.0991	0.1122	0.1369	DEM
	0.238	0.1938	0.1875	0.1838	CFD
		Double spaced			
	0.0422	0.0337	0.0303	0.0211	Data
	0.1608	0.1282	0.1611	0.233	DEM
	0.202	0.1692	0.1574	0.1614	CFD

Table C.12: Volume fraction results for the ballotini material, angled mesh configuration. To calculate the experimental volume fraction by including the volume in the upper slide gate valve bore that is larger than the cross sectional area, multiply these results by 0.952.

Hole size (mm)	2.54	1.905	1.532	1.306	
Mesh number (ppi)	8	10	12	14	
Single spaced					
Volume fraction	0.1520	0.1508	0.1486	0.1895	Data
	0.223	0.221	0.1891	0.253	DEM
	0.260	0.222	0.1774	0.206	CFD
Double spaced					
	0.1849	0.1602	0.1219	0.1553	Data
	0.204	0.201	0.1867	0.1971	DEM
	0.204	0.1763	0.1559	0.1799	CFD

Table C.13: Effect of coefficient of normal friction on mass flux, ID50-K material, DEM model.

k_n	0.1	0.5	0.9	Data
Mass flux (kg/sec-m^2)	113.5	67.7	59.1	68.7

Table C.14: Effect of coefficient of rolling friction on mass flux, ID50-K material, DEM model.

k_r	0.001	0.01	0.1	0.2	Data
Mass flux (kg/sec-m^2)	124.4	92.8	59.1	57.0	68.7

Table C.15: Effect of coefficients of normal and rolling friction on mass flux, ballotini material, DEM model.

	k_r			
k_n	0.001	0.01	0.1	Data
0.15	114.8	154.7	104.5	
0.9	92.8	87.6	69.8	
Mass flux (kg/sec-m^2)				123.5

Table C.16: Effect of normal contact model on mass flux, ID50-K material, DEM model.

Contact model	Hertz	Hooke	Data
Mass flux (kg/sec-m^2)	59.1	65.0	68.7

Table C.17: Effect of rolling resistance model on mass flux, ID50-K material, DEM model.

Rolling model	EPSD	EPSD2	CDT	Data
Mass flux (kg/sec-m^2)	64.3	71.7	74.5	68.7

Table C.18: Effect of time step on mass flux, ID50-K material, DEM model.

Time step (μsec)	1	0.5	0.1	0.01	Data
Mass flux (kg/sec-m^2)	59.8	60.0	59.1	60.9	68.7

Table C.19: Effect of Young's modulus on mass flux, ID50-K material, DEM model.

Young's modulus (Pa)	$3.7 * 10^7$	$3.7 * 10^9$	Data
Mass flux (kg/sec-m^2)	59.1	55.9	68.7

Table C.20: Effect of angle of internal friction on mass flux, ID50-K material, CFD model.

ϕ (degrees)	24	29	35	Data
Mass flux (kg/sec-m^2)	76.7	74.6	73.6	68.7

Table C.21: Effect of maximum packing fraction on mass flux, ID50-K material, CFD model.

Max packing fraction	0.55	0.60	0.65	Data
Mass flux (kg/sec-m^2)	71.7	74.6	84.1	68.7

Table C.22: Effect of frictional packing fraction on mass flux, ID50-K material, CFD model.

Frictional packing fraction	0.50	0.55	0.58	Data
Mass flux (kg/sec-m^2)	57.3	74.6	68.5	68.7

Table C.23: Effect of initial condition on mass flux, ID50-K material, CFD model.

	IC1	IC2	IC3	Data
Mass flux (kg/sec-m^2)	88.1	74.6	78.6	68.7

Table C.24: Effect of drag model on mass flux, ID50-K material, CFD model.

Drag model	Mass flux (kg/sec-m^2)
Gidaspow	74.6
Gibilaro	74.5
Huilin-Gidaspow	74.6
Syamlal-Obrien	74.5
Wen-Yu	74.5
Data	68.7

Table C.25: Effect of frictional viscosity-pressure model on mass flux, ID50-K material, CFD model. The asterisk indicates that the selected model did not produce a constant steady state value. In these cases, an average value was used.

Pressure-viscosity model	Mass flux (kg/sec-m^2)
Schaeffer-Johnson	74.6
Schaeffer-KTGF*	50.6
Johnson-Syamlal*	7.19
Johnson-KTGF	23.8
Data	68.7

Table C.26: Effect of machine precision on mass flux, ID50-K material, CFD model.

Precision	Souble	Single	Data
Mass flux (kg/sec-m^2)	74.6	75.4	68.7

Table C.27: Effect of wall boundary condition on mass flux, ID50-K material, CFD model.

	Specularity coefficient				
Boundary condition	0	0.5	1	No slip	Data
Mass flux (kg/sec-m^2)	121.0	102.9	95.0	74.6	68.7

Table C.28: Effect of granular temperature transport model on mass flux, ID50-K material, CFD model.

Granular model	Algebraic	PDE-Syamlal	Data
Mass flux (kg/sec-m^2)	74.6	80.0	68.7

Table C.29: Effect of time step and residual size on mass flux, ID50-K material, CFD model.

	Time step (μsec)					
Residual	12.5	25	50	100	200	Data
1e-3	86.5	78.0	71.5	67.6	66.8	
1e-6	94.6	85.3	84.9	82.8	88.2	
Mass flux (kg/sec-m^2)						68.7

Table C.30: Effect of particle size on mass flux, ID50-K material.

Hole size (mm)	2.54	1.905	1.532	1.306	
Mesh number (ppi)	8	10	12	14	Particle diameter (μm)
			DEM model		
Mass flux (kg/sec-m^2)	122.1	70.6	51.5	39.1	305
	98.3	59.1	43.6	35.2	355
	87.6	53.9	36.3	24.0	405
			CFD model		
	126.9	79.0	61.8	56.8	305
	108.3	74.6	55.1	50.1	355
	103.4	68.0	52.2	47.6	405

APPENDIX D

VELOCITY HISTOGRAMS

This appendix will present velocity histograms from the horizontal and angled mesh configurations that weren't presented in the results section.

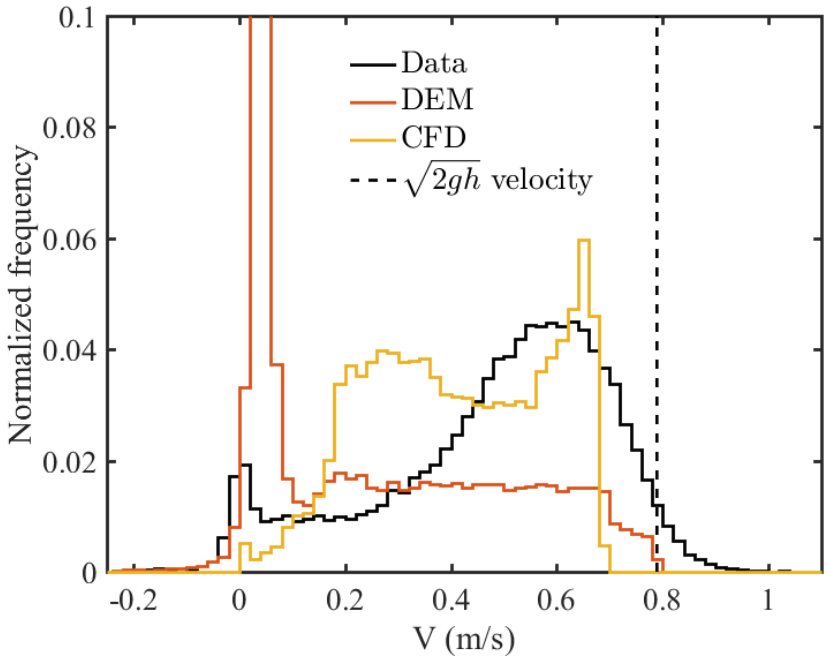

(a) Single spaced configuration

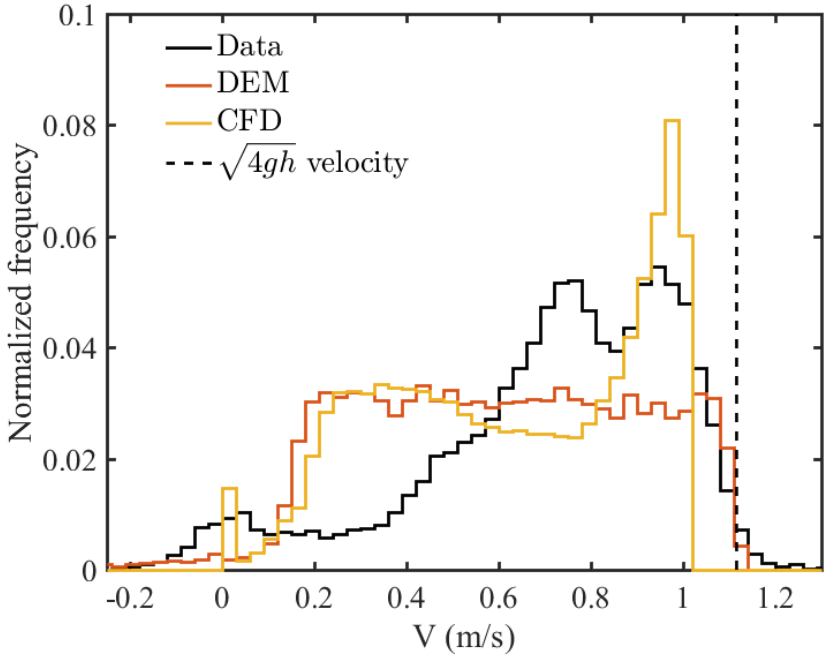

(b) Double spaced configuration

Figure D.1: Vertical velocity histograms for the ID50-K material, size 8 horizontal mesh.

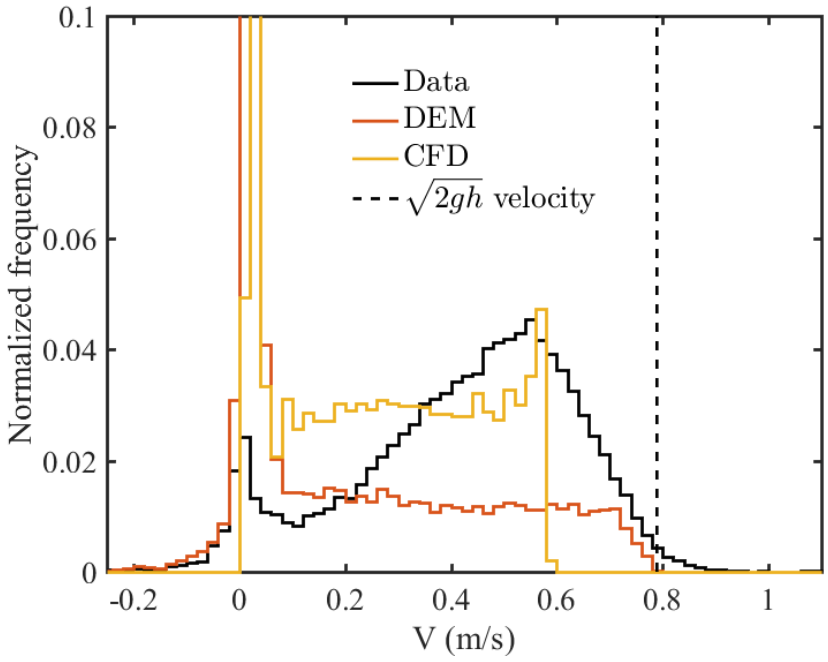

(a) Single spaced configuration

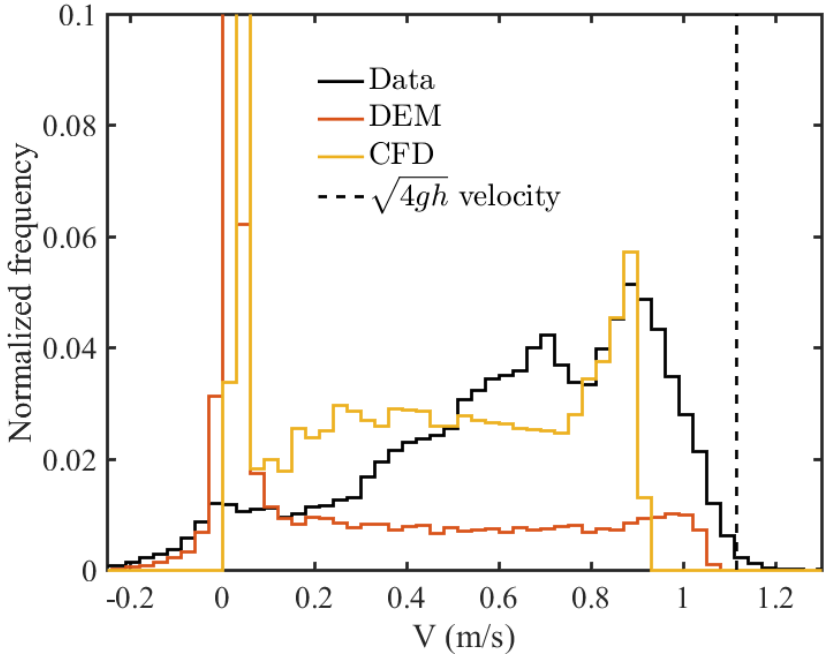

(b) Double spaced configuration

Figure D.2: Vertical velocity histograms for the ID50-K material, size 12 horizontal mesh.

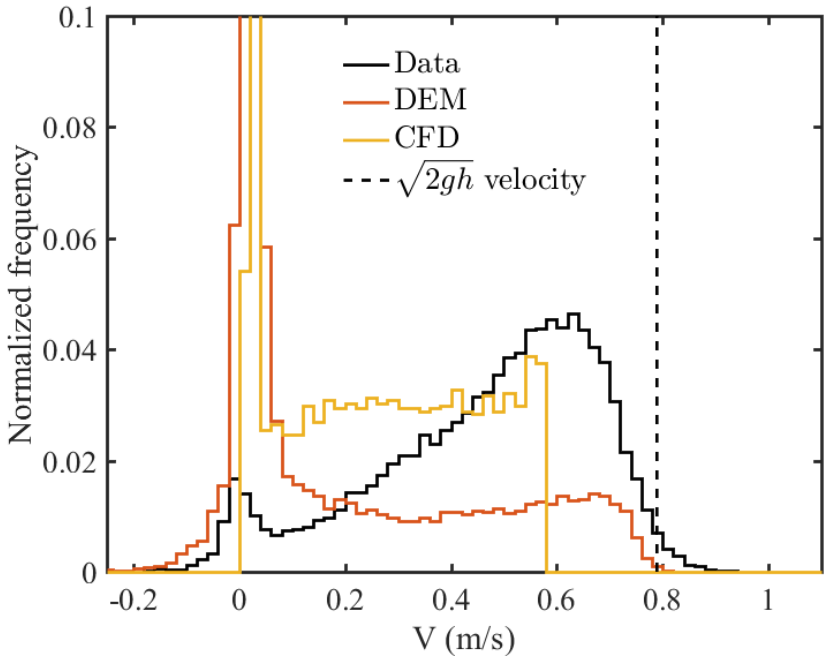

(a) Single spaced configuration

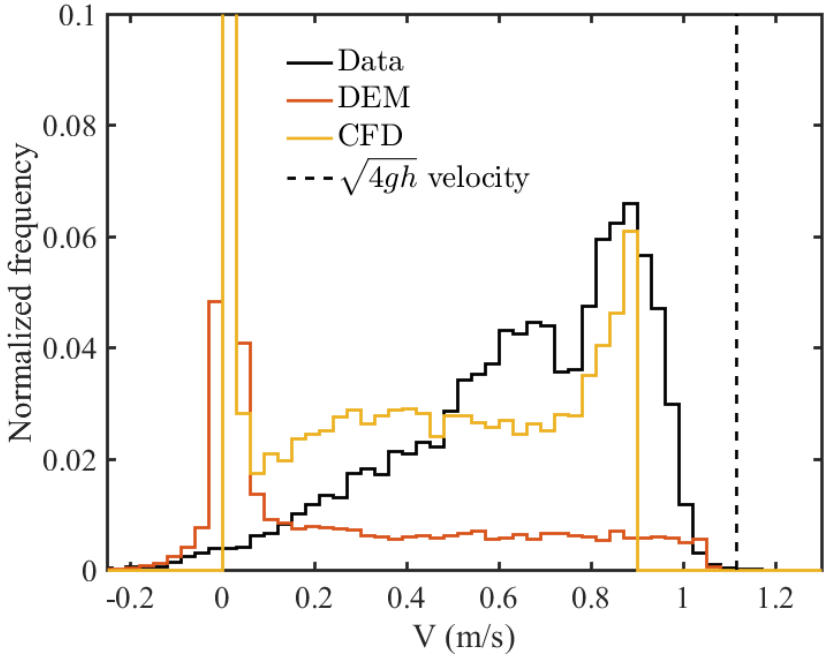

(b) Double spaced configuration

Figure D.3: Vertical velocity histograms for the ID50-K material, size 14 horizontal mesh.

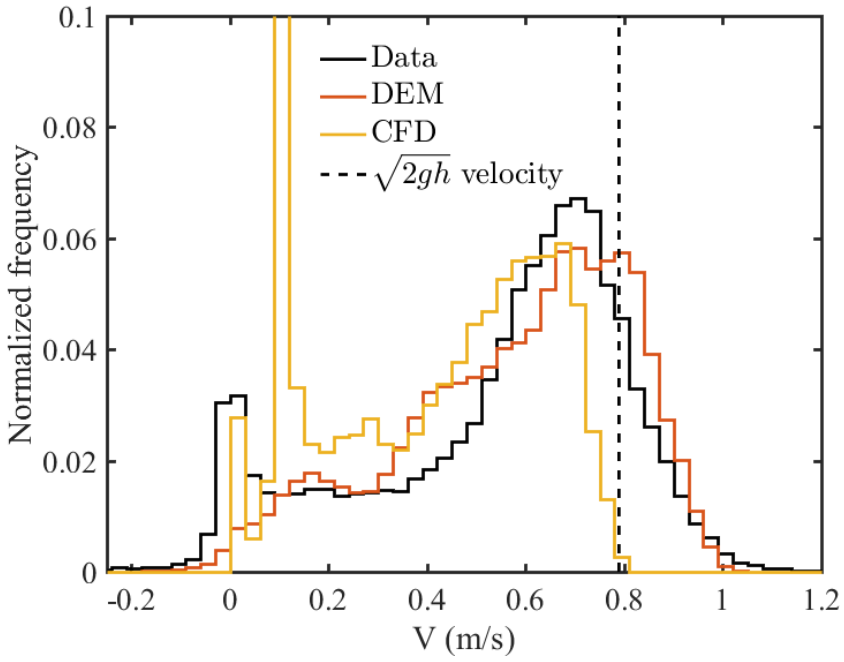

(a) Single spaced configuration

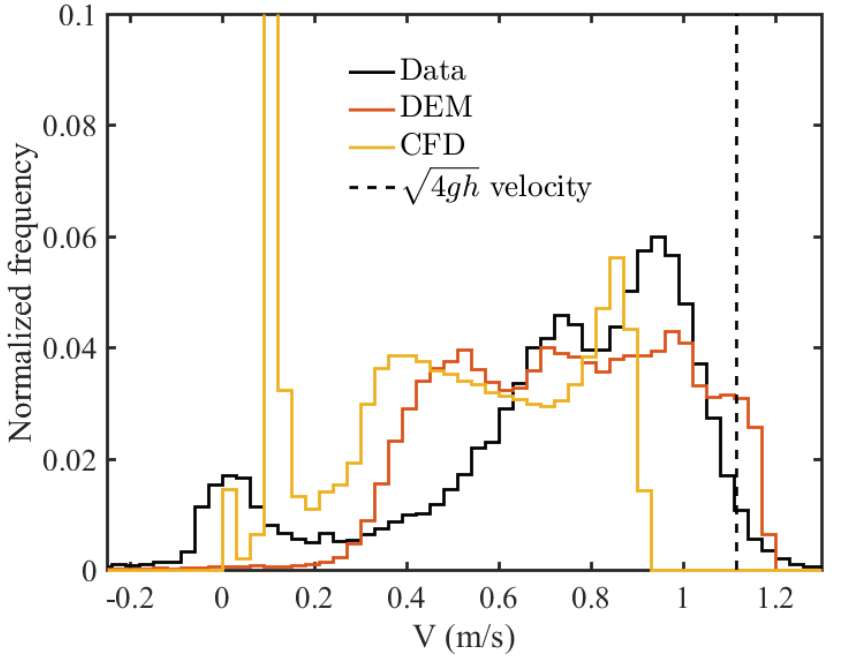

(b) Double spaced configuration

Figure D.4: Vertical velocity histograms for the ballotini material, size 8 horizontal mesh.

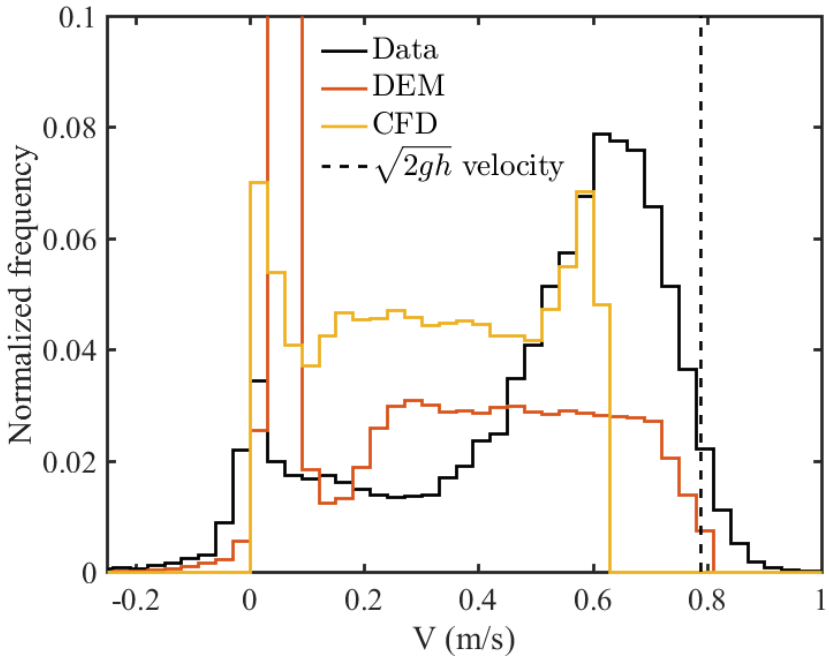

(a) Single spaced configuration

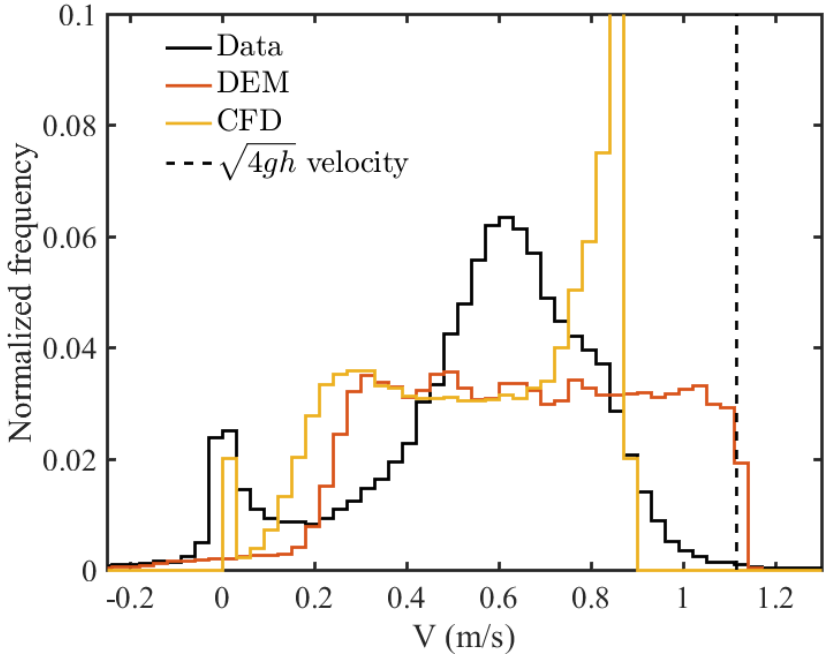

(b) Double spaced configuration

Figure D.5: Vertical velocity histograms for the ballotini material, size 12 horizontal mesh.

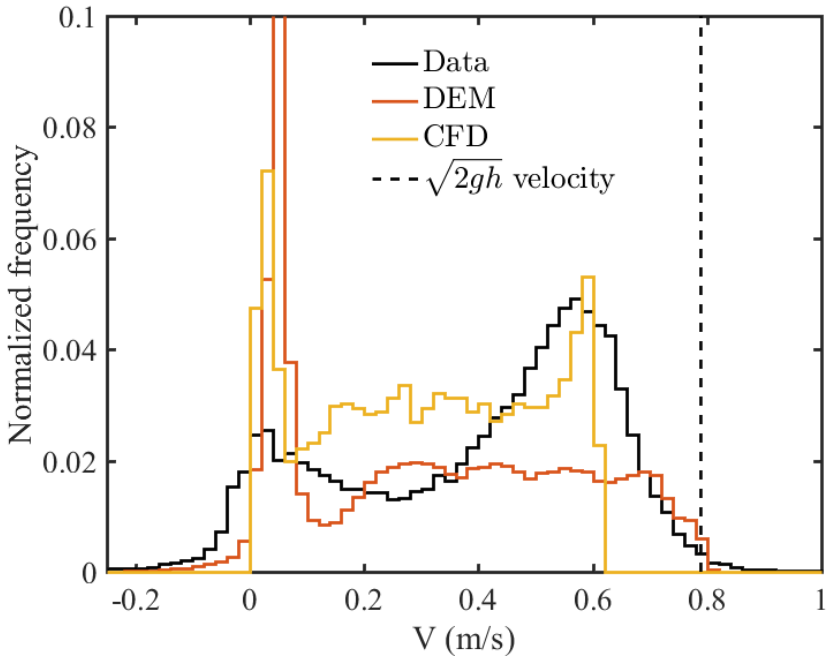

(a) Single spaced configuration

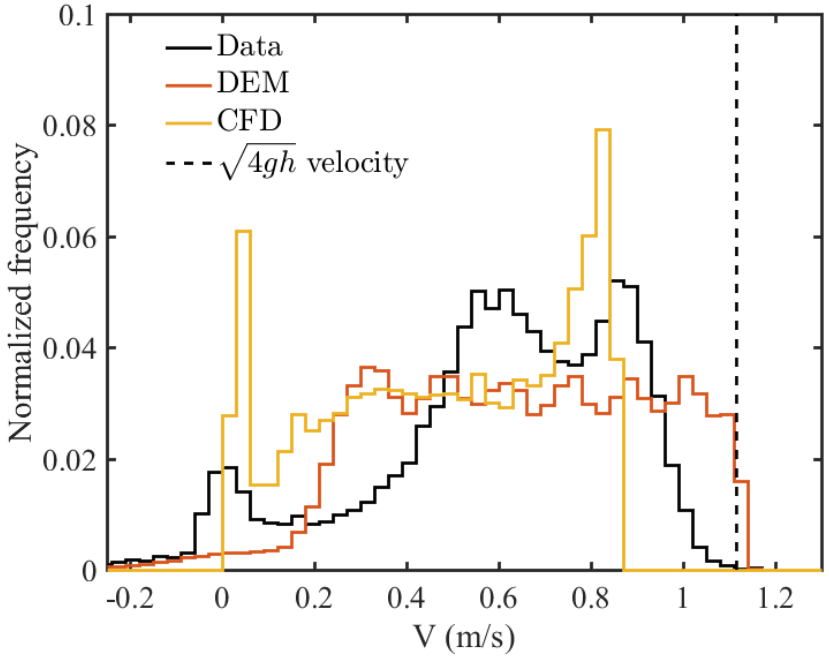

(b) Double spaced configuration

Figure D.6: Vertical velocity histograms for the ballotini material, size 14 horizontal mesh.

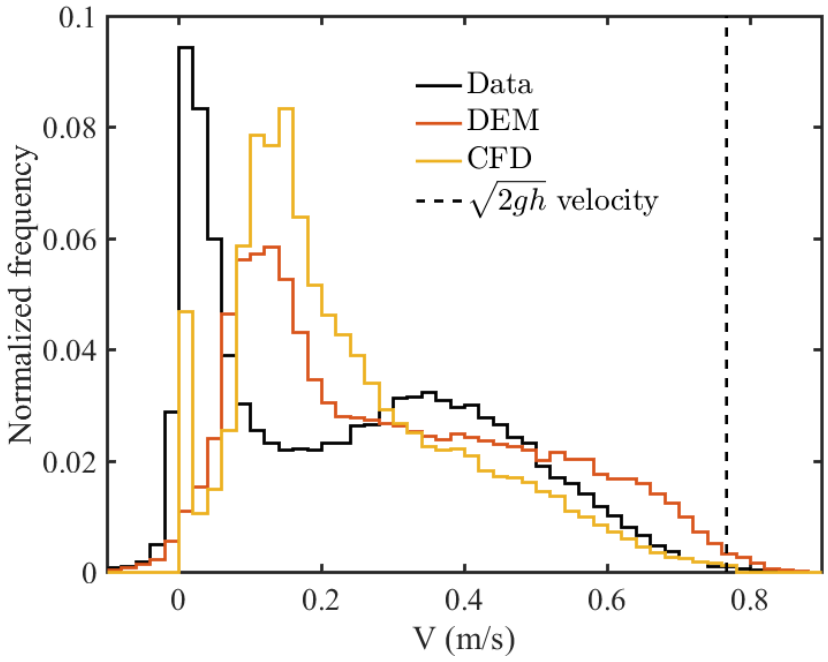

(a) Single spaced configuration

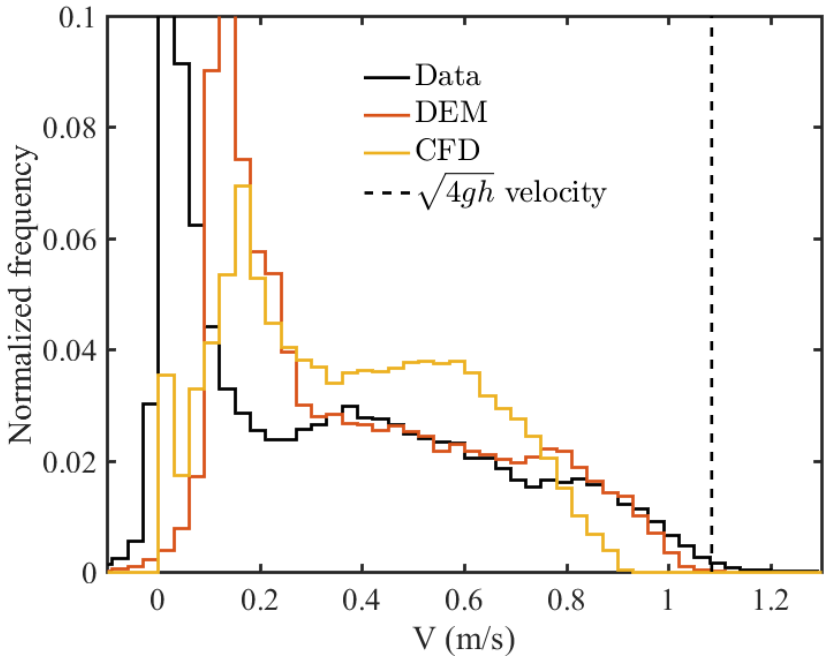

(b) Double spaced configuration

Figure D.7: Vertical velocity histograms for the ID50-K material, size 8 angled mesh.

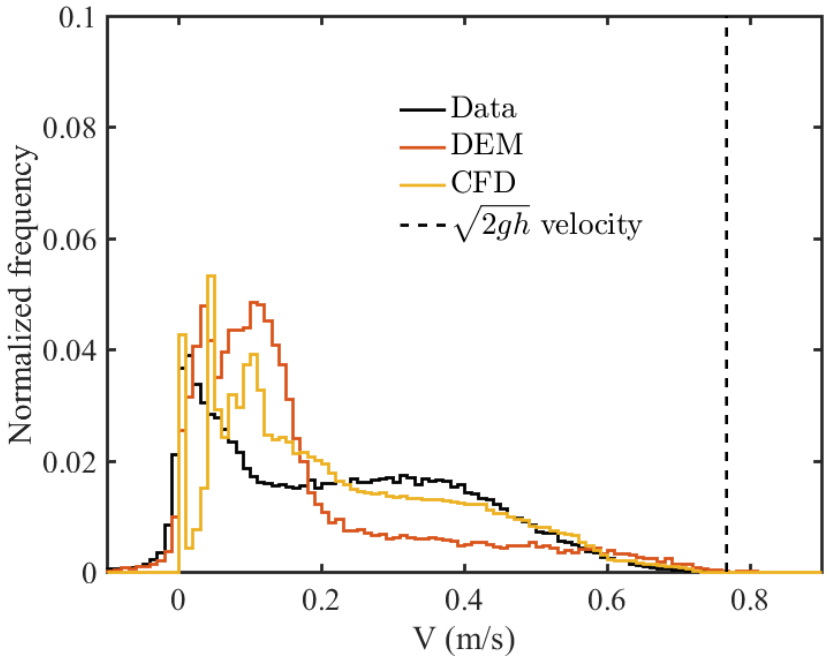

(a) Single spaced configuration

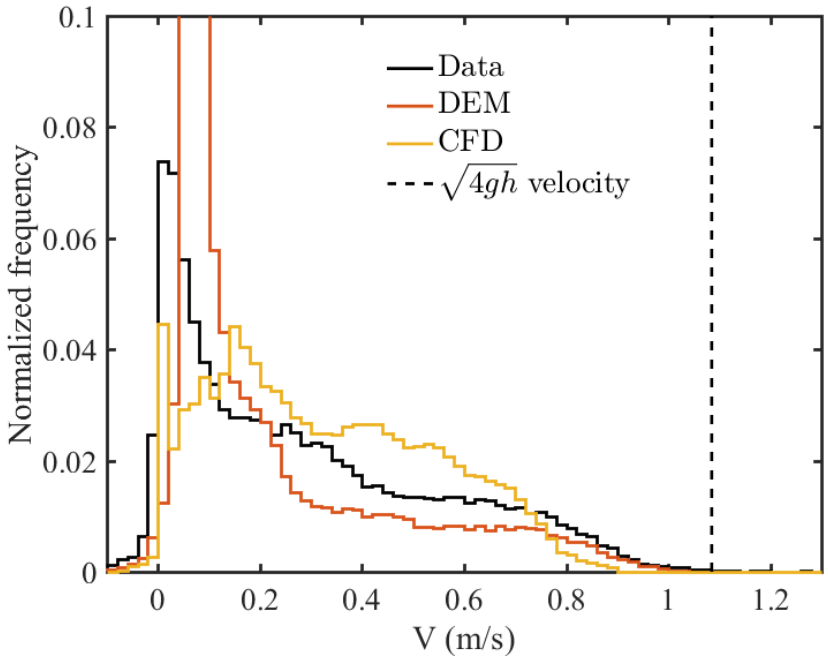

(b) Double spaced configuration

Figure D.8: Vertical velocity histograms for the ID50-K material, size 12 angled mesh.

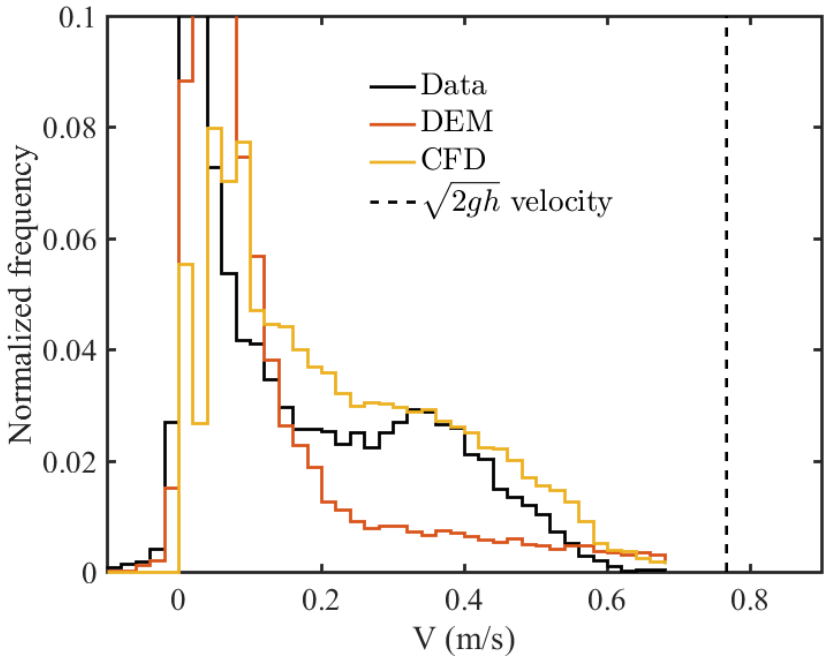

(a) Single spaced configuration

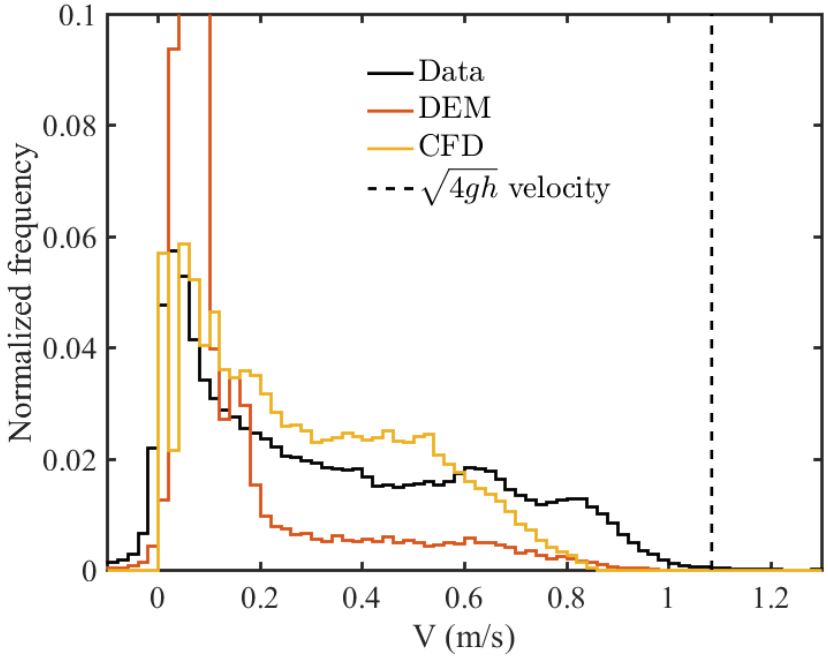

(b) Double spaced configuration

Figure D.9: Vertical velocity histograms for the ID50-K material, size 14 angled mesh.

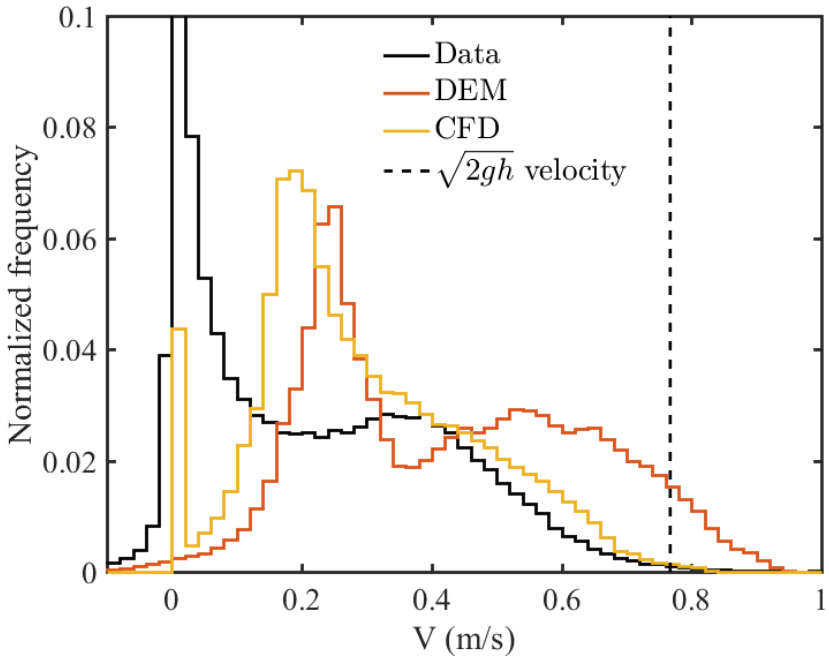

(a) Single spaced configuration

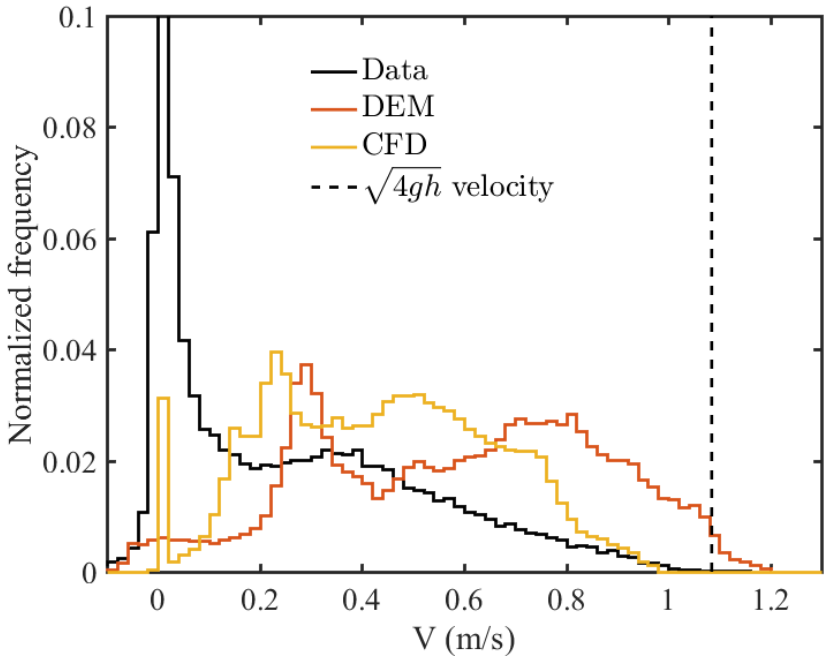

(b) Double spaced configuration

Figure D.10: Vertical velocity histograms for the ballotini material, size 8 angled mesh.

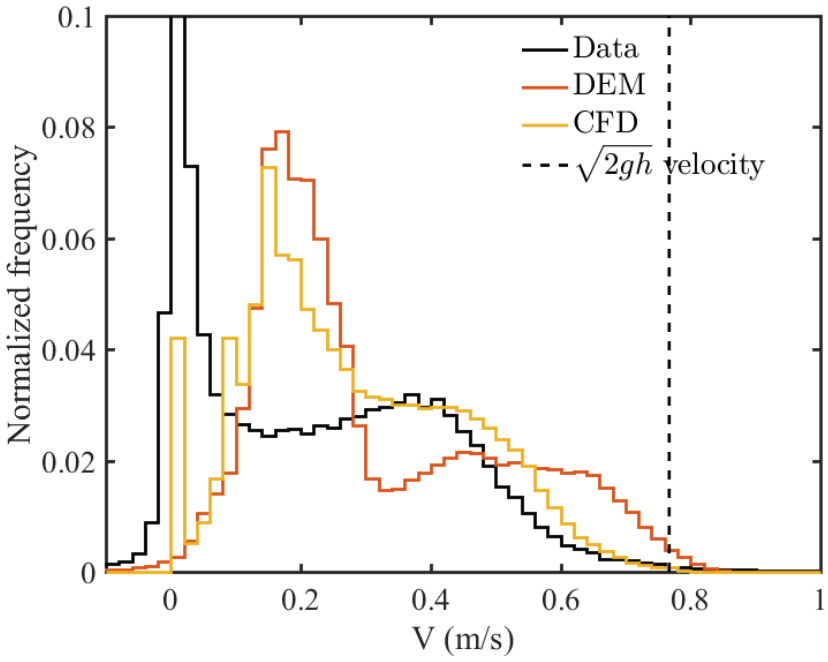

(a) Single spaced configuration

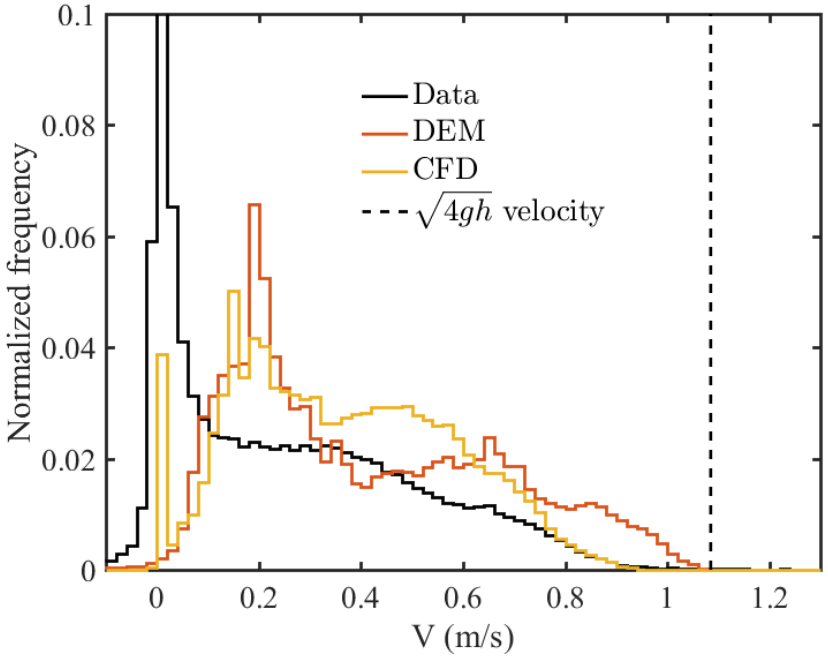

(b) Double spaced configuration

Figure D.11: Vertical velocity histograms for the ballotini material, size 10 angled mesh.

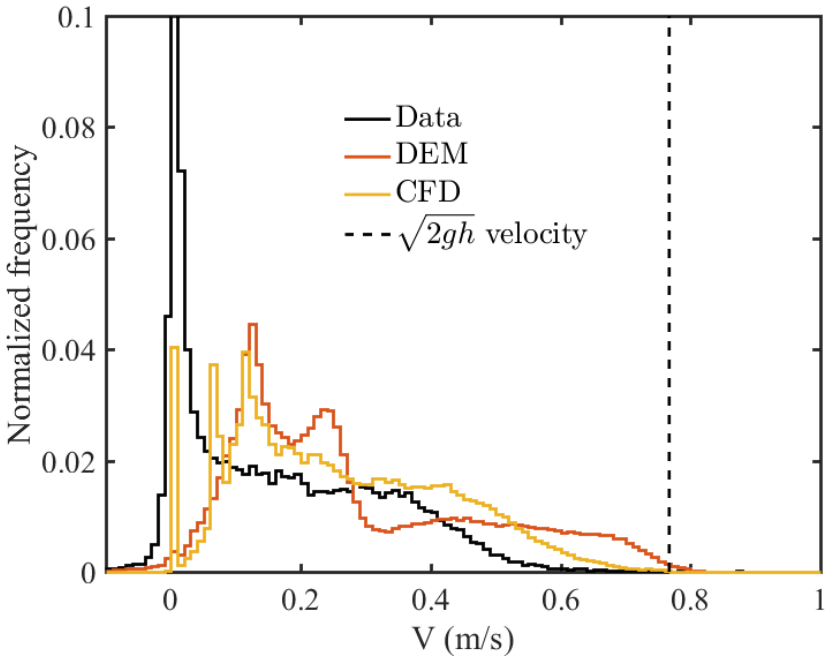

(a) Single spaced configuration

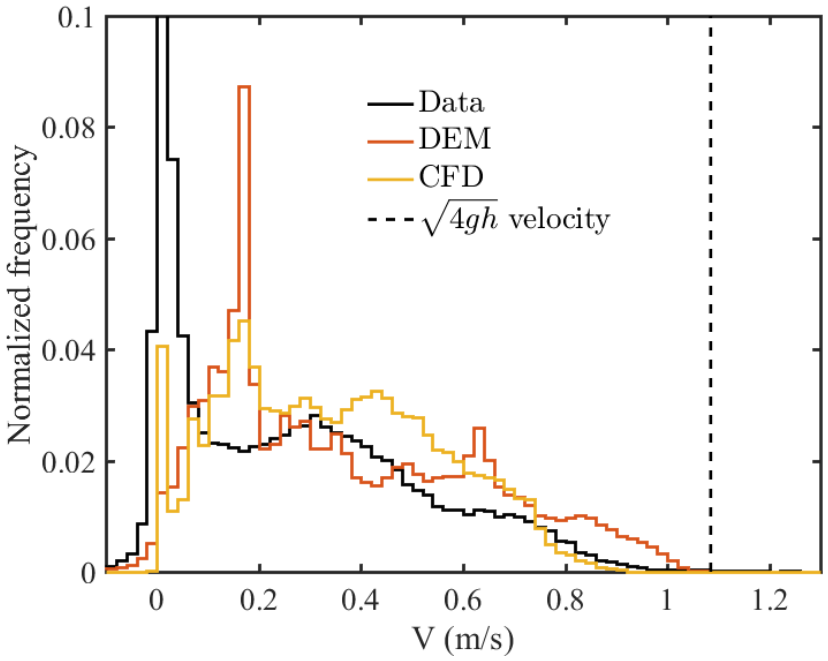

(b) Double spaced configuration

Figure D.12: Vertical velocity histograms for the ballotini material, size 12 angled mesh.

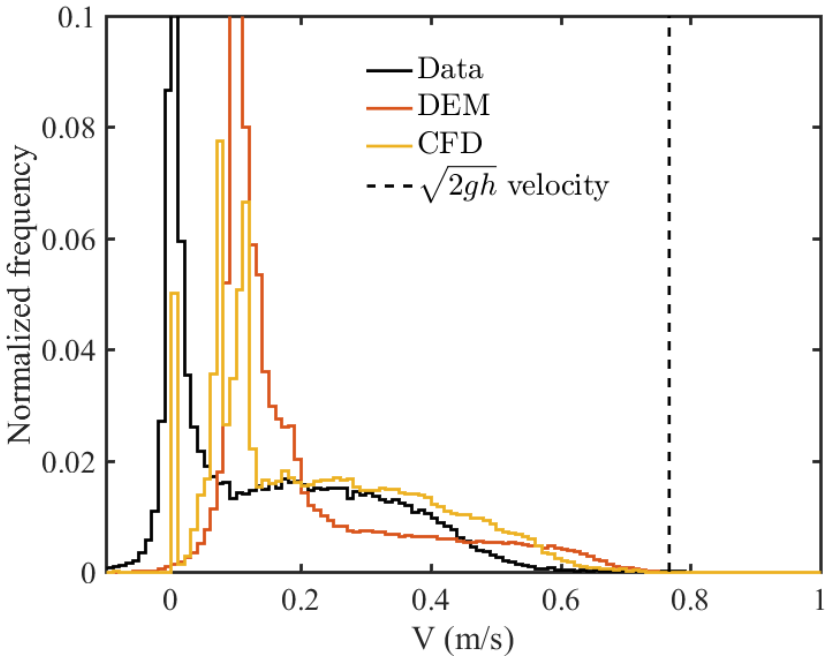

(a) Single spaced configuration

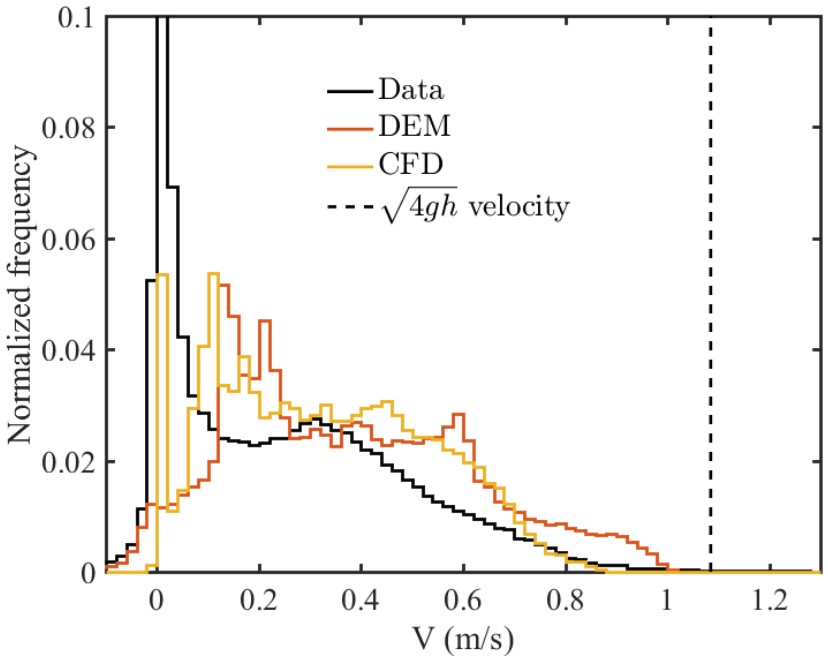

(b) Double spaced configuration

Figure D.13: Vertical velocity histograms for the ballotini material, size 14 angled mesh.

APPENDIX E

SILICON CARBIDE FOAM SQUARE RESULTS

This appendix will present the results of the ceramic foam test section. Development of the numerical models to simulate this configuration is on-going. Thus, the results are presented separately from the other geometries.

Table E.1 shows the results for both materials using 7.94 thick ceramic squares using whole squares and two different intra-square spacings. It should be noted that these squares would often break during dis-assembly and re-assembly of the test section, so square alignment and localized porosity is likely not identical between different flow tests. This also prevented slotted squares from being used, as the slotted shape was even weaker than the whole square. Therefore, these results may not be completely representative of the flow through the given square thickness. However, they are included here to show the general trends between a "wide" and a "narrow" spacing with the two different materials.

Table E.1: Mass flux results for the ceramic square configuration, 7.94 mm square thickness, whole squares.

Spacing (mm)	6.35	1.588
ID50-K material		
Mass flux (kg/sec-m^2)	55.7	21.0
Ballotini material		
	62.5	25.1

Table E.2 shows the results for both materials through the thicker 12.70 mm squares, through both whole and slotted squares. The slotted square configuration was unintentionally tested twice with the ballotini material. However, this led to an interesting observation. The squares within the test section were not inserted in an identical fashion for the two different rounds of flow testing. The difference in mass flux is likely due to the geometry

within the ceramic foam not being completely isotropic. On a full sized receiver geometry using many ceramic squares, such differences would likely be indistinguishable from inherent random "noise" between different flow tests. However, it could lead to localized variances of flow that could cause issues due to insufficient local cooling by the particles. More research should be done to see if the ceramic foam squares have a preferred orientation with regards to particle flow.

Table E.2: Mass flux results for the ceramic square configuration, 12.70 mm square thickness.

	Whole	Slotted
ID50-K material		
Mass flux (kg/sec-m^2)	43.4	49.3
Ballotini material		
	48.9	59.2
		55.2

Figures E.1 and E.2 show snapshots of the ceramic foam test section using the ID50-K material. The difference in accumulation between whole and slotted squares is quite obvious.

Figures E.3 and E.4 show snapshots from the ceramic foam test section using the ballotini material (which is much more visible against the black rubber backing sheet used in the ceramic foam test section). In addition to the differences in material accumulation, the individual streams of ballotini material flowing through the porous foam structure and into empty spaces are clearly seen.

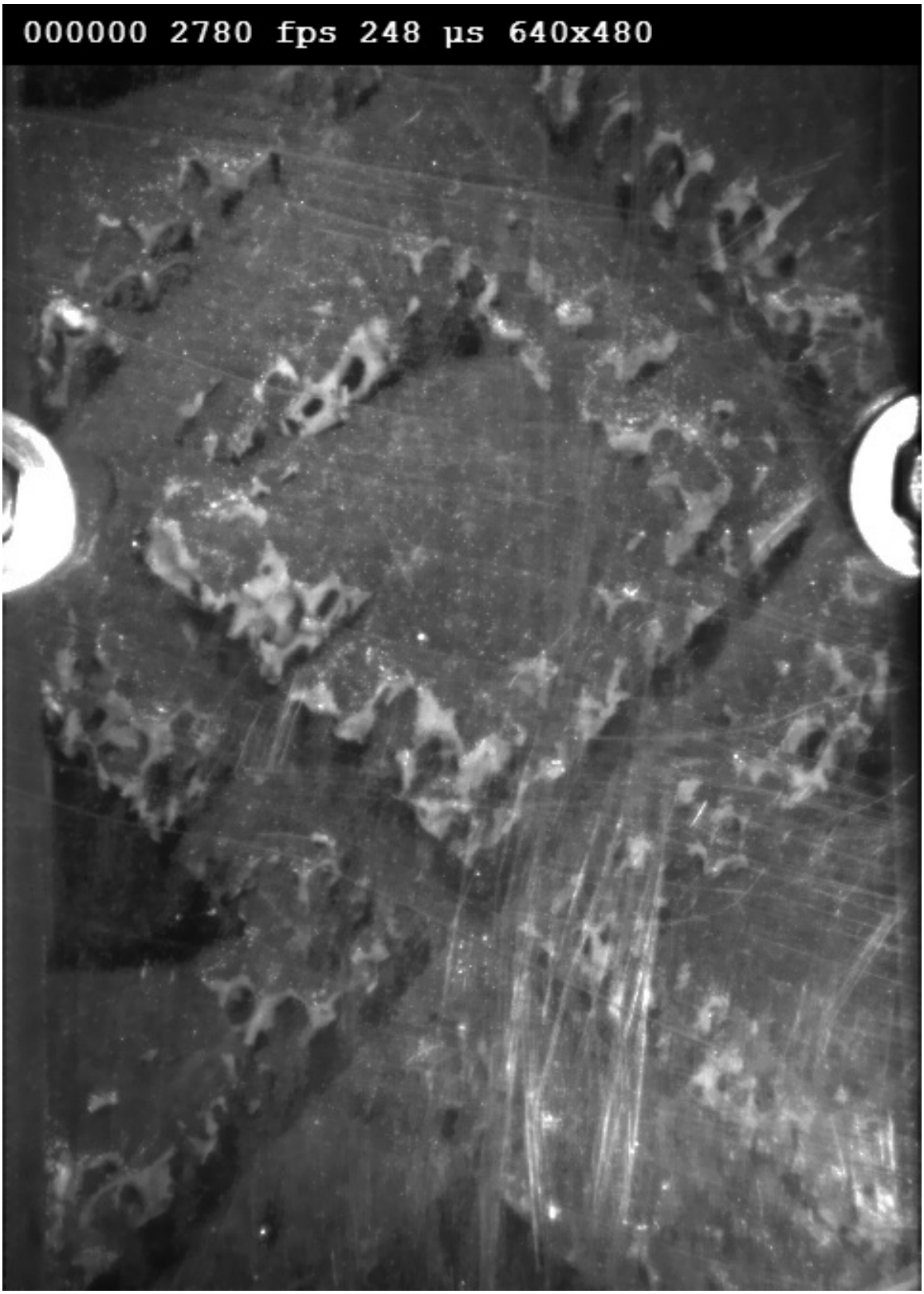

Figure E.1: Snapshot of the ceramic foam square test section, whole squares, ID50-K material.

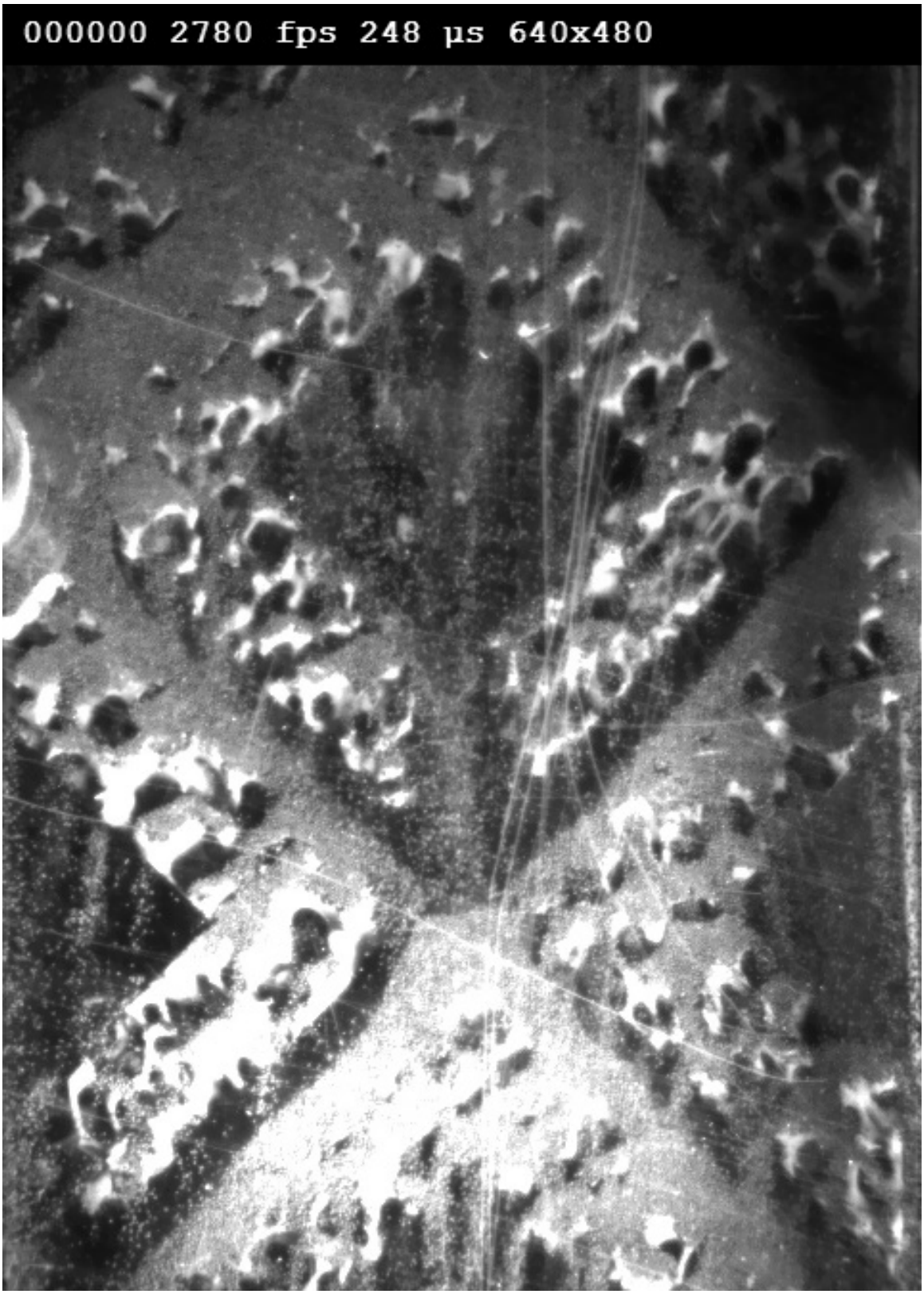

Figure E.2: Snapshot of the ceramic foam square test section, slotted squares, ID50-K material.

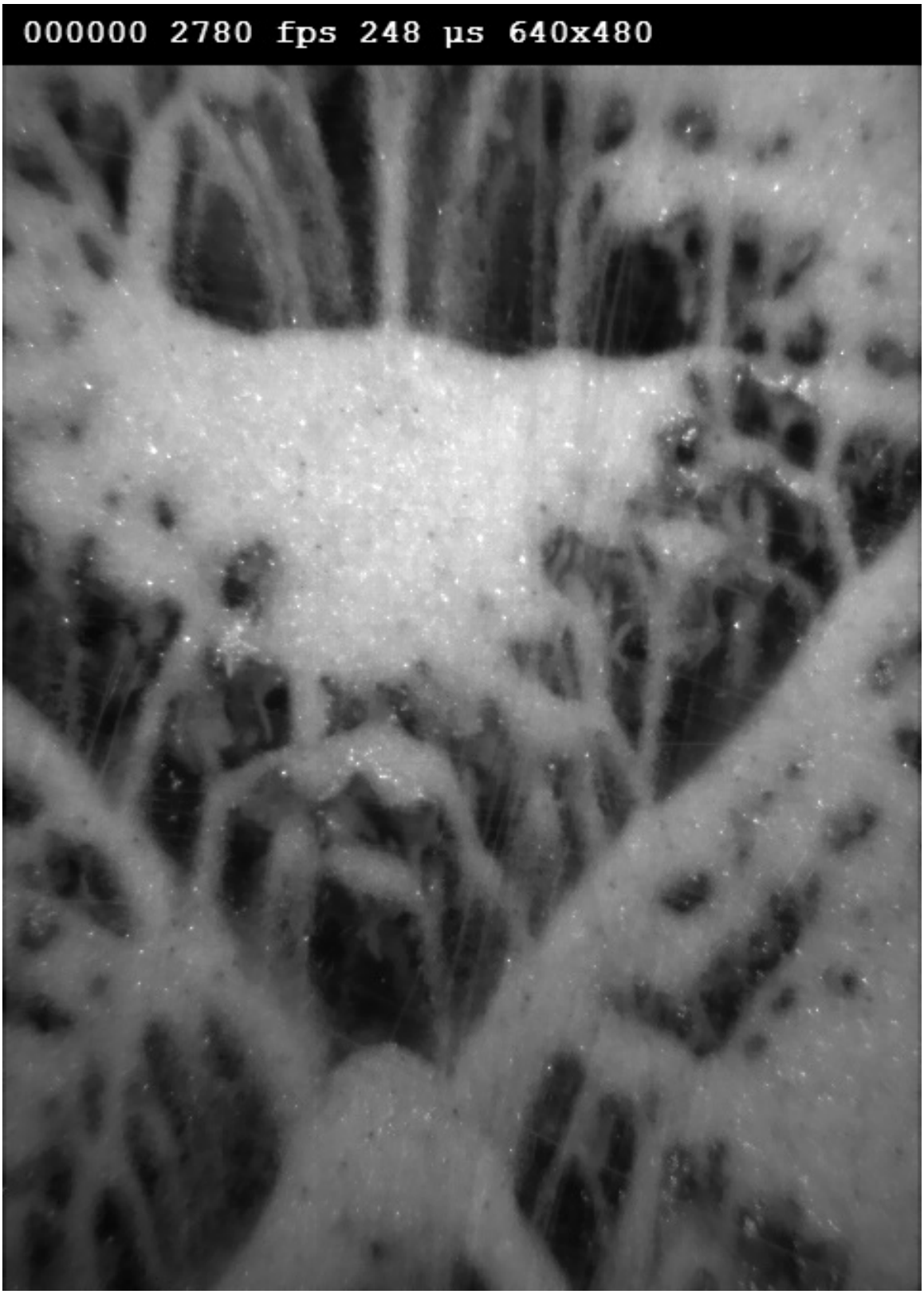

Figure E.3: Snapshot of the ceramic foam square test section, whole squares, ballotini material.

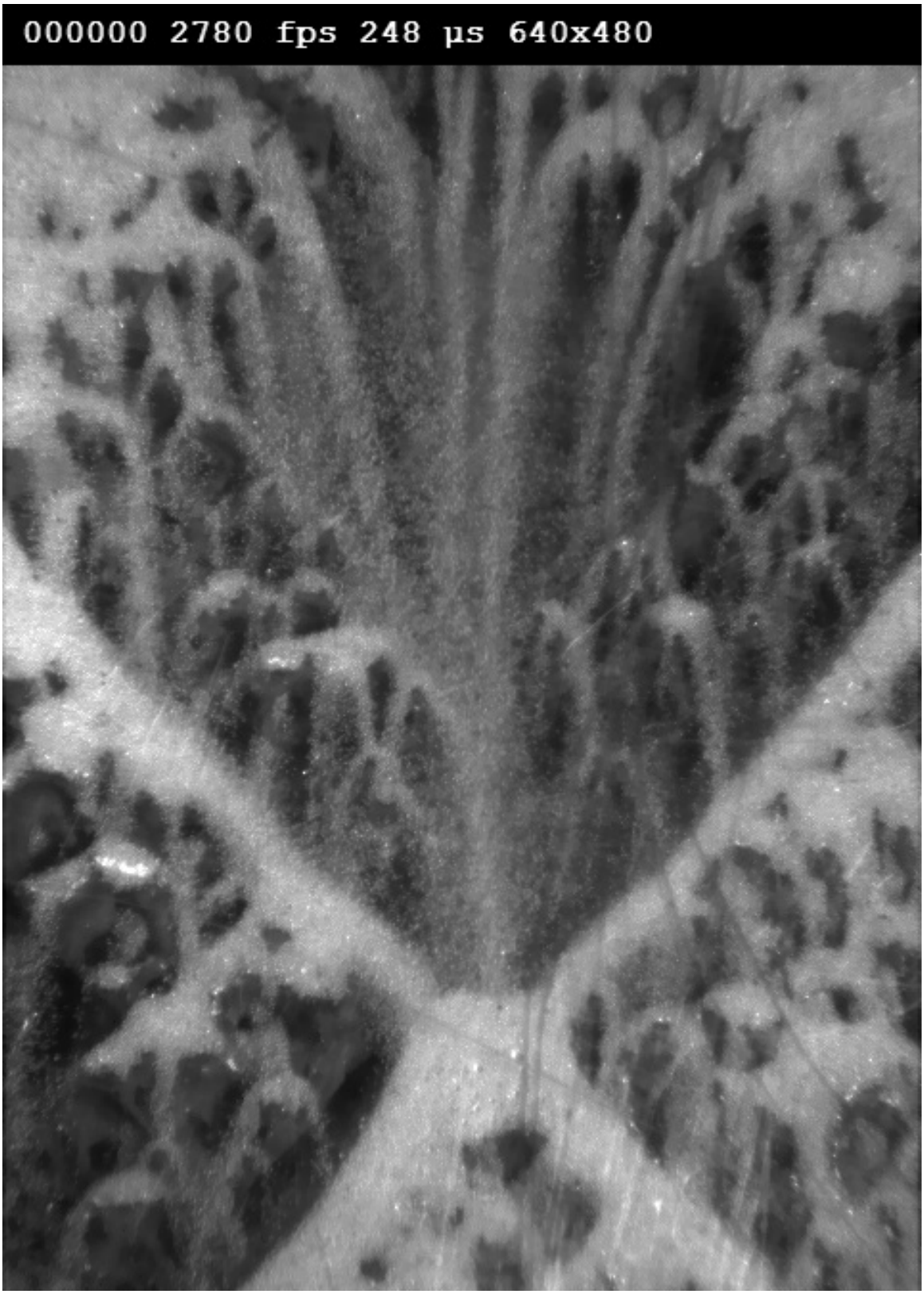

Figure E.4: Snapshot of the ceramic foam square test section, slotted squares, ballotini material.

REFERENCES

[1] Omar Behar, Abdallah Khellaf, and Kamal Mohammedi. "A review of studies on central receiver solar thermal power plants". *Renewable and Sustainable Energy Reviews* 23 (2013), pp. 12–39.

[2] H. L. Zhang et al. "Concentrated solar power plants: review and design methodology". *Renewable and Sustainable Energy Reviews* 22 (2013), pp. 466–481.

[3] Terresol Energy Investments, S. A. *Gemasolar Plant Information*. 2010.

[4] Rebecca I. Dunn, Patrick J. Hearps, and Matthew N. Wright. "Molten-salt power towers: newly commercial conentrating solar storage". *Proceedings of the IEEE* 100.2 (2012), pp. 504–515.

[5] J. Martin and J. Vitko Jr. *ASCUAS: A solar central receiver utilizing a solid thermal carrier, SAND82-8203*. Tech. rep. Sandia National Laboratories, 1982.

[6] P. K. Falcone, J. E. Noring, and J. M. Hruby. *Assessment of a solid particle receiver for a high temperature solar central receiver system, SAND85-8208*. Tech. rep. Sandia National Laboratories, 1985.

[7] Huajan Chen et al. "Computational Fluid Dynamics Modeling of Gas-Particle Flow Within a Solid-Particle Solar Receiver". *Journal of Solar Energy Engineering* 129 (2007), pp. 160–170.

[8] Kibum Kim et al. "A study of solid particle flow characterization in solar particle receiver". *Solar Energy* 83 (2009), pp. 1784–1793.

[9] Kibum Kim, Samir F. Moujaes, and Gregory J. Kolb. "Experimental and simulation study on wind affecting particle flow in a solar receiver". *Solar Energy* 84 (2010), pp. 263–270.

[10] Siri Sahib Khalsa et al. "CFD Simulation and Performance Analysis of Alternative Designs for High-Temperature Solid Particle Receivers". *Proceedings of ASME 2011 5th International Conference on Energy Sustainability and 9th Fuel Cell Science, Engineering and Technology Conference, ESFuelCell2011*. Aug. 2011.

[11] Marc Röger et al. "Face-down solid particle receiver using recirculation". *Journal of Solar Energy Engineering* 133 (2011).

[12] Clifford K. Ho et al. “Experimental and numerical studies of air curtains for falling particle receivers”. *Proceeding of ASME 2014 8th International Conference on Energy Sustainability and 12th Fuel Cell Science, Engineering and Technology Conference*. Boston, Massachusetts, 2014.

[13] Birgit Gobereit et al. “Assessment of a falling solid particle receiver with numerical simulation”. *Solar Energy* 115.Supplement C (2015), pp. 505 –517.

[14] R. Zanino et al. “Preliminary discrete element modeling of a falling particle curtain for CSP central tower receivers”. *AIP Conference Proceedings*. 2016.

[15] Hany Al-Ansary et al. “Solid particle receiver with porous structure for flow regulation and enhancement of heat transfer”. Pat. 9732986. Aug. 15, 2017.

[16] Matthew Golob et al. “Development and design prototype 300 kW-thermal high-temperature particle heating concentrator solar power system utilizing thermal energy storage”. *Proceedings of the ASME 2014 9th International Conference on Energy Sustainability ES2014*. 2014.

[17] Taegyu Lee et al. “Numerical simulation of particulate flow in interconnected porous media for central particle-heating receiver applications”. *Solar Energy* 113 (2015), pp. 14–24.

[18] A. W. Khayyat et al. “Measurement of particulate flow in discrete structure particle heating receivers”. *Proceedings of the ASME 2015 9th International Conference on Energy Sustainability*. 2015.

[19] Clifford K. Ho et al. “On-sun testing of an advanced falling particle receiver system”. *AIP Conference Proceedings* 1734.1 (2016).

[20] Clifford K. Ho et al. “Performance evaluation of a high-temperature falling particle receiver”. *Proceedings of the ASME 2016 10th International Conference on Energy Sustainability*. Charlotte, North Carolina, 2016.

[21] Brian P. Tighe and Matthias Sperl. “Pressure and motion of dry sand: translation of Hagen’s paper from 1852”. *Granular Matter* 9 (2007), pp. 141–144.

[22] W. A. Beverloo, H. A. Leniger, and J. Van de Velde. “The Flow of Granular Solids Through Orifices”. *Chemical Engineering Science* 15 (1961), pp. 260–269.

[23] Alvaro Janda, Iker Zurigual, and Diego Maza. “Flow rate of particles through apertures obtained from self-similar density and velocity profiles”. *Physical Review Letters* 108.248001 (2012).

[24] R. L. Brown and J. C. Richards. “Kinematics of the flow of dry powders and bulk solids”. *Rheologica Acta* 4 (1965), pp. 153–165.

[25] J. E. Hilton and P. W. Cleary. “Granular flow during hopper discharge”. *Physical Review E* 84 (2011).

[26] R. M. Nedderman et al. “The flow of granular materials - I: discharge rates from hoppers”. *Chemical Engineering Science* 37.11 (1982), pp. 1597–1609.

[27] B. J. Crewdson, A. L. Ormond, and R. M. Nedderman. “Air-impeded discharge of fine particles from a hopper”. *Powder Technology* 16 (1977), pp. 197–207.

[28] Mehmet Gundogdu. “Discharge characteristics of polydisperse powders through conical hoppers. Part 2: predictions for coarse, granular, free flowing powders”. *Particulate Science and Technology* 24 (2006), pp. 23–37.

[29] R. T. Fowler and J. R. Glastonbury. “The flow of granular solids through orifices”. *Chemical Engineering Science* 10 (1959), pp. 150–156.

[30] R. M. Nedderman. *Statics and Kinematics of Granular Materials*. Cambridge University Press, 1992.

[31] A. W. Jenike. “Gravity Flow of Bulk Solids”. *Bulletin of the Utah engineering experimental station* 108 (1961).

[32] István Oldal et al. “Outflow properties of silos: the effect or arching”. *Advanced Powder Technology* 23 (2012), pp. 290–297.

[33] Graham J. Weir. “Incompressible granular flow from wedge-shaped hoppers”. *Journal of Engineering Mathematics* 52 (2005).

[34] S. B. Savage. “The mass flow of granular materials derived from coupled velocity-stress fields”. *British Journal of Applied Physics* 16 (1965), pp. 1885–1888.

[35] J. C. Williams. “The rate of discharge of coarse granular materials from conical mass flow bins”. *Chemical Engineering Science* 32 (1977), pp. 247–255.

[36] Z. H. Gu, P. C. Arnold, and A. G. McLean. “Prediction of the flowrate of bulk solids from mass flow bins with conical hoppers”. *Powder Technology* 72 (1992), pp. 157–166.

[37] Z. H. Gu, P. C. Arnold, and A. G. McClean. “A simplified model for predicting the particle flowrate from mass flow bins”. *Powder Technology* 74 (1993), pp. 153–158.

[38] N. Standish and I. A. Meta. “Some kinetic aspects of continuous screening”. *Powder Technology* 41 (1985), pp. 165–171.

[39] Gary W. Delaney et al. “Testing the validity of the spherical DEM model in simulating real granular screening processes”. *Chemical Engineering Science* 68 (2012), pp. 215–226.

[40] P. J. Abrahamsson, S. Sasic, and A. Rasmuson. “On the continuum modeling of dense granular flow in high shear granulation”. *Powder Technology* 268 (2014), pp. 339–346.

[41] P. A. Cundall and O. D. L. Strack. “A Discrete Numerical Model for Granular Assemblies”. *Géotechnique* 29.1 (1979), pp. 47–65.

[42] C. R. K. Windows-Yule, D. R. Tunuguntla, and D. J. Parker. “Numerical modelling of granular flows: a reality check”. *Computational Particle Mechanics* 3 (2016), pp. 311–332.

[43] C. J. Coetzee. “Review: Calibration of the discrete element method”. *Powder Technology* 310 (2017), pp. 104–142.

[44] Z. Yan et al. “Discrete element modelling (DEM) input parameters: understanding their impact on model predictions using statistical analysis”. *Computational Particle Mechanics* 2 (2015), pp. 289–299.

[45] Paul W. Cleary and Mark L. Sawley. “DEM modelling of industrial granular flows: 3D case studies and the effect of particle shape on hopper discharge”. *Applied Mathematicl Modeling* 26 (2002), pp. 89–111.

[46] K. J. Dong, B. Wang, and A. B. Yu. “Modeling of particle flow and sieving behavior on a vibrating screen: from discrete particle simulation to process performance prediction”. *Industrial & Engineering Chemistry Research* 52 (2013), pp. 11333–11343.

[47] Xiaofang Wang et al. “Modeling on the hydrodynamics of a high-flux circulating fluidized bed with Geldart group A particles by kinetic theory of granular flow”. *Energy and Fuels* 24 (2010), pp. 1242–1259.

[48] Schalk Cloete, Shahriar Amini, and Stein Tore Johansen. “A fine resolution parametric study on the numerical simulation of gas-solid flows in a periodic riser section”. *Powder Technology* 205 (2011), pp. 103–111.

[49] Mukesh Upadhyay and Jong Ho Park. “CFD simulation via conventional two-fluid model of a circulating fluidized bed riser: influence of models and model parameters on hydrodynamic behavior”. *Powder Technology* 272 (2015), pp. 260–268.

[50] Anders Darelius et al. “CFD simulation of the high shear mixing process using kinetic theory of granular flow and frictional stress models”. *Chemical Engineering Science* 63 (2008), pp. 2188–2197.

[51] Chrestella Wardjiman et al. “Behaviour or a curtain of particles falling through a horizontally-flowing gas stream”. *Powder Technology* (2008).

[52] Chrestella Wardjiman et al. “Shape of a particle curtain falling in stagnant air”. *Powder Technology* (2009).

[53] Clifford K. Ho. “Advandes in central receivers for concentrating solar applications”. *Solar Energy* 152 (2017), pp. 38–56.

[54] W. Wu et al. “Numerical simulation of a centrifugal particle recevier for high-temperature concentrating solar applications”. *Numerical Heat Transer, Part A: Applications* 68.2 (2015), pp. 133–149.

[55] Janna Martinek and Zhiwen Ma. “Granular flow and heat-transfer study in a near-blackbody enclosed particle receiver”. *Journal of Solar Energy Engineering* 137 (2015).

[56] A. B. Morris et al. “Simulations of heat transfer to solid particles flowing through an array of heated tubes”. *Solar Energy* 130 (2016), pp. 101–115.

[57] A. B. Morris et al. “A conductive heat transfer model for particle flows over immersed surfaces”. *International Journal of Heat and Mass Transfer* 89 (2015), pp. 1277–1289.

[58] Gilles Flamant et al. “Desns suspension of solid particles as a new heat transfer fluid for concentrated solar thermal plants: on-sun proof of concept”. *Chemical Engineering Science* 102 (2013), pp. 567–576.

[59] H. Benhoit et al. “On-sun demonstratcion of a 750 °C heat transfer fluid for concentrating solar systems: dense particle suspension in tube”. *Solar Energy* 118 (2015), pp. 622–633.

[60] Pablo Fernández del Campo, Fletcher Miller, and Adam Crocker. “Three-dimensional modeling of a small particle solar receiver”. *Proceedings of the ASME 2013 7th International Conference on Energy Sustainability ES2013*. 2013.

[61] A. M. Mecit, F. J. Miller, and A. Whitmore. “Optical analysis and thermal modeling of a window for a small particle solar receiver”. *Energy Procedia* (2014).

[62] C. Ho et al. “Technology advancements for next generation falling particle receivers”. *Energy Procedia* 49 (2014), pp. 398–407.

[63] N. Siegel et al. “Physical properties of solid particle thermal energy storage media for concentrating solar power applications”. *Energy Procedia* 49 (2014), pp. 1015–1023.

[64] Clifford K. Ho et al. “Characterization of particle flow in a free-falling solar particle receiver”. *Proceedings of the ASME 2015 9th International Conference on Energy Sustainability*. San Diego, California, 2015.

[65] *Carboaccucast technical data sheet*. CARBO Ceramics Inc.

[66] *Performance Specification Glass Beads: For Cleaning and Peening*. 2009.

[67] *Potters Beads ballotini properties*. Potters Beads LLC.

[68] *Manual on Test Sieving Methods*. ASTM STP 447 B. 1985.

[69] *Test Sieving: Principles and Procedures*. Advantech Mfg. 2001.

[70] M. D. Abramoff, P. J. Magalhaes, and P. J. Ram. “Image processing with ImageJ”. *Biophotonics International* 11.7 (2004), pp. 36–42.

[71] Przemyslaw B. Kowalczuk and Jan Dryzmala. “Physical meaning of the Sauter mean diameter of spherical particulate matter”. *Particulate Science and Technology* 34.6 (2016), pp. 645–647.

[72] Jörg Schwedes. “Review on testers for measuring flow properties of bulk solids”. *Granular Matter* 5 (2003), pp. 1–43.

[73] I. Baker. *A Tretise on Masonry Construction*. John Wiley and Sons, Inc., 1914.

[74] Ramesh Kandasami and Tejas Gorur Murthy. “Effect of particle shape on the mechanical response of a granular ensemble”. *Geomechanics from Micro to Macro*. 2014.

[75] Takehiro Kojima and James A. Elliott. “Incipient flow properties of two-componenet fine powder systems and their relationships with bulk density and particle contacts”. *Powder Technology* 228 (2012), pp. 359–370.

[76] A. Melling. “Tracer particals and seeding for particle image velocimetry”. *Measurement Science and Technology* 8.12 (1997).

[77] William Thielicke. “The flapping flight of birds: analysis and application”. PhD thesis. University of Groningen, 2014.

[78] H. Huang, D. Dabiri, and M Gharib. “On errors of digital particle image velocimetry”. *Measurement Science and Technology* 8 (1997), pp. 1427–1440.

[79] William Thielicke and Eize J. Stamhuis. “PIVlab - towards user-friendly, affordable and accurate digital particle image velocitomitry in MATLAB”. *Journal of Open Research Software* 2.1 (2014), e30.

[80] Markus Raffel et al. *Particle Image Velocimitry: A Practical Guide*. 2nd edition. Springer, 2007.

[81] J. Westerweel, D. Dabiri, and M. Gharib. “The effect of a discrete window offset on the accuracy of cross-correlation analysis of digital PIV recordings”. *Experiments in Fluids* 23 (1997), pp. 20–28.

[82] D. P. Hart. “Super-resolution PIV by recursive local-correlation”. *Journal of Visualization* 3 (2000), pp. 187–194.

[83] F. Scarano. “Iterative image deformation methods in PIV”. *Measurement Science and Technology* 13 (2002), R1–R19.

[84] Stephen M. Pizer et al. “Adaptive histogram equalization and its variations”. *Computer Vision, Graphics, and Image Processing* 39 (19877), pp. 355–368.

[85] Matteo Frigo and Steven G. Johnson. “The design and implimentation of FFTW3”. *Proceeding of the IEEE* 93.2 (2005), pp. 216–231.

[86] Jerry Westerweel and Fulvio Scarano. “Universal outlier detection for PIV data”. *Experiments in Fluids* 39 (2005), pp. 1096–1110.

[87] R. M Lueptow, A. Akonur, and T. Shinbrot. “PIV for granular flows”. *Experiments in Fluids* 20 (2000), pp. 183–186.

[88] Richard D. Keane and Ronald J. Adrian. “Theory of cross-correlation analysis of PIV images”. *Applied Scientific Research* 49 (1992), pp. 191–215.

[89] Jeffery Avuilar and Daniel I. Goldman. “Robophysical study of jumping dymanics on granular media”. *Nature Physics* 12 (2016), pp. 278–283.

[90] H. Hertz. “On the contact of elastic solids”. *Journal für die reine und angewandte Mathematik* 92 (1881), pp. 156–171.

[91] R. D. Mindlin and H. Deresiewicz. “Elastic spheres in contact under varying oblique forces”. *Transactions of ASME, Series E. Journal of Applied Mechanics* 20 (1953), pp. 327–344.

[92] Alberto Di Renzo and Francesco P. Di Maio. “Comparison of contact-force models for the simulation of collisions in DEM-based granular flow codes”. *Chemical Engineering Science* 59 (2004), pp. 525–541.

[93] Christoph Kloss et al. “Models, algorithms and validation for opensource DEM and CFD-DEM”. *Progress in Computational Fluid Dynamics* 12.2/3 (2012), pp. 140–152.

[94] Steve Plimpton. “Fast parallel algorithms for short-range molecular dynamics”. *Journal of Computational Physics* 117 (1995), pp. 1–19.

[95] Utkarsh Ayachit. *The Paraview Guide: A Parallel Visualization Application*. 2015.

[96] Jun Ai et al. “Assessment of rolling resistance models in discrete element simulations”. *Powder Technology* 206 (2011), pp. 269–282.

[97] Robert L. Jackson, Itzhak Green, and Dan B. Marghitu. “Predicting the coefficient of restitution of impacting elastic-perfectly plastic spheres”. *Nonlinear Dynamics* 60.3 (2010), pp. 217–229.

[98] Richard G. Budynas and J. Keith Nisbett. *Shigley’s Mechanical Engineering Design*. 8th ed. McGraw Hill, 2008.

[99] *Lexan 9034 Sheet*. SABIC Innovative Plastics.

[100] Harold E. Sliney and Christopher DellaCorte. *The friction and wear of ceramic/ceramic and ceramic/metal combinations in sliding contact, NASA TM-106348*. Tech. rep. National Aeronautics and Space Administration, 1993.

[101] A. Lorenz, C. Tuozzolo, and M. Y. Lounge. “Measurements of impact properties of small, nearly spherical particles”. *Experimental Mechanics* 37 (1997), pp. 292–298.

[102] F. P. Bowden and D. Tabor. *The Friction and Lubrication of Solids: Part 2*. Clarendon Press, 1964.

[103] Michel Y. Louge and Michael E. Adams. “Anomalous behavior of normal kinematic restitution in the oblique impacts of a hard sphere on an elastoplastic plate”. *Physical Review E* 65 (2002).

[104] Christophe Geuzaine and Jean-François Remacle. “Gmsh: a three-dimensional finite element mesh generator with built-in pre- and post-processing dacilities”. *International Journal for Numerical Methods in Engineering* 0 (2009), pp. 1–24.

[105] Suhas V. Patankar. *Numerical Heat Transfer and Fluid Flow*. CRC Press, 1980.

[106] S. Acharya et al. “Pressure-based finite-volume methods in computational fluid dynamics”. *Journal of Heat Transfer* 129 (2007), pp. 407–424.

[107] Michael Schäfer. *Computational Engineering - Introduction to Numerical Methods*. Sringer, 2006.

[108] R. Courant, K. Friedrichs, and H. Lewy. “Über die partiellen differenzengleichungen der mathematischen physik”. *Mathematische Annalen* 1 (1927), pp. 32–74.

[109] R. Courant, K. Friedrichs, and H. Lewy. “On the partial difference equations of mathematical physics”. *IBM Journal of Research and Development* (1967), pp. 215–234.

[110] *Fluent Theory Guide*. Ansys Inc.

[111] B. E. (Brian Edward) Launder. *Lectures in mathematical models of turbulence*. London, New York: Academic Press, 1972.

[112] Dimitri Gidiaspow, Rukmini Bezburuah, and J. Ding. “Hydrodynamics of Circulating Fluidized Beds: Kinetic Theory Approach”. *7th Fluidization Conference*. 1992.

[113] M. Syamlal. *The particle-particle drag term in a multiparticle model of fluidization*. Tech. rep. Springfield, VA: National Technical Information Service, 1987.

[114] Satoru Ogawa, Akira Umemura, and Nobunori Oshima. “On the equations of fully fluidized granular materials”. *Journal of Applied Mathematics and Physics* 31 (1980), pp. 483–493.

[115] C. K. K. Lun et al. “Kinetic Theories for Granular Flow: Inelastic Particles in Couette Flow and Slightly Inelastic Particles in a General Flowfield”. *J. Fluid Mech.* 140 (1984), pp. 223–256.

[116] Jianmin Ding and Dimitri Gidaspow. “A bubbling fluidization model using kinetic theory of granular flow”. *AIChE Journal* (1990).

[117] M. Syamlal, W. Rogers, and T. J. O’Brien. *MFIX Documentation: Volume1, Theory Guide*. National Technical Information Service. Springfield, VA, 1993.

[118] David G. Schaeffer. “Instability in the Evolution Equations Describing Incompressible Granular Flow”. *Journal of Differential Equations* 66 (1987), pp. 19–50.

[119] Matthew Sandlin. “An experimental and numerical study of granular hopper flows”. MA thesis. The Georgia Institute of Technology, 2013.

[120] Peter J. Blau. *Friction Science Technology: From Concepts to Applications*. Second. CRC Press, 2008.

[121] Masahide Otsubo, Catherine O'Sullivan, and Tom Shire. "Empirical assessment of the critical time increment in explicit particulate discrete element method simulations". *Computers and Geotechnics* 86 (2017), pp. 67–79.

[122] S. Torquato, T. M. Truskett, and P. G. Debenedetti. "Is random close packing of spheres well defined?" *Physical Review Letters* 84.10 (2000), pp. 2064–2067.

[123] Robert S. Farr and Robert D. Groot. "Close packing density of polydisperse hard spheres". *The Journal of Chemical Physics* 131 (2009), p. 244104.

[124] P. C. Johnson and R. Jackson. "Frictional-collisional constitutive relations for granular materials, with application to plane shearing". *J. Fluid Mech.* 176 (1987), pp. 67–93.

[125] Hanbin Zhong et al. "The difference between specularity coefficient of 1 and no-slip solid phase wall boundary conditions in CFD simulation of gas-solid fluidized beds". *Powder Tecnhology* 286 (2015), pp. 740–743.

[126] Loup Verlet. "Computer "experiments" on classical fluids. I. Thermodynamical properties of Lennard-Jones molecules". *Physical Review* 159 (1967), pp. 98–103.

[127] Kyle J. Berger and Christine M. Hrenya. "Challenges of DEM: II. Wide particle size distributions". *Powder Technology* 264 (2014), pp. 627–633.

[128] G. Lu, J. R. Third, and C. R. Müller. "Discrete element models for non-spherical particle systems: from theoretical developments to applications". *Chemical Engineering Science* 127 (2015), pp. 425–465.

[129] Doraiswami Ramkrishna. *Population balances theory and applications to particulate systems in engineering*. San Diego, CA: Academic Press, 2000.

[130] Alan D. Randolph. *Theory of particulate processes; analysis and techniques of continuous crystallization*. New York: Academic Press, 1971.

[131] Robert McGgraw. "Desscription of aerosol dynamics by the quadrature method of moments". *Aerosol Science and Technology* 27.2 (1997), pp. 255–265.

[132] Rong Fand, Daniele L. Marchisio, and Rodney O. Fox. "Application of the direct quadrature method of mements to polydisperse gas-solid fluidized beds". *Powder Technology* 139 (2004), pp. 7–20.

[133] Schalk Cloete, Stein Tore Johansen, and Shahriar Amini. "Grid independence behaviour or fluidized bed reactor simulations using the two fluid model: Effect of particle size". *Powder Technology* 269 (2015), pp. 153–165.

[134] Tsan Hsing Shih et al. "A new k-ϵ eddy viscosity model for high Reynolds number turbulent flows". *Computers Fluids* 24.3 (1995), pp. 227–238.

[135] A. B. Morris et al. "Development of soft-sphere contact models for thermal heat conduction in granular flows". *AIChE Journal* 62.12 (2016), pp. 4526–4535.

[136] Hamada M. Abdelmotalib et al. "Heat transfer process in gas-solid fluidized bed combusters: A review". *International Journal of Heat and Mass Transfer* 89 (2015), pp. 567–575.

[137] Tarek J. Jamaleddine and Madhumita B. Ray. "Application of computational fluid dynamics for simulation of drying process: A review". *Drying Technology* 28 (2010), pp. 120–154.

[138] Machael F. Modest. *Radiateve Heat Transfer*. 2nd edition. Academic Press, 2003.

[139] Joshua A. Dickenson and John J. Sansalone. "Deiscrete phase model representation of particulate matter (PM) for simulating PM separation by hydrodynamic unit operations". *Environmental Science and Technology* 43 (2009), pp. 8220–8226.

[140] S. Cloete et al. "Evalutaion of a Lagrangian discrete phase modeling approach for application to industrial scale bubbling fluidized beds". *10th International Conference on Circulating Fluidized Beds and Fluidization Technology CFB-10*.

[141] Kun Lou et al. "CFD-DEM study of mixing and dispersion behaviors of solid phase in a bubbling fluidized bed". *Powder Technology* 274 (2015), pp. 482–493.

[142] A. Nikolopouos et al. "Numerical investigation and comparison of coarse grain CFD-DEM and TFM in teh case of a 1MW$_t h$ fluidized bed carbonator simulation". *Chemical Engineering Science* 163 (2017), pp. 189–205.

[143] T. Oschmann and M. Schiemann a nd H. Kruggel-Emden. "Development and verification of a resolved 3D inner particle heat transfer model for the discrete element method (DEM)". *Powder Technology* 291 (2016), pp. 392–407.

[144] Hao Wu et al. "Numerical simulation of heat transfer in packed pebble beds: CFD-DEM coupled with particle thermal radiation". *International Journal of Heat and Mass Transfer* 110 (2017), pp. 393–405.

[145] Amit Amritkar, Surya Deb, and Danesh Tafti. “Efficient parallel CFD-DEM simulations using OpenMP”. *Journal of Computational Physics* 256 (2014), pp. 501–519.

[146] C. L. Wu et al. “Parallel algorithms for CFD-DEM modeling of dense particulat flows”. *Chemical Engineering Science* 118 (2014), pp. 221–244.

[147] J. Q. Gan, Z. Y. Zhou, and A. B. Yu. “A GPU-based DEM approached for mofelling of particulate systems”. *Powder Technology* 301 (2016), pp. 1172–1182.

[148] Ping Lin et al. “Simulation of Heat Transfer in Granular Systems with DEM on GPUs”. *Proceedings of the 7th International Conference on Discrete Element Methods*. Ed. by Xikui Li, Yuntian Feng, and Graham Mustoe. Singapore: Springer Singapore, 2017, pp. 1389–1397.

[149] Anthony J. Wheeler and Ahmad R. Ganji. *Introduction to Engineering Experimentation*. 2nd edition. Pearson Eductaion, 2004.

[150] *Agilent 34970A user's guide*. Agilent Technologies, Inc. 2003.

[151] *Keli DEFY load cell specifications*. Keli Sensing Technology Co. 2014.

[152] Kazuyoshi Iwashita and Masanobu Oda. “Rolling resistance at contacts in simulation of shear band development by DEM”. *Journal of Engineering Mechanics* 124.3 (1998), pp. 285–292.

[153] M. Syamlal and T. J. O'Brien. “Computer simulations of bubbles in a fluidized bed”. *AIChE Symposium Series* 85 (1989), pp. 22–31.

[154] L. G. Gibilaro et al. “Generlized friction factor and drag coefficient correlations for fluid-particle interactions”. *Chemical Engineering Science* 40.10 (1985), pp. 1817–1823.

[155] C.-Y. Wen and Y. H. Yu. “Mechanics of fluidization”. *Chemical Engineering Progress Symposium Series* 62 (1966), pp. 100–111.

[156] Lu Huilin and Dimitri Gidaspow. “Hydrodynamics of bindary fluidization in a riser: CFD simulaiton using two granular temperatures”. *Chemical Engineering Science* 58 (2003), pp. 3777–3792.

[157] Sabri Ergun. “Fluid flow through packed colums”. *Chemical Engineering Progress* 48.2 (1952), pp. 89–94.

[158] G. K. Batchelor. *An Introduction to Fluid Dynamics*. 2nd edition. Cambridge University Press, 1999.